Mechanics of Hybrid Bonded-Bolted Joints

Kobyé Bodjona

Department of Mechanical Engineering
McGill University, Montreal

July 2016

A thesis submitted to McGill University in partial fulfillment of
the requirements of the degree of Doctor of Philosophy

Dinner in the Alfama during ICCS18 in Lisbon (June 2015)

Left to right: Larry Lessard (supervisor), the author and Gyu-Hyeong Lim (master's student)

Dedication

To my parents

My most ardent supporters

Abstract

Large mechanical structures, for example aircraft and motor vehicles, usually consist of a number of subassemblies. This necessitates the use of joints, which locate the subassemblies and transfer loads between them. While necessary, joints introduce discontinuities into the structure that act as stress raisers and regions of possible failure initiation. Consequently, joint design is crucial for achieving satisfactory structural strength.

Joining composite structures is all the more challenging compared to metallic structures. This is due to the brittle nature of many composite materials, which permits only modest plastic deformation and limits the corresponding mitigation of stress concentrations prior to fracture. This is particularly problematic for bolted composite structures. In order to fully exploit the potential of composites, it is thus necessary to develop more efficient means of joining them.

In recent years, several investigators have shown experimentally that a combination of bonding and bolting can, sometimes, produce a joint that is stronger than either of these joints by itself. This could potentially result in a more efficient joint and is therefore of particular interest for composite structures. These investigators found that load sharing between the adhesive and bolt is important for achieving the benefits of "hybridization". However, they had only limited understanding of the most effective way to achieve load sharing. Furthermore, they made no attempt to predict the strength of hybrid joints by means of mathematical modelling.

In response to these shortcomings in the literature, this thesis follows a two-pronged approach. First, in Chapters 3-4, load sharing in hybrid bonded-bolted joints is addressed. An efficient numerical model is developed in Chapter 3 for this end. This model is validated experimentally, after which it is used in a global sensitivity analysis in Chapter 4 to determine the most important factors influencing load sharing. Of the various parameters considered, it is found that the adhesive yield strength, overlap length and adhesive hardening modulus have the greatest effects, by a considerable margin.

Next, in Chapters 5-10, strength is addressed. For this purpose, an original mathematical model of a hybrid bonded-bolted joint is developed from first principles. This model distills the physical problem to the essentials, yet accounts for many complex effects found in real joints. Through comparison with the experimental results presented in Chapter 10, the model is shown to be capable of providing a basic prediction of bonded-, bolted-, and hybrid-bonded-bolted joint strength. Agreement to within 8% of the experiment is demonstrated. The model is subsequently used to elucidate key behaviours of hybrid bonded-bolted joints in Chapter 11.

Based on the findings of this thesis, increased confidence has been established in the feasibility of the hybrid bonding-bolting concept. Furthermore, the developed analysis methodology has demonstrated significant promise for use as part of a design tool.

Abrégé

Des grandes structures mécaniques, par exemple celles des avions ou des véhicules automobiles, se composent généralement d'un certain nombre de sous-ensembles. Ces sous-ensembles doivent être reliés entre eux par des joints, dont le but principal est de localiser les composants et transférer des charges structurales entre eux. Bien que nécessaire, les joints introduisent des discontinuités dans la structure qui agissent comme des concentrations de contrainte et sont les emplacements ou des fissures s'amorcent. La conception et l'analyse des joints sont donc de la plus haute importance pour la réalisation d'une résistance structurale acceptable.

L'assemblage de structures composites est d'autant plus difficile par rapport à celui de structures métalliques. Cela est dû à la nature fragile de beaucoup de matériaux composites, ce qui ne permet qu'une légère redistribution de la charge/réduction limitée des concentrations de contrainte par des déformations plastiques avant la fissuration. Afin d'exploiter pleinement le potentiel des composites, il est donc nécessaire de trouver des moyens efficaces pour les assembler.

Au cours des dernières années, plusieurs chercheurs ont montré lors d'essais expérimentaux qu'il existe des situations dans lesquelles une combinaison de collage et boulonnage mène à un joint plus résistant. Cela pourrait aboutir à une connexion plus efficace et est donc d'un intérêt particulier pour les structures composites. Ces chercheurs ont découvert que la répartition de charge entre l'adhésif et le boulon est importante pour réaliser les avantages d'hybridation. Cependant, ils avaient seulement une compréhension limitée de la meilleure façon de réaliser cette répartition de charge. En outre, ils n'ont fait aucune tentative pour prédire la résistance de ces joints au moyen de modèles mathématiques.

En réponse à ces lacunes dans la littérature, cette thèse fait suite à une approche à deux volets. Dans Chapitres 3-4, un modèle numérique efficace est développé pour prédire la répartition de charge dans les joints hybrides. Ce modèle est validé expérimentalement, après quoi il est utilisé dans une analyse de sensibilité globale pour déterminer les facteurs les plus importants qui influent sur la répartition de charge.

Dans la deuxième partie de la thèse, Chapitres 5-10, la résistance est adressée. A cette fin, un modèle mathématique original d'un joint hybride collé-boulonné est développé à partir de zéro. Ce modèle représente le problème du joint hybride à l'essentiel, tout en représentant la plupart des effets complexes trouvés dans des joints réels. Le modèle est indiqué comme étant en mesure de fournir une prévision de base de la résistance. Il est ensuite utilisé pour élucider les comportements clés de ces joints dans Chapitre 11.

Sur la base des conclusions de cette thèse, un bon degré de confiance a été établi dans la faisabilité même de la notion de collage-boulonnage hybride. De plus, la méthodologie d'analyse surdéveloppée a démontré un fort potentiel pour utilisation dans le cadre d'un outil de conception.

Preface

The idea for this thesis germinated in 2011, when Professor Lessard (supervisor) was appointed principal investigator of a CRIAQ research project entitled "COMP 506: Design and analysis of hybrid (bonded and bolted) joints for aerospace structures." Soon after, I was admitted to McGill to pursue a doctoral degree in the Structures and Composite Materials Laboratory, and it was decided that I would participate in this project. The actual work would commence upon my arrival in Montreal in August 2012.

COMP 506 is a collaborative research effort between various Canadian research institutes, universities and industry, aimed at investigating the merits of combining bonding and bolting for joining composite aerospace structures. Another goal of the project is to develop an analysis methodology that can be used to optimize hybrid bonded-bolted joint design, and to incorporate this into a specialist software package. The project partners include Bombardier, L3-Com, Delastek, National Research Council of Canada, Carleton University, École Polytechnique de Montréal and, of course, McGill University, where the work presented in this thesis was undertaken.

The main research tasks are divided among the three partner universities, with McGill tasked primarily with modelling hybrid-bonded bolted joints and developing an analysis methodology. Carleton is focused on experimental research, while École Polytechnique is responsible for design optimization. Invariably, there has been and continues to be some overlap of this division of labor. Nevertheless, mostly as originally intended, this thesis is primarily on modelling of hybrid bonded-bolted joints. The models developed and described herein strive to address a range of complex effects while maintaining good computational efficiency; this was done expressly in order that they might be useful for the optimization portion of the project. Furthermore, in order to facilitate its inclusion in the desired specialist software, the strength model presented in Chapters 5-9 was implemented as a fully standalone MATLAB code.

It is my hope that this thesis has made at least some small contribution towards improving understanding of hybrid bonded-bolted joints. If even a single reader should find the work to be of interest, then the endeavour will have been well worth it.

Kobyé Bodjona

Montreal, July 2016

Acknowledgements

I would like to start this acknowledgements section by expressing my profound gratitude to my supervisor, Professor Larry Lessard. Throughout my PhD, Larry entrusted me with significant freedom to explore my varied interests. Nevertheless, he was always available for discussion and to offer suggestions when needed. This arrangement contributed greatly to the intellectual and personal growth that I enjoyed during my time at McGill.

I would also like to thank the various academic and industrial partners of the COMP 506 project for their support and for many interesting exchanges over the past four or so years. In this last regard, a special mention must go to Karthik Raju and Gyu-Hyeong Lim, my colleagues at McGill, with whom I established a close working relationship.

I am much obliged to the Antje Graupe-Pryor foundation and McGill University for providing me with a McGill Engineering Doctoral Award (MEDA). This funding was pivotal in allowing me to pursue my doctoral studies in Canada. Equally, I would also like to thank CRIAQ for providing supplementary financial support.

It goes without saying that I am grateful to all of the members of the Composites and Structures Materials Laboratory, past and present, for their advice and friendship. The memories that I have created inside and outside of the lab with you all will remain with me forever.

My appreciation is also extended to my committee members, Professor Pascal Hubert and Professor Damiano Pasini, for taking the time and effort to read and correct this thesis.

The support, encouragement and empathy of my parents have been invaluable throughout my studies. Without them, this journey would have been immeasurably more difficult.

This final paragraph is reserved for my beloved wife, Diana, who never hesitated a moment to come on this adventure with me and stood by me every step of the way. Thanks for being a calming influence in my life.

Contributions of the Author

All of the work presented in this thesis was performed by the author with the exception of the adhesive stress-strain characterization mentioned in Chapters 3 and 10. This characterization was performed by a master's student, Gyu-Hyeong Lim, and colleagues at Carleton University; it is appropriately referenced in the text wherever encountered. In addition, the author acknowledges the assistance of Sean Fielding, Nicholas Gilbert, Karthik Prasanna Raju, Denis Campagne, Kavish Bujun and Nicolas Krumenacker in the manufacture and quality control of the laminated composite plates used in the experiments of Chapters 3 and 10. Sean Fielding and Karthik Raju furthermore helped to cut these plates and manufacture joint specimens. Stéphane Héroux (Delastek Inc.) provided invaluable assistance with drilling and measurement of bolt holes in these specimens. Finally, Adam Smith is gratefully acknowledged for his help with soldering lead wires to the miniscule strain gauges on the instrumented bolt (Chapter 3).

Table of Contents

Table of Figures

List of Acronyms

ASTM	American Society for Testing and Materials
BVP	Boundary Value Problem
CFRP	Carbon Fibre Reinforced Polymer
CLT	Classical Lamination Theory
CRIAQ	Consortium de Recherche et d'Innovation en Aérospatiale au Québec
EFAST	Extended Fourier Amplitude Sensitivity Test
ESL	Equivalent Single Layer
ETW	Elevated Temperature and Wet
FAA	Federal Aviation Administration
FAST	Fourier Amplitude Sensitivity Test
FEA	Finite Element Analysis
FEM	Finite Element Method
FRP	Fibre Reinforced Polymer
GBJM	Global Bolted Joint Method
GFRP	Glass Fibre Reinforced Polymer
GHJM	Global Hybrid Joint Method
GR	Goland and Reissner
GRPIM	Galerkin Radial Point Interpolation Method
GSA	Global Sensitivity Analysis
HBB	Hybrid Bonded-Bolted
HBF	Hybrid Bonded-Fastened
HBP	Hybrid Bonded-Pinned
HSM	Hertz-Signorini-Moreau
LHS	Left Hand Side
MNO	Materially-Nonlinear Only
MQ	Multi-Quadratic
MR	Mindlin-Reissner

PVW	Principle of Virtual Work
RBF	Radial Basis Function
RHS	Right Hand Side
RPI	Radial Point Interpolating
RPIM	Radial Point Interpolation Method
RTD	Room Temperature and Dry
RTW	Room Temperature and Wet
SRIM	Short Random fibre Injection Molded
TAST	Thick Adherend Shear Test

Chapter 1: Introduction

Large aerospace structures are increasingly made of composite materials. These materials typically consist of two phases: matrix and reinforcement. The matrix is a binding phase that serves primarily to align, protect, and support the reinforcement. The reinforcement provides most of the material's stiffness and strength in the direction in which it is aligned. When the matrix is a polymer and the reinforcement consists of fibres, the material is referred to as a fibre reinforced polymer (FRP). When multiple sheets or *plies* of this material are stacked in a layerwise fashion, the combination is known as a laminated composite (see Figure 1.1). In aerospace structures, the fibres are typically semi-continuous carbon filaments, arranged in bundles or *tows* in either a unidirectional or woven pattern.

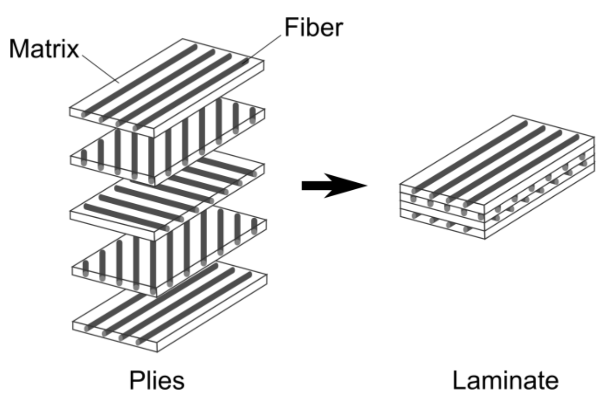

Figure 1.1: Composition of a laminated composite

Laminated composites offer excellent performance in terms of stiffness- and strength-to-weight ratio, corrosion resistance and fatigue resistance. In the late 1970s and early 1980s, "laminates" were first introduced in secondary civil aircraft structures such as flaps, nacelles and spoilers. In 1984, the first CFRP primary aircraft structure was put into service in the Boeing 737 horizontal tailplane [1]. Subsequently, in the 1990s and early 2000s composites spread to many other primary structures such as center wingboxes and pressure bulkheads. Today, they are found in almost all major primary aircraft structures. Figure 1.2 shows an overview of their use in a contemporary passenger aircraft.

Figure 1.2: Use of composites in the Boeing 787 [2]

Besides the aerospace industry, composite materials are also growing in popularity in the marine, automotive and renewable energy industries. As a case in point, it is predicted that wind turbine manufacturers' use of carbon fibre will exceed that of aerospace manufacturers within the next ten years [3].

Nevertheless, composites are not without their problems. Because the fibres provide most of their strength, laminated composites are weak when loaded transversely to the plies. This places them at risk of a transverse failure mode known as delamination. Furthermore, the large aspect ratios of fibres used in high-performance composites means that they are prone to microbuckling and that the materials are generally poor in compression. Yet another issue is that they are problematic to join. This last issue constitutes the overarching theme of this thesis.

1.1 Issues in the Joining of Composite Structures

Most large, complex structures are assemblies. As an example, an exploded view of the Bombardier Global Express 6000 airframe is shown in Figure 1.3. Importantly, assemblies require joints to locate their various subassemblies and transfer loads between them. Although there are many different kinds of joints, three principal classes can be identified; these are shown schematically in Figure 1.4.

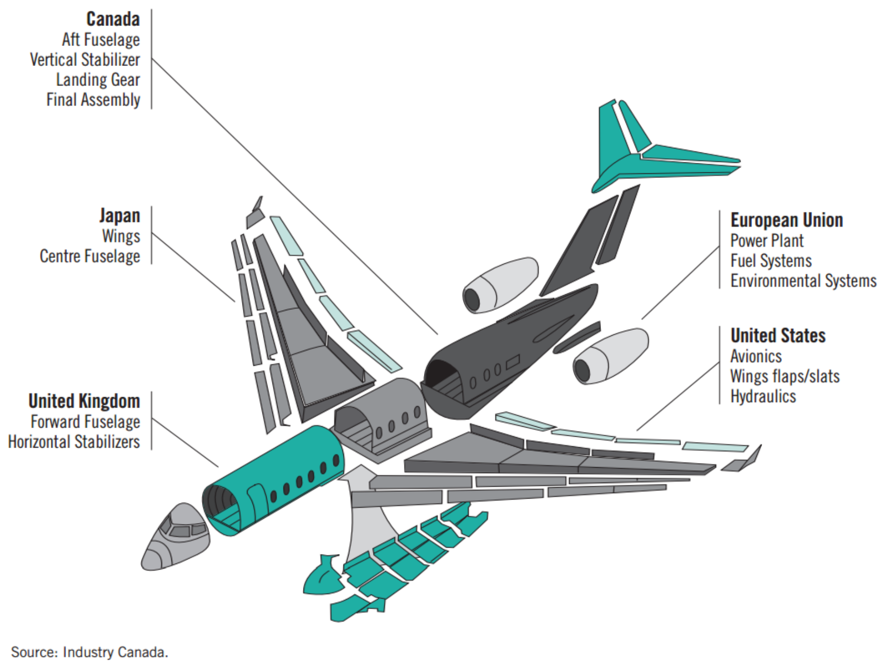

Figure 1.3: Bombardier Global Express assembly [4]

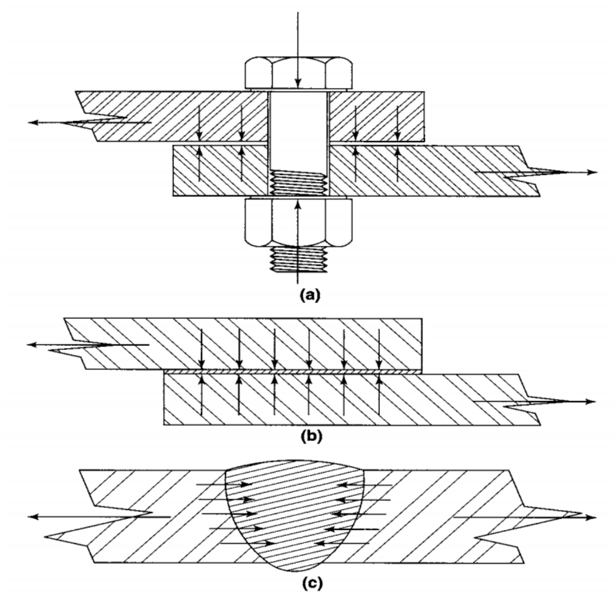

Figure 1.4: Principal classes of joints (a) mechanical fastening (b) chemical adhesion (c) welding [5]

Joints are an important consideration in the design of structures because they introduce geometric and material discontinuities that act as stress raisers. They are thus high-risk regions for the initiation of material failures. Some example sources of stress concentration in joints are depicted in Figure 1.5.

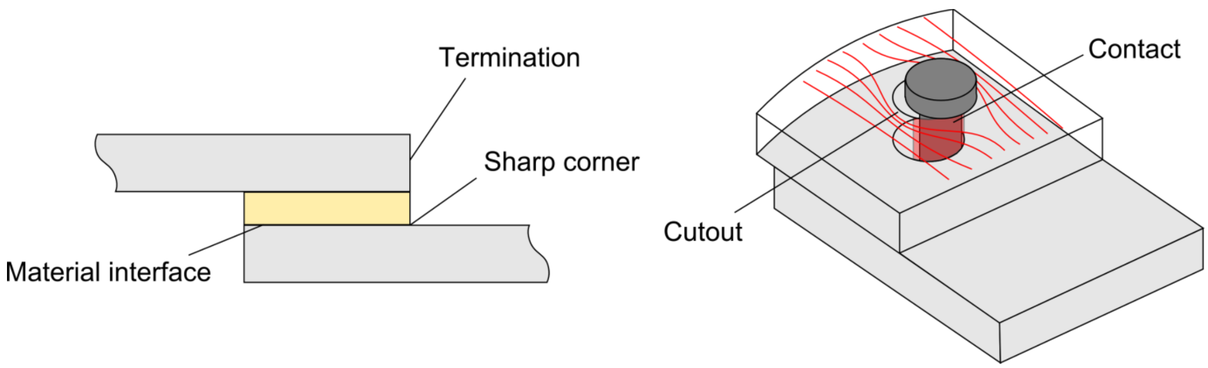

Figure 1.5: Example sources of stress concentration in joints

For the joining of *thermoset* composite structures in particular, only two of the principal classes of joints shown in Figure 1.4 are applicable[1], namely:

- Mechanical fastening (bolting, riveting…)
- Adhesive bonding

Regarding the former, it is well-known that mechanically fastened joints are typically more efficient in metallic structures than those in composite structures. This is shown for bolted joints in Figure 1.6 [6]. The reason is that metal alloys are, generally speaking, significantly more ductile than FRP composites. Thus, the inevitable stress concentrations that occur at bolt holes can be substantially relieved through gross plastic yielding of the metal in the vicinity of the holes. By contrast, in composite structures there is only limited stress relief through plastic yielding. Fracture therefore typically occurs at a lower load and at a lower ratio of joint-strength-to-adherend-strength (also known as the joining efficiency).

[1] Welding is in fact applicable to *thermoplastic* composite structures; however, neither welding nor thermoplastics are further addressed in this thesis.

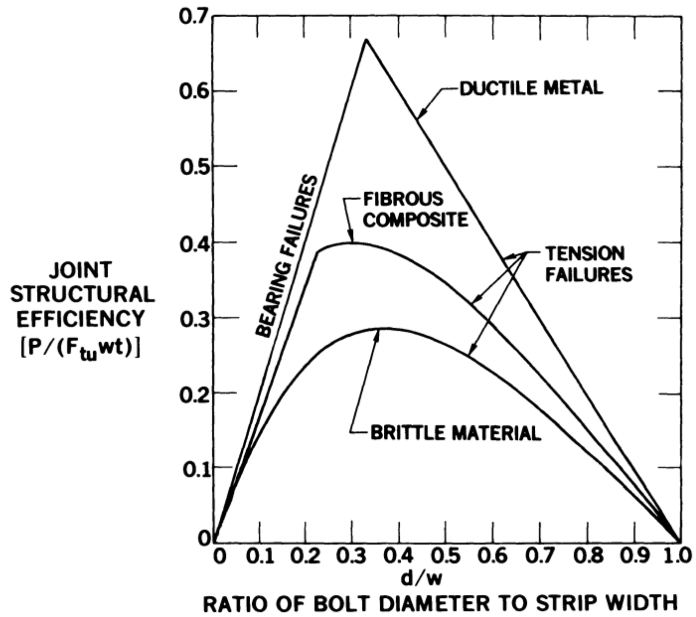

Figure 1.6: Strengths of bolted joints in brittle, ductile and composite materials [6]

This decreased joining efficiency results in the need for more bolt rows, thickened adherends, inserts and similar features, resulting in relatively heavy joints. Ultimately, this limits the overall weight saving that is achievable by using composite instead of metal alloy. There is consequently a growing realization that the full potential of composites will not be realized as long as fasteners are required in composite structures [7].

Contrary to bolting, bonding of composite structures and of metallic structures is fundamentally quite similar. Given two joints—one with composite adherends and one with metallic adherends, but otherwise with the same bonding system and dimensions—if the adherend in-plane and bending stiffnesses are similar then so are the stresses and strains set up in the adhesive. Consequently, similar cohesive strengths are achieved.[2]

---

[2] For both composite and metallic adherends, careful surface preparation is tantamount for achieving optimal bond strength and the coveted cohesive (intra-bondline) failure mode shown in Figure 1.7-c. A recent FAA best practices workshop on bonded joints revealed that OEMs consider consistent surface preparation to be the most important issue in manufacturing high quality bonded joints [8].

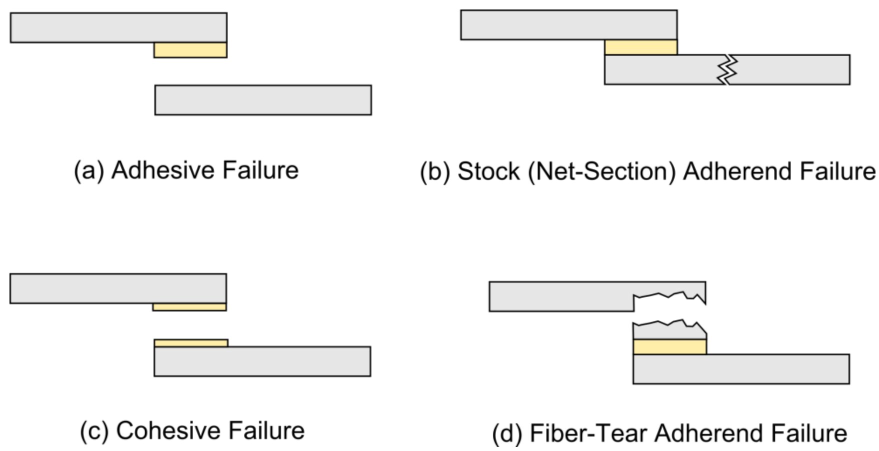

Figure 1.7: Possible failure modes in a composite-to-composite bonded joint

A caveat to the similarity of bonding composites and metals is adherend failure. In many bonded joints, the bondline is so strong that the failure must run outside the bondline and into the adherends. Metallic adherends will typically yield prior to fracture, while composites will undergo brittle fracture. In addition, the two adherend materials react quite differently to out-of-plane loading. Such loading occurs, for example, in the single-lap joint depicted in Figure 1.7; the eccentricity of the load path and lack of midplane symmetry of this joint result in a significant bending moment (called secondary bending) in the overlap region (see Figure 1.8).

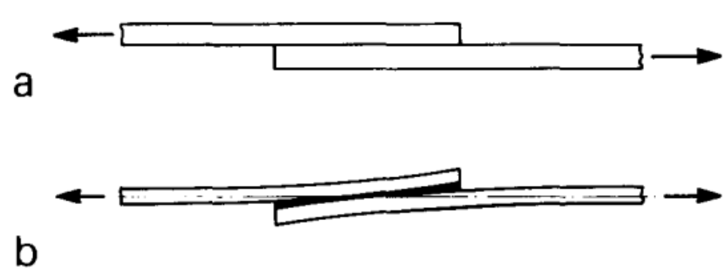

Figure 1.8: Secondary bending in a single-lap joint (a) undeformed configuration (b) deformed configuration showing bending of overlap [9]

Secondary bending creates peel stresses in both the adhesive and adherends. These are greatest near the overlap edges. Since composite laminates are weak in the transverse direction, interlaminar failure may ensue in these regions. This results in the fibre-tear adherend failure mode shown in Figure 1.7-d. Bonded composite joints should thus be designed to minimize secondary bending wherever possible. In thick composite structures, this can potentially be achieved by replacing single-lap joints with stepped-lap or splice joints. Importantly, if transverse failures are suppressed or minimized, bonded composite joints can achieve similar joining efficiencies to bonded metallic joints, both of which are greater than what can be achieved using bolts [10]. There thus appears to be significant scope to replace bolted joints in new structures with more efficient bonded joints, which could help to move towards the goal of realizing the full potential of composite structures.

Nevertheless, a major issue is that bonded joints cannot currently be certified in primary aircraft structures. The U.S. Federal Aviation Administration (FAA) regulations for design and construction of transport aircraft (14 CFR 25.601) state that:

"The airplane may not have design features or details that experience has shown to be hazardous or unreliable." [11]

Unfortunately, bonded joints in both composite and metallic structures are highly sensitive to processing conditions and are prone to hard-to-detect defects known as kissing bonds [12, 13]. Making matters worse, bonded joint failure is not progressive but is typically sudden and catastrophic. Consequently, at the present time, bonded joints are practically impossible to certify as a standalone joining mechanism in primary aircraft structures.

A potential solution to this conundrum is to somehow impart the adhesive joint with a damage tolerance mechanism. The question of exactly how this might be achieved is a trending topic of research. Preliminary suggestions include the use of corrugated bonding surfaces to potentially arrest cracks [14], stitching of the composites [15] or the use of mechanical fasteners in conjunction with adhesive. The latter approach is hereafter called hybrid bonding-fastening, encompassing both hybrid bonding-bolting and hybrid bonding-pinning. The particular focus of the present thesis, in the scope of the overarching research program, shall be on the hybrid bonding-bolting technique.

1.2 The Case for Hybrid Bonding-Bolting

Hybrid bonding-bolting is an alternative joining technique that consists of simultaneous bonding and bolting of the components to be joined (hereafter called the adherends). An example of a hybrid bonded-bolted (HBB) joint is shown in Figure 1.9. In the previous section, this technique was presented as a potential means of imparting an adhesive joint with a certain level of damage tolerance. There is no doubt that when used in a HBB joint, the bolts are able to provide the joint with residual strength following failure of the adhesive. This fact has long been understood and was comprehensively shown by Hart-Smith in the 1980s [16].

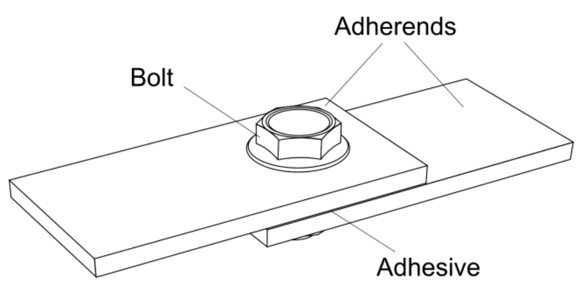

Figure 1.9: Hybrid bonded-bolted joint

Hart-Smith was also among the first to argue that the addition of bolts to a bonded joint does not necessarily provide any additional benefits beyond fail safety. He showed that the dissimilarity in stiffness between the adhesive load path and the bolt load path causes the adhesive to carry almost the entire load. The bolts thus effectively remain inactive unless the adhesive fails. The implication of this appears to be that there is no particular difficulty in designing a HBB joint. It is merely a question of designing a bonded joint to withstand a given target load, in addition to a bolted joint that provides an acceptable level of residual strength in case of adhesive damage. In other words, the bolts “guarantee” the minimum joint strength to be expected[3]. This leads to two important observations regarding the use of hybrid bonding-bolting as a damage tolerance mechanism:

1) HBB joints can potentially enable weight savings if the target strength and the minimum acceptable residual strength of the joint are different. For example, if the target joint strength is 15 kN but, in the case of initial failure it is acceptable to have only 10 kN residual strength. In this case, a bolted joint may be designed that can carry 10 kN. If the addition of adhesive is able to increase the joint's strength to 15 kN, then this "hybrid" may be a lighter joint than a bolted joint designed to carry the entire 15 kN.

2) If the target joint strength and the minimum permissible residual joint strength are equal then, of course, it is obvious that there is no potential to save any weight on the structure. In this case, the hybrid joint can never be more efficient than the bolted joint since it will be at least as heavy as the bolted joint with the same minimum strength. Meanwhile, the primary reason for using bonding is to save weight! In this case, other damage tolerance features that are much lighter than bolts would present a much better option. Probably the most promising approach in this case is the use of pins, as in a hybrid bonded-pinned joint (see Chapter 2).

The use of HBB joints may thus potentially be justified in the case of (1). Nevertheless, it is still necessary to be able to increase the joint strength from the acceptable residual strength to the target strength by adding adhesive to a bolted joint. It is far from evident that this is achievable. Perhaps the overlap length may need to be extended, increasing the weight of the joint. Alternatively, it may be possible to take advantage of an *active* hybrid bonded-bolted joint. Such joints are the main topic of this thesis.

---

[3] The practice of adding mechanical fasteners to bonded joints purely as a fail-safety device was widely employed in the Fokker 100 aircraft, as well as in several other aircraft programs. These fasteners came to be affectionately known as "chicken rivets".

1.3 Active Hybrid Bonded-Bolted Joints

In recent years, a number of investigators have challenged Hart-Smith's original assertion that the bolts in a hybrid joint are inactive and do not contribute unless the joint experiences damage [17-19]. These investigators showed that, for judiciously designed hybrid bonded-bolted joints, the load is able to be shared between both the adhesive and bolts, with the latter actively partaking in structural load transfer. HBB joints that exhibit this behaviour are hereafter referred to as *active*.

Active HBB joints can potentially increase a joint's strength beyond that of both the underlying bonded joint and bolted joint. This is important, because it could enable the necessary strength improvement discussed in section 1.2. There are many open questions regarding active hybrid bonded-bolted joints, some of which shall be addressed in this thesis. To better understand the current state-of-the-art and determine what these open questions are, an in-depth literature review should first be carried out. This is presented in the next chapter.

Chapter 2: Literature Review & Objectives

In order to join thermoset composite structures (the most widespread type of composite used in the aerospace industry), there are currently two established overarching techniques:

- Adhesive bonding
- Mechanical fastening

These are illustrated in Figure 2.1. The research that has been carried out regarding their application in composite structures has previously been extensively reviewed by a number of authors [9, 20-24].

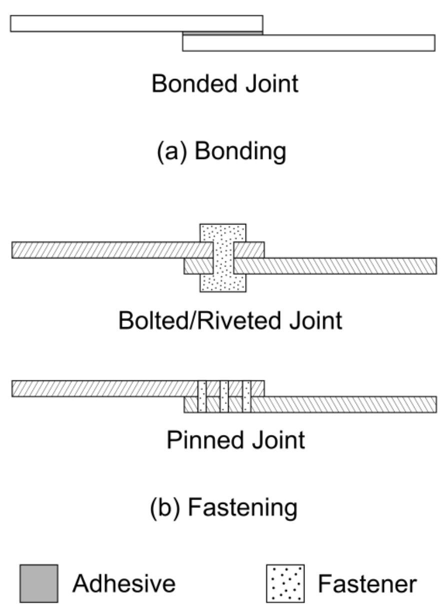

Figure 2.1: Established joining techniques

An alternative technique, namely hybrid bonding-fastening (HBF), has also started to generate interest due to its potential advantages over the established techniques. In HBF, adhesive bonding and mechanical fastening are used simultaneously to connect the components of interest (adherends). HBF joints can be divided into two main categories: (a) those that use bolts/rivets, hereafter called hybrid bonded-bolted (HBB) joints and (b) those that use pins, hereafter called hybrid bonded-pinned (HBP) joints. An example of each is shown in Figure 2.2. This thesis focuses on HBB joints in particular, and thus HBP joints are purposely ignored from this point onwards. Nevertheless, the interested reader is referred to the author's review on HBF joints in the Journal of Reinforced Plastic and Polymers, which includes a detailed review of HBP joints [25].

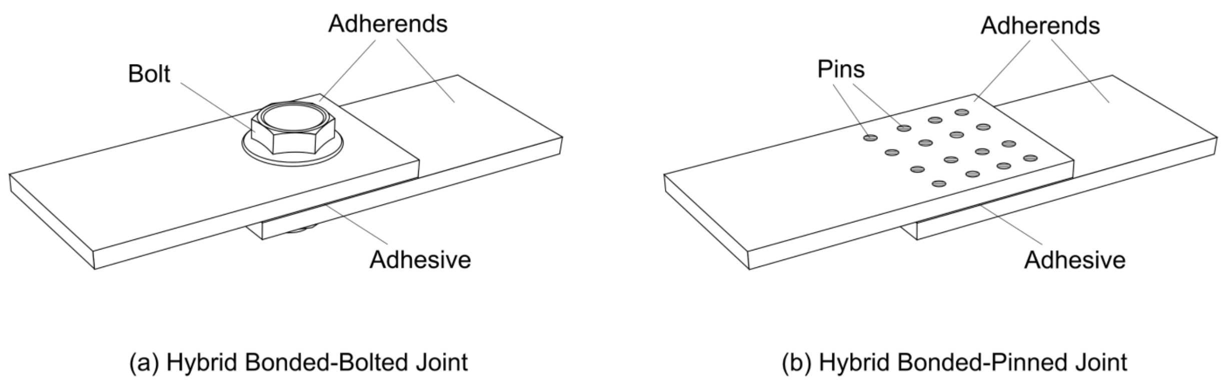

Figure 2.2: Main categories of HBF joints

2.1 Shims & Sealants

Many bolted joints in existing composite structures are technically HBB joints since they contain a layer of liquid shim to fill gaps caused by manufacturing tolerances/errors. A sealant is also sometimes used to prevent fretting and fluid/particulate ingress and egress to the structure. Most bolted joint analyses, however, ignore this shim/sealant layer. Several authors have shown experimentally that this leads to overprediction of joint stiffness [26-28]. Furthermore, moderate decreases in joint strength have been reported as the shim/sealant layer thickness becomes excessive [27, 28]. This can be ascribed to the increased load eccentricity and bolt tilting caused by the adherend offset due to the adhesive layer. Since most shims/sealants have very low elastic properties, they do not themselves transmit significant structural loads and hence do not directly modify the joint stiffness and adherend stresses.

Crucially, when stronger, stiffer structural adhesives are used, or when the composite adherends are co-cured, the adhesive layer *does* transmit significant loads and the joint stiffness and adherend stresses *are* directly modified. HBB joints of this kind have shown promise for improving joint strength [19], fatigue life [29] and energy absorption [30] compared to bonding or fastening separately. Consequently, they constitute the main focus of this review.

2.2 Design & Manufacture

In the design of a HBB connection, multiple types of joint (single-lap, double-lap, stepped-lap, scarf, butt ...), adherend material (composite, metal ...), adhesive material (polyurethane, epoxy, ...), fastener head (protruding, countersunk, ...), fastener pattern (single-row/column, multi-row/column, ...), loading (uniaxial tension, in-plane shear, peel, ...) and spew fillet geometry (flush, triangular, ...) may be considered. Some of these options are shown in Figure 2.3.

The HBB joints that have been studied in the literature to date are almost exclusively lap joints loaded in uniaxial tension. Single-lap joints are the most frequently studied joint type, likely due to their specification in the popular ASTM D1002 and ASTM D3165 standards [31, 32]. Most of the remaining studies concern double-lap joints. A solitary reference was found [16] in which stepped-lap and scarf joints were investigated.

The use of protruding head bolts is ubiquitous in the HBB literature. Countersunk bolts have been considered by relatively few authors [26, 33]. While the latter provide aerodynamic and aesthetic benefits, they also reduce bolted joint bearing strength [6, 34]. In addition, riveting has also been investigated in a number of works [35-39]. Despite its ability to reduce manufacturing times and eliminate bolt-hole clearance [40], the riveting process can potentially damage composite adherends [38, 39].

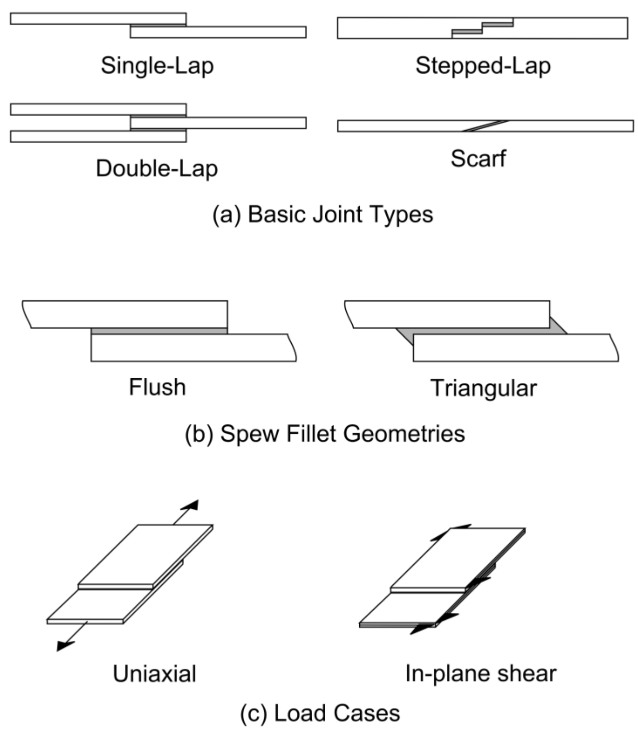

Figure 2.3: Various joint design options

Conveniently, the most commonly studied fastener configuration is single-row, single-column bolting. This configuration eliminates many complex effects and interactions, enabling researchers to distinguish the fundamental mechanisms influencing the joint behaviour. Unfortunately, it is not representative of most practical joint designs, which tend to be multi-row and multi-column [41]. To date, few studies exist on the latter.

Similarly to bonding and bolting separately, HBB joints can be used to join composite-to-composite, composite-to-metal or metal-to-metal. The composite adherends used by investigators are mostly continuous fibre laminates with quasi-isotropic layups [26, 42] or cross-ply layups [43, 44]. Carbon fibre reinforced polymer (CFRP) is the preferred material and is generally used in the form of pre-impregnated tape or pre-impregnated fabric. The popularity of quasi-isotropic CFRP laminates is surely influenced by their widespread use in the aerospace industry. In addition, glass fibre reinforced polymer (GFRP)—in the form of fabrics [29, 38], randomly oriented continuous strand mats [45] and filament wound shells [46]—has also been considered by several investigators. Studies on composite-to-metal and metal-to-metal HBB joints have investigated steel [47, 48], titanium [16] and aluminum [39, 42, 49] adherends.

Bolt holes are drilled through the overlap region either prior to or after bonding. Arguments can be made for either approach, and in practice both are used with similar frequency. However, if drilling is performed prior to bonding, then it is necessary to insert a pin through the holes during cure to ensure hole alignment. One suggested use for HBB joints, other than to improve the joint mechanical performance, is to affix bonded structures as they cure and thus enable subsequent manufacturing operations to be performed sooner [19, 49].

As an alternative to drilling, Matsuzaki et al. [29] examined the possibility of diverting the composite fibres around the bolts in order to avoid fibre terminations and drilling-related damage. While no static strength improvement was observed using this technique versus a drilled joint, it was suggested that fatigue life may have benefited.

Advanced joint design features such as externally tapered adherends, complex adhesive fillet geometries [18, 19] and complex bolting patterns [35, 36, 44, 50] have been taken into account in relatively few studies.

2.3 Elastic & Inelastic Behaviour

In a HBB joint, the underlying bonded joint and bolted joint ideally act as parallel load paths. However bonded joints are generally significantly stiffer than bolted joints of similar dimensions [16, 18]. This is a consequence of both material and geometry, since the adhesive material is intrinsically less stiff than that of the bolt [30]. During elastic loading of a typical HBB joint, this stiffness discrepancy causes the adhesive to transfer most of the load by itself [16, 18, 19, 30]. The relevant region of the load-displacement curve is shown between the origin and point A in

Figure 2.4. In this region, the HBB joint has essentially the same stiffness as the underlying bonded joint [18, 29, 51].

At higher loads, nonlinear adhesive behaviour (due to e.g. hyperelasticity or plasticity) reduces the bonded joint stiffness [17, 52]. The bolt will at this stage begin to assume an increasing share of the load [18, 53] and the HBB joint stiffness will begin to exceed that of both underlying joints [18, 19]. In the case of a neat fit hole, this stiffening effect occurs as soon as nonlinear adhesive effects manifest (point A in Figure 2.4). In the case of a clearance fit hole, it only occurs once the adhesive has sufficiently deformed to overcome bolt-hole clearance (point B in Figure 2.4) or if sufficient bolt-clamp up is applied to allow load to be transferred to the bolt through bolthead friction.

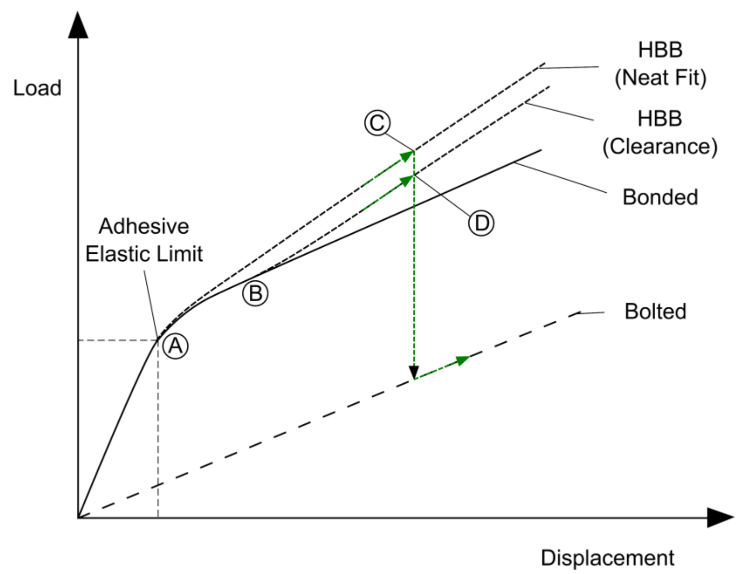

Figure 2.4: Typical load-displacement behaviour of a HBB joint

Should gross failure of the adhesive layer occur at any stage during loading—an abrupt event for monotonically loaded HBB joints [49]—then the joint load will drop to the level that the bolted joint by itself would have sustained at the given displacement (the gross failure event is represented by points C and D in Figure 2.4 for a neat fit and clearance fit hole, respectively). Subsequently, the HBB joint behaves similarly to a bolted joint [18, 29, 54].

It should be noted that many HBB joints (a) use adhesives that do not exhibit significant material nonlinearity or (b) use adhesives that have low strain to failure (i.e., are brittle) or (c) have very thin bondlines (e.g. co-cured joints). In such cases, the HBB joint response will be quasi-linear up to adhesive failure, akin to the underlying bonded joint. The stiffening effect due to the bolts is not observed in such joints [29].

2.4 Load Sharing

Load sharing refers to the proportion of externally applied load transferred by the bolts versus that transferred by the adhesive [18, 51]. In a HBB joint, load may be transferred by the bolts by means of (a) contact between the hole bearing surface and the bolt shank and (b) friction between the adherend outer surface and the bolthead/washer. Bodjona and Lessard [51] found that the former mechanism is best suited to transferring significant loads in HBB joints. The latter is less dependable since it relies on bolt clamp-up, which is known to reduce as a consequence of joint deformation [55, 56] and temporally due to viscoelastic creep of the composite [57, 58]. In addition, creep of the adhesive under clamp-up is also likely to be important, although this has not as yet been investigated.

Hart-Smith [16] showed that, for a bonded lap joint of practical proportions loaded in uniaxial tension, the bolts remain almost devoid of load (i.e., there is little or no load sharing) until failure of the adhesive. The bolts' sole contribution was found to be as a redundant load path (fail-safe mechanism). Consequently, it was concluded that HBB joining would not typically improve the static strength of bonded joints. This conclusion was based on a joint design with long overlap length, thin bondlines and a strong adhesive with a high Young's modulus. While these can be considered hallmarks of a well-designed traditional bonded joint, they are not conducive to load sharing.

Several decades later, Kelly [19] showed experimentally that load sharing is the essential mechanism by which the stiffness of a HBB joint can be improved beyond those of the underlying joints, and by which crack initiation can be delayed.

Several researchers have since tried to induce significant load sharing (defined as ≥10% in [51]) by means of purposeful joint design [18, 51, 59]. Graham et al. [30] protested that such an approach equates to suboptimal joint design in order to get load sharing to work. However, the possibility should be considered that a poorly designed joint, as judged against existing bonded joint and bolted joint design practices, could in fact prove to be a performant HBB design. Such a situation can only conceivably arise in the event of significant load sharing.

2.4.1 Experimental Measurements

The most compelling evidence that significant load sharing can be achieved has been provided by experiments. Specially instrumented bolts have been used by a number of investigators to directly measure the bolt shear load in single-lap HBB joints loaded in uniaxial tension. Bolt loads of 32% (out of an applied 8 kN load) and 36% (out of an applied 10 kN load) have been reported [18, 59]. Both of these studies used a single bolt, short overlaps, relatively thick bondlines and low yield-strength, ductile adhesives.

In contrast, a similar study of a double-row single-lap joint with a long overlap [52] reported load sharing of less than 5%, even at 14 kN of applied load. The same adhesive and bondline thickness as in [18] were used. Direct comparison of these two studies suggests the importance of geometric parameters and or the adherend material in load sharing.

2.4.2 Design Parameter Influence

Load sharing is a nonlinear function of the joint design parameters. A number of investigators have used modelling approaches [18, 52] to determine the effects of various parameters. No experimental parametric studies have been performed, likely due to the significant cost and time involved in coupon manufacture, in addition to the difficulty of the load sharing measurement. Furthermore, only single-lap joints have been considered.

2.4.2.1 Effect of Materials

An overview of the effect of increasing several material parameters on load sharing is given in Table 2.1. A general consensus exists on these basic effects. It is remarked that these are qualitative in nature; there is no quantitative indication of which factor is most important. In other words, effect size has not as yet been addressed in the literature.

Table 2.1: The effect of increasing several material parameters on load sharing

Parameter	Effect on load sharing	Reference
Adhesive Young's modulus	Decrease	[18, 60]
Adhesive tangent modulus	Decrease	[18]

2.4.2.2 Effect of Geometrical Parameters

An overview of the effect of increasing several geometric parameters on load sharing is given in Table 2.2. Once again, effect size has not as yet been addressed.

Table 2.2: The effect of increasing several geometrical parameters on load sharing

Parameter	Effect on load sharing	Reference
Adherend thickness	Increase	[18, 60]
Overlap length	Decrease	[18, 60]
Width	Decrease*	[18, 60]
Bondline thickness	Increase	[18, 60]
Bolt-hole clearance	Decrease	[18]

*Fixed overall load

2.5 Quasi-Static Strength

A major touted advantage of HBB joints is that they can potentially improve joint monotonic strength beyond those of the underlying bonded joint and fastened joint separately. Since reported loading rates in the HBB literature range from 0.36-1.27 mm/min, this section addresses quasi-static strength in particular. Future investigations concerning dynamic strength would be most valuable additions to the literature, since rate effects are known to greatly influence adhesive behaviour [61]. Approximately half of investigations regarding HBB quasi-static strength report substantial improvements, with the remainder reporting no improvements. An overview of the reported strength improvements is given in Table 2.3.

Table 2.3: Reported quasi-static strength improvements in the HBB literature

							Strength improvement	
Reference	**Joint type**	**Adherend type**	**Composite type**	**Adhesive**	**Adhesive thickness (mm)**	**Overlap length (mm)**	**Vs Bonded**	**Vs Bolted**
[62]	Double-lap	Composite-aluminum	Boron FRP pre-preg, UD laminate, angle-ply layup	Hysol Shell 951 epoxy	0.25	19.1	41%[a]	325%
[45]	Single-lap	Composite-composite	GFRP SRIM laminate	Unspecified polyurethane	0.76	25.4	82%	33%
[19]	Single-lap	Composite-composite	CFRP pre-preg UD laminate, quasi-isotropic layup	Pliogrip 7400/7410 polyurethane	0.5	25	25%	34%
[42]	Double-lap	Composite-aluminum	CFRP pre-preg UD laminate, quasi-isotropic layup	Hysol EA9394S epoxy	Undefined	25.4	186%	19%
[17]	Double-lap	Composite-aluminum	CFRP prepreg UD laminate, quasi-isotropic layup	3M 2216 epoxy	0.5	60	132%	54%
[50]	Double-lap	Aluminum-aluminum	N/A	Montagefix-PU polyurethane	0.1	40	11%	130%

[a] Bonded joint overlap was 25.4 mm versus 19.1 mm for the HBB/bolted joints, hence this value is conservative

2.5.1 Design Parameter Influence

Studies that achieved significant static strength improvements almost exclusively used low stiffness, high ductility adhesives and relatively thick bondlines (all used secondary bonding), as shown in Table 2.3. The exception is a study by Sadowski et al. [50] who reported an improvement despite using a thin bondline (it should be noted that in this study rivets were used which eliminated any bolt-hole clearance). Studies that used stiff, strong adhesives such as FM300-2K epoxy [33, 35, 36], FM73 epoxy [48] and Hysol EA 9317 epoxy [43, 44] in conjunction with thin bondlines invariably failed to improve the joint strength beyond that of the strongest constituent joint.

Note that the studies in Table 2.3 all used relatively short overlap lengths. It is expected that longer overlap lengths would yield less substantial improvements. In [18] it was furthermore found that when the laminate thickness was doubled, the strength improvement increased. This is likely due to two mechanisms (a) deformation of the adhesive becomes energetically more efficient for thicker adherends, resulting in greater adhesive deformation (b) the bolted connection is stiffer when the laminates are thicker [63, 64]. Both of these effects result in greater load sharing, likely explaining the improved joint strength.

2.5.2 Failure Modes

Failure mode depends on the HBB joint design. However, almost always, the first failure is in the adhesive. At a critical load level, the adhesive fractures, with the crack starting at the overlap edges and growing towards the center of the overlap region [19, 65, 66]. The fracture of the adhesive causes an increase in the joint compliance and transfers load to the bolts. If the underlying bolted joint strength is inferior to the bonded joint strength, the adhesive failure causes the entire joint to fail, since the bolted joint cannot sustain the load transferred to it. However, if the underlying bolted joint strength is greater than the bonded joint strength, then following adhesive failure, the joint will continue to support load akin to a bolted joint [29, 49, 65]. Failure of the composite adherend occurs by normal composite bolted joint failure modes and may be by delamination, net section, bearing, shear-out or cleavage [62]. An example of a failed HBB joint is shown in Figure 2.5; the failure modes of adhesive disbonding/delamination and hole bearing failure are clearly visible.

Figure 2.5: Failure of a CFRP-aluminum HBB joint [42], reproduced with permission from Elsevier

2.6 Fatigue Strength

Experimental testing by various investigators [19, 26, 29, 45, 55, 65-68] has revealed that the fatigue strength of HBB joints generally surpasses that of the underlying joints separately.

Fu and Mallick [45], in a study using SRIM composite adherends, found that fibre tear (an SRIM specific type of failure) initiated in the adherends at the overlap edges and grew inwards toward the hole. The fatigue strength of the HBB joint exceeded that of simply bolted and bonded joints by an order of magnitude. Final failure was a combination of cleavage, delamination and partial adhesive disbonding.

For more standard composite materials, however, fatigue damage typically initiates in the adhesive at the overlap edges [19, 65, 66]. This has been verified by means of backface strain measurements [19, 66]. When the adhesive is stiff and brittle such that there is little load sharing, the two joining mechanisms act independently. In this case, the fatigue life is approximately equal to the sum of the lives of the underlying joints separately [19]. Initially, the fatigue life of the adhesive is exhausted, followed by a transition period during which a bondline crack grows rapidly and load is transferred to the bolt. Subsequently, the bolted joint fatigue life is exhausted prior to final joint failure, with failure modes that are similar to those observed during quasi-static testing [19, 29]. Importantly, damage initiation in the adhesive is not delayed in this case versus a bonded joint [19, 66].

When a more ductile adhesive is used and there is load sharing, however, it was shown using the backface strain technique that crack initiation is significantly delayed [19]. In addition, a period of stable crack propagation is observed prior to gross bondline failure [19, 66]. Thus, the fatigue strength can be increased to a level that is greater than the sum of the lives of the underlying joints [19].

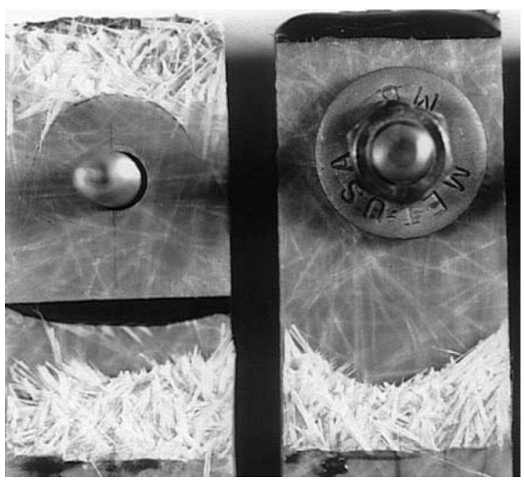

Figure 2.6: Evidence of adherend crack arrest underneath the washer in a HBB joint [45], reproduced with permission from Elsevier

An additional mechanism that may contribute to improved fatigue life in HBB joints is clamp-up due to bolt torque tightening. Clamp-up causes compressive stresses in the adherends and adhesive underneath the bolthead/washer [65, 67], which hinders crack opening and thereby slows or arrests crack propagation [45, 65]. Adherend crack arrest underneath the washer in the SRIM joint study described earlier is clearly seen in Figure 2.6 [45]. As expected, greater clamp-up forces result in greater fatigue life for both HBB and bolted joints [65, 67]. The improvement is more profound at low amplitude cyclic loading, which is likely due to bolt tension relaxation (caused by Poisson's effect) and thus loss of clamp-up at higher applied in-plane loads [55]. This explains why the crack arrest in Figure 2.6 was not observed during quasi-static loading [45]. Overall, the research suggests that (a) HBB load sharing can delay fatigue crack initiation (b) once a crack has formed, bolt clamp-up can slow its propagation, leading to improved HBB fatigue performance and (c) bolt tension relaxation reduces clamp-up and the associated benefit.

2.7 Energy Absorption

There are only a few studies that refer to the important subject of energy absorption of HBB joints. Sadowski et al. [50] found experimentally that the absorbed energy during quasi-static loading of a HBB joint is approximately equal to the energy of the two mechanisms separately. Di Franco et al. [37] found the energy absorbed during quasi-static loading of a different HBB configuration to be better than a bonded joint but no better or even slightly worse than that of a simply riveted joint. It seems logical that the failure mode is highly influential on energy absorption, with failure modes that involve extensive damage (e.g. progressive hole bearing damage or multiple delaminations) being able to absorb the most energy. This would imply that HBB joints do not necessarily absorb more energy than bolted joints, although they should generally absorb more energy than bonded joints. This hypothesis needs to be further tested. Experimental investigations of energy absorption during dynamic loading of HBB joints are sorely lacking in the literature, especially since this is the loading scenario for which energy absorption is of the greatest interest (e.g., impact).

2.8 Modelling Approaches

In order to facilitate the design of HBB joints and to improve our understanding of the fundamental mechanisms governing their behaviour, several researchers have developed mathematical models to predict the structural response and failure of these joints.

Closed-form analytical models [17, 52, 69] can provide a basic representation of the stresses and strains in the adhesive of double-lap/stepped-lap and single-lap HBB joints. These models are based on the classical 2D bonded joint models of Volkersen [70] and Goland and Reissner [71], respectively. In Volkersen's model, the adhesive transverse shear strain γ_{xz} is defined purely in terms of the longitudinal adherend displacements:

$$\gamma_{xz} = \frac{1}{t_a}\left(u_x^{(1)} - u_x^{(2)}\right) \tag{2.1}$$

where t_a is the adhesive thickness and $u_x^{(i)}$ is the longitudinal displacement of the ith adherend. To take into account the effects of out-of-plane loading, Goland and Reissner extended Volkersen's model with the following expression for the out-of-plane normal strain or "peel" strain ε_{zz}:

$$\varepsilon_{zz} = \frac{1}{t_a}\left(u_z^{(1)} - u_z^{(2)}\right) \tag{2.2}$$

where $u_z^{(i)}$ is the out-of-plane displacement of the *i*th adherend. The analytical HBB models extend the above models by including the effect of the bolts, which are discretely modelled as either springs or beams. The resulting system of differential equations can be solved exactly for a linear elastic problem. When adhesive plasticity is taken into account, an iterative solution must be used. These models are extremely efficient to solve and are thus ideally suited for design trade-off studies. However, bolt tilting, bolt-hole contact and in-plane stress variations and concentrations cannot be intrinsically predicted.

Numerical models of HBB joints are generally capable of the above. 3D finite element models have taken into account wide range of complex effects such as clearance, friction, bolt tilting and laminate coupling effects [18, 19, 68]. However, these models are highly time consuming to construct and solve and as such are of limited use for sizing studies and optimization. A compromise appears to be 3D numerical models that use simplified structural elements such as shells and beams, combined with Volkersen's shear lag model for the adhesive. These models, such as the one by Barut and Madenci [72], can account for most complex effects and a pseudo-3D stress field, while being easy to construct and achieving acceptable computation times. However, Barut and Madenci’s model does not account for a nonlinear constitutive response of the adhesive, which is a key behaviour influencing the joint response. Key behaviour that should be taken into account in any HBB joint model includes nonlinear adhesive behaviour and the effect of bolt-hole clearance, which have been shown to have an important effect on the joint response.

To date few studies have attempted to predict the strength of HBB joints [17]. It is acknowledged that this is a very complex analysis indeed, and strength prediction may initially be limited to failure modes that are relatively easy to predict. Furthermore, modelling of thermal effects and dynamic effects has also not been attempted. Fatigue has been studied only qualitatively [69].

2.9 Gaps in the Literature & Thesis Objectives

Based on the presented review of the literature, a number of important shortcomings in the knowledge of HBB joints have been identified. These include:

- A lack of understanding of how strongly different design parameters affect load sharing in composite HBB joints

- A lack of a suitable model to efficiently predict composite HBB joint mechanics and strength

- A lack of experimental data on energy absorption in composite HBB joints

The thesis objectives shall aim to address these shortcomings. They are formally stated as follows:

2.9.1. Objective 1: Determine the effect size of different design parameters on load sharing in composite HBB joints

2.9.2. Objective 2: Develop an analysis methodology to predict HBB joint mechanics and strength in a simple but representative manner

2.9.3. Objective 3: Experimentally investigate the energy absorption of a composite HBB joint compared to its constituents separately

2.10 Structure of the Thesis

This thesis begins with an investigation of load sharing in Chapters 3-4. This includes the development of an efficient numerical model in Chapter 3 for predicting load sharing in HBB joints. This model is validated experimentally, after which it is used in a global sensitivity analysis in Chapter 4 to determine the most important factors influencing load sharing.

Subsequently, strength is addressed in Chapters 5-10. An original mathematical model of a HBB joint is developed in Chapter 5 for this purpose. This model distills the physical problem to the essentials, yet accounts for many complex effects found in real joints. Its predictions are compared with new experimental results in Chapter 10. The model is subsequently used to elucidate key behaviours of hybrid bonded-bolted joints in Chapter 11.

Energy absorption is also considered in the experiment of Chapter 10.

Note that Chapters 6-8 are almost entirely dedicated to the problem of achieving a robust numerical solution of the model formulated in Chapter 5. This is necessary since this thesis represents the first time that the meshless Galerkin method is applied to the analysis of joints. The reader who is primarily interested in HBB joints and not so much in the intricacies of the numerical analysis is advised to simply skip these chapters. This will not hamper comprehension of the results presented in Chapters 9-12.

Chapter 3: Load Sharing Model

As discussed in Chapter 2, a number of experimental studies have demonstrated that HBB joints can potentially achieve greater static strength [18, 19, 29, 42, 45] and a longer fatigue life [19, 29, 45] than the underlying bonded and bolted joints separately. A recurring conclusion in the literature is that the most significant "across-the-board" improvements (compared to *both* constituent joints) are achieved when there is substantial load sharing between the adhesive and bolts [18, 19, 52].

In practice, however, few HBB joint designs experience load sharing. Since it is quite challenging to achieve load sharing and it is not obvious whether this phenomenon occurs for a particular HBB joint design, it is of interest to be able to predict it and—more fundamentally—understand the mechanisms causing it. In this chapter, a suitable model is developed for this purpose.

The configuration considered for this model consists of a single-lap, single-bolt joint, since this is the preeminent test configuration in both civilian and military bolted composite joint standards [41, 73, 74]. These joints exhibit a range of complex effects such as secondary bending and bolt rotation, while being simple enough to allow the results to be readily understood, compared and interpreted.

3.1 Objectives

The objective of this chapter is to develop an efficient model of a HBB joint that takes into account all of the major factors potentially affecting load sharing (including clearance, bolt clamp-up and nonlinear adhesive behaviour—factors which have to date been largely ignored). This model should be validated through comparison with experimental measurements.

3.2 Problem Description

The physical problem considered is a uniaxial tensile test of a single-lap hybrid bonded-bolted composite joint. The studied configuration is adapted from the ASTM D5961 standard [73] and consists of two composite adherends that partially overlap and are joined in the overlap region by means of adhesive and one or more bolts. A doubler, having the same material and layup as the laminate, is bonded to the grip end of each adherend to minimize the eccentricity that would otherwise result when installed in a testing machine. Only the single-bolt case is considered, for the reasons outlined in the chapter introduction. A schematic of this configuration is shown in Figure 3.1. The parameters that define the joint geometry are the adherend length L, adherend width W, adherend thickness t, adhesive thickness t_a, adherend gripped length L_g, adherend free length L_f, overlap length L_a, edge distance E, hole diameter D and bolt head diameter D_h.

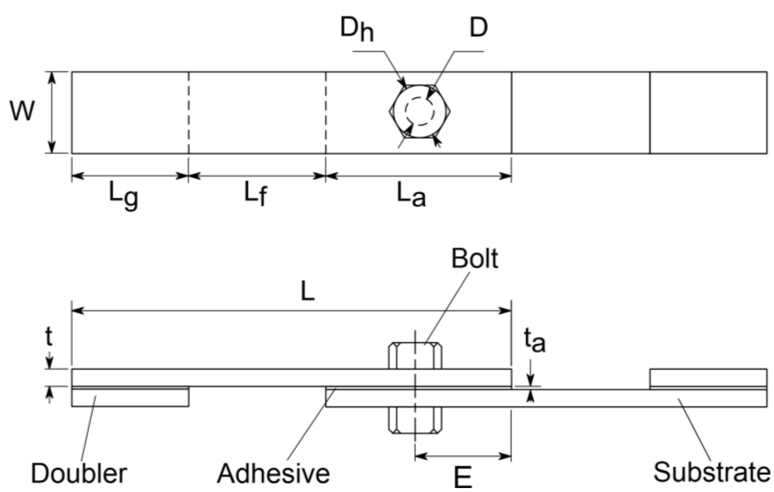

Figure 3.1: Single-bolt, single-lap joint geometry

The adhesive is assumed to exhibit an elastoplastic response, which is characteristic of virtually all aerospace adhesives. It is noted that some of the stiffer aerospace adhesives have only very limited ductility, but are nevertheless known to exhibit permanent plastic deformation prior to fracture. Viscous effects are ignored for simplicity, although it is acknowledged that these may actually be important for many polymeric adhesives such as acrylics, urethanes and epoxies.

3.3 Finite Element Model

In order to simultaneously account, in a detailed manner, for the complex geometry, nonlinear behaviour and contact that exist in a single-lap bonded-bolted joint, a numerical solution technique is required. A well suited technique for taking into account all of these phenomena is the displacement-based finite element method. It was thus decided to develop a suitable model in the commercial finite element software ABAQUS, in order to leverage both the efficient contact algorithms of the software and the ability to implement user defined subroutines.

To achieve the desired computational efficiency, an equivalent single layer (ESL) approach was used in a similar vein to the *Global Bolted Joint Method* of Gray et al. [75]. In this FE model, the authors used shells/beams to efficiently model the laminates/bolts, respectively. In the current work, the model of Gray et al. is extended to take into account bolt head clamp-up and bonding. As shall be described, the new method, which is named the *Global Hybrid Joint Method* (GHJM), contains a single layer of quadratic solid elements to simulate the adhesive.

3.3.1 Element Choice & Mesh

The GHJM consists of four main components: (1) the top laminate (2) the bottom laminate (3) the bolt and (4) the adhesive. The laminates are modelled as Reissner-Mindlin shells, the bolt as a Timoshenko beam and the adhesive as a continuum solid, respectively. The corresponding elements are designated S8R, B32 and C3D20R in ABAQUS. Quadratic element shape functions are used, allowing a single element to be meshed through the adhesive thickness and giving a fast solution convergence rate. To simplify the analysis, the grip regions are not considered;

Saint Venant's principle is invoked to justify their omission. A typical GHJM mesh is shown in Figure 3.2.

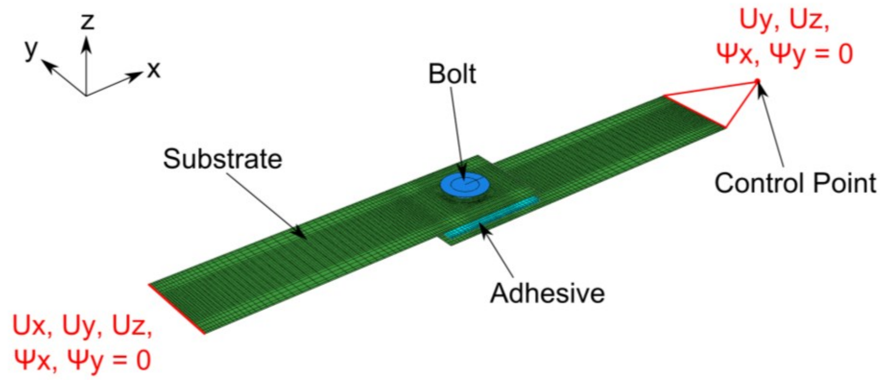

Figure 3.2: Finite element mesh and boundary conditions

To limit the required number of elements, biased meshing is used for the laminates and adhesive, with an increased mesh density in regions that experience significant stress and displacement gradients. This includes the vicinity of the hole and the overlap edges. An extensive convergence study was performed and showed that a single layer of quadratic solid elements through the adhesive thickness typically provides converged results for both bolt load and displacement. Less than 0.5% change was observed in these solutions as a result of switching from 1 to 3 elements through the thickness, for both 0.1 mm and 1 mm thick bondlines (it is important to note that this did not hold true when linear elements were used). Close agreement was furthermore verified with Goland and Reissner's analytical bonded joint model [71] for both shear and peel stresses in the midplane of the bondline, including when plasticity was taken into account. Bois et al. [17], who also used a single layer of quadratic elements to mesh the adhesive and compared it with their analytical solution, obtained a similarly good agreement for the plastic strains. In the GHJM, only a single layer of quadratic solid C3D20R elements is therefore meshed through the adhesive thickness, simultaneously limiting the analysis cost and enabling good element aspect ratios to be achieved when thin bondlines are modelled.

By comparison, the bolt mesh is simple, consisting of only four elements. The latter are demarcated by a “bolthead” master node at either bolt extremity, a “clamp-up” node at the bolt center and a “shank” master node at each laminate midplane. Unlike in the Gray et al. model [75], the full length of the bolt is modelled in order to properly account for axial bolt deformation and clamp-up.

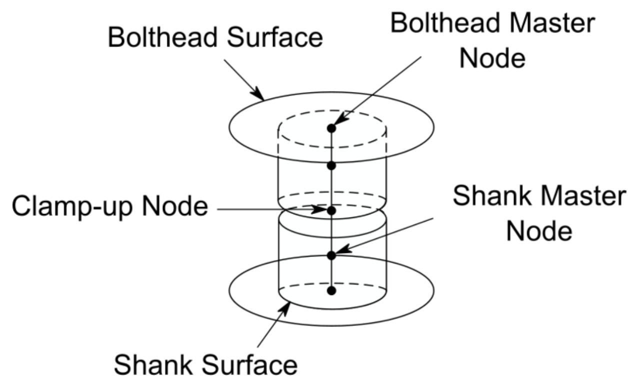

Figure 3.3: Bolt model

Analytical rigid surfaces, tied to the respective master nodes, are used to detect and transmit contact forces into the beam. This furthermore allows clearance to be accurately modelled. Cylindrical surfaces are used at each laminate midplane to represent the bolt shank while the boltheads are modelled as discs. The use of rigid contact surfaces for the bolt is a suitable representation, as previous studies have shown little effect of bolt surface elasticity on contact stress distribution [76]. The complete bolt model is depicted in Figure 3.3.

3.3.2 Multi-Point Constraints

Similarly to Gray et al.'s model [75], the shell reference surfaces must be located at the laminate midplanes in order to accurately capture bolt bending and flexibility. This causes an issue with regard to the adhesive-laminate interface as their nodes are consequently offset by half a laminate thickness (see Figure 3-4). In a realistic depiction of a bonded joint, the adhesive surface nodes should behave as though on the hypothetical shell surface. This can be described using Reissner-Mindlin plate kinematics as:

$$U_{\alpha}^{(ta)}(x,y,z) = u_{\alpha}^{(tl)}(x,y) + \theta_{\alpha}^{(tl)}(x,y)\frac{t^{(tl)}}{2}|\alpha = x,y \tag{3.1}$$

$$U_{z}^{(ta)}(x,y,z) = u_{z}^{(tl)}(x,y) \tag{3.2}$$

$$U_{\alpha}^{(ba)}(x,y,z) = u_{\alpha}^{(bl)}(x,y) - \theta_{\alpha}^{(bl)}(x,y)\frac{t^{(bl)}}{2}|\alpha = x,y \tag{3.3}$$

$$U_{z}^{(bl)}(x,y,z) = u_{z}^{(bl)}(x,y) \tag{3.4}$$

Here U_{α}, U_{z} are the adhesive surface displacement components, u_{α}, u_{z} are the laminate midplane displacement components, θ_{α} are the laminate midplane rotation components and t is the laminate thickness. The superscript in brackets defines the adhesive surface or laminate in question – ta, ba referring to the top and bottom adhesive surfaces, respectively while tl, bl refer to the top and bottom laminates. In the GHJM, the relationships in Eqns. (3.1-3.4) are enforced in the joint overlap region by means of the *MPC ABAQUS user subroutine. A suitable FORTRAN code must be written for this purpose, which is compiled by the software at runtime. The developed code was extensively tested on a number of two and three element cases to ensure correct implementation and functionality. The shell nodes are designated as master nodes while the corresponding adhesive surface nodes are the slave nodes. Evidently, the $x - y$ plane discretization of the adhesive and shells must match in the overlap region. The constraints in Eqns. (3.1-3.4) are valid for linear as well as nonlinear elastic analysis.

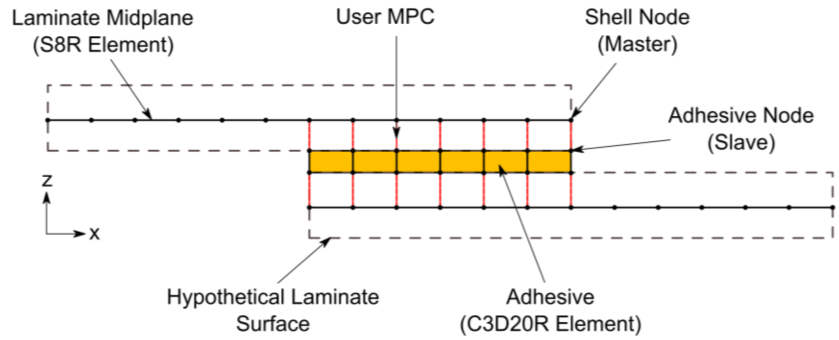

Figure 3.4: User defined MPCs

3.3.3 Contact

Contact is defined between the “shank” analytical surfaces and respective hole edges using a surface-to-surface finite sliding contact formulation. The analytical rigid surface is designated as the master surface while the hole perimeter nodes are designated as the slave surface. A Coulomb friction model is used for tangential contact, while in the normal direction the penalty method is used for contact constraint enforcement.

The same approach is used to model bolt head contact. Use of the shell contact offset option in ABAQUS instructs the software to use the hypothetical shell surface during contact detection instead of the shell midplane.

3.3.4 Boundary Conditions & Loading

The applied boundary conditions are chosen so as to be representative of a uniaxial test of a joint clamped in a tensile testing machine. On the left boundary, both translations u_x, u_y, u_z and rotations θ_x, $\theta_y = 0$. On the right boundary, in order to simulate a clamped load, the nodes are tied to the motion of a control point using a *COUPLING constraint. To simulate clamping, u_y, u_z, θ_x, $\theta_y = 0$ is applied to this control point. If the desired simulation is a test in displacement control, then u_x is also prescribed at the control point. If the desired simulation is a test in force control, then u_x is not prescribed and the desired force F_x is applied instead. These boundary conditions are shown in Figure 3.2. Furthermore, a bolt clamp-up load may easily be applied to the bolt model described previously. This is achieved using the bolt load option in ABAQUS, which automatically adjusts the bolt length to achieve the desired preload.

3.3.5 Material model

The laminates are not considered to suffer damage and are thus modelled as linear elastic anisotropic plates following classical lamination theory (CLT). The relevant properties are automatically calculated by ABAQUS, which requires only the anisotropic elastic material constants, ply thickness and layup as inputs. A number of authors, however, have established that nonlinear adhesive behaviour is important in load sharing [17, 18]. This must be taken into account by using an appropriate material model for the adhesive. The use of solid elements for the adhesive renders the GHJM compatible with a wide range of material models.

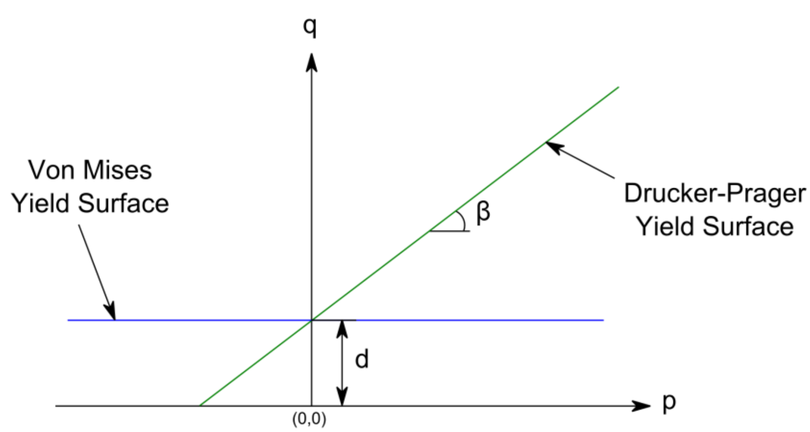

Figure 3.5: Linear Drucker-Prager plasticity

As mentioned in section 3.2, the adhesive is assumed to exhibit elastoplastic behaviour. Generally, this involves sensitivity to both the deviatoric and hydrostatic components of the stress tensor[4]. The simplest elastoplastic material model that exhibits both of these sensitivities is the Drucker-Prager plasticity model; this theory has previously been successfully used to model a range of stiff and flexible adhesives [18, 19, 61, 77]. In particular, the linear version of the model is used, in which the yield surface is a cone in Haigh-Westergaard stress space. This surface is defined by Eqn. (3.5):

$$F = q - p\tan(\beta) - d = 0 \tag{3.5}$$

where q is the equivalent von Mises stress,

$$q = \sqrt{\frac{3}{2}\boldsymbol{S}:\boldsymbol{S}} \tag{3.6}$$

p is the usual hydrostatic pressure and $\boldsymbol{S}$ the deviatoric stress tensor. The friction angle β is the slope of the yield surface in the $p-q$ plane, as shown in Figure 3.5. Finally, the adhesion strength of the adhesive, d, is related to the adhesive tensile yield strength σ_{yt} as follows:

$$d = \left[1 + \frac{\tan(\beta)}{3}\right]\sigma_{yt} \tag{3.7}$$

In the elastic regime of the adhesive, Hookean behaviour is assumed and is fully defined by Young's modulus E_a and Poisson's ratio ν_a. Strain hardening is taken into account by means of an isotropic associative flow rule. In ABAQUS, this involves the specification of a tensile strain hardening curve. As $\beta \rightarrow 0$, the model becomes equivalent to Von Mises plasticity.

[4] By contrast, metals are usually only assumed to exhibit sensitivity to the deviatoric components of the stress tensor.

3.4 Experimental Validation

The accuracy of the mathematical model for predicting the load sharing and deformation behaviour of a HBB joint was verified by means of an experiment. This firstly involved the selection of a set of design parameters that would allow significant bolt load transfer to occur (based on model predictions). Specialized tooling was used to manufacture the corresponding joint. An instrumented bolt was subsequently designed, manufactured and calibrated in order to allow the bolt shear load to be measured. Finally, the instrumented bolt was installed in the joint and a uniaxial tensile test was performed. The bolt shear load measurements, together with the MTS displacement and load cell data, constitute the validation data.

3.4.1 Joint Design & Manufacture

The validation joint geometry was adapted from the ASTM D5961 standard and was designed to promote load sharing. The final (measured) joint dimensions are given in Table 3.1.

Table 3.1: Validation joint dimensions

L_a (mm)	L_f (mm)	L_g (mm)	D (mm)	W (mm)	t_a (mm)	t (mm)	D_h (mm)
32.0	77.0	30.0	8.002	28.0	0.51	4.39	11.9

Table 3.2: Cytec 5320 CFRP tape properties

E_{11} (GPa)	$E_{22} = E_{33}$ (GPa)	$G_{12} = G_{13}$ (GPa)	G_{23} (GPa)	ν_{12}	ν_{13}	ν_{23}
141	9.70	5.10	3.40	0.33	0.33	0.44

The adherends and doublers were made from Cytec 5320 CFRP pre-preg tape, whose properties are given in Table 3.2 as provided by the manufacturer. The following manufacturing process was used:

1) A flat plate was made with a stacking sequence of $[45/0/-45/90]_{4s}$. Debulking was performed every 4 plies during the layup process, followed by a vacuum cure using the manufacturer recommended cure cycle.

2) A diamond-tipped saw was used to cut the adherends and doublers from the plate.

3) The various components were assembled and bonded inside a custom-built mold (see Figure 3.6). This permitted precise control of the adherend alignment. Spacers were used to control the bondline thickness, spew fillet geometry and joint overlap length.

Figure 3.6: Joint assembled inside the mold

To maximize the likelihood of observing significant load sharing, a ductile and low-yielding epoxy paste adhesive was chosen to bond the components, in the form of Hysol EA9361. The two adhesive parts were mixed using a Thinky ARE-310 centrifugal mixer to ensure uniform mixing and deareation. The adhesive was left to cure for 1 week at room temperature, as specified by the manufacturer.

4) The joint and spacers were removed from the mold. Excess adhesive that had spilled from the joint sides was removed using a hack saw and the sides were sanded to the final dimension. Note that the use of rectangular spacers resulted in a flush bondline along the overlap edges.

5) A hole was drilled at the center of the joint overlap using a CNC drill. A composite specific drill bit (Sandvik-Coromant Corodrill 854) was used to ensure a tight diametric tolerance and to minimize the delamination and fibre pullout damage often encountered when drilling composites. No such damage was visually evident following the drilling. Using a go/no-go gauge, the diametric tolerance of the hole was found to be within 8mm +25.4/-0 μm. This was the highest level of measurement accuracy that was readily available. However, since a high precision CNC drill and collet were used, it can be assumed that the actual achieved clearance was close to the lower bound of the manufacturer specified tolerance of +16/-0 μm.

3.4.2 Instrumented Bolt Design & Calibration

A basic schematic of the instrumented bolt design is shown in Figure 3.7. Effectively an M8 stud, the bolt was machined from a tight-tolerance, precision ground rod of easy-to-machine 416 stainless steel. A close diametric tolerance of 8 mm +0/-4 μm was consequently achieved (a diameter of 7.999 mm was measured using a micrometer). The screw threads were turned on a lathe while diametrically opposed strain gauge slots were precision cut into the bolt shank using a CNC milling machine. Within each slot, a pair of shear strain gauges (Micro-Measurements EA-13-062TV-350) was bonded to the bolt surface. Figure 3.7 shows the first pair of strain gauges (SG1 / SG2) on one side of the bolt; the other pair (SG3 / SG4) was located in the opposing slot. Extremely small gauge wires (38 AGW) were soldered to the gauges and routed out of the joint through the wiring channels shown and slots cut into the top washer. Outside the joint, the wires were soldered to a printed circuit board (PCB) on which they were connected in a full Wheatstone bridge configuration. An electromagnetically shielded cable was used to connect the PCB to the data acquisition setup.

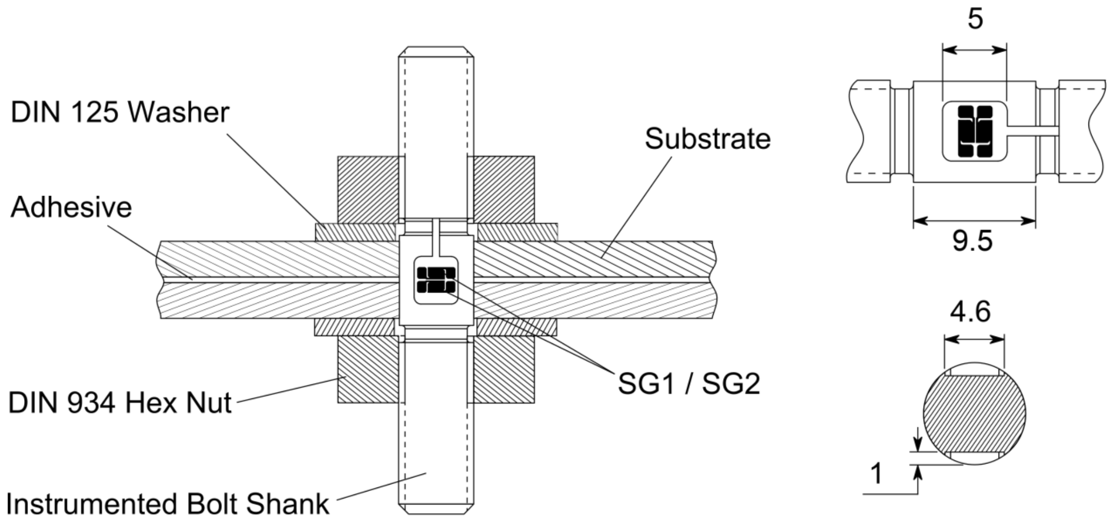

Figure 3.7: Instrumented bolt assembly section view from side

The adopted stud design enabled the bolt's through-thickness location within the joint to be adjusted such that the strain gauge shear plane could be precisely aligned with the adhesive midplane. A hex slot, machined into one end of the bolt, furthermore allowed the bolt to be rotationally located using an Allen key. This allowed the strain gauge slots to be precisely oriented at a right angle to the loading direction.

Despite these considerations, it was a practical impossibility for the bolt to be installed completely accurately. To gauge the effect of this installation error, and to determine the relationship between the Wheatstone bridge output (in mV/V) and the applied bolt shear load (in N), five separate calibration runs of the instrumented bolt were performed inside a bolted joint. Barring the absence of the adhesive layer, this calibration joint was identical to the bonded-bolted joint specimen. A thin layer of silicon was used to simulate the bondline. Since little to no torque was applied to the nuts, the silicon itself did not transfer any significant load through friction. The calibration setup is shown in Figure 3.8. For each calibration run, a linear relationship was determined between the potential difference measured by the Wheatstone bridge and the known bolt shear load. An average relationship was calculated and it was found that the maximum error predicted for any calibration run using this averaged relationship was 8%. This lends a good degree of confidence that the measurement precision of the instrumented bolt, taking into account the installation error, was within 10% for the tested 0-5 kN range.

Figure 3.8: Instrumented bolt installed in the bolted calibration joint

Note that all calibration tests were performed in the elastic regime of the adherends and bolt to avoid damage to the bolt, adherends and instrumentation. This was verified by the fact that when the load was removed at the end of each run, the bolt shear load measurements invariably returned to zero.

3.4.3 Adhesive Characterization

The EA9361 tensile stress-strain curve was obtained experimentally following the ASTM D638 standard [78]. This characterization work was mostly performed by Gyu-Hyeong Lim, a master's student, as described in his thesis [79]. The obtained curve is shown in Figure 3.9. A 5 kN electromechanical MTS tensile testing machine was used to load the specimen at a rate of 0.006 mm/s, while digital image correlation (DIC) was used to record the relatively large strains observed. These exceeded the measurement range of typical strain gauges and extensometers. Due to time and cost constraints, the pressure sensitivity of the adhesive was not characterized. In the GHJM, it was therefore simply assumed that the adhesive is pressure insensitive, i.e., β = 0.

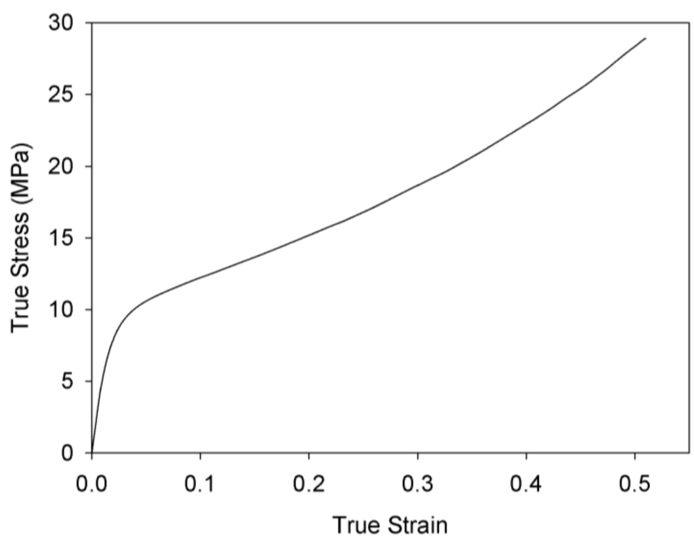

Figure 3.9: EA9361 stress-strain curve [79]

3.4.4 Validation Experiment

The final validation experiment using the bonded/bolted joint specimen was performed on a 100 kN hydraulic MTS tensile testing machine. The instrumented bolt was installed in exactly the same manner as in the calibration joint, without any torque applied to the nut beyond light finger tightening. The specimen was hence loaded to 10 kN at a displacement rate of 0.006 mm/s. During the test, displacement, the total applied load and the instrumented bolt shear signal were recorded.

3.4.5 3D FEM

As an additional verification, a detailed 3D FEM of the validation problem was created in ABAQUS. This high fidelity model was intended to serve as a benchmark numerical solution by relaxing the simplifying assumptions of the GHJM regarding the problem kinematics and geometry. The geometry of the problem, given in the preceding sections, was accurately modelled. The grip regions omitted in the GHJM were taken into account, including the doublers and adhesive layers used to bond the doublers. The strain gauge slot cut-outs in the bolt were also modelled (see Figure 3.10).

Solid continuum elements were used to discretize the substrates, bolt and adhesive (in particular, hexahedral C3D8R elements were used) with very fine meshes used for all of the components. Six element layers were meshed through the adhesive thickness while eight layers were meshed through the substrate thickness, i.e., each substrate element was assigned four plies through-the-thickness.

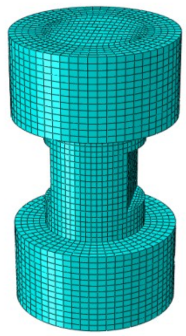

Figure 3.10: Detailed bolt mesh used in the 3D FEM

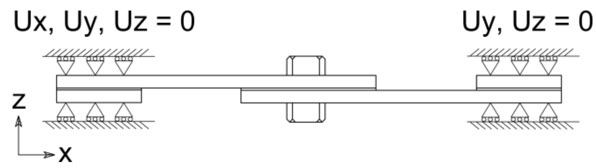

Figure 3.11: 3D FEM boundary conditions

The previously described isotropic Drucker-Prager material model was assigned to elements in the adhesive regions, while the substrate and bolt elements were assigned anisotropic and isotropic elastic material models, respectively. Composite solid sections were used for substrate elements while solid sections were used for the bolt and adhesive. Boundary conditions representative of clamping, shown in Figure 3.11, were applied to the grip region surface nodes.

As in the GHJM, contact was modelled between the bolt and substrates using a surface-to-surface contact algorithm with finite sliding. Both contact between the boltheads/substrates and shank/hole bearings was defined. It should be noted that in the 3D FEM the shank/hole bearing contact was defined over an area (the bearing surfaces) rather than along an edge (the plate hole edges) as done in the GHJM. Finally, the U_x degrees of freedom of the surface nodes in the right grip region were tied to the motion of a control point, to which the simulated machine displacement was applied.

A GHJM instance was realized for the same validation joint material and geometric parameters. As a measure of the difference in detail and complexity between the two models, the number of elements in the 3D FEM was 143,232 (all solids) versus 10,022 in the GHJM (of which 7,500 shells, 2,500 solids and 4 beams). Note that the solution accuracy of both meshes was verified by a mesh convergence study, finding the strain energy of each model to be converged to within 0.5% between successive mesh refinements.

3.4.6 Results Comparison

The bolt load transfer predicted by the GHJM and 3D FEM for the validation joint is plotted and compared with the instrumented bolt data in Figure 3.12. It can be seen that the GHJM and 3D FEM provide very similar predictions, to within 100 N across the entire range tested. Both models also correspond reasonably well with the experimental measurements, with a maximum absolute discrepancy of 300 N at the top of the measurement range. A likely reason for some of the observed discrepancy with the experiment is that neither the GHJM or 3D FEM modelled the presence of a washer, which results in a longer bolt shank length and is likely to somewhat reduced the bolted joint stiffness. Furthermore, the omission of potential hyperelastic and/or viscoplastic behaviour of the adhesive would cause some effect[5]. Overall, however, it is considered that there is satisfactory agreement with the experiment.

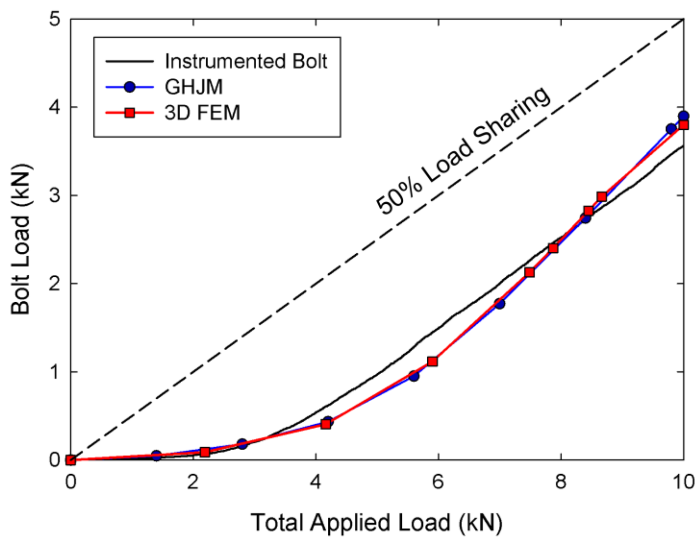

Figure 3.12: Load sharing validation

[5] Evidence of at least mildly viscoplastic behaviour of EA9361 was experimentally obtained by Lim [79].

Both finite element models predict an initial lack of bolt load transfer, which is similar to the experimental data. This is due to initially existing bolt-hole clearance. Once the adhesive has sufficiently deformed such that this clearance is taken up, bolt load transfer starts to develop. The rate of bolt load transfer increases rapidly following yielding of the adhesive, after which it steadies and tends to a constant value. As seen in Figure 3.12, the bolt load reaches 3.6 kN, representing a condition of 36% load sharing. This confirms that the experiment is in the significant load sharing regime.

Out of interest, repeated loading was also investigated experimentally. After the first joint loading, when the joint was unloaded, a residual bolt shear load remained, as predicted by plasticity theory. However, over time this load was found to relax almost completely, indicating perhaps some form of creep or hyperelastic behaviour of the adhesive that allowed a significant amount of the residual strain to be recovered. This could further explain some of the observed discrepancies with the model predictions. When the joint was subsequently reloaded, the measured load sharing was very similar to the first experimental run, albeit slightly higher at 40%. This is shown in Figure 3.13. The slight increase in load sharing can be explained by the elimination of clearance in the first run.

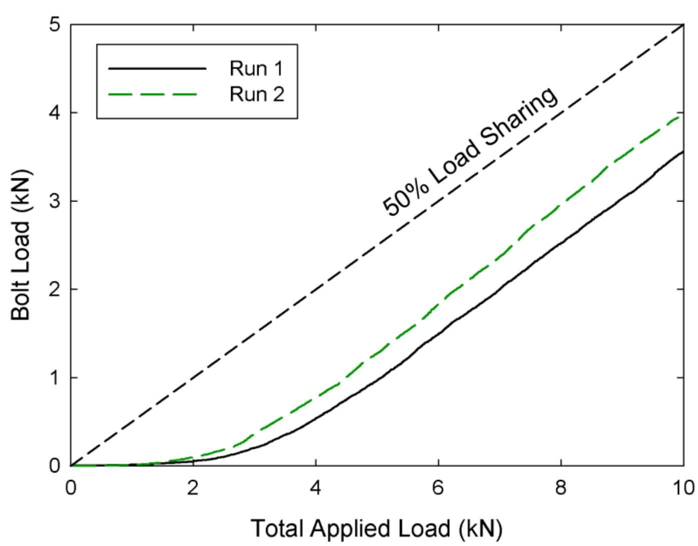

Figure 3.13: Measured load sharing when joint was unloaded and reloaded

3.4.7 Computational Efficiency Comparison

The GHJM took 242 seconds to solve with the same in-plane mesh density as the solid element model. The latter took 5436 seconds (a significant portion of the computation time spent making very small solution increments during contact detection). This represents a computational saving of > 95%, rendering the model suitable for use in a detailed sensitivity analysis.

3.5 Conclusions

An efficient model (GHJM) was developed in this chapter for predicting load sharing in single-bolt, single-lap bonded-bolted composite joints. This model takes into account clearance, contact, material nonlinearity and bolt clamp-up. An experiment was devised to validate the model, necessitating the design and manufacture of both a HBB joint that would experience load sharing and an instrumented bolt capable of measuring the bolt load. Significant load sharing was observed, with the bolt carrying up to 40% of the overall applied load. The model predictions were found to agree reasonably well with these measurements and a detailed 3D FEM. Observed differences are likely explained by the omission of washers in the model and complex adhesive behaviour such as viscoplasticity and/or hyperelasticity. The validated model is considered to be applicable for use in the global sensitivity analysis to be presented in Chapter 4.

Chapter 4: Load Sharing Global Sensitivity Analysis

In this chapter, the model developed in Chapter 3 is used in a global sensitivity analysis in order to determine the relative importance of different design parameters in load sharing in HBB joints. Furthermore, insights are obtained into the fundamental mechanisms that enable load sharing to take place.

4.1 Background

A number of researchers have previously investigated load sharing by means of modelling. Kelly [18, 19] used detailed 3D finite element models (FEM) to study the influence of various design parameters on load sharing in single-lap HBB joints. By varying one parameter at a time, he was able to determine the effects of the adhesive material, adhesive thickness (positive effect), E/D ratio (negative effect) and laminate thickness (positive effect). However, bolt-hole clearance and clamp-up were not considered and this qualitative analysis did not provide any indication of the relative importance of or interaction between design parameters. Paroissien [60] similarly varied one input at a time in his analytical model. The effect of each was described as either "weak" or "strong". The simplicity of the particular model used, however, meant that many possibly pertinent design parameters and joint behaviours were ignored. Both of these studies can be classified in the *local* sensitivity analysis (gradient-based) bracket.

Ideally, a *global* sensitivity analysis (GSA) should be performed, allowing the entire volume of the design space to be explored. This type of analysis provides both a quantitative assessment of the importance of the various design parameters (factors) and takes into account the effect of interactions between them. Such an analysis is presented in this chapter.

4.2 Problem Description

The joint configuration considered in the GSA is identical to the one described in Chapter 3. A schematic of this configuration is shown in Figure 4.1. The parameters that define the joint geometry are the substrate length L, substrate width W, substrate thickness t, adhesive thickness t_a, substrate free length L_f, overlap length L_a, edge distance E, hole diameter D and bolt head diameter D_h.

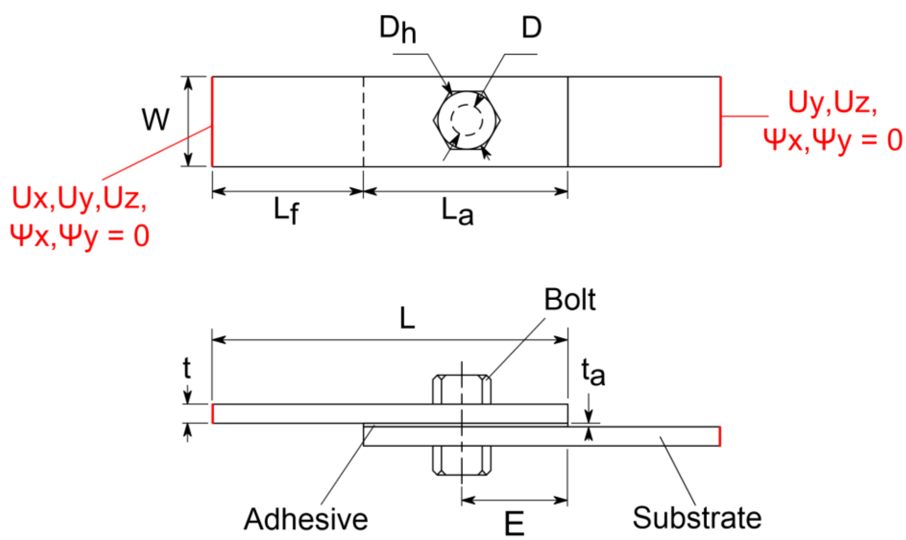

Figure 4.1: Single-bolt, single-lap joint geometry

The composite and bolt materials are kept constant throughout the GSA. The former is Cycom 5320 carbon fibre unidirectional pre-preg, whose properties were previously defined in Table 3.1, while the bolt is considered to be made of steel (E = 205 GPa, ν = 0.3). Note that only a single quasi-isotropic layup of [+45/-45/0/90]$_{4S}$ is considered for both substrates in order to render the sensitivity analysis tractable. To account for the effect of different laminate stiffnesses, the ply thickness is allowed to vary to simulate a range of laminate thicknesses.

As per the model in Chapter 3, the adhesive is assumed to exhibit rate-independent elastoplastic behaviour. This is modelled in the form of Hookean elasticity combined with linear Drucker-Prager plasticity. Linear isotropic hardening is assumed. This formulation represents a fairly broad and general description of elastoplastic aerospace adhesives. Based on this formulation, the adhesive behaviour is fully defined by 5 parameters, namely Young's modulus E_a, Poisson's ratio ν_a, tangent modulus H, friction angle β and the initial yield stress σ_{yt}.

4.3 Model Description

An efficient computational model of a single-bolt, single-lap hybrid bonded-bolted composite joint, called the *Global Hybrid Joint Method* (GHJM), was developed in Chapter 3. This model, which is applicable to the problem described in section 4.2, follows an equivalent single layer (ESL) approach, with the laminates modelled as shells, the bolt as a beam and the adhesive as an isotropic continuum solid. The model is solved using the displacement-based finite element method in ABAQUS, subject to the boundary conditions shown in Figure 4.1. It was shown in Chapter 3 that the model predictions compare satisfactorily with both a detailed 3D finite element model and experimental measurements, while providing computational savings of > 95% compared to the former.

4.4 Global Sensitivity Analysis

A global sensitivity analysis (GSA) was performed of the GHJM in order to quantitatively assess the importance of the various model input factors in load sharing. A variance-based GSA method was chosen for this purpose, as these permit consideration of general nonlinear, non-monotic models without making underlying assumptions about their response characteristics. Consider that the GHJM can be simply represented, without further consideration of its inner workings, as:

$$Y = f(\boldsymbol{X}) \qquad (4.1)$$

Here Y is the model output of interest (i.e., load sharing), $\boldsymbol{X} = (X_1, X_2, \dots, X_n)$ is a vector of n input factors (i.e., a given joint design) and f is a function representing the inner workings of the model. The variance of the model output can be partitioned into variance due to individual factors (V_i) and interactions within sets of factors (V_{ij}, … , $V_{ij\dots n}$) as follows (notation from Saltelli et al. [80]):

$$\mathrm{var}(Y) = \sum_{i=1}^{n} V_i + \sum_{i<j}^{n} V_{ij} + V_{12\dots n} \qquad (4.2)$$

where:

$V_i = \mathrm{var}_{X_i}[E(Y|X_i)]$

$V_{ij} = \mathrm{var}_{X_{ij}}\left[E(Y|X_i, X_j)\right]$

var = variance

var_{X_i} = variance taken over all possible values of X_i

$E(Y|X_i) =$ = expected value of Y given a fixed value of X_i

$E\left(Y\middle|X_i, X_j\right) =$ = expected value of Y given fixed values of X_i, X_j

The extension of the above definition of V_{ij} to higher order interactions (V_{ijk}, …,$V_{ij\dots n}$) is self-evident. Based on this decomposition of variance, two measures of sensitivity or importance can be calculated for each factor:

- A main effect index S_i. This is the proportion of the main effect variance V_i (i.e., the variance due to the factor X_i by itself) to the total output variance, as given by Eqn. (4.3):

$$S_i = \frac{V_i}{\mathrm{var}(Y)} \qquad (4.3)$$

- A total effect index S_{Ti}. This is the proportion of the main effect variance V_i as well as variance due to interactions involving X_i to the total output variance, as given by Eqn. (4.4):

$$S_{Ti} = \frac{V_i + V_{ij} + \dots + V_{ij\dots n}}{\mathrm{var}(Y)} \tag{4.4}$$

Among variance-based GSA methods, the Sobol method [81] and Extended Fourier Amplitude Test (EFAST [82]) are the most useful since they permit both the main effects and total effects to be calculated. In this work, the EFAST was preferred over the Sobol method due to its lower computational cost and superior convergence rate. A brief summary of the EFAST method is given as follows. The n-dimensional input space is first mapped onto the unit hypercube $K^n = (\boldsymbol{X} | 0 \leq X_i \leq 1; i = 1, \dots, n)$. The following steps are hence taken:

1) Each input factor is intelligently assigned two frequencies; a main effect frequency ω_i and a second, complementary frequency $\omega_i{}'$.

2) For each factor, the input space is uniformly sampled along a search curve, along which the factor in question X_i oscillates at the main effect frequency ω_i and the remaining factors oscillate at their complementary frequencies $\omega_i{}'$. The search curve proposed by Saltelli et al. [82] was used in this work, as defined by Eqn. (4.5):

$$X_i = \frac{1}{2} + \frac{1}{\pi} \arcsin(\sin(\omega_i s) + \varphi_i) \tag{4.5}$$

where $-\pi \leq s \leq \pi$ and φ_i is a random phase shift chosen in [0,2 π)

3) The overall output variance is calculated.

4) The output variance spectrum is decomposed by frequency. By evaluating the output variance spectrum at each factor's main effect frequency ω_i and its higher harmonics $p\omega_i$, the output variance attributable to each factor by itself can be calculated. This allows for calculation of a main effect sensitivity index.

   By evaluating the output spectrum at the complementary frequencies of the remaining factors $\omega_i{}'$ and their higher harmonics $p\omega_i{}'$, a residual variance can be calculated

$$D - \Sigma D_{(-i)}$$

   where D is the total output variance and $D_{(-i)}$ is the partial variance due to all factors but X_i. This allows for the calculation of a total effect sensitivity index (first order + interaction effects).

5) Steps 2-4 are repeated for each separate factor.

A key consideration in the EFAST method is the proper selection of the sampling frequencies. Note that the computational cost of this method is

$$C = nN_r(2M\omega_{max} + 1) \tag{4.6}$$

Here the maximum frequency ω_{max} is equal to the main effect frequency ω_i, while N_r is the number of reseeds of the search curve. N_r was chosen as $N_r = 1$ based upon the recommendations of Saltelli for the number of GHJM input factors (12). It is clear that a low main effect frequency is desirable to limit computational cost. Nevertheless, a sufficient spread in frequencies must simultaneously be achieved to avoid interference between the main effect frequency and complementary frequencies. This is achieved through an interference factor, M, which should normally be $M = 4$.

As recommended by Saltelli [82], the complementary frequencies were chosen to be different to achieve a better scanning of the input space. However, to ensure that they are all unique requires a large main effect frequency ω_{max}, which strongly impacts computational cost. Therefore each complementary frequency was repeated twice, as a good compromise between optimal scanning and computational efficiency (note that each complementary frequency could have been repeated up to 12 times, with 1 repetition being the ideal target). Based on the number of input factors (12), the number of reseeds of the search curve (1) and the main effects frequency (a value of $\omega_{max} = 48$ was used based on repeating each frequency only twice), the computational effort for the analysis was limited to 4620 model evaluations[6].

The EFAST method as described was programmed in MATLAB. Its correct implementation was verified by running the code for two classical analytical SA test cases: the Sobol g-function and the Ishigami function. The obtained results were compared with the reference results in [82] and were found to match closely. This provides a high degree of confidence that the method was correctly implemented. For further details on the selection of the factor frequencies and Fourier decomposition, the reader is referred to Saltelli et al. [82].

4.4.1 Design Space Justification

The input space from which the GSA designs were sampled is presented in Table 4.1. The choice of the geometric parameter ranges is justified as follows. From bolted joint design, it is well known that E/D and W/D should be greater than 3 and 5, respectively, in order to avoid shear-out and net-section failure of the substrates [83]. Ply thicknesses were selected so as to provide a broad range of substrate thicknesses. The minimum adhesive thickness was chosen as 0.1 mm as this is a recommended minimum for optimizing bond strength [84]. Meanwhile, the maximum thickness was taken an order of magnitude higher as it was hypothesized

[6] The average wall-clock time taken per GHJM evaluation in the GSA was 3 minutes 49 seconds. The total wall-clock time was thus 12 days 5 hours 48 minutes 59 seconds. These computations were performed on four Intel i7-2600 CPUs @ 3.40 GHz running in parallel. Note that all three load levels were considered in different load steps of a particular GHJM evaluation.

that this could promote load transfer. The chosen clamp-up load ranges from finger tight to the maximum recommended by McCarthy et al. [85] for composite substrates. Finally, bolt-hole clearances were chosen to mimic typical tolerances achieved in the aerospace industry [86, 87].

Table 4.1: Input Space for Sensitivity Analysis

Geometric Parameter	**Unit**	**Minimum**	**Maximum**
Width ratio (W/D)	-	5	10
Edge distance ratio (E/D)	-	3	6
Bolthead diameter ratio (D_h/D)	-	1.1	2.5
Ply thickness (t_{ply})	mm	0.1	0.25
Adhesive thickness (t_a)	mm	0.1	1
Clamp-up load (F_{cl})	kN	0.2	8
Bolt-hole clearance (δ)	mm	0	0.15
Adhesive Parameter	**Unit**	**Minimum**	**Maximum**
Young's modulus (E_a)	MPa	500	5000
Poisson's ratio (ν_a)	-	0.2	0.45
Hardening slope (H)	MPa	0	30
Yield stress (σ_{yt})	MPa	6	60
Angle of friction (β)	Deg	0	70

With regards to adhesive parameters, the maximum Young's modulus was selected to be representative of a stiff structural adhesive while the lower bound was set at a sensible 500 MPa [88]. The adhesive tensile yield strength covers an order of magnitude, from 6-60 MPa, broadly representative of current structural adhesives, while the yield surface friction angle spans the entire physically feasible range. Note that the bolt diameter was kept constant at D = 6 mm. Consequently, the substrate free length L_f was also a constant 24 mm, based on ASTM D5961 which specifies a free length of 4D for bolted joint tests [14]. The coefficient of friction was also kept constant at a value of 0.2.

4.5 Convergence study

As a consequence of the use of the *MPC subroutine in ABAQUS (see Chapter 3), adaptive re-meshing was not a feasible option for GHJM solution accuracy control. Instead, a single, fine element size was used in all of the meshes in the sample. It was empirically determined that this would lead to globally reliable solutions. From the complete sample, 10% was uniformly, randomly sampled without replacement. These models were run with both the chosen 0.6 mm element size and a 33% finer mesh (i.e., an element size of 0.4 mm). Convergence of the solutions was verified by calculating the change in total bolt shear load.

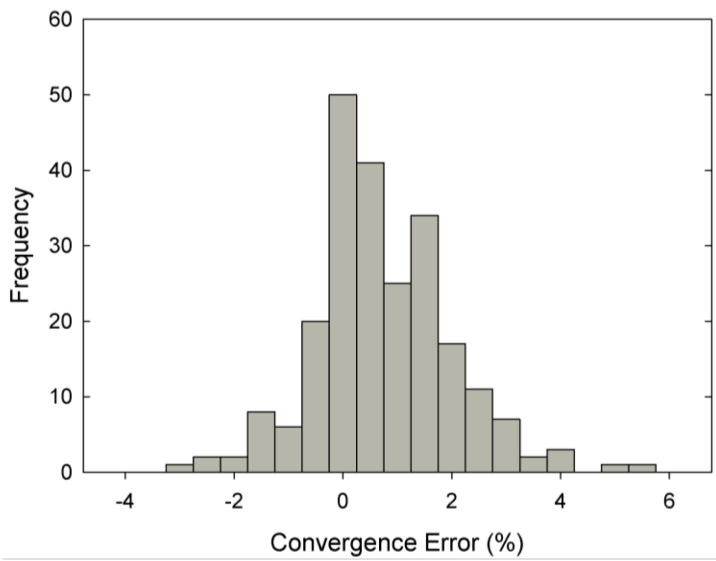

Figure 4.2: GHJM solution convergence for the GSA sample

The obtained results are shown in the histogram in Fig. 4.2. All of the sampled runs showed an absolute convergence error of less than 5% with a maximum of 4.7%. Without further statistical analysis, it is concluded from these results that a 0.6 mm element size is a suitable choice and leads to globally reliable results of the GHJM in the GSA design space.

4.6 Results & Discussion

The GSA was performed at three different edge load levels: low (200 kN/m), medium (450 kN/m) and high (650 kN/m). The choice of these edge load levels is motivated in Appendix A. The raw data at the high load level is plotted in Figure 4.3.

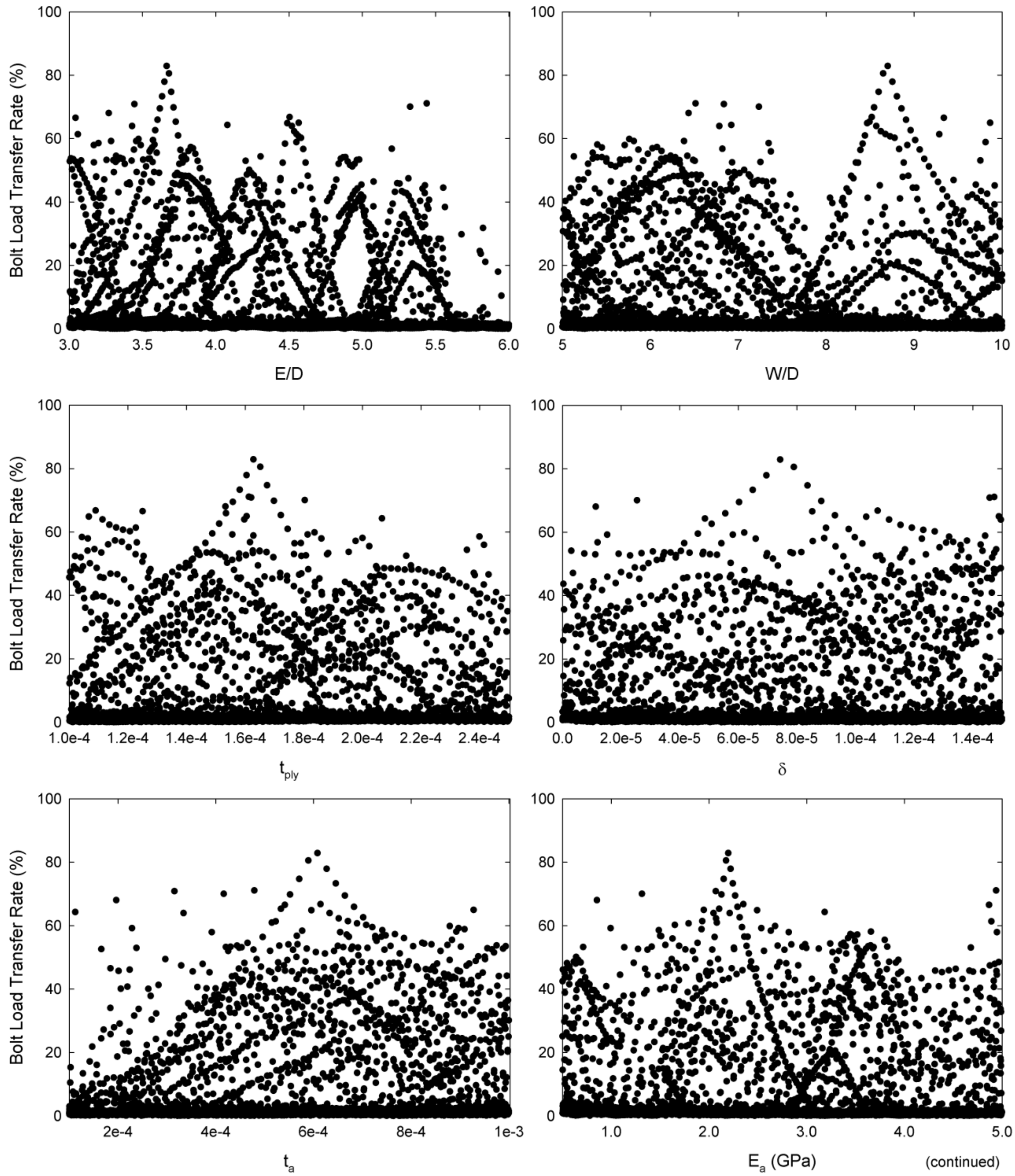

Figure 4.3: Scatterplots of model output versus the different design parameters at the high load level

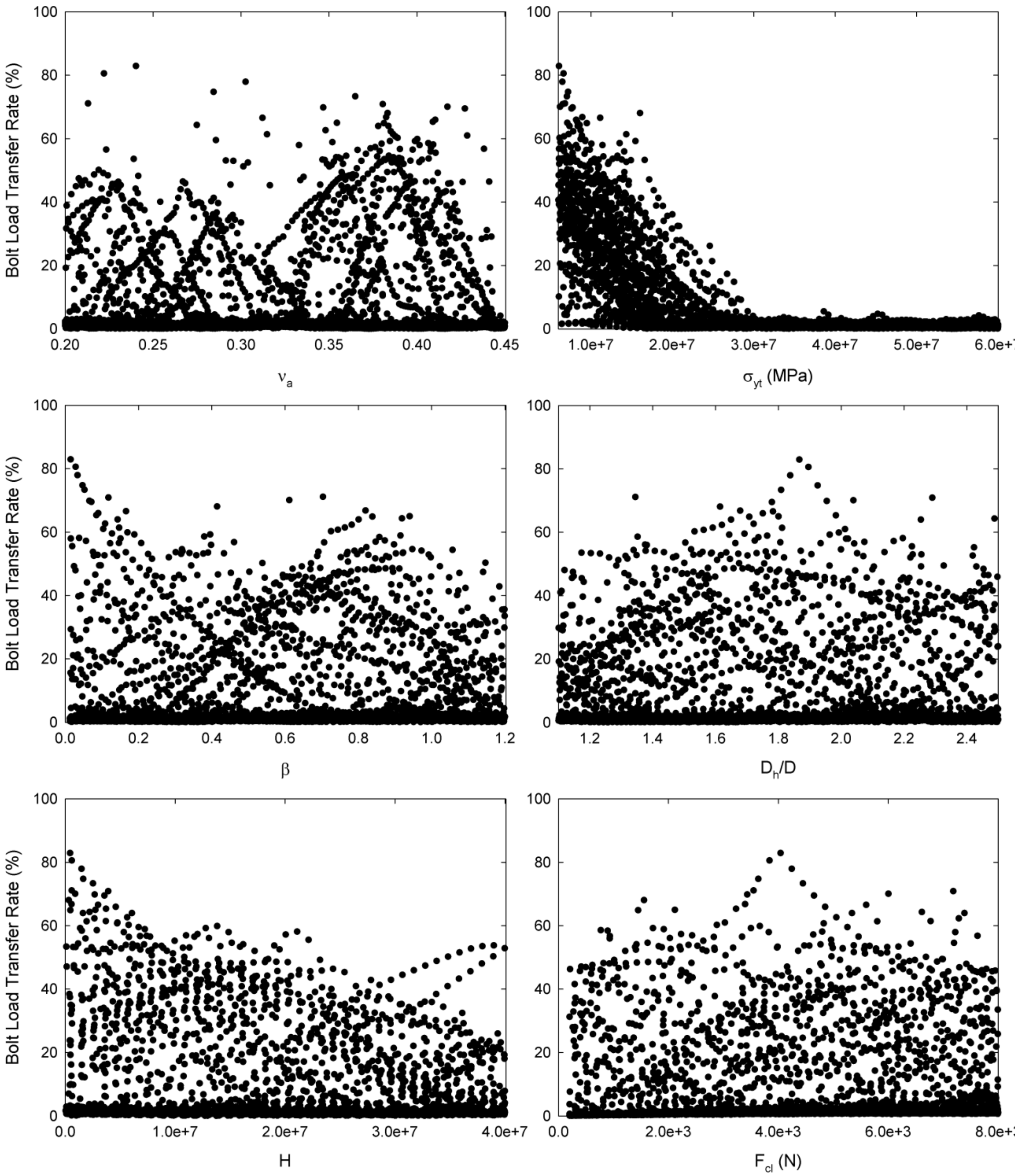

Figure 4.3: Scatterplots of model output versus the different design parameters at the high load level (continued)

The sampling periodicities of the different factors can be clearly distinguished in the raw data. While care should be taken to not overinterpret Figure 4.3, it appears safe to conclude that σ_{yt} has a strong effect on load sharing, with not a single design achieving substantial load sharing (≥ 10%) when σ_{yt} > 30 MPa. No further conclusions are drawn at this stage regarding the effects of the various parameters—the processed GSA results are relied upon to objectively interpret this data.

From the raw results files, the separate components of bolt load transfer (bearing and bolthead) were also extracted. Individual consideration of these components, in addition to the overall bolt load, led to some useful insights that are shown in Table 4.2.

Table 4.2: Load sharing breakdown of raw data

Total No. of Designs = 4620	**High Load Level**	**Medium Load Level**	**Low Load Level**
No. of designs with load sharing ≥ 10%	894	289	59
- Among these, designs with bearing load transfer	894	289	43
- Among these, average contribution of bearing load transfer to overall bolt load	94.5%	87.4%	52.0%

As can be seen from this breakdown, at the high load level, 894 of the 4620 designs (19% of the design space) experienced substantial load sharing. At the medium load level this fell to 6% and at the ≥ low load level to 1%. At the high load level, 100% of designs that experienced significant load sharing also experienced bearing load transfer. This component of bolt load transfer was responsible for on average 94.5% of the total bolt load. At the medium load level, the same observation was valid, with the average bearing load transfer contribution falling to 87.4%. Very few designs were able to achieve substantial load sharing at the low load level. It can be concluded from these results that at medium and high load levels, bearing load transfer is by far the most important component of bolt load transfer and is effectively a prerequisite for achieving substantial load sharing. At low load levels, it is almost impossible to achieve substantial load sharing in the design space studied.

The processed GSA results are presented in Figures 4.4-a,b. These bar charts, respectively, compare the main and total effect indices calculated for the different factors.

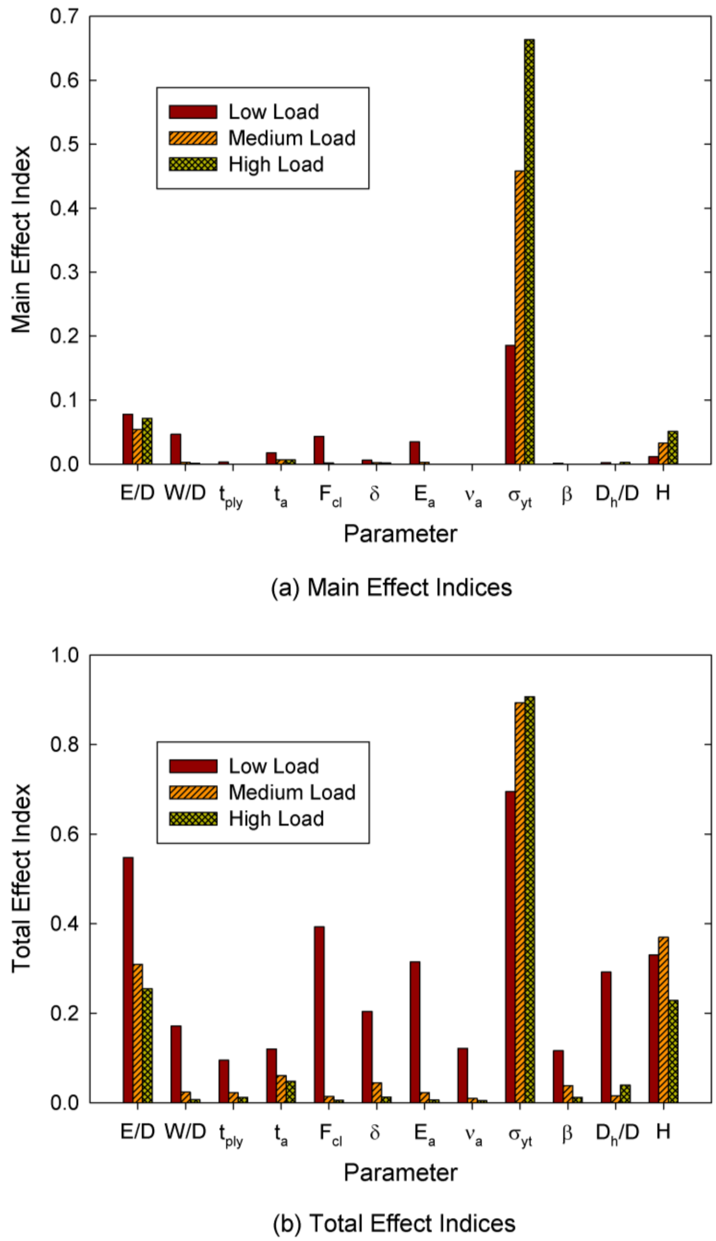

Figure 4.4: Bolt load transfer rate sensitivity indices

It is clear from Figure 4.4 that the adhesive yield strength σ_{yt} is indeed the most important design parameter influencing load sharing, at all three edge load levels considered. Its importance increases with increasing load level. At the medium load level, not considering interactions, it is 8.5 times as important as any other parameter (based on the main effect indices). Considering interactions, it is 2.4 times as important as any other parameter (based on the total effect indices). The following explanation is proposed for why this parameter is so important and the mechanism by which it works. Load prefers to travel through the stiffer load path, which in the elastic regime of a HBB joint is easily the bonded joint. However, as the adhesive yields, it stiffness decreases locally by typically an order of magnitude or more. If plasticity is able to spread through the entire bondline, from the overlap edges all the way to the hole, and assuming adequate ductility of the adhesive such that failure does not occur before this happens, then:

- The bondline stiffness as a whole drastically reduces and the bondline compliance drastically increases. The increased compliance allows bolt-hole clearance to be overcome and bearing contact to be established.

- The decrease in the bondline stiffness means that the bolt becomes comparatively stiffer. As long as bearing contact has been established, this causes the bolt to take up a much larger proportion of any additional load than it would if the adhesive were linearly elastic.

To demonstrate the two points just above, an example of a bonded joint with a hole is considered. The geometric parameters from Chapter 3 are assumed, as well as an idealized bilinear behaviour for the adhesive (E_a = 600 MPa, ν_a = 0.42, σ_{yt} = 10 MPa, H = 34.5 MPa, β = 0). During tensile loading of this joint, the relative displacement between the holes in the top and bottom substrates or *hole closure* allows the substrates to “grip” a hypothetical bolt (not modelled). This is shown schematically in Figure 4.5. Once the hole closure equals the initial bolt-hole clearance, hole bearing contact hypothetically starts to develop. It was previously shown that this is the bolt load transfer component that is capable of transferring large amounts of load. Hole closure is plotted in Figure 4.5 assuming both a 10 MPa and 15 MPa adhesive yield strength. It can be seen that in either case the GHJM initially predicts an identical, slow rate of hole closure. At this stage of loading, there may well be yielding of the adhesive near the overlap edges, away from the hole. However, it is only once the adhesive has plasticized all the way through to the hole edge that the hole closure rate increases significantly (in the present example by a factor of 37). This faster closing of the hole allows bolt-hole clearance to be overcome, bearing contact to be established and significant load to be transferred to the bolt through bearing contact.

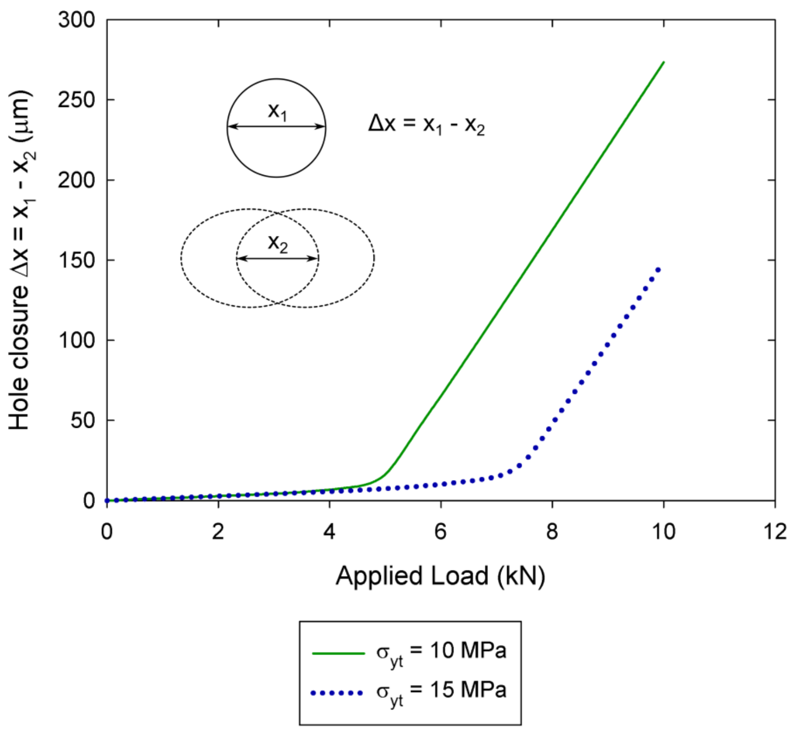

Figure 4.5: Hole closure versus applied load for different adhesive yield strengths

For the same example, the maximum principal plastic strain along the adhesive centerline is plotted in Figure 4.6 (in the adhesive midplane) at loads of 3 kN and 4.7 kN. At the 3 kN load, when the hole closure rate is low (as evident from Figure 4.5) there is no adhesive plasticity near the hole (only near the overlap edges). The closure rate starts to increase drastically at the 4.7 kN mark. Figure 4.6 reveals that this corresponds to the first instance of plasticity at the hole edge, i.e., once the adhesive has yielded all the way through to the hole.

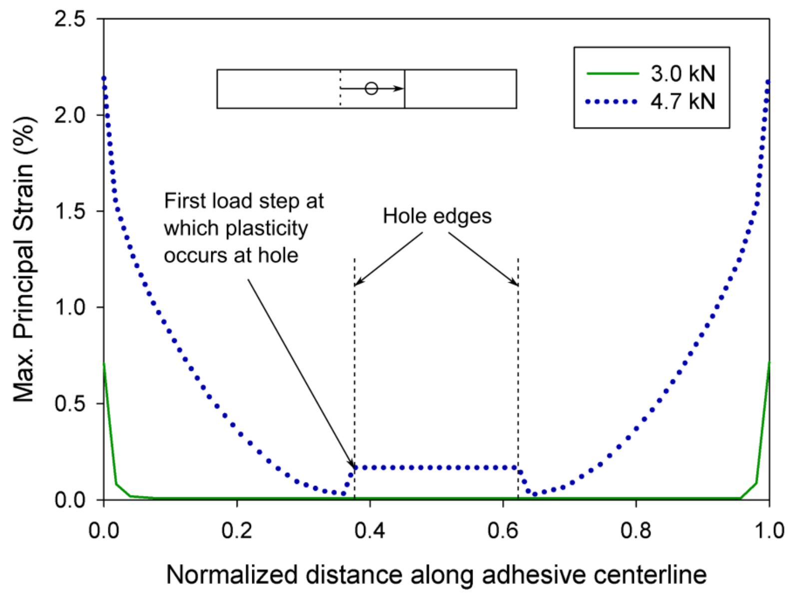

Figure 4.6: Maximum principal plastic strain along the adhesive centerline

The effect of lower adhesive yield strength is thus to facilitate plasticisation of the overlap, bringing forward the point at which the bonded joint stiffness is drastically reduced and the hole closure rate is increased. Note that at high joint loads, a larger subset of the design space experiences sufficiently high adhesive stresses for overlap plasticisation to occur. This explains the increased importance of this parameter at higher loads.

After σ_{yt}, the next most important parameters are E/D and H. Their respective main and total effect indices are very similar across the various load levels, although E/D is slightly more important at low load levels while H is slightly more important at high load levels. At the medium load level, their total effect indices are 0.31 and 0.37, respectively, compared to 0.89 for the adhesive yield strength, but well above the next most important parameter (t_a at 0.06). Both of these parameters work strongly by interaction, as evidenced by their substantially larger total effect indices compared to their main effect indices. The mechanism by which they contribute to load sharing is intimately tied to the plastic flow mechanism described previously. A smaller E/D ratio leads to higher adhesive stresses, which in turn leads to earlier onset of yield and plasticisation of the overlap. A smaller H increases the plastic flow rate of the adhesive once it has yielded, leading to faster hole closure and a lower bondline stiffness once the overlap has fully plasticised.

All other parameters in the design space are, by comparison, relatively unimportant in achieving substantial load sharing. At the medium load level and considering the total effect indices, they are at best 5 times less important than E/D and 15 times less important than σ_{yt}. It is therefore inefficient to focus primarily on optimizing these variables when designing a joint for substantial load sharing.

Perhaps the most counterintuitive finding from the GSA is the relative lack of importance of bolt-hole clearance. This variable ranks fifth in importance, after adhesive thickness, and considering main effect indices is 8 times less important than the adhesive hardening slope H at the medium load level. The reason for this becomes clear when a local sensitivity analysis is performed. The same example joint as earlier is considered for this purpose, this time including a bolt and a variety of bolt-hole clearances and hardening slopes. Figure 4.7, which plots the results of this analysis, shows that when H = 0.1 MPa the bolt load transfer rate is almost entirely insensitive to clearance. This can be simply explained as follows. If the adhesive behaviour is elastic-perfectly plastic (H = 0.1 MPa in Figure 4.7), then once the overlap has fully plasticised, the adhesive cannot support any additional load. It will thus deform an infinite amount for each additional increment of load. Consequently, the adhesive can theoretically overcome *any* clearance and bolt load transfer becomes completely insensitive to clearance. Interestingly, even when the adhesive has considerable strain hardening, such as H = 35 MPa, bolt load transfer is still relatively insensitive to bolt-hole clearance. This is shown by the dashed line in Figure 4.7, which demonstrates that for the given example, a huge increase of 50 μm in bolt-hole clearance results in a relative drop of only 30% in the predicted bolt load transfer rate, from 37% to 28%.

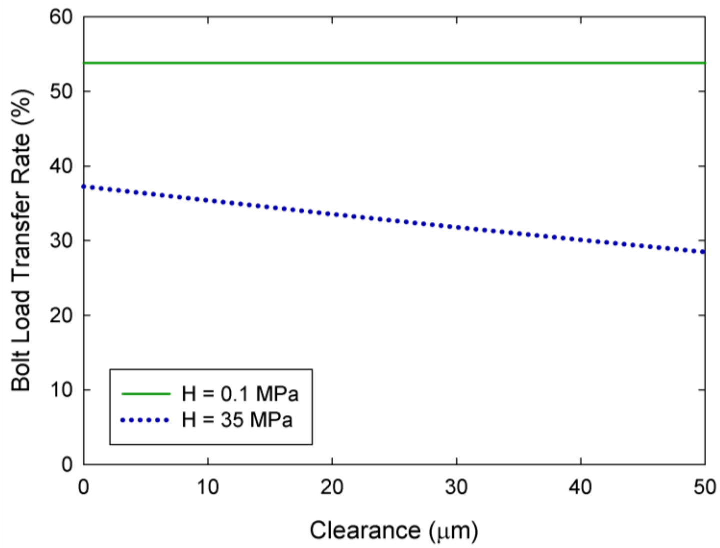

Figure 4.7: Effect of hardening slope and clearance on bolt load transfer

The above observations are consistent at the medium and high load levels. At the low edge load level, while σ_{yt} and E/D remain the most important parameters, their relative importance is significantly reduced. Bolthead diameter and clamp-up load in particular become relatively more important. This is because complete yielding of the overlap, and thus bolt-shank-to-hole-bearing load transfer, cannot occur for most designs at this load level. Consequently, at low load the bolthead load transfer component becomes relatively more important. However, as has been shown before, only limited load is able to be transferred to the bolt in this manner, which is exacerbated by the stiffness mismatch that exists when the adhesive has not yielded. Furthermore, very few designs are able to achieve substantial load sharing at low load levels.

4.7 Implications for HBB joint design

The primary mechanism by which substantial load sharing can be achieved in HBB composite joints was shown in section 4.6 to be plastic flow of the adhesive. This is governed by the σ_{YT}, E/D and H parameters, which are consequently the most important factors in load sharing. This finding is important in a number of ways. Primarily, it implies that if a HBB joint is designed in the traditional way, using a stiff, strong and brittle adhesive, then regardless of how well geometric parameters such as bolt-hole clearance and adhesive thickness are chosen and controlled, no substantial load sharing can be achieved. If it is indeed desired to have substantial load sharing, then an unconventional approach must be taken. The adhesive must be allowed to incur large strains; this is only possible if it has a low resistance to deformation. In elastoplastic adhesives of the type considered in the present GSA, it was found that this can be achieved most effectively through yielding the material. In addition, the adhesive must of course be sufficiently ductile such that it is able to incur these large strains without failing. The experimental studies in the literature that report significant overall strength improvements of HBB joints all verifiably used adhesives where this is the case. There are understandably concerns regarding this approach. Load rate and temperature both have a strong influence on the behaviour of adhesives and could drastically change their load sharing suitability. Furthermore, permanent deformation of the adhesive is a source of concern. Further research is required to better understand these possible issues[7].

Of the top five most important parameters, the two parameters that were found to be least important were adhesive thickness and bolt-hole clearance. The adhesive thickness finding was explained by the fact that when a perfectly elastoplastic thin bondline yields, it can theoretically flow with similar ease to a thick bondline (since neither have any resistance to additional load). However, if the adhesive is thin then the shear strain must be much greater to generate the same relative displacement of the substrates as a thicker bondline. Also, if the hardening slope is substantial, then this will severely inhibit the deformation of a thin bondline and thus bolt load transfer. Here it is useful to revisit the example

[7] Other, non-traditional (in aerospace) types of adhesives, e.g. elastomers, are able to incur very large strains without permanent plastic deformation and therefore also seem like promising candidate materials. The anticipated problem with these adhesives is that their stiffness may be *too* low to transfer any substantial load, while they will also need to be qualified for aerospace use, which may be cost-prohibitive.

joint of section 4.6. This time, the adhesive thickness is varied and the effect on plastic strain at the overlap edge and bolt load transfer is considered as shown in Figure 4.8.

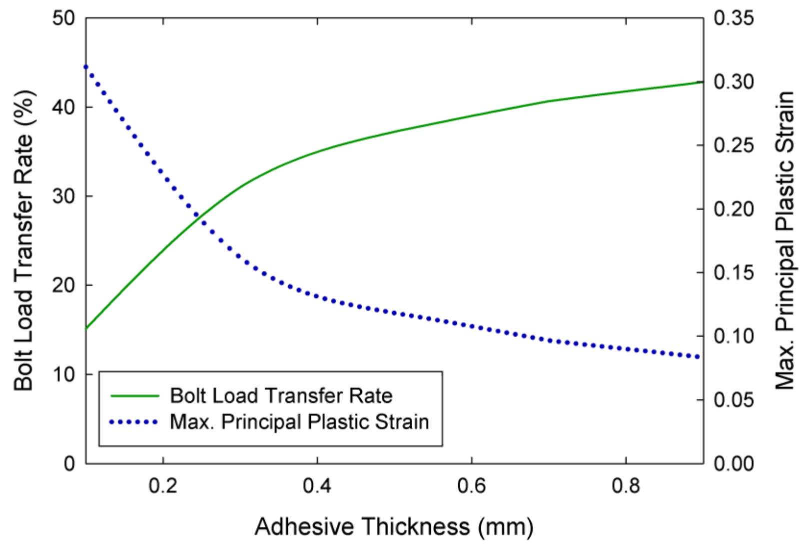

Figure 4.8: Effect of bondline thickness on bolt load transfer and adhesive strain

It can be seen that at adhesive thicknesses below 0.4 mm, the adhesive strain increases rapidly with diminishing adhesive thickness. Meanwhile, load sharing decreases rapidly. Above adhesive thicknesses of 0.4 mm, both of these response variables become far less sensitive to adhesive thickness. Interestingly, this value seems to hold for the entire design space, as can be observed from the raw data plot in Figure 4.3. Below t_a = 0.4 mm, the maximum load transfer decreases strongly with adhesive thickness. Above 0.4 mm, there appears to be no such trend. The implication for active HBB joint design appears to be that the adhesive thickness should be at least 0.4 mm. Simultaneously, it should be kept in mind that there is a well-known relationship between bondline thickness and bond strength [20]. This precludes the use of bondlines that are *very much* thicker than 0.4 mm.

Like adhesive thickness, bolt-hole clearance was also not found to be a "make-or-break parameter" and had a relatively low importance compared to the top three factors. However, one point not considered in the sensitivity analysis was that, much like a thin bondline, the amount of plastic flow required to overcome larger clearances also entails increasingly high levels of strain in the adhesive, which may be sufficient to engender adhesive failure. This is demonstrated in Figure 4.9 for a joint with the example parameters of section 4.5, in which the maximum principal plastic strain at the overlap edge is plotted versus bolt load transfer and clearance.

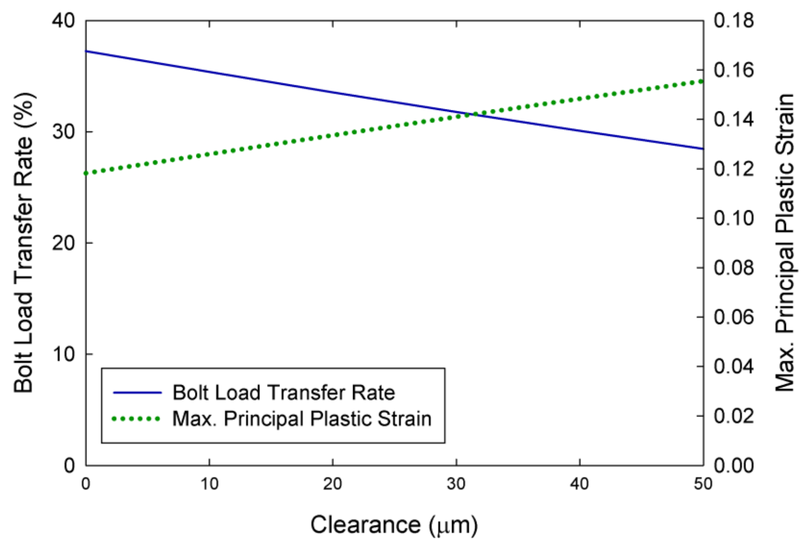

Figure 4.9: Effect of clearance on bolt load transfer and adhesive strain

It can be seen that a 50 μm increase in the bolt-hole clearance leads to a 30% relative decrease in load sharing and a 30% relative increase in the adhesive strain, compared to a 0 μm clearance. It should therefore be kept in mind that, unless the adhesive has a very high strain to failure, it is desirable to have small bolt-hole clearances in order to limit the strain in the adhesive prior to bolt-hole contact and avoid premature adhesive failure. This simultaneously maximizes bolt load transfer.

Summarily: when designing bonded-bolted joints for load-sharing, the bondline thickness should be at least 0.4 mm, while bolt-hole clearance should be minimized in order to ensure low adhesive strains. The adhesive should be as ductile as possible to ensure that the adhesive does not fail prematurely.

4.8 Conclusions

A detailed global sensitivity analysis of load sharing in HBB joints containing an elastoplastic adhesive was conducted. From this analysis, it was determined that:

- For substantial load sharing (≥ 10%) to occur, the adhesive overlap must fully plasticise. For designs in which this did not occur (σ_{yt} > 30 MPa) no substantial load sharing was observed at the medium and high load levels.

- More designs are able to achieve overlap plasticisation at higher loads. Consequently, more designs experience substantial load sharing at higher load levels (1%, 6% and 19% of the design space at the low, medium and high load levels, respectively). At low load levels, it is extremely difficult to achieve load sharing and the adhesive will transfer most of the load.

- The most important factors influencing load sharing are categorically σ_{yt}, E/D and H (total effect index = 0.89, 0.37, 0.31, respectively, at the medium load level). This is due to their role in plasticisation of the overlap and plastic flow of the adhesive, which is the dominant mechanism by which substantial load sharing can occur.

- Despite being less important in load sharing, adhesive thickness and bolt-hole clearance have a major influence on the maximum plastic strain that is developed in the adhesive at the overlap edges and should thus be carefully controlled.

- The remaining joint design parameters are relatively unimportant in load sharing.

Chapter 5: Mathematical Model of the Hybrid Bonded-Bolted Joint Problem

In the previous two chapters, the problem of load sharing was addressed. The *GHJM* model that was developed, however, is not ideally suited for use in a HBB joint strength analysis. The reasons for this are:

- The adhesive stresses and strains at the bondline edge interfaces do not converge as the finite element discretization is refined, i.e., they are singular. This is a well-known feature of finite element models of bonded joints that model the adhesive as a continuum solid [89, 90]. This complicates the goal of achieving a simple, robust (mesh-insensitive) adhesive failure prediction.

- While *GHJM* model generation has been automated using MATLAB, ABAQUS CAE is nevertheless required to write and solve the ABAQUS input deck and thus an ABAQUS license is necessary. Meanwhile, a standalone joint analysis tool is desired by the project partners.

In response to these issues, in the next few chapters a new mathematical model of the HBB joint problem is developed. This model is implemented as a fully standalone computer code in MATLAB. The relevant mathematical framework is formulated from first principles and combines the preeminent analytical bonded joint model [71] with the power of the meshless Galerkin method. This approach successfully eliminates bondline singularities. Although the model is able to predict load sharing, its principal aim is to predict stresses and strains and to achieve a basic strength prediction.

The developed model incorporates a new adhesive kinematic model and takes into account nonlinear constitutive behaviour of the adhesive. Bolt clamping and bolt-hole clearance are also considered. Finally, by simply altering the boundary conditions, both single-lap and double-lap joints are able to be analyzed.

5.1 Single-Lap Joint

Problem Description

The problem of interest is the quasi-static stress analysis of a composite single-lap hybrid bonded-bolted joint. This type of joint consists of two composite substrates that partially overlap and are joined in the overlap region using both adhesive and one or more bolts (see Figure 5.1). Alternatively, one of the substrates may be metallic, since composite-to-metal joints are also important in composite structures.

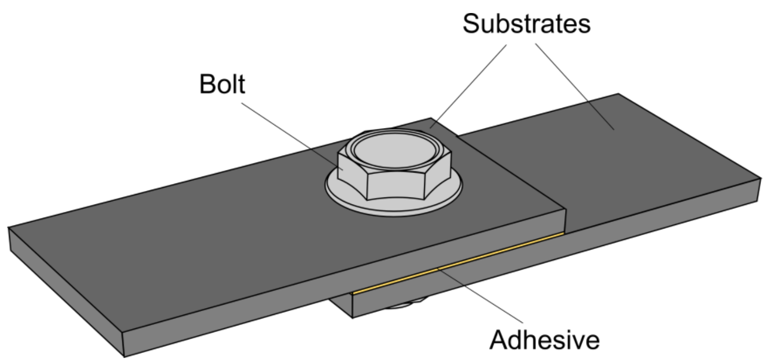

Figure 5.1: Single-lap HBB joint

Model Description

To obtain an efficient mathematical model of the aforementioned problem, the various components of the joint are represented using simple “single layer” and “single line” structural entities (see Figure 5.2). In particular, the substrates are represented as shear deformable plates while the bolt is represented as a shear deformable beam. The adhesive is modelled using an original shear lag theory, as shall be described in section 5.1.3. Small strains and frictionless contact are assumed throughout the formulation.

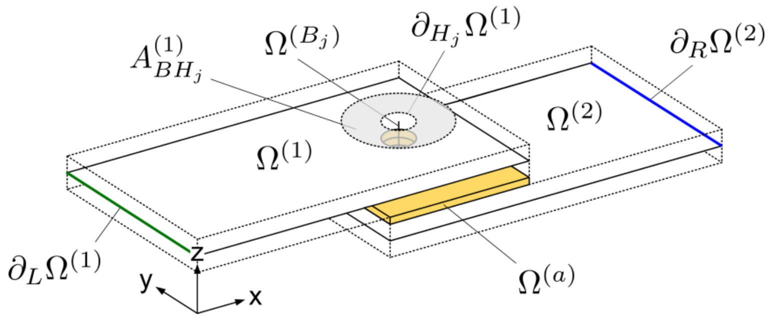

Figure 5.2: Model representation of the problem

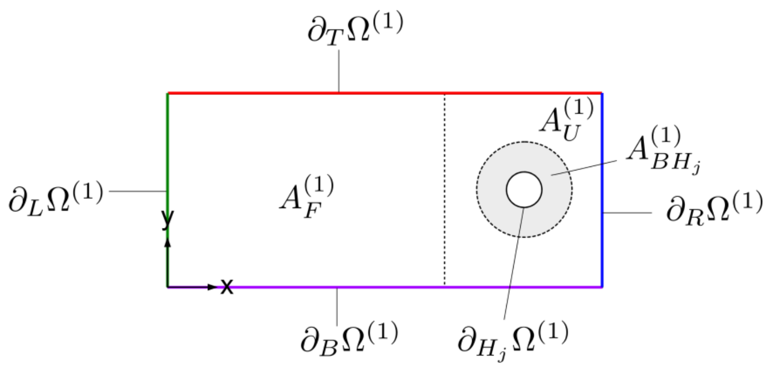

(a) Top Adherend Boundaries and Areas

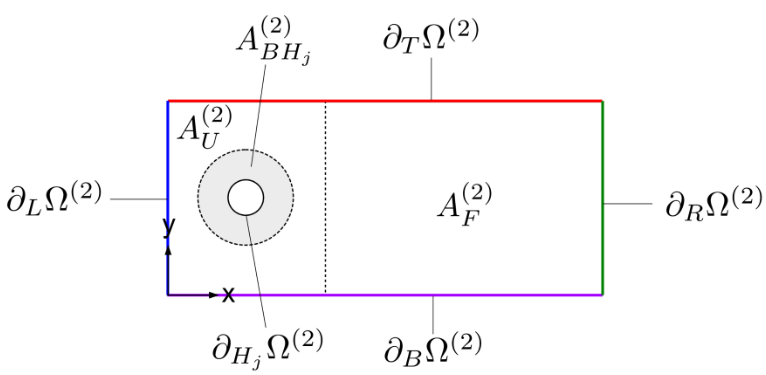

(b) Bottom Adherend Boundaries and Areas

Figure 5.3: Domain boundaries and areas

A number of distinct boundaries exist along which Neumann and Dirichlet boundary conditions may be applied. These are shown in Figure 5.2 for the case of uniaxial tension of a finite width joint. For other load cases, additional boundaries may be necessary. A more general definition of the model boundaries and areas for each adherend is thus given in Figure 5.3. Provision is made for the case of a joint with multiple bolts through inclusion of the j subscript in the bolt boundaries, areas and domains (j being the bolt identifier).

5.1.1 Equilibrium Equations

In accordance with established continuum mechanics theory, the equilibrium equations are assumed to hold pointwise everywhere in the problem domain $\Omega = \Omega^{(1)} \cup \Omega^{(2)} \cup \Omega^{(a)} \cup \left(\bigcup_{j=1}^{N_B} \Omega^{(Bj)}\right)$:

$$\rho\,\ddot{\mathbf{u}} + \boldsymbol{\nabla} \cdot \boldsymbol{\sigma} - \rho\,\mathbf{b} = \mathbf{0} \qquad \text{(Balance of linear momentum/Cauchy's first law)} \qquad (5.1)$$

$$\boldsymbol{\sigma} = \boldsymbol{\sigma}^T \qquad \text{(Balance of angular momentum/Cauchy's second law)} \qquad (5.2)$$

where ρ is the mass density, $\ddot{\mathbf{u}}$ is the point acceleration, $\boldsymbol{\nabla}$ is the Del operator, $\boldsymbol{\sigma}$ is the Cauchy stress tensor and $\mathbf{b}$ is the body force density. Assuming quasi-static loading and negligible impact of body forces, Eqn. (5.1) reduces to:

$$\boldsymbol{\nabla} \cdot \boldsymbol{\sigma} = \mathbf{0} \qquad (5.3)$$

5.1.2 Plate Equations

The adherends $\Omega^{(i)} \mid i \in \{1,2\}$ are modelled as Mindlin-Reissner (MR) plates. The choice of MR theory is due to it taking into account transverse shear deformation, which is important in thick composite plates.

5.1.2.1 Kinematic Equations

According to MR theory, the displacement field of the *i*th plate is considered to be a linear combination of the plate midplane translations $u_x^{(i)}, u_y^{(i)}, u_z^{(i)}$ and plate midplane rotations $\theta_x^{(i)}, \theta_y^{(i)}$ as follows:

$$\begin{aligned} U_x^{(i)}(x,y,z) &= u_x^{(i)}(x,y) - (z - z_i)\theta_x^{(i)}(x,y) \\ U_y^{(i)}(x,y,z) &= u_y^{(i)}(x,y) - (z - z_i)\theta_y^{(i)}(x,y) \\ U_z^{(i)}(x,y,z) &= u_z^{(i)}(x,y) \end{aligned} \qquad (5.4\text{-a,b,c})$$

where z_i is the plate midplane z-coordinate.

5.1.2.2 Strain-Displacement Equations

The MR strain-displacement relations in the plate midplane are:

$$\begin{aligned} &\varepsilon_x^{(i)} = u_{x,x}^{(i)}, \quad \varepsilon_y^{(i)} = u_{y,y}^{(i)}, \quad \gamma_{xy}^{(i)} = u_{y,x}^{(i)} + u_{x,y}^{(i)} \\ &\gamma_{xz}^{(i)} = u_{z,x}^{(i)} - \theta_x^{(i)}, \quad \gamma_{yz}^{(i)} = u_{z,y}^{(i)} - \theta_y^{(i)} \end{aligned} \qquad (5.5\text{-a,b,c,d,e})$$

where $,j$ denotes the partial derivative with respect to variable j. In addition, the plate curvature vector $\boldsymbol{\kappa}^{(i)} = \left\{\kappa_x^{(i)}, \kappa_y^{(i)}, \kappa_{xy}^{(i)}\right\}^T$ consists of the following components:

$$\kappa_x^{(i)} = -\theta_{x,x}^{(i)}, \quad \kappa_y^{(i)} = -\theta_{y,y}^{(i)}, \quad \kappa_{xy}^{(i)} = -\theta_{y,x}^{(i)} - \theta_{x,y}^{(i)} \qquad (5.6\text{-a,b,c})$$

The strains at a general point in the plate domain (which need not be located on the midplane) can hence be defined in terms of the previously defined identities as follows:

$$\epsilon_x^{(i)} = \varepsilon_x^{(i)} + (z - z_i)\kappa_x^{(i)}, \quad \epsilon_y^{(i)} = \varepsilon_y^{(i)} + (z - z_i)\kappa_y^{(i)}$$
$$\Gamma_{xy}^{(i)} = \gamma_{xy}^{(i)} + (z - z_i)\kappa_{xy}^{(i)}, \quad \Gamma_{xz}^{(i)} = \gamma_{xz}^{(i)}, \quad \Gamma_{yz}^{(i)} = \gamma_{yz}^{(i)} \qquad \text{(5.7-a,b,c,d,e)}$$

5.1.2.3 Constitutive Equations

Yang, Norris and Stavsky [91] extended classical lamination theory (CLT) to MR plates. In accordance with this theory, the constitutive behaviour between the strains/curvatures and stress resultants/moments for an anisotropic laminated composite plate is:

$$\begin{Bmatrix} \mathbf{N} \\ \mathbf{M} \\ \mathbf{Q} \end{Bmatrix}^{(i)} = \begin{bmatrix} \mathbf{A} & \mathbf{B} & \mathbf{0} \\ \mathbf{B} & \mathbf{D} & \mathbf{0} \\ \mathbf{0} & \mathbf{0} & \mathbf{G} \end{bmatrix}^{(i)} \begin{Bmatrix} \boldsymbol{\varepsilon} \\ \boldsymbol{\kappa} \\ \boldsymbol{\gamma} \end{Bmatrix}^{(i)} \qquad (5.8)$$

where $\mathbf{N}^T = \{N_x, N_y, N_{xy}\}$ are the plate in-plane stress resultants, $\mathbf{M}^T = \{M_x, M_y, M_z\}$ are the plate bending moments and $\mathbf{Q}^T = \{Q_{xz}, Q_{yz}\}$ are the plate transverse shear stress resultants. The vectors $\boldsymbol{\varepsilon}^T = \{\varepsilon_x, \varepsilon_y, \varepsilon_{xy}\}$ and $\boldsymbol{\gamma}^T = \{\gamma_{xz}, \gamma_{yz}\}$ are collections of the in-plane strains and transverse shear strains, respectively. $\boldsymbol{\kappa}$ is the previously defined curvature. The $\mathbf{A}$, $\mathbf{B}$, and $\mathbf{D}$ matrices are the in-plane, coupling and bending stiffness matrices from CLT, respectively, while the $\mathbf{G}$ matrix is the transverse shear stiffness matrix. The calculation of these matrices is detailed in e.g. [8]. Meanwhile, for an isotropic metallic plate the constitutive equation is:

$$\begin{Bmatrix} \mathbf{N} \\ \mathbf{M} \\ \mathbf{Q} \end{Bmatrix}^{(i)} = \begin{bmatrix} \mathbf{A} & \mathbf{0} & \mathbf{0} \\ \mathbf{0} & \mathbf{D} & \mathbf{0} \\ \mathbf{0} & \mathbf{0} & \mathbf{G} \end{bmatrix}^{(i)} \begin{Bmatrix} \boldsymbol{\varepsilon} \\ \boldsymbol{\kappa} \\ \boldsymbol{\gamma} \end{Bmatrix}^{(i)} \qquad (5.9)$$

where the components of the $\mathbf{A}$ matrix are:

$$\mathrm{A}_{\alpha\beta} = \int_{-h}^{h} C_{\alpha\beta}\, dz \mid \alpha, \beta \in \{1,2,3\} \qquad (5.10)$$

The components of the bending matrix $\mathbf{D}$ are:

$$\mathrm{D}_{\alpha\beta} = \int_{-h}^{h} C_{\alpha\beta} z^2 \, dz \mid \alpha, \beta \in \{1,2,3\} \tag{5.11}$$

And the transverse shear stiffnesses $\mathbf{G}$ matrix can be calculated as:

$$\mathrm{G}_{\alpha\beta} = \frac{5}{6} \int_{-h}^{h} C_{(\alpha+3)(\beta+4)} \, dz \mid \alpha, \beta \in \{1,2\} \tag{5.12}$$

$C_{\alpha\beta}$ are the components of the elasticity tensor (following Voigt notation). It is remarked that for isotropic plates, there is no coupling between extension and bending, i.e., $\mathbf{B}$ is a null matrix. This is generally not the case for a composite laminate.

5.1.3 Adhesive Equations

The adhesive $\Omega^{(a)}$ is modelled using shear lag theory, first proposed by Volkersen [70] and later adapted to single-lap joints by Goland and Reissner [71]. The vast majority of bonded joint analytical models in the literature are based on this theory. An original extension of this classical model is presented in this section that enables it to be used in a nonlinear elastic analysis.

5.1.3.1 Strain-Displacement Equations

In accordance with Goland and Reissner's shear lag theory, the out-of-plane adhesive strains are defined in terms of the plate displacements as:

$$\gamma_{jz}^{(a)} = \frac{1}{t_a}\left(U_j^{(1)}|_{z=z_1-h^{(1)}} - U_j^{(2)}|_{z=z_2+h^{(2)}}\right) \mid j \in \{x,y\}$$
$$\varepsilon_{zz}^{(a)} = \frac{1}{t_a}\left(U_z^{(1)} - U_z^{(2)}\right) \qquad (5.13\text{-a,b})$$

where t_a is the adhesive thickness and $h^{(i)}$ is half the *i*th plate thickness. There is no dependence on the thickness coordinate in these equations. However, these three out-of-plane strain components transform inconsistently (they constitute an incomplete strain tensor) and are thus incompatible with the mathematical theory of plasticity. In this work, it is proposed to define the missing in-plane strain components in terms of the plate strains as follows:

$$\gamma_{xy}^{(a)} = \frac{1}{2}\left(\Gamma_{xy}^{(1)}|_{z=z_1-h^{(1)}} + \Gamma_{xy}^{(2)}|_{z=z_2+h^{(2)}}\right)$$
$$\varepsilon_{jj}^{(a)} = \frac{1}{2}\left(\epsilon_{jj}^{(1)}|_{z=z_1-h^{(1)}} + \epsilon_{jj}^{(2)}|_{z=z_2+h^{(2)}}\right) \mid j \in \{x,y\} \qquad (5.14\text{-a,b})$$

As in the original shear lag theory, there is again no dependence of these strain components on the adhesive thickness coordinate. This is not strictly accurate; however, the assumption's suitability is demonstrated in the following. To aid the discussion, the ε_{xx} strain field at a point in the adhesive is illustrated in Figure 5.4.

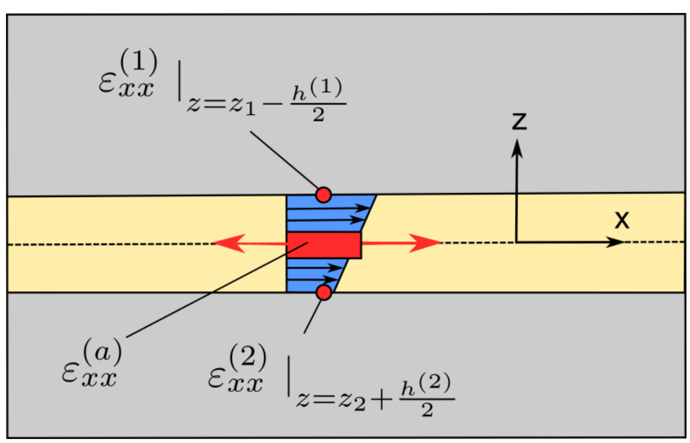

Figure 5.4: Normal strain component distribution through the adhesive thickness

Two key observations can be made:

1) The in-plane strains at the adhesive-adherend interfaces must be compatible and are generally different at the upper and lower interfaces

2) If the bondline is quite thin then the distribution of ε_{xx} will be quasi-linear through-thickness

These observations are also valid for the ε_{yy} and γ_{xy} in-plane strains. The reader may have remarked that the proposed strain identities in Eqns. (5.14-a,b) correspond to the average strains based on a linear through-thickness variation. Importantly, this assumption provides a close approximation to the adhesive deformation energy in the in-plane modes. This is demonstrated by considering the $\gamma_{xy}^{(a)}$ strain component. With the average strain assumption, the section strain energy density (through-thickness integral of the strain energy density) for the $\gamma_{xy}^{(a)}$ component is:

$$\rho_{average}^{(xy)} = C_{66}t\left(\frac{1}{3}\gamma_{xy1}^2 + \frac{1}{3}\gamma_{xy1}\gamma_{xy2} + \frac{1}{3}\gamma_{xy2}^2\right) \tag{5.15}$$

where γ_{xy1} and γ_{xy2} are shorthand for $\gamma_{xy}^{(a)}$ at the upper and lower interfaces, respectively. With the linear strain energy assumption, the section strain energy density is:

$$\rho_{linear}^{(xy)} = C_{66}t\left(\frac{1}{4}\gamma_{xy1}^2 + \frac{1}{2}\gamma_{xy1}\gamma_{xy2} + \frac{1}{4}\gamma_{xy2}^2\right) \tag{5.16}$$

These two functions are plotted in Figure 5.5. The x-axis shows the ratio $\frac{\gamma_{xy1}}{\gamma_{xy2}}$ while the y-axis shows the section strain energy density. It is evident from inspection of Eqns. (5.15) and (5.16) that the ratio of these two equations is independent of $C_{66}t$, thus the plot functions have been normalized by this expression.

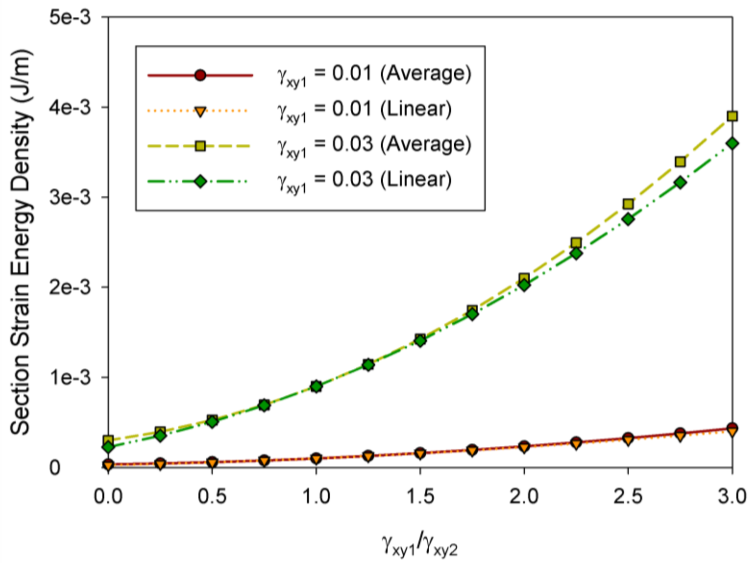

Figure 5.5: Comparison of strain energy densities for average and linear assumptions

It is observed that the average through-thickness strain assumption results in very similar strain energy to the exact strain energy based on a linear strain variation. This is important since an energy method shall be used to solve the model developed in this chapter. The energies are virtually identical when neither strain exceeds 0.05 strain. Strains in the adherends will generally not exceed this level prior to failure, thus the assumptions of Eqn. (5.14) should generally expect to yield good results. Following solution of the model, it should of course be kept in mind that the obtained adhesive in-plane strain components are through-the-thickness averages while the out-of-plane strains correspond to those of the classical Goland and Reissner model.

5.1.3.2 Constitutive Equations

The adhesive is assumed to behave in an elastoplastic manner. In accordance with the mathematical theory of rate-independent small strain plasticity, the adhesive stress tensor is thus related to the adhesive strain tensor as follows:

$$\boldsymbol{\sigma}^{(a)} = \boldsymbol{C}^{(a)} : \boldsymbol{\varepsilon}_e^{(a)} = \boldsymbol{C}^{(a)} : \left(\boldsymbol{\varepsilon}^{(a)} - \boldsymbol{\varepsilon}_p^{(a)}\right) \tag{5.17}$$

where $\boldsymbol{C}^{(a)}$ is the isotropic elasticity tensor:

$$\boldsymbol{C}^{(a)} = \begin{bmatrix} 2\mu+\lambda & \lambda & \lambda & 0 & 0 & 0 \\ \lambda & 2\mu+\lambda & \lambda & 0 & 0 & 0 \\ \lambda & \lambda & 2\mu+\lambda & 0 & 0 & 0 \\ 0 & 0 & 0 & \mu & 0 & 0 \\ 0 & 0 & 0 & 0 & \mu & 0 \\ 0 & 0 & 0 & 0 & 0 & \mu \end{bmatrix}^{(\boldsymbol{a})}$$

The subscripts e and p denote "elastic" and "plastic, respectively. Also $\mu = E\nu/[(1+\nu)(1-2\nu)\,]$ and $\lambda = E/[2(1+\nu)]$ are the Lamé parameters, where E is Young's modulus and ν is Poisson's ratio. The particular yield criterion and evolution equations employed in the current work are those of J_2-plasticity with associative linear isotropic hardening. The former is the well-known von Mises yield criterion, which is defined in stress space as:

$$f\left(\boldsymbol{\sigma}^{(a)}, \alpha\right) = \sqrt{\tfrac{3}{2}\boldsymbol{s}^{(a)} : \boldsymbol{s}^{(a)}} - \left(\sigma_y + H\alpha\right) \le 0 \tag{5.18}$$

where $\boldsymbol{s}^{(a)}$ is the deviatoric component of the stress tensor, α is an internal hardening variable, σ_y is the tensile yield strength and H is the hardening modulus of the adhesive. The J_2 theory is completed by definition of the following evolution equations:

$$\overline{\boldsymbol{N}} = \frac{\boldsymbol{s}^{(a)}}{\|\boldsymbol{s}^{(a)}\|} \quad , \quad \gamma = \frac{\overline{\boldsymbol{N}} : \dot{\boldsymbol{\varepsilon}}^{(a)}}{1 + \frac{\sigma_y + H\alpha}{3\mu}} \quad , \quad \dot{\alpha} = \gamma\sqrt{\frac{2}{3}} \quad , \quad \dot{\boldsymbol{\varepsilon}}_p^{(a)} = \gamma\overline{\boldsymbol{N}} \tag{5.19-a,b,c,d}$$

Note that $\overline{\boldsymbol{N}}$ defines the direction of the plastic flow. The parameter γ is the *plastic multiplier* (absolute value of the plastic flow rate) and, following the mathematical theory of plasticity, is required to obey the following complementarity conditions:

$$\gamma \geq 0 \quad , \quad f\left(\boldsymbol{\sigma}^{(a)}, \alpha\right) \leq 0 \quad , \quad \gamma f\left(\boldsymbol{\sigma}^{(a)}, \alpha\right) = 0 \tag{5.20-a,b,c}$$

Finally, the persistency condition is also required to hold on the yield surface:

$$\gamma \dot{f}\left(\boldsymbol{\sigma}^{(a)}, \alpha\right) = 0 \mid f\left(\boldsymbol{\sigma}^{(a)}, \alpha\right) = 0 \tag{5.21}$$

Eqn. (5.21) basically states that for plastic flow to occur (i.e., $\dot{\boldsymbol{\varepsilon}}_p^{(a)} \neq \mathbf{0}$) at a point on the yield surface at a particular point in time, the yield condition must persist instantaneously in time (i.e., $\dot{f}\left(\boldsymbol{\sigma}^{(a)}, \alpha\right) = 0$).

5.1.4 Bolt Equations

In order to take into account both shear deformation and bending, the bolt $\Omega^{(b)}$ is modelled as a Timoshenko beam.

5.1.4.1 Kinematic Equations

The following equations describe the kinematics of a Timoshenko beam:

$$\begin{gathered} U_x^{(b)}(x,y,z) = u_x^{(b)}(z) \ , \quad U_y^{(b)}(x,y,z) = u_y^{(b)}(z) \\ U_z^{(b)}(x,y,z) = u_z^{(b)}(z) - (x - x_0)\theta_x^{(b)}(z) - (y - y_0)\theta_y^{(b)}(z) \end{gathered} \tag{5.22-a,b,c}$$

Similarly to plate kinematics, $u_x^{(b)}, u_y^{(b)}, u_z^{(b)}$ are the bolt neutral axis displacements and $\theta_x^{(b)}, \theta_y^{(b)}$ are the neutral axis rotations. The ordered pair (x_0, y_0) defines the bolt neutral axis location.

5.1.4.2 Strain-Displacement Equations

The strains and curvatures along the bolt neutral axis can be obtained from the displacements as follows:

$$\varepsilon_{zz}^{(b)} = u_{z,z}^{(b)} \ , \quad \gamma_{xz}^{(b)} = u_{z,x}^{(b)} - \theta_x^{(b)} \ , \quad \gamma_{yz}^{(b)} = u_{z,y}^{(b)} - \theta_y^{(b)}$$
$$\kappa_x^{(b)} = -\theta_{x,z}^{(b)} \ , \quad \kappa_y^{(b)} = -\theta_{y,z}^{(b)} \tag{5.23-a,b,c,d,e}$$

As was the case with the plate equations, the strain field at a generic point in the bolt (which need not be on the neutral axis) can hence be described in terms of the above identities as:

$$\epsilon_z^{(b)} = \varepsilon_z^{(b)} + (x - x_0)\kappa_x^{(b)} + (y - y_0)\kappa_y^{(b)}$$
$$\Gamma_{xz}^{(b)} = \gamma_{xz}^{(b)} \ , \quad \Gamma_{yz}^{(b)} = \gamma_{yz}^{(b)} \tag{5.24-a,b,c,}$$

5.1.4.3 Constitutive Equations & Clamp-Up

An isotropic elastic constitutive relation is appropriate for metallic bolts. For a Timoshenko beam, this is simply:

$$\begin{Bmatrix} N_z \\ M_x \\ M_y \\ Q_{xz} \\ Q_{yz} \end{Bmatrix}^{(b)} = \begin{bmatrix} EA & 0 & 0 & 0 & 0 \\ 0 & EI & 0 & 0 & 0 \\ 0 & 0 & EI & 0 & 0 \\ 0 & 0 & 0 & k\mu A & 0 \\ 0 & 0 & 0 & 0 & k\mu A \end{bmatrix}^{(b)} \begin{Bmatrix} \varepsilon_{zz} \\ \kappa_x \\ \kappa_y \\ \gamma_{xz} \\ \gamma_{yz} \end{Bmatrix}^{(b)} + \begin{Bmatrix} N_{z0} \\ 0 \\ 0 \\ 0 \\ 0 \end{Bmatrix}^{(b)} \tag{5.25}$$

where A is the bolt's cross-sectional area, I is the second moment of area and $k = 6(1 + \nu)/(7 + 6\nu)$ is the shear correction factor. N_z is the bolt axial stress resultant, M_x and M_y are the bolt section moments and Q_{xz} and Q_{yz} are the bolt transverse shear stress resultants. The unfamiliar term on the right hand side of

Eqn. (5.25) is remarked. This represents the initial axial force N_{z0} in the bolt due to clamp-up loading.

5.1.5 Bolthead-Adherend Interaction

The interaction between the boltheads and adherends is complex but shall be distilled here to the essentials. First, it is assumed that the bolthead protrudes from the joint and is not countersunk. Subsequently, two separate situations are considered:

1) The clamp-up load is high; the bolthead is thick; there are no washers
2) The clamp-up load is not necessarily high; the bolthead is not necessarily thick; there may be washers

In the first case, the bolthead is effectively rigid and sits flush on the adherend. It can hence be assumed that there is perfect contact between the bolthead and the adherend. This means that the bolthead and adherend plane underneath the bolthead are parallel planar surfaces, as shown in Figure 5.6-a. Mathematically, this can be expressed as:

$$
\begin{aligned}
U_z^{(1)}(x,y,z_1+h) &= \left(u_z^{(B_j)} - r_x\theta_x^{(B_j)} - r_y\theta_y^{(B_j)}\right)\Big|_{z=z_1+h^{(1)}} \;\mid\; (x,y)\in\Omega_{H_j}^{(1)} \\
U_z^{(2)}(x,y,z_2-h) &= \left(u_z^{(B_j)} - r_x\theta_x^{(B_j)} - r_y\theta_y^{(B_j)}\right)\Big|_{z=z_2-h^{(2)}} \;\mid\; (x,y)\in\Omega_{H_j}^{(2)}
\end{aligned}
\qquad (5.26\text{-a,b})
$$

where $\boldsymbol{r}(x,y) = \{r_x, r_y\}^T$ is the Euclidean vector from the hole center to the point under consideration. It is remarked that this equation represents a constraint on the displacement solution.

In the second case, it is again assumed that the adherend region underneath the bolthead remains plane; however, the requirement that it and the bolthead must remain parallel is relaxed. In other words, an allowance is made for a relative rotation angle between the two planes. This rotation angle depends on the effective bolthead stiffness k_θ, which is hypothesized to be a function of the adherend (thickness, stiffness) and bolthead (size, shape) and washer (presence, size, type). To describe this mathematically several new variables are introduced: $\theta_x^{H_j^{(i)}}$, $\theta_y^{H_j^{(i)}}$ and $u_z^{H_j^{(i)}}$ represent the rotations and average z-displacement of the plane adherend region, respectively (see Figure 5.6-c). Following the convention maintained thus far, $i = 1$ denotes the upper adherend and $i = 2$ denotes the lower adherend while j identifies the bolt in question. It can hence be stated:

$$u_z^{H_j^{(i)}} = u_z^{B_j^{(i)}}$$
$$F_x = k_\theta \left(\theta_x^{H_j^{(i)}} - \theta_x^{B_j^{(i)}} \right) \quad , \quad F_y = k_\theta \left(\theta_y^{H_j^{(i)}} - \theta_y^{B_j^{(i)}} \right) \ \mid \ i \in \{1,2\} \tag{5.27-a,b,c}$$

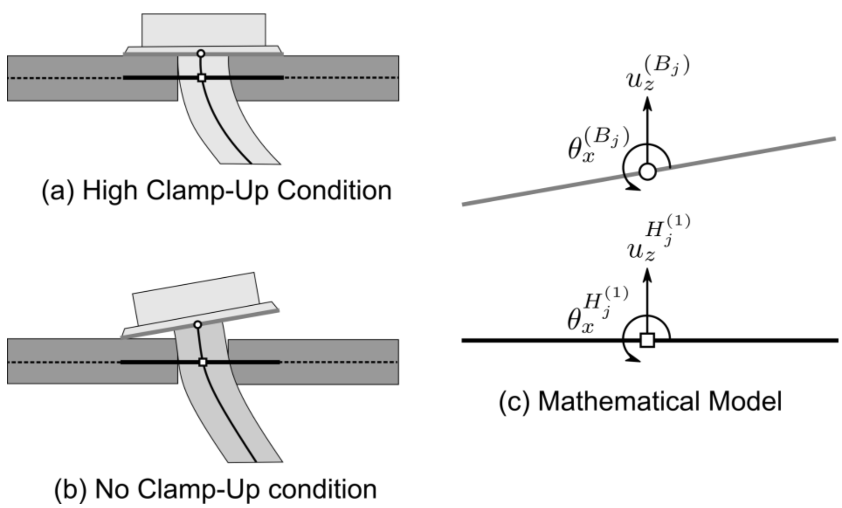

Figure 5.6: Different bolthead-adherend interactions and mathematical representation

where $B_j^{(1)}$ and $B_j^{(2)}$ denote the points of the *j*th bolt on the top and bottom adherend outer surfaces, respectively. Eqns. (5.27-b,c) state there is a restoring force opposing the relative rotation between the boltheads and adherends that is dependent on the effective bolthead stiffness k_θ. This can be interpreted as a spring that acts between the $\theta_x^{H_j^{(i)}}$ and $\theta_x^{B_j^{(i)}}$ degrees of freedom, shown in Figure 5.6-c. Interestingly, in the limit as the spring stiffness tends to infinity, the conditions of

Eqns. 5.26-a,b are recovered since the spring will effectively resist any relative rotation between the bolthead and adherend. Thus the proposed spring model can account for both types of bolthead conditions. The only remaining challenge is to determine the value of k_θ for a given bolthead condition. This can be achieved by means of physical testing or detailed 3D finite element analysis. It is noted that such testing need only be performed once for a particular combination of bolt, washer and laminate. Furthermore, it is not required at all when the case of high bolt clamp-up, thick bolthead and no washers is considered.

5.1.6 Bolt Shank-Substrate Contact

Unilateral contact is considered between the bolt surface and the *i*th substrate *j*th hole edge in the adherend midplane ($x - y$ plane). This can be formally stated as:

$$g_n^{(i)} = g^{(i)} - \mathbf{n} \cdot \left\{ \left[u_x^{(i)}, u_y^{(i)} \right]^T - \left[u_x^{(b)}, u_y^{(b)} \right]^T |_{z=z_i} \right\} \tag{5.28}$$

$$g_n^{(i)} \geq 0 \quad , \quad P_c^{(i)} \geq 0 \quad , \quad g_n^{(i)} P_c^{(i)} = 0 \qquad \text{(5.29-a,b,c)}$$

$$\forall\, \mathbf{x} \in \partial_{H_j} \Omega^{(i)}$$

In Eqns. 5.28-5.29, $g_n^{(i)}$ is the current gap in the normal direction $\mathbf{n}$ to the bolt surface, $g^{(i)}$ is the initial gap and $P_c^{(i)}$ is the contact pressure. A schematic of the contact problem is shown in Figure 5.7. In keeping with Timoshenko beam theory, the transverse displacements in the bolt are assumed to be constant throughout its cross-section. This is equivalent to assuming a rigid bolt surface. Previous studies in the literature have shown that this simplification does not have a significant effect on the stresses in the plate [76].

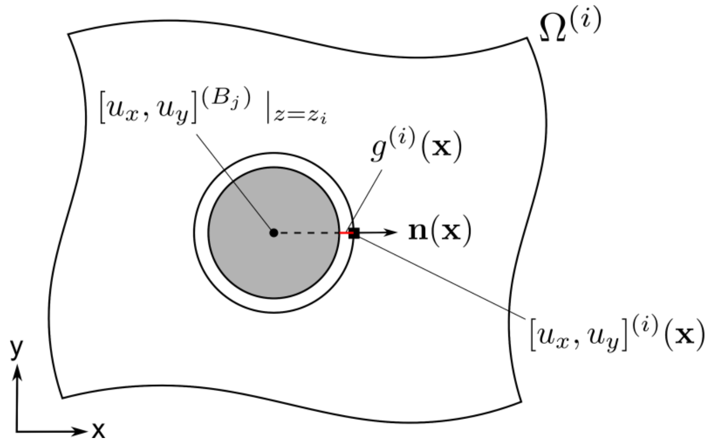

Figure 5.7: Variables involved in contact analysis. Representative hole boundary point $\boldsymbol{x}$ *indicated by square*

The active contact region (the region in which $g_n^{(i)} = 0$) is not known a priori and must be determined as part of the solution.

5.1.7 Boundary Conditions

The proposed model may be arbitrarily loaded with line loads, pressure loads and body forces. The traditional load case of interest, however, is uniaxial tension/compression with both longitudinal joint edges clamped except for free sliding on the right hand boundary. To simulate this type of loading condition, the following boundary conditions are applied:

$$u_x^{(1)} = 0, u_y^{(1)} = 0, u_z^{(1)} = 0, \theta_x^{(1)} = 0, \theta_y^{(1)} = 0 \text{ on } \partial_L\Omega^{(1)}$$
$$u_y^{(2)} = 0, u_z^{(2)} = 0, \theta_x^{(2)} = 0, \theta_y^{(2)} = 0 \text{ on } \partial_R\Omega^{(2)} \qquad (5.30\text{-a,b})$$

$$n_x\sigma_{xx}^{(2)} = \bar{t}_x \textit{ on } \partial_R\Omega^{(2)} \qquad (5.31)$$

In addition, it is desired that all points on the right boundary move together in the x-direction, as though the boundary were constrained by a rigid clamping device:

$$u_x^{(2)} = \text{constant on } \partial_R \Omega^{(2)} \tag{5.32}$$

5.1.8 Failure Criteria

In this section, a simple approach is proposed for assessing joint failure. This consists of separately checking for in-plane failure of the adherends and ductile failure of the adhesive. If either of these conditions is met, then the joint is assumed to have failed.

5.1.8.1 Adhesive Failure

Since the adhesives of interest in HBB joint design typically exhibit significant ductility, a variation of the maximum strain failure criterion represents a rational choice for predicting adhesive failure. In this work, the criterion suggested by Hoyt et al. [92] is used:

$$\frac{\varepsilon_{ult}}{\varepsilon_{eqv}} = 1 \tag{5.33}$$

where ε_{eqv} is the equivalent Von Mises strain, defined as follows:

$$\varepsilon_{eqv} = \sqrt{\frac{3\left(\varepsilon_{xx}^2 + \varepsilon_{yy}^2 + \varepsilon_{zz}^2\right)}{2} + \frac{3\left(\gamma_{xy}^2 + \gamma_{yz}^2 + \gamma_{xz}^2\right)}{4}} \tag{5.34}$$

This criterion takes into account the effects of both the shear and peel strains on the adhesive failure.

5.1.8.2 Adherend Failure

Failure of the composite adherends is rather more involved. Firstly, in reality there is through-thickness contact between the bolt and adherends. This has so far been neglected. While the through-thickness stress resultants will be well approximated in the model (since they are averages), the stress distribution through-thickness near the hole boundary will not be. Some plies will react a disproportionate amount of contact load, which will lead to a through-thickness stress concentration. In order to determine the amplitude of this stress concentration such that the in-plane stress results can be corrected, the method of Ramkumar and Saether [93] is used. This method is briefly described in Appendix B.

Once the corrected ply loads have been calculated, the failure in each ply is evaluated along a concentric path around the hole, as shown in Figure 5.9. This method was also proposed by Ramkumar and Saether [93] and is similar to the method of Chang et al. [94]. The failure criterion employed in this thesis is the Yamada-Sun criterion [95], given in Eqn. 5.35:

$$\left(\frac{\sigma_x}{X}\right)^2 + \left(\frac{\sigma_{xy}}{S_c}\right)^2 \geq 1 \tag{5.35}$$

In Eqn. 5.35, X is the longitudinal ply strength and S_c is the ply shear strength. a_0 is the characteristic curve radius and θ is the radial location measured clockwise from the positive x-axis (see Figure 5.8). It is noted that a_0 is an empirical parameter which needs to be determined by testing both a notched and an unnotched laminate specimen, combined with an in-plane analysis from which the parameter can be fitted.

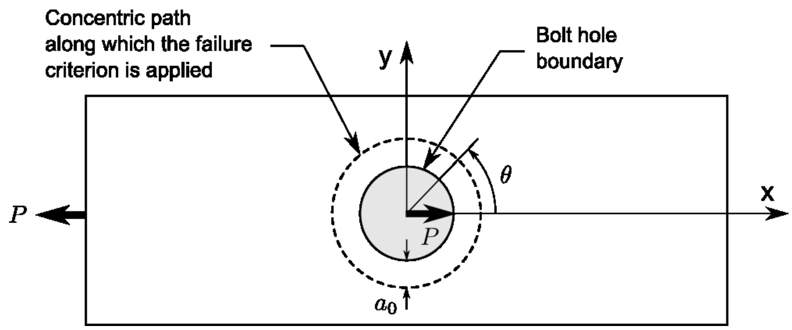

Figure 5.8: Characteristic distance where Yamada-Sun criterion is applied. Figure adapted from Ramkumar et al. [93]

Finally, depending on the angle at which the failure is found to occur, the failure mode can be determined. According to Chang et al. [94], failure near an angle $\theta \approx 0°$ corresponds to a bearing failure mode, failure near an angle $\theta \approx 45°$ corresponds to a shearout or cleavage mode while failure near an angle $\theta \approx 90°$ corresponds to a net-section mode. This is summarized in Eqns. (5.36-a,b,c).

$$\begin{gathered} -15° \leq \theta \leq 15° \text{ bearing mode} \\ 30° \leq \theta \leq 60° \text{ shearout or cleavage mode} \\ 75° \leq \theta \leq 90° \text{ net-section mode} \end{gathered} \qquad (5.36\text{-a,b,c})$$

These three failure modes are demonstrated in Figure 5.9.

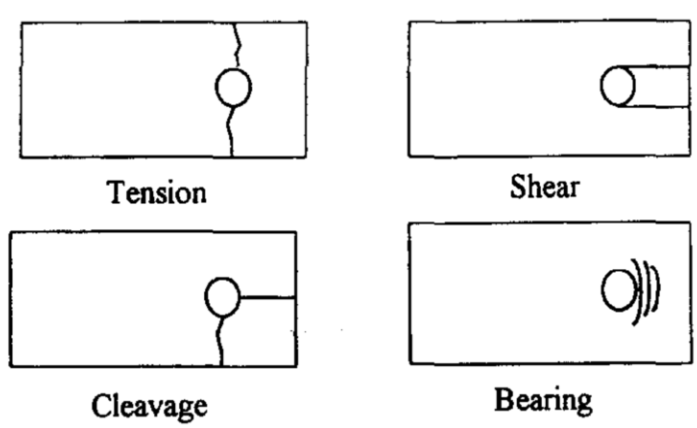

Figure 5.9: Bolted joint in-plane failure modes [22]

Note that Kradinov et al. and Ramkumar and Saether [93] both performed a progressive failure analysis based on the above method, degrading the ply stiffness and solving their respective bolted joint models incrementally. However, this is likely to introduce gross inaccuracy into the present model, since unlike in a bolted joint, in a HBB joint composite failure causes complex bolt load redistribution, damage to the adhesive, etc. In other words, it shall not be pretended that a simple method based on equivalent single layers can accurately capture the complicated progressive failure process of a HBB joint. The present analysis is thus only indicative of the onset of adherend nonlinearity due to damage. It is noted that this approach is expected to be conservative.

5.2 Double-Lap Joint

Problem Description

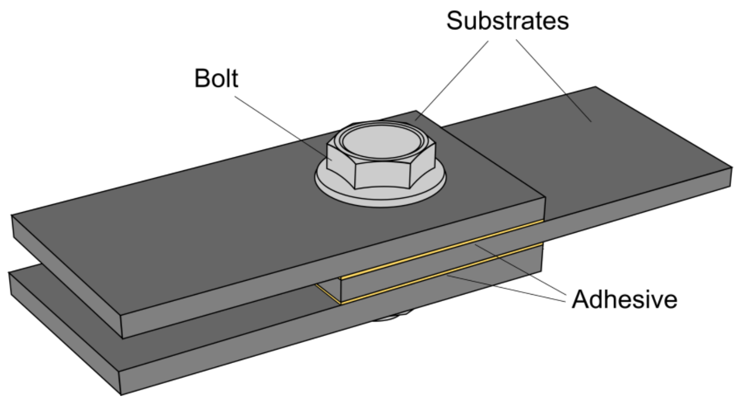

Figure 5.10: Double-lap HBB joint

Double-lap bonded-bolted joints are conceptually similar to single-lap joints. In a double-lap joint, an inner adherend is “sandwiched” by two outer adherends, as shown in Figure 5.10. This results in two overlap regions, hence the “double-lap” descriptor. As in the single-lap joint, the outer adherends are connected to the inner adherend using adhesive and one or more bolts. As for the single-lap joint, the objective is to determine the displacements and stresses of this type of joint when subjected to quasi-static external loads.

Model description

Only the special case where the outer adherends are identical shall be considered. Assuming that the inner adherend is symmetric about its midplane and that the external loading is in the $x-y$ plane (as is usually the case), then symmetry conditions apply. The double-lap joint can hence be idealized as shown in Figure 5.11. Consequently, the analysis is identical to the single-lap analysis subject to the additional Dirichlet boundary conditions stated in Figure 5.11.

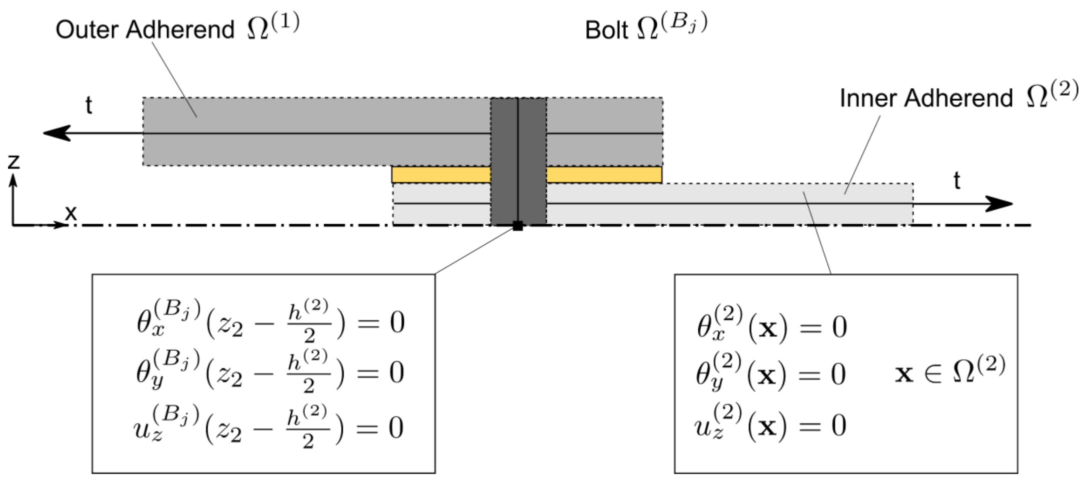

Figure 5.11: Symmetry conditions used to simulate a double-lap joint

Chapter 6: Meshless Interpolation of Scattered Data

The solution of the model described in Chapter 5 can potentially be achieved by a number of different numerical methods, including (but not limited to) the finite difference method (FDM), finite element method (FEM), spectral method and meshless method. Each of these methods has particular advantages and disadvantages. In the present work a type of meshless method known as the Galerkin Radial Point Interpolation Method (GRPIM) is used. This decision was motivated by the following considerations:

- Ease of domain discretization: In the scope of this thesis, it was desired to use a method for which discretization of the spatial domain is simple and efficient. The FEM requires the problem domain to be discretized into both nodes and elements, which is a challenging and time consuming task. Furthermore, the element quality, determined by their shape, has an important effect on the solution accuracy and restricts automation of the discretization process. Similarly, the FDM typically requires a regular grid, hindering its use in the analysis of complex domains. In contrast, meshless methods only require discretization of the domain into nodes or particles, whose arrangement need in general not be structured, thus greatly simplifying computational implementation.

- Completeness: Depending on the formulation used, meshless shape functions often possess C^{∞} continuity (compared to C^{0} or C^{1} continuity for typical finite elements). This high degree of smoothness can lead to high convergence rates of the solution for certain types of problems in solid mechanics.

- Analysis of fracture and extreme deformation: Meshless methods are ideally suited to fracture mechanics and nonlinear geometric deformation analyses, since it is possible to treat moving discontinuities without a need to "remesh" and because the integration accuracy does not degrade (as typically occurs in FEM when elements become extremely deformed) [96]. The developed code can thus be readily adapted in future to incorporate such features.

- Novelty: To the present date, there is no public account of the use of a meshless method in the analysis of structural joints. The extension of this technique to the analysis of joints is thus also a question of academic interest. Basic questions such as the existence of the RPIM interpolation are addressed in this chapter which have not been adequately answered to date. In addition, interpolation parameters specific to the HBB joint problem are identified in Chapter 7.

Among possible meshless methods, the GRPIM in particular was chosen, based on prior studies which showed this method to exhibit excellent performance compared to other meshless methods such as Galerkin Moving Kriging (GMK) and Galerkin Point Interpolation (GPIM).

6.1 Radial Point Interpolation

The GRPIM uses radial point interpolating (RPI) functions to approximate the field functions based on discrete scattered data. For example, in a displacement-based continuum mechanics analysis the nodal displacement values constitute the scattered data used to construct the approximation. An overview of the RPI technique and its use in scattered data interpolation is presented in this section. In addition, the conditions guaranteeing existence of the interpolation are presented. Let a body of interest, occupying the domain Ω in n-dimensional real coordinate space $\mathbb{R}^s : s \in \mathbb{N} \leq 3$, be discretized by an arbitrarily scattered set of nodes. A 2D example of such a discretization is shown in Figure 6.1.

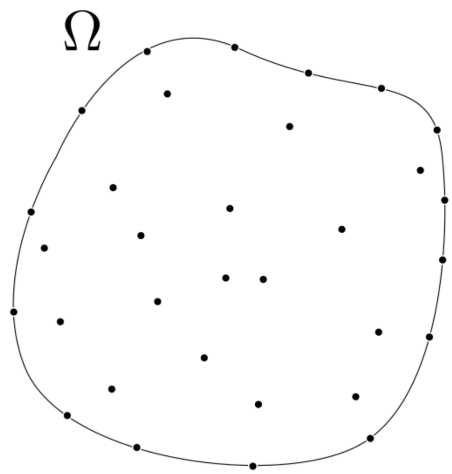

Figure 6.1: Example 2D nodal discretization

At each node, the field function values may be assumed to be known, although this not a strict requirement. Let $\boldsymbol{x}$ be any point belonging to the domain Ω. A combination of radial basis functions $R(\boldsymbol{x}, \boldsymbol{x}_i)$ and monomial basis functions $P_i(\boldsymbol{x})$ may hence be used to construct an interpolating function $u^h(\boldsymbol{x})$ on the domain as follows:

$$u^h(\mathbf{x}) = \sum_{i=1}^{n} R\,(\mathbf{x}, \mathbf{x}_i)a_i + \sum_{i=1}^{m} P_i\,(\mathbf{x})b_i \qquad (6.1)$$

where $\boldsymbol{x}_i$ is the *i*th node, n is the total number of nodes in the domain and m is the number of monomials in the monomial basis. The choice of the monomial basis is arbitrary and can be determined to any desired polynomial degree d using the multinomial expansion $(x + y + \cdots)^d$. This is demonstrated for 2D real coordinate space in Figure 6.2.

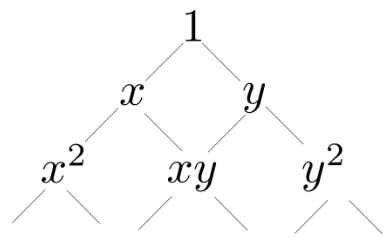

Figure 6.2: Multinomial expansion of 2D monomial basis

In 1D, the following monomial bases are natural choices:

Table 6.1: Typical 1D monomial bases

Type	Monomials	m	d
Constant	$[1]$	1	0
Linear	$[1 \quad x]$	2	1
Quadratic	$[1 \quad x \quad x^2]$	3	2

The 2D bases of corresponding order are:

Table 6.2: Typical 2D monomial bases

Type	Monomials	m	d
Constant	$[1]$	1	0
Linear	$[1 \quad x \quad y]$	3	1
Quadratic	$[1 \quad x \quad y \quad x^2 \quad xy \quad y^2]$	6	2

Eqn. (6.1) can be equivalently expressed in matrix notation as:

$$u^h(\boldsymbol{x}) = \boldsymbol{r}^T(\boldsymbol{x})\boldsymbol{a} + \boldsymbol{p}^T(\boldsymbol{x})\boldsymbol{b} \tag{6.2}$$

In Eqn. (6.2), the radial basis function vector $\boldsymbol{r}$ is simply:

$$\boldsymbol{r}^T(\boldsymbol{x}) = [R(\boldsymbol{x}, \boldsymbol{x}_1) \quad R(\boldsymbol{x}, \boldsymbol{x}_2) \quad \cdots \quad R(\boldsymbol{x}, \boldsymbol{x}_n)] \tag{6.3}$$

where the radial basis function $R(\boldsymbol{x}, \boldsymbol{x}_i): i \in [1, n]$ can take a number of forms, as shall be discussed in section 6.1.2. Meanwhile, the monomial basis function vector $\boldsymbol{p}(\boldsymbol{x})$ is:

$$\boldsymbol{p}^T(\boldsymbol{x}) = [P_1(\boldsymbol{x}) \quad P_2(\boldsymbol{x}) \quad \cdots \quad P_m(\boldsymbol{x})] \tag{6.4}$$

where the $P_i: i \in [1, m]$ are the monomials of the chosen monomial basis. To determine the coefficients $a_i: i \in [1, n]$ and $b_i: i \in [1, m]$ in Eqns. (6.1-6.2), interpolation of the function $u^h(\boldsymbol{x})$ at the nodes is enforced as follows:

$$\boldsymbol{r}^T(\boldsymbol{x}_i)\boldsymbol{a} + \boldsymbol{p}^T(\boldsymbol{x}_i)\boldsymbol{b} = \boldsymbol{u}_i: i \in [1, n] \tag{6.5}$$

Eqn. (6.5) results in a system of n linear equations, which can also be written as:

$$\boldsymbol{Ra} + \boldsymbol{Pb} = \boldsymbol{u} \tag{6.6}$$

where the $\boldsymbol{R}$ matrix is called the correlation matrix and is of size $n \times n$:

$$\boldsymbol{R}(\boldsymbol{x}) = \begin{bmatrix} R(\boldsymbol{x}_1, \boldsymbol{x}_1) & R(\boldsymbol{x}_1, \boldsymbol{x}_2) & \cdots & R(\boldsymbol{x}_1, \boldsymbol{x}_n) \\ R(\boldsymbol{x}_2, \boldsymbol{x}_1) & R(\boldsymbol{x}_2, \boldsymbol{x}_2) & \cdots & R(\boldsymbol{x}_2, \boldsymbol{x}_n) \\ \vdots & \vdots & \ddots & \vdots \\ R(\boldsymbol{x}_n, \boldsymbol{x}_1) & R(\boldsymbol{x}_n, \boldsymbol{x}_2) & \cdots & R(\boldsymbol{x}_n, \boldsymbol{x}_n) \end{bmatrix} \tag{6.7}$$

It is useful to state some properties of the radial basis function $R(\boldsymbol{x}_i, \boldsymbol{x}_j)$.

Box 6.1: Radial basis (correlation) function properties

Property 1 $R(\boldsymbol{x}_i, \boldsymbol{x}_j): \mathbb{R}^s \times \mathbb{R}^s \rightarrow \mathbb{R}$

Property 2 $|R(\boldsymbol{x}_i, \boldsymbol{x}_j)| \geq 0$

Property 3 Commutativity, i.e., $R(\boldsymbol{x}_i, \boldsymbol{x}_j) = R(\boldsymbol{x}_j, \boldsymbol{x}_i)$

Property 4 Strict conditional positiveness of order m on $\mathbb{R}^s$

Property 5 $R(\boldsymbol{x}_i, \boldsymbol{x}_j) = R(\boldsymbol{x}_i - \boldsymbol{x}_j)$

The size $n \times m$ monomial basis matrix $\boldsymbol{P}(\boldsymbol{x})$ can be stated as:

$$\boldsymbol{P}(\boldsymbol{x}) = \begin{bmatrix} p_1(\boldsymbol{x}_1) & p_2(\boldsymbol{x}_1) & \cdots & p_m(\boldsymbol{x}_1) \\ p_1(\boldsymbol{x}_2) & p_2(\boldsymbol{x}_2) & \cdots & p_m(\boldsymbol{x}_2) \\ \vdots & \vdots & \ddots & \vdots \\ p_1(\boldsymbol{x}_n) & p_2(\boldsymbol{x}_n) & \cdots & p_m(\boldsymbol{x}_n) \end{bmatrix} \tag{6.8}$$

This matrix is generally non-square. In this thesis, only linear monomial bases are considered for reasons which shall be expanded upon later.

Eqn. (6.6), however, clearly does not have a unique solution since there are fewer equations than unknown coefficients. To resolve this problem the constraint condition $\boldsymbol{P}^T(\boldsymbol{x})\boldsymbol{a} = \boldsymbol{0}$ is enforced, resulting in the following augmented system of equations:

$$\begin{bmatrix} \boldsymbol{R} & \boldsymbol{P} \\ \boldsymbol{P}^T & \boldsymbol{0} \end{bmatrix} \begin{bmatrix} \boldsymbol{a} \\ \boldsymbol{b} \end{bmatrix} = \boldsymbol{G} \begin{bmatrix} \boldsymbol{a} \\ \boldsymbol{b} \end{bmatrix} = \begin{bmatrix} \boldsymbol{u} \\ \boldsymbol{0} \end{bmatrix} \tag{6.9}$$

The $\boldsymbol{G}$ matrix of dimension $(n+m) \times (n+m)$ is sometimes also called the moment matrix. To ensure well-posedness of the interpolation, it is desirable to understand for which conditions the $\boldsymbol{G}$ matrix is invertible. To be able to prove these conditions, the following definitions are required, as given in [97]:

Definition 1 A real symmetric $n \times n$ matrix R is said to be conditionally positive semi-definite of order one if its associated quadratic form is non-negative:

$$\sum_{i=1}^{n}\sum_{j=1}^{m} c_i c_j\, R(\boldsymbol{x}_i, \boldsymbol{x}_j) \geq 0 \tag{6.10}$$

for any $\boldsymbol{c} = [c_1, \dots, c_n]^T \in \mathbb{R}^n$ satisfying:

$$\sum_{i=1}^{n} c_i = 0 \tag{6.11}$$

If $\boldsymbol{c} \neq 0$ implies strict inequality in (6.10), then R is called conditionally positive definite of order m.

Definition 2 A real-valued even continuous function is said to be conditionally positive definite of order m on $\mathbb{R}^s$ if:

$$\sum_{i=1}^{n}\sum_{j=1}^{n} c_i c_j\, R(\boldsymbol{x}_i - \boldsymbol{x}_j) \geq 0 \tag{6.12}$$

for n points $x_1, \dots, x_n \in \mathbb{R}^s$ and $\boldsymbol{c} = [c_1, \dots, c_n]^T \in \mathbb{R}^n$ satisfying:

$$\sum_{i=1}^{n} c_i\, x_j^{\alpha} \tag{6.13}$$

The function R is said to be strictly positive definite of order m on $\mathbb{R}^s$ if $x_1, \dots, x_n \in \mathbb{R}^s$ are distinct and $\boldsymbol{c} \neq 0$ implies strict inequality in (6.13).

Definition 3 The set of points $\chi = [\, x_1, \dots, x_n] \subset \mathbb{R}^s$ is said to be m-unisolvent if the only polynomial of total degree m interpolating zero data on χ is the zero polynomial.

Definition 3 leads to the following important theorem regarding existence of the $\boldsymbol{G}$ matrix inverse:

Box 6.2: $\boldsymbol{G}$ matrix invertibility theorem

> **Theorem 1** If the real-valued even function $R(\boldsymbol{x}_i, \boldsymbol{x}_j)$ is strictly conditionally positive definite of order m on $\mathbb{R}^s$ and the points $x_1, \dots, x_n \in \mathbb{R}^s$ for an $(m-1)$-unisolvent set, then the $\boldsymbol{G}$ matrix is uniquely solvable.

Proof: The following proof is derived from a similar proof in [97]. First, it is recalled that the $\boldsymbol{G}$ matrix has the following structure:

$$\boldsymbol{G}\begin{bmatrix}\boldsymbol{a}\\\boldsymbol{b}\end{bmatrix} = \begin{bmatrix}\boldsymbol{R} & \boldsymbol{P}\\\boldsymbol{P}^T & \boldsymbol{0}\end{bmatrix}\begin{bmatrix}\boldsymbol{a}\\\boldsymbol{b}\end{bmatrix} = \begin{bmatrix}\boldsymbol{u}\\\boldsymbol{0}\end{bmatrix} \tag{6.14}$$

Next, assume that $[\boldsymbol{a}, \boldsymbol{b}]^T$ is a solution of the homogenous linear system ($\boldsymbol{u} = \boldsymbol{0}$). The proof consists in showing that $[\boldsymbol{a}, \boldsymbol{b}]^T = \boldsymbol{0}$ is the only possible solution. Pre-multiplying the top row by $\boldsymbol{a}^T$ gives:

$$\boldsymbol{a}^T\boldsymbol{R}\boldsymbol{a} + \boldsymbol{a}^T\boldsymbol{P}\boldsymbol{b} = \boldsymbol{0} \tag{6.15}$$

From the bottom row, it is known that $\boldsymbol{a}^T\boldsymbol{P} = \boldsymbol{0}$ and thus:

$$\boldsymbol{a}^T\boldsymbol{R}\boldsymbol{a} = \boldsymbol{0} \tag{6.16}$$

Since the $\boldsymbol{R}$ matrix is itself clearly conditionally positive definite by properties 4-5 and definitions 1-2, then we get that $\boldsymbol{a} = \boldsymbol{0}$. Unisolvency of the data points and the fact that $\boldsymbol{a} = \boldsymbol{0}$ guarantee $\boldsymbol{b} = \boldsymbol{0}$ from the top row. ■[8]

---

[8] The tombstone or Halmos symbol ■ denotes the end of a mathematical proof.

Box 6.3: Theorem 1 implication

Theorem 1 Implication The implication of Theorem 1 is that the $\boldsymbol{G}$ matrix with a linear polynomial basis has an inverse in $\mathbb{R}^1$ and $\mathbb{R}^2$ if and only if:

a) None of the nodes in the domain are coincident
b) In 2D real coordinate space $\mathbb{R}^2$, the set of points must contain at least 3 non-collinear points. This is necessary to guarantee 1-unisolvency (since 3 collinear points are not 1-unisolvent, as a plane through three arbitrary heights at these 3 points is not uniquely determined [97])

The conditions specified in Box 6.3 are a useful clarification, since other mechanicians have previously (erroneously) claimed that for RPIM functions the interpolation always exists for any nodal distribution [98]. This has been disproven and the conditions for the existence of the interpolation have been clarified.

It is noted that unisolvency of set of data points by linear monomial interpolants is easily established. A similar statement for higher order monomial interpolants is not trivial or perhaps even possible and will not be attempted here. Such higher order bases will therefore be avoided in this thesis. It is also noted that the extension of point (2) in Box 6.3 to higher-dimensional real coordinate spaces is straightforward, but is not required for the purposes of this thesis.

A number of nodal configurations in $\mathbb{R}^2$ were tested to demonstrate the existence conditions of the interpolation given in Box 6.3. The results are shown in Table 6.3. As can be seen, the existence conditions are confirmed by these numerical experiments. Note that a suitable RBF satisfying the properties of Box 6.1 was used, as well as a linear monomial basis, i.e., $[1 \quad x \quad y]$. Three nodes were used as a representative discretization.

Table 6.3: Interpolation existence verification

Configuration	Nodes	Comment	G matrix condition	
			Expected	*Calculated*
A	(0,0) (0,0) (0,0)	All nodes coincident	S	Inf (S)
B	(1,0) (0,0) (0,0)	Two nodes coincident	S	Inf (S)
C	(0,2) (1,2) (2,2)	Nodes aligned on straight line (y=2)	S	Inf (S)
D	(0,0) (1,1) (2,2)	Nodes aligned on straight line (y=x)	S	Inf (S)
E	(0,1) (1,0) (1,1)	Nodes neither coincident nor fully collinear (structured, partially collinear)	NS	1 (NS)
F	(0.8,0.7) (0.2,0.5) (0.4,0.6)	Unstructured, random nodes	NS	114 (NS)

S = Singular, NS = Non-Singular

With an appropriate nodal distribution resulting in a well-posed $\boldsymbol{G}$ matrix, the system of equations (6.9) can hence be solved to determine the unknown coefficients:

$$\begin{bmatrix} \boldsymbol{a} \\ \boldsymbol{b} \end{bmatrix} = \boldsymbol{G}^{-1} \begin{bmatrix} \boldsymbol{u} \\ \boldsymbol{0} \end{bmatrix} \tag{6.17}$$

Eqn. (6.17) can be equivalently expressed in matrix notation as:

$$u^h(\boldsymbol{x}) = \boldsymbol{\Phi}^T(\boldsymbol{x})\boldsymbol{u}(\boldsymbol{x}) \tag{6.18}$$

where $\boldsymbol{\Phi}^T(\boldsymbol{x}) = [\boldsymbol{r}^T(\boldsymbol{x})\boldsymbol{a} + \boldsymbol{p}^T(\boldsymbol{x})\boldsymbol{b}]$ is called the shape function vector. In continuum mechanics, the first and second derivative of the shape function are also frequently required. These derivatives can easily be determined as follows:

$$\frac{\partial \boldsymbol{\Phi}^T(\boldsymbol{x})}{\partial j} = \left[\frac{\partial \boldsymbol{r}^T(\boldsymbol{x})}{\partial j}\boldsymbol{a} + \frac{\partial \boldsymbol{p}^T(\boldsymbol{x})}{\partial j}\boldsymbol{b}\right] \tag{6.19}$$

$$\frac{\partial^2 \boldsymbol{\Phi}^T(\boldsymbol{x})}{\partial j^2} = \left[\frac{\partial^2 \boldsymbol{r}^T(\boldsymbol{x})}{\partial j^2}\boldsymbol{a} + \frac{\partial^2 \boldsymbol{p}^T(\boldsymbol{x})}{\partial j^2}\boldsymbol{b}\right] \tag{6.20}$$

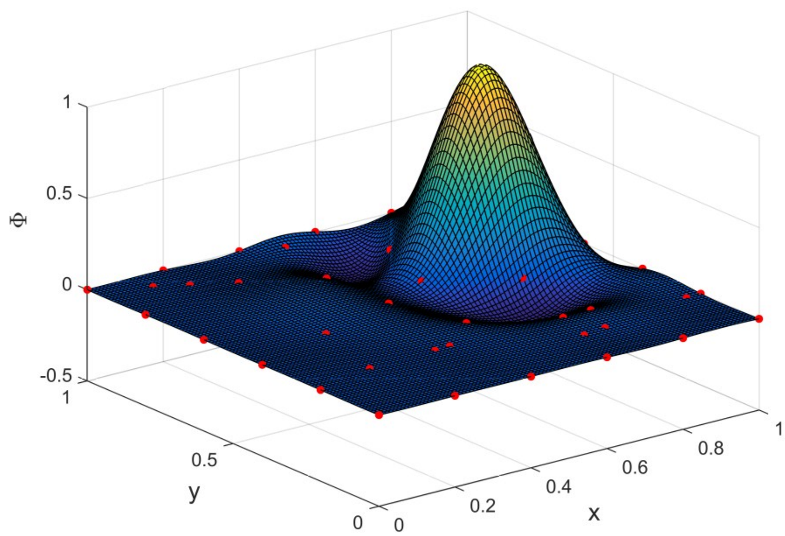

Figure 6.3: RPI shape function (linear polynomial basis, Multi-Quadratic RBF)

As an example, a set of scattered nodes in the unit square is considered. The RPI shape function corresponding to the node located at (0.792, 0.699) is depicted in Figure 6.3. Node locations are shown in red. It is clearly visible that the shape function has a value of 1 at its corresponding node and a value of zero at all other nodes. This is called the interpolating property. In addition, the sum of all shape functions evaluated at a particular point in the domain equals 1, known as the partition of unity.

A summary of RPI shape function properties is provided in Box 6.4. The interpolating, compatibility and reproducibility properties follow directly from the theory presented in this section. Proof of the partition of unity property is given by Liu [99].

Box 6.4: RPI Shape function properties

RPI Shape Function Properties

a) Partition of unity
b) Kronecker-Delta (interpolating) property
c) Continuity/compatibility
d) Reproducibility: any polynomial with a degree less than or equal to that of the monomial basis can be exactly reproduced

6.2 Moving Radial Point Interpolation

The support domain is the set of nodes that is used to construct the radial point interpolation at a point $\boldsymbol{x}$. When all of the nodes in the domain are used, as was assumed without loss of generality in section 6.1, this is called a global support domain and the shape function is called a global shape function. However, the construction of the $\boldsymbol{R}$ and $\boldsymbol{G}$ matrices using all of the nodes in the domain is extremely computationally expensive when the number of nodes is large, as is generally the case in a computational mechanics analysis. The inversion of the $\boldsymbol{G}$ matrix alone has a complexity of $O(n^3)$. It is therefore often interesting to use a local support domain, i.e., only a subset $\Omega_s \subseteq \Omega$ when constructing the interpolation for $\boldsymbol{x}$. The idea behind such a domain is that only the nodes near the point of inquiry directly affect its field function value.

Typically, the support domain is constructed by searching for all the nodes within a square or circular domain centered on $\boldsymbol{x}$, as shown in Figure 6.4-a and Figure 6.4-b, respectively.

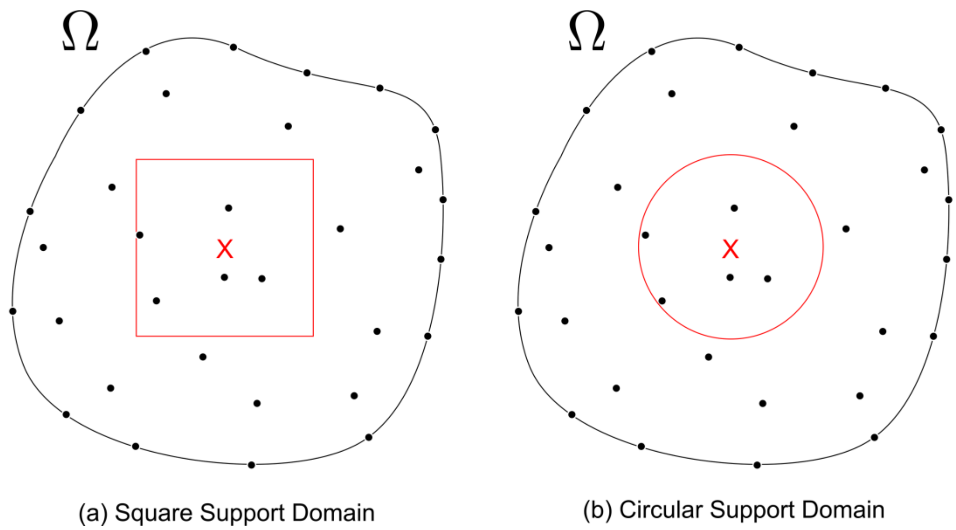

Figure 6.4: Typical support domains

However, this approach works poorly when the nodal distributions are very irregular. It is also important that the local support domains overlap; otherwise it is possible to end up with a situation where there is no way for the nodes in one part of the domain to influence the nodes in another part, akin to having a discontinuity in the body.

A more sophisticated approach is used in this work. To ensure that the local support domains overlap and to achieve consistency in the construction of the local support domains irrespective of the irregularity of the nodal distribution, the Delaunay triangulation of the nodes to determine the natural neighbours of any given node. The Delaunay triangulation is the dual graph of the Voronoi diagram of a set of points or nodes, as shown in Figure 6.5. Every node has a Voronoi Polygon (VP) that encases it. Therefore, the support domain of a node consists of the union of its VP and the VPs of its natural neighbours.

The proposed approach is similar to Voronoi tessellation of the nodes to generate influence cells recently proposed by Belinha et al. [100]. However, since the Voronoi tessellation does not actually need to be calculated, the algorithm proposed in this thesis is arguably more efficient. The algorithm is stated as follows:

1) Calculate the Delaunay triangulation of the nodal discretization, subject to certain restrictions on the convex hull boundaries e.g. cut-outs.

2) For each node, perform a search to find all Delaunay triangles that share this node. Once all triangles that share the node have been determined, form the set of unique nodes representing the vertices of these triangles minus the node itself. This set comprises the node's natural neighbours.

3) To find the support domain of the point $\boldsymbol{x}$, the closest node must first be found (a KD-tree is used for efficient implementation of this nearest neighbour search). This is theoretically equivalent to determining in which Voronoi Polygon the point lies. The support domain of the point $\boldsymbol{x}$ corresponds to this node's natural neighbours, determined in steps 1-2.

Note that steps 1-2 need only be performed once for a given discretization. The proposed algorithm is simple yet sophisticated. Another advantage of this algorithm is that the Delaunay triangles are a natural choice for numerical integration of the field functions, as shall be discussed in section 7.4.

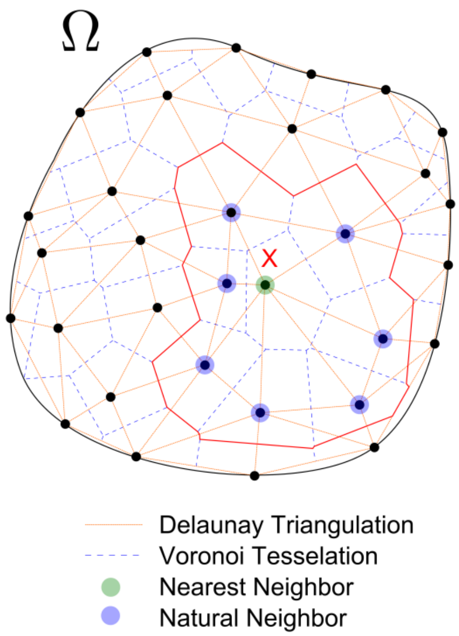

Figure 6.5:Delaunay triangulation algorithm for finding natural neighbours

Figure 6.5 shows the most important concepts of the algorithm. For the point x, the nearest neighbour node is shown in green. The support domain of the point x consists of the Voronoi Polygons of this nearest neighbour and the nearest neighbour's natural neighbours, shown in blue. It is important to note is that the natural neighbours do not necessarily correspond to the closest nodes. It can be see that if a circular support domain of radius slightly less than the distance to the rightmost natural neighbour was used, then this node would not be included in the support domain while many nodes to the left of x not that are not natural neighbours would be.

It is also of note that what are shown in Figure 6.5 can be considered the "1st degree natural neighbours." The influence domain of each node can easily be extended to the nth order by the same algorithm, by considering the union of the natural neighbours and their neighbours, and their neighbours, and so on, n times.

Compared to the global RPI functions, the moving RPI shape functions of the moving RPIM have the properties summarized in Box 6.5.

Box 6.5: Moving RPI shape function properties

Moving RPI Shape Function Properties

a) Partition of unity
b) Kronecker-Delta (interpolating) property
c) Compact support
d) Reproducibility: any polynomial with a degree less than or equal to that of the monomial basis can be exactly reproduced

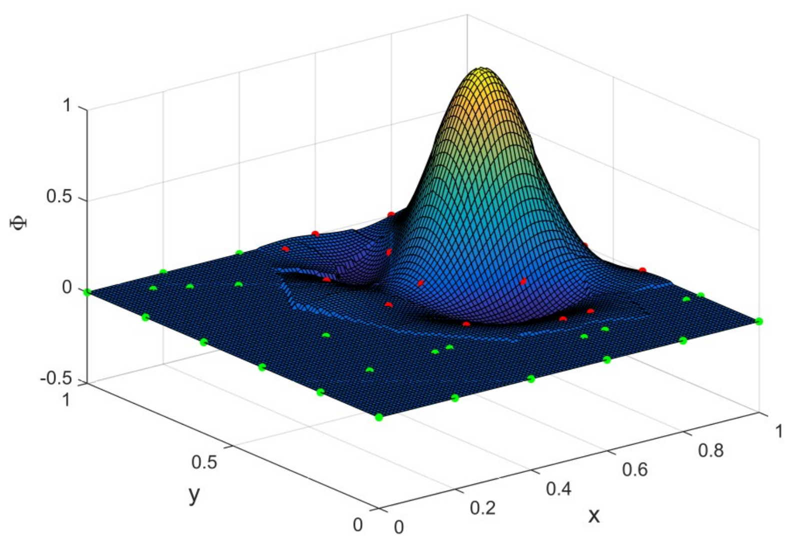

Figure 6.6: RPI moving shape function (linear polynomial basis, Multi-Quadratic RBF)

Figure 6.6 demonstrates a number of these properties. The moving shape function corresponding to a particular node, again located at (0.792, 0.699), is shown. The domain nodes are plotted in green and the natural neighbours (i.e., the nodes in the local support domain) are plotted in red. It can be seen that the moving shape function value is 1 at the node location (interpolating property) and 0 at all other nodes in the local support domain (partition of unity property). Outside the local support domain, the function is zero (compact support property). Note that discontinuities in the shape function at the support domain boundaries are clearly visible (lack of compatibility). This is because whenever nodes enter or leave the local support domain, the shape functions and their derivatives are discontinuous. This is in contrast to the smooth global shape function shown in Figure 6.3. Importantly, various investigators have found that this lack of compatibility is not prejudicial to convergence and does not considerably hamper the accuracy of the method [99, 100].

6.3 Choice of the Radial Basis Function

The radial basis function or *correlation function* has an important effect on the performance and accuracy of the interpolation. One weakness of meshless methods is that the choice of the correlation function and its parameters can affect its convergence rate. That is to say; generally, with fine discretizations the solution converges, however, the convergence be much improved for even coarse discretizations if appropriate correlation functions and their parameters are selected. This selection has been found to be problem dependent, and it is thus important for this thesis that appropriate parameters be found for the hybrid bonded-bolted joint problem, characterized by the stress field for a plate with a hole. The first requirement for the correlation function is that for a fixed local support domain it must satisfy the properties set out in Box 6.1. The following are examples of functions that satisfy these properties and that have been used with success in the literature to date:

Table 6.4: Summary of common radial basis functions

Function name	Reference	Equation	Parameter
Gaussian	[99, 100]	$e^{-\alpha\left(\frac{s}{d_s}\right)^2}$	α
Multi-quadratic (MQ)	[99]	$[s^2 + (d_s\xi)^2]^q$	ξ, q
Quartic Spline	[101]	$\begin{cases} 1 - 6\left(\frac{s}{d_s}\right)^2 + 8\left(\frac{s}{d_s}\right)^3 - 3\left(\frac{s}{d_s}\right)^4 & \text{if } \left\lvert\frac{s}{d_s}\right\rvert \le 1 \\ 0 & \text{if } \left\lvert\frac{s}{d_s}\right\rvert > 1 \end{cases}$	None

In these functions, s is the normalized distance between a point $\boldsymbol{x}$ and node $\boldsymbol{x}_i$:

$$s = |\boldsymbol{x}_i - \boldsymbol{x}| \tag{6.21}$$

Furthermore d_s is the mean internodal spacing in the local support domain. A common definition for d_s which is frequently used in the RPIM literature is given by Eqn. (6.22). However, a search of the literature was not able to determine how this expression was derived. It seems to have originally been proposed by Liu [99] and has since been repeated by various investigators in reference to the former without any critical assessment of its validity.

$$d_s = \frac{\sqrt{A_s}}{\sqrt{n_s} - 1} \tag{6.22}$$

In this work, use of the following expression is suggested instead:

$$d_s = \frac{\sqrt{A_s}}{2\sqrt{n_s}} \tag{6.23}$$

Eqn. (6.23) has its roots in molecular physics, having been originally derived by Hertz [102] as the mean nearest neighbour distance of randomly scattered point particles in a plane. It is based on the probability of finding a nearest neighbour at a distance between $\boldsymbol{x}$ and $\boldsymbol{x} + d\boldsymbol{x}$ from any given particle [103]. It is clearly preferable to use such a rigorously derived expression to Eqn. (6.22). The different correlation functions are plotted in Figure 6.7:

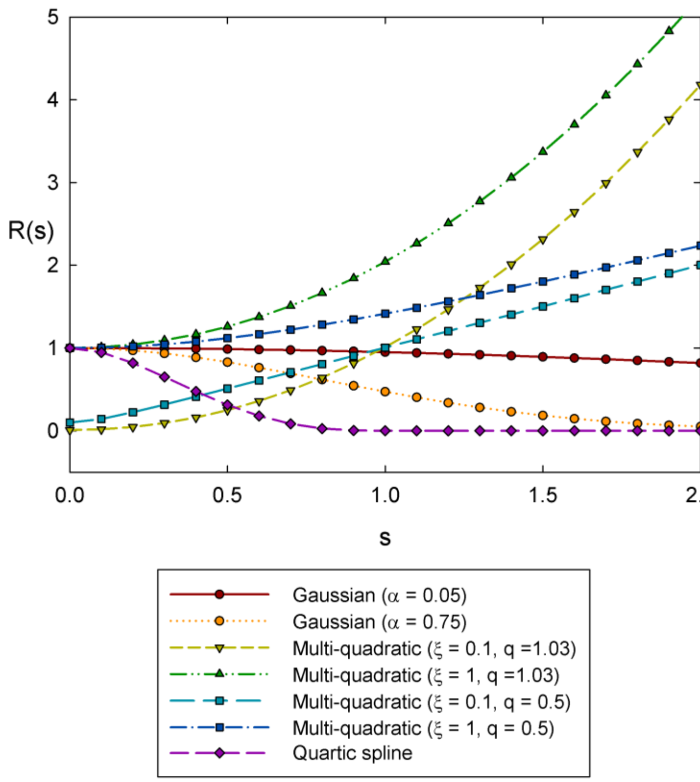

Figure 6.7: Comparison of radial basis functions $(d_s = 1)$

As shown in Figure 6.7, the Gaussian and Quartic spline RBFs always have a value of 1 at a distance of 0 which decreases with increasing s. The Gaussian's shape is dependent on the α parameter; small α values result in a "flatter" function meaning that the output is less sensitive to changes in s. The Quartic spline's shape does not depend on any parameter, which upon first consideration appears to be a desirable trait. In addition, this is the only of the considered functions which has intrinsic compact support since it is zero if $\left|\frac{s}{d_s}\right| > 1$. Finally, unlike the other two functions, the Multi-quadratic (MQ) function increases with distance s. It is sensitive to both the ξ and q parameters; greater ξ values increase the base value of the function at $s = 0$ while q again controls the flatness or sensitivity of the function, with greater q values increasing the function sensitivity.

The optimal radial basis function (and corresponding parameters) for the hybrid bonded-bolted joint problem is determined in Chapter 7.

Chapter 7: Galerkin Radial Point Interpolation Method

The meshless interpolating functions introduced in Chapter 6 are used in this chapter to solve several relevant benchmark problems in continuum mechanics. One purpose of this chapter is to demonstrate the use of RPI functions in the solution of boundary value problems (BVPs). Another is to determine a suitable type of radial basis function (RBF) for the hybrid bonded-bolted joint problem and to optimize its parameters. To obtain a discrete set of system equations, the Galerkin method in the form of the principle of virtual work is used. This combination of the RPIM and PVW shall be called the Galerkin Radial Point Interpolation Method (GRPIM).

7.1 Principle of Virtual Work

The problems considered in this chapter are all 2D elastostatic problems in either plane stress or plane strain. From continuum mechanics, the 2D elastostatic problem without body forces can be stated in direct tensor form as:

$\boldsymbol{\nabla}\cdot\boldsymbol{\sigma}=\mathbf{0}$ (Balance of linear momentum) (7.1)

$\boldsymbol{\sigma}=\boldsymbol{\sigma}^{\mathrm{T}}$ (Balance of angular momentum) (7.2)

$\boldsymbol{\varepsilon}=\frac{1}{2}[\boldsymbol{\nabla}\mathbf{u}+(\boldsymbol{\nabla}\mathbf{u})^{\mathrm{T}}]$ (Strain-displacement relation) (7.3)

$\boldsymbol{\sigma}=\boldsymbol{C}:\boldsymbol{\varepsilon}$ (Constitutive relation) (7.4)

$\mathbf{u}=\tilde{\mathbf{u}}$ on Γ_u (Dirichlet boundary condition) (7.5)

$\boldsymbol{\sigma}\cdot\mathbf{n}=\tilde{\mathbf{t}}$ on Γ_σ (Neumann boundary condition) (7.6) where $\tilde{\mathbf{u}}$ and $\tilde{\mathbf{t}}$ denote prescribed displacement and traction fields, respectively. The elasticity tensor $\boldsymbol{C}$ depends on the simplifying assumption made. If plane stress is assumed, the elasticity tensor is:

$$\boldsymbol{C} = \frac{E}{1-\nu^2}\begin{bmatrix} 1 & \nu & 0 \\ \nu & 1 & 0 \\ 0 & 0 & 1-\nu \end{bmatrix} \tag{7.7}$$

If plane strain is assumed, then it is:

$$\boldsymbol{C} = \frac{E}{(1+\nu)(1-2\nu)}\begin{bmatrix} 1-\nu & \nu & 0 \\ \nu & 1-\nu & 0 \\ 0 & 0 & 1-2\nu \end{bmatrix} \tag{7.8}$$

To solve the system of partial differential equations given by Eqn. (7.1) numerically, the Galerkin method is used. Supposing that the solution $\mathbf{u}$ is sufficiently smooth then Eqn. 7.1 may be multiplied by a test function $\mathbf{w}$ and integrated over the problem domain as follows:

$$\int_{\boldsymbol{A}} [\boldsymbol{\nabla} \cdot \boldsymbol{\sigma}] \cdot \mathbf{w} \, dA = 0 \tag{7.9}$$

$\mathbf{w}$ is arbitrary other than it must have square-integrable derivatives and be homogeneous on Γ_{u}. Using integration by parts and the divergence theorem, Eqn. (7.9) becomes:

$$\int_{\boldsymbol{A}} [\boldsymbol{\sigma}: \boldsymbol{\nabla}\mathbf{w}] \, dA - \int_{\Gamma} [\boldsymbol{\sigma} \cdot \mathbf{n}] \cdot \mathbf{w} \, d\Gamma = 0 \tag{7.10}$$

Given the homogeneity requirement $\mathbf{w} = 0$ on Γ_{u} and considering Eqn. (7.6), Eqn. (7.10) becomes:

$$\int_{\boldsymbol{A}} [\boldsymbol{\sigma}: \boldsymbol{\nabla}\mathbf{w}] \, dA - \int_{\Gamma_\sigma} \tilde{\mathbf{t}} \cdot \mathbf{w} \, d\Gamma = 0 \tag{7.11}$$

If it is assumed that $\mathbf{w} = \mathbf{u}^*$ (i.e., that $\mathbf{w}$ is an independent deformation state with consistent strains $\boldsymbol{\varepsilon}^*$ that are work conjugate to $\tilde{\mathbf{t}}$ and $\boldsymbol{\sigma}$, respectively), then the Galerkin weak form of Eqn. (7.12) specializes to the principle of virtual work. At this point, an interpretation may be made, leading to two distinct variational principles. Should equilibrated forces and stresses be assumed and it be considered that $\mathbf{u}^*$ and $\boldsymbol{\varepsilon}^*$ are variations of the real displacements and strains, then we speak of the principle of virtual displacements. Should equilibrated displacements and strains be assumed and it be considered that $\boldsymbol{\sigma}$ and $\tilde{\mathbf{t}}$ are variations of the real forces and stresses, then the variational principle is called the principle of virtual forces. In this work, the principle of virtual displacements is used, i.e.:

$$\mathbf{w} \equiv \mathbf{u}^* \equiv \delta\mathbf{u} \quad , \quad \nabla\mathbf{w} \equiv \boldsymbol{\varepsilon}^* \equiv \delta\boldsymbol{\varepsilon} \tag{7.12}$$

Hence the following familiar weak form is obtained:

$$\delta\mathrm{G} = \int_{\boldsymbol{A}} [\boldsymbol{\sigma}: \delta\boldsymbol{\varepsilon}]\, dA - \int_{\Gamma_\sigma} \tilde{\mathbf{t}} \cdot \delta\mathbf{u}\, d\Gamma = 0 \tag{7.13}$$

7.2 GRPIM Solution of the 2D Elastostatic BVP

To obtain an approximate solution, RPI functions are substituted in Eqn. (7.13). In accordance with Chapter 6, these functions can be written in matrix notation as:

$$u_i(\mathbf{x}) = \boldsymbol{\Phi}(\mathbf{x})^{\mathrm{T}}\mathbf{U}_i \;\mid\; i \in \{x, y\} \tag{7.14}$$

where $\mathbf{U}_i$ is the solution vector (vector of nodal values) for the *i*th independent field variable. In the case of 2D elastostatics, this consists of x and y displacements only. Furthermore, the function derivatives are:

$$u_{i,j}(\mathbf{x}) = \boldsymbol{\Phi}(\mathbf{x})_{,x}^{\mathrm{T}}\mathbf{U}_i \;\mid\; i \in \{x, y\} \tag{7.15}$$

This leads to the following discrete expression for the displacement field:

$$\mathbf{u}(\mathbf{x}) = \begin{bmatrix} \mathbf{\Phi} & \mathbf{0} \\ \mathbf{0} & \mathbf{\Phi} \end{bmatrix}^{\mathrm{T}} \mathbf{U} \tag{7.16}$$

where $\mathbf{u} = \{u_x, u_y\}^{\mathrm{T}}$ and $\mathbf{U} = \{\mathbf{U}_x^T, \mathbf{U}_y^T\}^{\mathrm{T}}$. Based on the definition of Eqn. (7.3), the strains can be expressed as follows:

$$\boldsymbol{\varepsilon} = \mathbf{BU} \tag{7.17}$$

where the strain-displacement matrix $\mathbf{B}$ is:

$$\mathbf{B} = \begin{bmatrix} \mathbf{\Phi}_{,x}^{\mathrm{T}} & \mathbf{0} \\ \mathbf{0} & \mathbf{\Phi}_{,y}^{\mathrm{T}} \\ \mathbf{\Phi}_{,y}^{\mathrm{T}} & \mathbf{\Phi}_{,x}^{\mathrm{T}} \end{bmatrix} \tag{7.18}$$

The discrete approximations (7.16-7.17) are at this point substituted into the weak form (7.13). Given the linear elastic constitutive relation of Eqn. (7.4), this results in:

$$\delta \mathrm{G} = \delta \mathbf{U}^{\mathrm{T}} \int_{\boldsymbol{A}} [\mathbf{B}^{\mathrm{T}} \mathbf{C} \mathbf{B}] \, dA \, \mathbf{U} - \delta \mathbf{U}^{\mathrm{T}} \int_{\Gamma_\sigma} \tilde{\mathbf{t}} \, d\Gamma = 0 \tag{7.19}$$

or:

$$\delta \mathrm{G} = \delta \mathbf{U}^{\mathrm{T}} \mathbf{K} \, \mathbf{U} - \delta \mathbf{U}^{\mathrm{T}} \mathbf{F} = 0 \tag{7.20}$$

where:

$$\mathbf{K} = \int_{\boldsymbol{A}} [\mathbf{B}^{\mathrm{T}} \mathbf{C} \mathbf{B}] \, dA \tag{7.21}$$

$$\mathbf{F} = \int_{\Gamma_\sigma} \tilde{\mathbf{t}} \, d\Gamma \tag{7.22}$$

$\mathbf{K}$ is called the stiffness matrix while $\mathbf{F}$ is called the force vector. Since the variation of the displacement in Eqn. (7.20) is assumed to be arbitrary:

$$\delta\mathbf{U} \neq 0 \Rightarrow (\mathbf{K}\,\mathbf{U} - \mathbf{F}) = \mathbf{0} \tag{7.23}$$

Finally resulting in the following discrete system of equations:

$$\mathbf{K}\,\mathbf{U} = \mathbf{F} \tag{7.24}$$

7.3 Dirichlet Boundary Conditions & Contact

For the displacement based Galerkin method described in the preceding sections, it is easily shown that the Neumann boundary conditions given by Eqn. (7.6) are automatically satisfied. However, the Dirichlet boundary conditions of Eqn. (7.5) need to be imposed on the solution by modification of the $\mathbf{K}$ and $\mathbf{U}$ matrices in Eqn. (7.24). Consider that the *i*th equation of this system can be written as:

$$\sum_{j=1}^{\mathrm{ndof}} \mathrm{K}_{ij}\mathrm{U}_{\boldsymbol{j}} = \mathrm{F}_i \tag{7.25}$$

where ndof is the total number of degrees of freedom. Now consider the set of nonhomogeneous boundary conditions $\{\mathrm{U}_{\boldsymbol{k}}(\mathbf{x}_{\boldsymbol{k}}) \mid \mathbf{x}_{\boldsymbol{k}} \in \Gamma_\sigma\}$. Any rows for which $i = k$ may be directly modified to impose these conditions as follows:

$$\mathrm{K}_{kj} = \delta_{kj} \tag{7.26}$$

$$\mathrm{F}_k = \mathrm{U}_{\boldsymbol{k}} \tag{7.27}$$

where δ_{kj} is the Kronecker delta. Furthermore, for all rows for which $i \neq k$, since the $\mathrm{U}_{\boldsymbol{k}}$ are known these terms can be moved to the RHS of Eqn. (7.25):

$$\sum_{j=1}^{\mathrm{ndof}} \mathrm{K}_{ij}\mathrm{U}_{\boldsymbol{j}} - \sum \mathrm{K}_{\boldsymbol{ik}}\mathrm{U}_{\boldsymbol{k}} = \mathrm{F}_i - \sum \mathrm{K}_{\boldsymbol{ik}}\mathrm{U}_{\boldsymbol{k}} \tag{7.28}$$

The $\mathbf{K}$ and $\mathbf{F}$ matrices obtained after these operations are known as the modified stiffness matrix and modified force vector, respectively.

In addition to Dirichlet conditions, contact is also considered since the benchmark problem of section 7.5.3 includes this phenomenon. In that particular problem, frictionless unilateral contact is considered between a cylinder and a fixed/rigid horizontal surface as shown in Figure 7.1. The contact equations of the HBB joint model, given by Eqns. (5.28-5.29,) also hold. However, given the sign convention adopted in Figure 7.1 and the fact that the surface is rigid, they specialize to the following form:

$$g_n = g + \mathbf{n} \cdot \left\{\left[u_x, u_y\right]^T\right\} \tag{7.29}$$

$$g_n \geq 0 \quad , \quad P_n \geq 0 \quad , \quad g_n P_n = 0 \qquad \text{(7.30-a,b,c)}$$

on Γ_c

At this juncture, an active node shall be defined as any node on the contact boundary Γ_c that is participating in contact, i.e., for which $g_n^{(i)} = 0$. If this is the case, then by Eqns. (7.29-7.30), the following constraints must hold:

$$-u_y^{(b)} = g^{(i)} \text{ on } \Gamma_c \tag{7.31}$$

In this special case, given the fixed rigid surface and since there is no coupling between internal degrees of freedom, i.e., since the constraint is a single freedom constraint, the contact condition simplifies to a Dirichlet condition. The only thing that remains is to determine the active contact region $\Gamma_{\mathrm{active}} \subset \Gamma_c$. Determining this region is part of the solution. Throughout this thesis, the contact region is determined using a simple active set algorithm, described in Box 7.1.

Box 7.1: Active set contact algorithm

Active Set Algorithm

1) Assume an initial set of active contact nodes and solve Eqn. 7.24 subject to the relevant Dirichlet conditions

2) Check if any inactive contact nodes violate Eqn. 7.30-a. If yes, add them to the active set

3) Check if any active contact nodes violate Eqn. 7.30-b. If yes, remove them from the active set

4) If the active set did not change in steps 2 and 3, go to step 5. If the active set did change, solve Eqn. 7.24 subject to the relevant Dirichlet conditions for the new active set and go to 2

5) The solution has been obtained

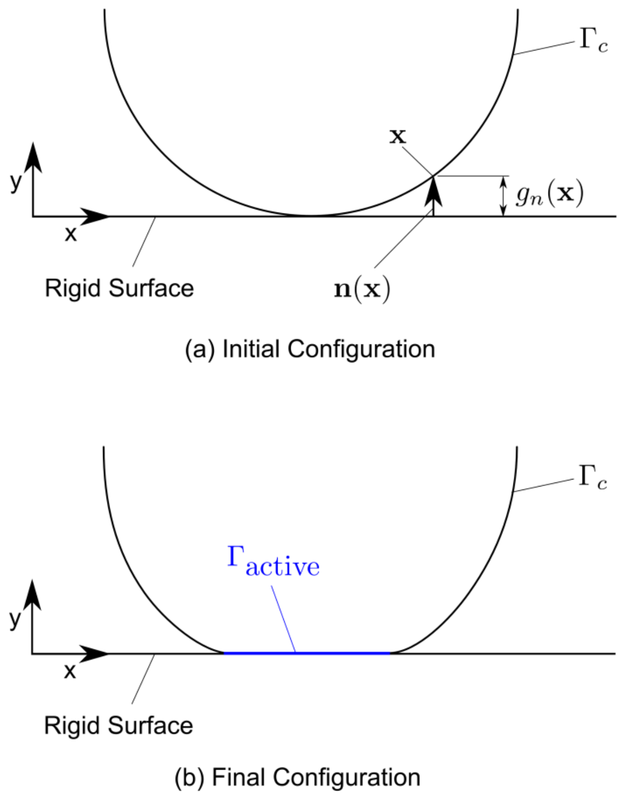

Figure 7.1: Plane contact of a deformable body with rigid horizontal surface

7.4 Computational Implementation Aspects

In order to evaluate the stiffness matrix in Eqn. (7.21), a numerical integration needs to be performed over the problem domain. This is slightly different for meshless methods than for other numerical methods, since there is no obvious grid over which the integration should be performed. Two strategies are often adopted, which are shown in Figure 7.2.

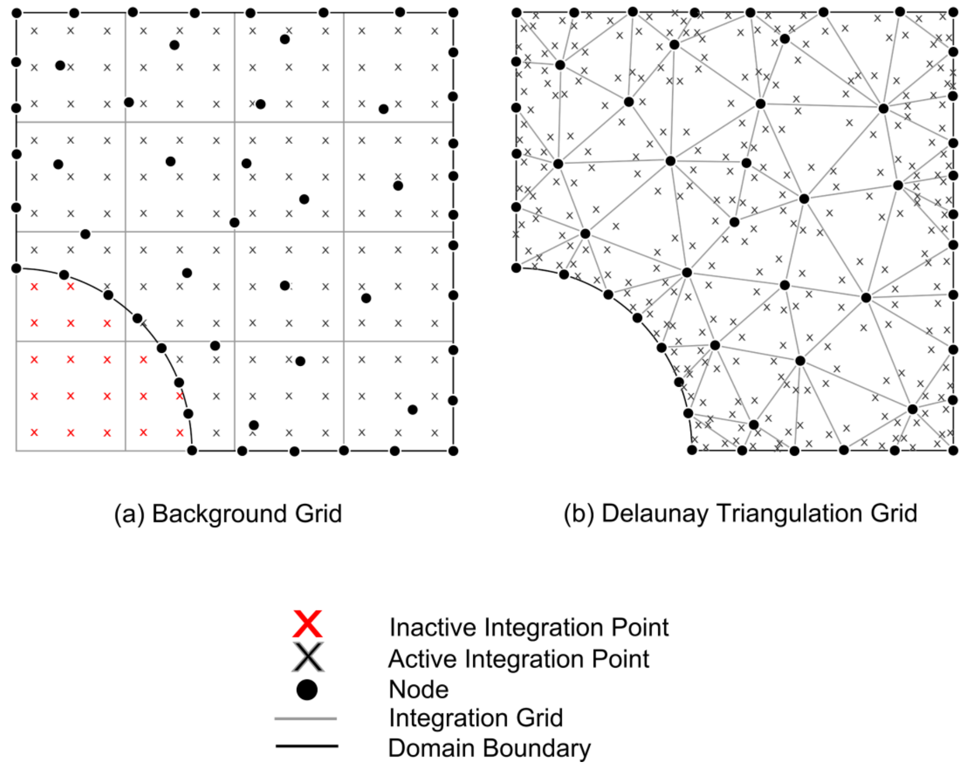

Figure 7.2: Numerical integration approaches

The background grid method consists of constructing a regular grid that encompasses the problem domain. The weights of any integration points that fall outside the domain boundaries, shown in red in Figure 7.2-a, are set to zero and thus not taken into account in the stiffness calculation. A disadvantage of this method is that in curved regions, a very fine grid becomes necessary to achieve acceptable results. The second method is to construct a Delaunay triangulation on the nodal discretization, as shown in Figure 7.2-b. This approach is able to achieve much better accuracy in curved regions and is relatively easy to automate. This is the method that is used throughout this thesis. It must be stressed, however, that the integration grid is quite independent of the interpolation. For example, one or more nodes may be added to the interior of any of the Delaunay triangles in Figure 7.2-b without issue.

Once a Delaunay triangulation has been constructed, the integration point locations and weights can easily be determined by mapping the distorted triangles to a right triangle, using standard Gaussian quadrature rules (see for example

Lehman and Hawley [62] for further details). Throughout this thesis, a 3×3 rule is used unless otherwise stated.

It is remarked that there has recently been significant progress in nodal integration for meshless methods [104]. This is one of the most promising avenues for the future of these methods. Such schemes were not investigated in the scope of this thesis, but offer interesting possibilities for future developments of the solution scheme developed herein.

7.5 Suitable RBF Parameters for the HBB Joint Problem

In this section, a number of benchmark problems are analyzed in order to assess the performance of the different radial basis functions considered in section 6.3 and to determine optimal function parameters for the HBB joint problem.

7.5.1 Infinite Plate with a Hole

The problem shown in Figure 7.3-a is the classical problem of an infinite elastic plate with a circular hole under remote uniaxial stress. Assuming plane strain, the analytical solution is given by Timoshenko [105] as:

$$\sigma_x = \sigma_\infty \left[1 - \frac{R^2}{r^2}\left(\frac{3}{2}\cos 2\theta + \cos 4\theta\right) + \frac{3}{2}\frac{R^2}{r^2}\cos 4\theta \right] \tag{7.32}$$

$$\sigma_y = \sigma_\infty \left[-\frac{R^2}{r^2}\left(\frac{1}{2}\cos 2\theta - \cos 4\theta\right) + \frac{3}{2}\frac{R^4}{r^4}\cos 4\theta \right] \tag{7.33}$$

$$\tau_{xy} = \sigma_\infty \left[-\frac{R^2}{r^2}\left(\frac{1}{2}\sin 2\theta + \sin 4\theta\right) + \frac{3}{2}\frac{R^4}{r^4}\sin 4\theta \right] \tag{7.34}$$

Through the constitutive relations, the displacements can hence be obtained as:

$$\mathrm{u}_x = \sigma_\infty\left[1 - \frac{R^2}{r^2}\left(\frac{3}{2}\cos 2\theta + \cos 4\theta\right) + \frac{3}{2}\frac{R^2}{r^2}\cos 4\theta\right] \tag{7.35}$$

$$\mathrm{u}_y = \sigma_\infty\left[1 - \frac{R^2}{r^2}\left(\frac{3}{2}\cos 2\theta + \cos 4\theta\right) + \frac{3}{2}\frac{R^2}{r^2}\cos 4\theta\right] \tag{7.36}$$

This problem was chosen since the solution possesses the essential characteristics of the HBB joint problem, namely strong stress gradients and complex stress contours in the vicinity of the hole. To simulate the problem using the GRPIM, only a quarter plate was considered and symmetry boundary conditions were applied, as shown in Figure 7.3-b. The displacement components given by Eqns. (7.35-7.36) were applied as Dirichlet boundary conditions along the outer boundaries of the considered region.

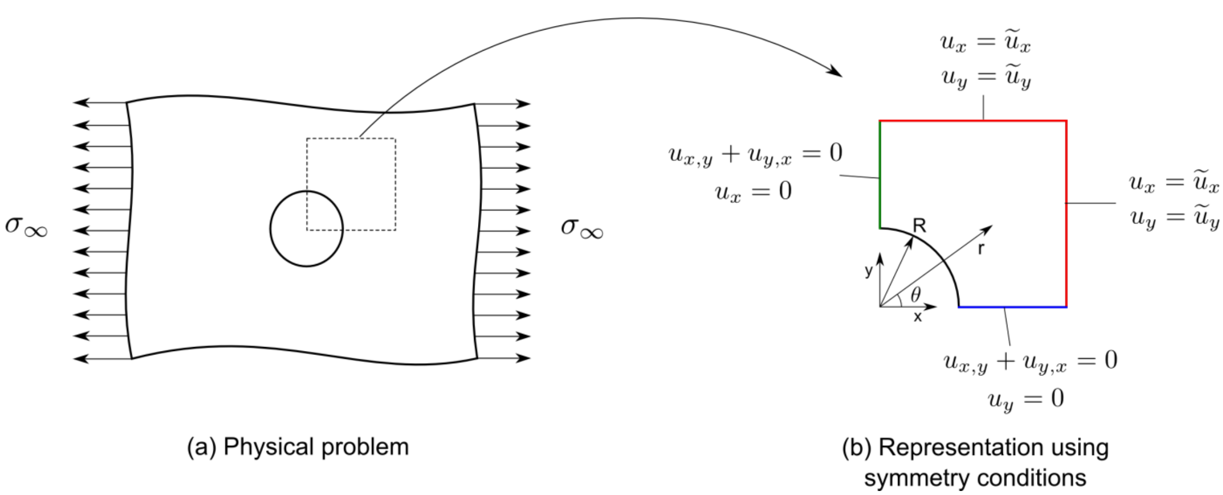

Figure 7.3: Infinite plate with a hole problem

The numerical solution to this problem was obtained using each of the three different radial basis functions described previously. The discretization was kept constant between different analyses and is shown in Figure 7.4-a,b. Both a regular discretization (shown in Figure 7.4-a) and an irregular discretization (shown in Figure 7.4-b) were considered. The irregular discretization was generated by randomly displacing the interior nodes of the regular discretization by anywhere between 0-0.5 times the internodal spacing for that node (defined by Eqn. (6.23)) following a Gaussian distribution. Once generated, the same irregular discretization—shown in Figure 7.4-b—was used in all the analyses.

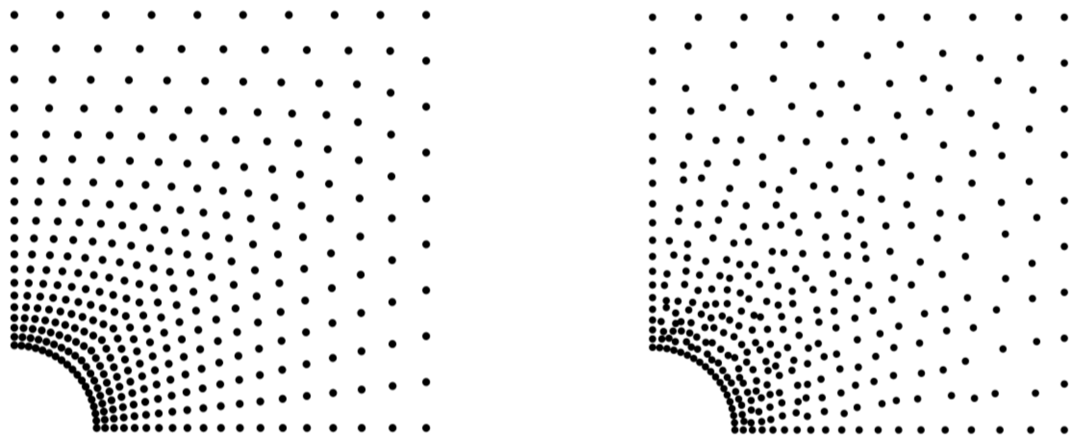

Figure 7.4: Nodal discretization of quarter plate. 19x19 mesh with (a) regular grid (b) irregular grid

Two measures of the error between the numerical solution and the analytical solution were used to quantify the performance of the GRPIM for a given basis function and set of parameters. These are the L^2-displacement norm:

$$E_d = \sqrt{\frac{\sum_{i=1}^{n_{\text{node}}}\left(\mathbf{u}_i^{\text{exact}} - \mathbf{u}_i^{\text{num}}\right)^T\left(\mathbf{u}_i^{\text{exact}} - \mathbf{u}_i^{\text{num}}\right)}{\sum_{i=1}^{n_{\text{node}}}\left(\mathbf{u}_i^{\text{exact}}\right)^T\left(\mathbf{u}_i^{\text{exact}}\right)}} \tag{7.37}$$

And the L^2-energy norm:

$$E_e = \sqrt{\frac{\int_A\left(\boldsymbol{\varepsilon}_i^{\text{exact}} - \boldsymbol{\varepsilon}_i^{\text{num}}\right)^T\boldsymbol{C}\left(\boldsymbol{\varepsilon}_i^{\text{exact}} - \boldsymbol{\varepsilon}_i^{\text{num}}\right)dA}{\int_A\left(\boldsymbol{\varepsilon}_i^{\text{exact}}\right)^T\boldsymbol{C}\left(\boldsymbol{\varepsilon}_i^{\text{exact}}\right)dA}} \tag{7.38}$$

To construct the RPI functions, a 2nd degree natural neighbour strategy was adopted with a linear polynomial basis. The choice of the linear polynomial basis was motivated in detail in Chapter 6. The 2nd degree natural neighbour strategy was adopted since computational cost increases with $O(n^3)$. Higher degree natural neighbour strategies exponentially increase the computational cost with limited benefits in terms of accuracy. The 2nd degree natural neighbour strategy is maintained throughout the rest of the thesis.

The Gaussian RBF was investigated first. This RBF has only a single parameter, namely α. A wide range of values was considered for this parameter, ranging from $1e-4 \leq \alpha \leq 1e1$. The results for both the regular and irregular discretizations are shown in Figures 7.5 and 7.6 for the displacement norm and energy norm, respectively.

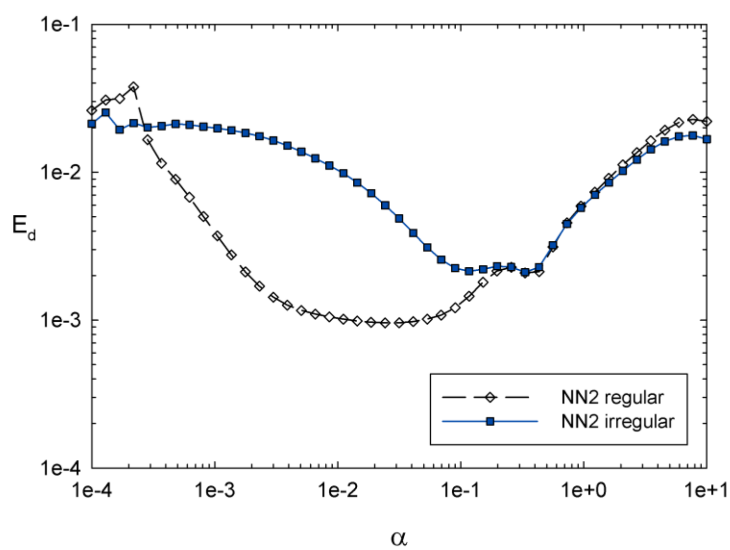

Figure 7.5: Displacement error norm for Gaussian-GRPIM. All axes use log scales

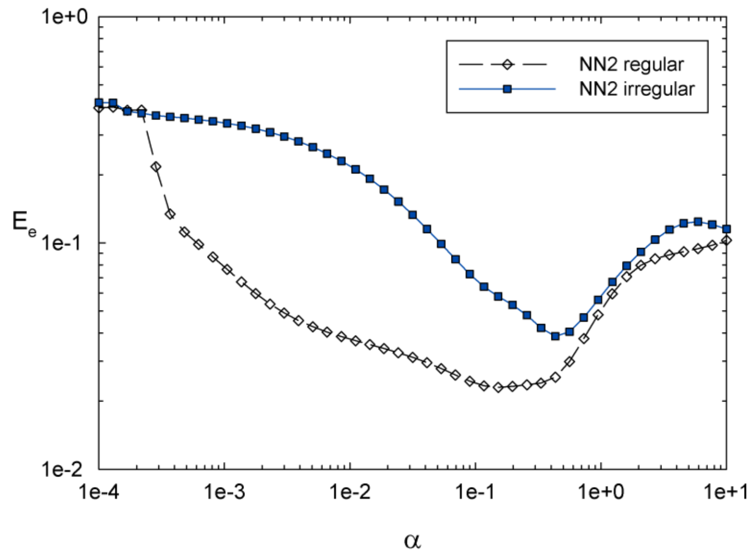

Figure 7.6: Energy error norm for Gaussian-GRPIM. All axes use log scales

It can be seen that in each case, the error is minimized in the region around 0.5e-2 $\leq \alpha \leq$ 1e+0. However, the precise minima of the errors do not coincide precisely (they conflict). In order to determine an optimal value of α that simultaneously optimizes performance of the Gaussian-GRPIM for regular and irregular grids for both displacement and energy error, a basic multi-objective optimization (MOO) was performed based on the classical weighted sum (scalarization) method [106]. In this approach, the multi-objective problem is reduced to a single-objective optimization by scalarizing the conflicting objectives. In other words, the optimization problem becomes:

$$\min_{\alpha} \sum_{i=1}^{4} \lambda_i \bar{J}_i\,(\alpha) \tag{7.39}$$

where J_1 is E_d for the regular grid, J_2 is E_e for the regular grid, J_3 is E_d for the irregular grid and J_4 is E_e for the irregular grid. A linear interpolation was constructed of the datasets shown in Figures 7.5-7.6 to represent J_1-J_4. The overbar in the $\bar{J}_i$ notation signifies that the particular objective function has been normalized by the dataset minimum. To obtain a set of non-inferior solutions, the weights λ_i

may be varied arbitrarily as long as their sum equals one. However, with no preference being given to any objective in particular, the only case considered was where all objectives are weighted equally, i.e., λ_i=0.25. The resulting function is shown in Figure 7.7. The minimum of this function occurs at $\alpha = 1.09\text{e-}1$, which is thus the simultaneously optimal value of α for the Gaussian-GRPIM.

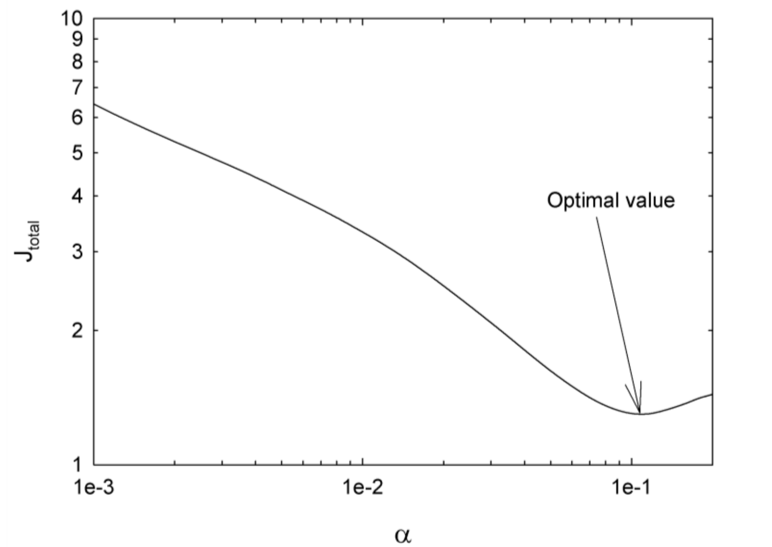

Figure 7.7: Normalized weighted sum of error norms (displacement and energy for both regular and irregular grids) for Gaussian-GRPIM. All axes use log scale

Next, the Multi-Quadratic RBF was considered (this combination shall be called MQ-GRPIM for brevity). In this case, there were two parameters to be simultaneously optimized. Figures 7.8-7.9 show the various errors as a function of the parameters. It can be seen that in each case there is a relatively large region of the parameter space for which the error is low and does not vary much (see the annotation on the figure). There also appears to be a greater overlap of these regions for various types of error and levels of grid irregularity (less conflict between the various objectives than for the Gaussian-GRPIM). As for the one parameter Gaussian parameter MOO, linear interpolations of the error values were created to represent J_1-J_4. These functions were hence normalized and weighted, then summed. The weighted total function, which in this case is a surface, was hence minimized in order to determine the optimal MQ parameters.

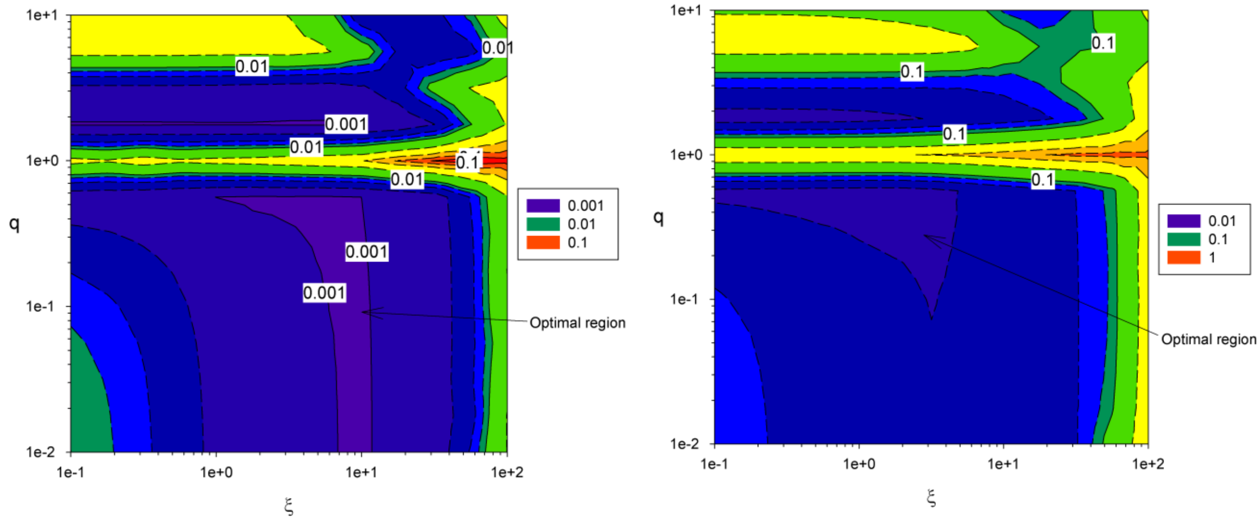

(a) Displacement norm

(b) Energy norm

Figure 7.8: Parameter optimization for MQ-GRPIM using a regular grid. All axes use log scale, minor contour intervals have a spacing of 0.25 decades

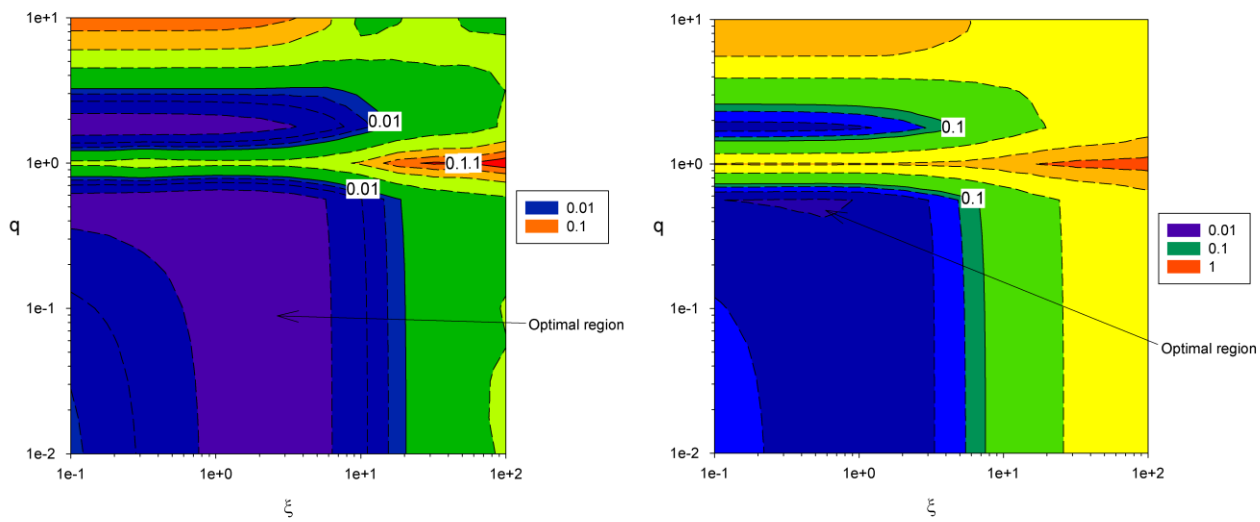

(a) Displacement norm

(b) Energy norm

Figure 7.9: Parameter optimization for MQ-GRPIM using irregular grid. All axes use log scale, minor contour intervals have a spacing of 0.25 decades

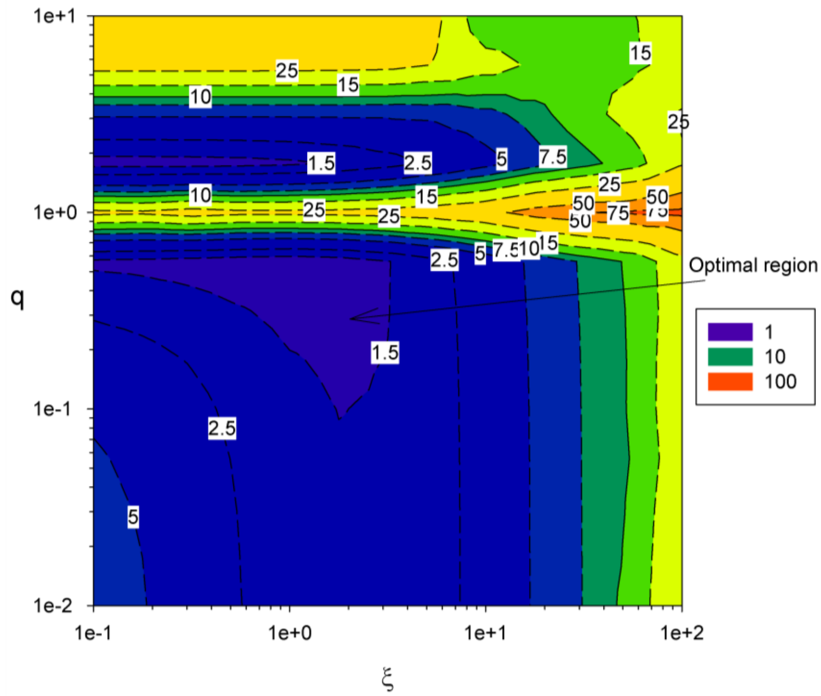

Figure 7.10: Normalized weighted sum of error norms (displacement and energy for both regular and irregular grids) for MQ-GRPIM. All axes use log scale

Figure 7.10 shows the normalized weighted sum of the error norms for the MQ-GRPIM. A 13x13 log grid of the MQ parameter space was used to construct the contour plot. The optimal point was determined as ξ=1.8, q=0.6 (it is remarked that values of $1.5 \leq \xi \leq 2.5$ and $0.5 \leq q \leq 0.9$ are clearly also acceptable).

Finally, the quartic spline has no parameters and thus did not require any optimization. With the optimal parameters having been determined for each type of RBF, their performances were compared. The results are shown in Table 7.1. To benchmark the performance for an irregular grid while taking into account the effect of variability, 10 new irregular grids were generated and analyzed and the average error was calculated. The standard deviations are indicated in parentheses.

Table 7.1: Performance of different RBF with optimized parameters

RBF Type	E_d **(regular)**	E_e **(regular)**	E_d **(irregular)**	E_e **(irregular)**
Gaussian	1.37e-3	2.36e-2	2.13e-3 (σ = 7.72e-5)	6.81e-2 (σ = 2.83e-4)
Multi-quadratic (MQ)	9.34e-4	1.91e-2	1.32e-3 (σ = 5.23e-5)	4.41e-2 (σ = 8.84e-4)
Quartic spline (QS)	1.84e-2	9.20e-2	1.59e-2 (σ = 5.46e-4)	1.27e-1 (σ = 1.92e-3)

On all error metrics, the optimized NN-MQ-GRPIM is seen to significantly outperform the other RBFs. The quartic spline performs poorest. Based on this comparison, the MQ-GRPIM with the optimized values determined in this section is used exclusively throughout the remainder of the thesis. Plots of the MQ-GRPIM solution for the stress fields are shown next the analytical solution in Figure 7.12 for the optimized MQ parameters. It is clear that there is very good agreement between the two solutions, as expected based on the error analysis.

Finally, the convergence properties of the optimized NN-MQ-GRPIM were studied. A number of successively refined discretizations were analyzed and the effect on the calculated stress concentration factor was considered. For the irregular grid, 10 random grids were analyzed for each different number of nodes and the results averaged. The results are plotted in Figure 7.11. It is seen that the optimized GRPIM converges to the theoretical value of 3 for both regular and irregular grids at a similar rate. This confirms the convergence property of the method, regardless of the lack of conformability.

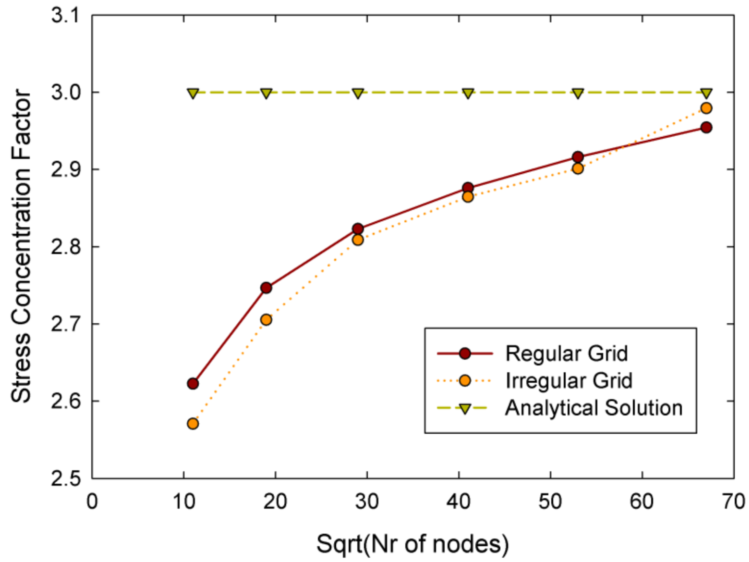

Figure 7.11: Convergence of solution with refinement of discretization

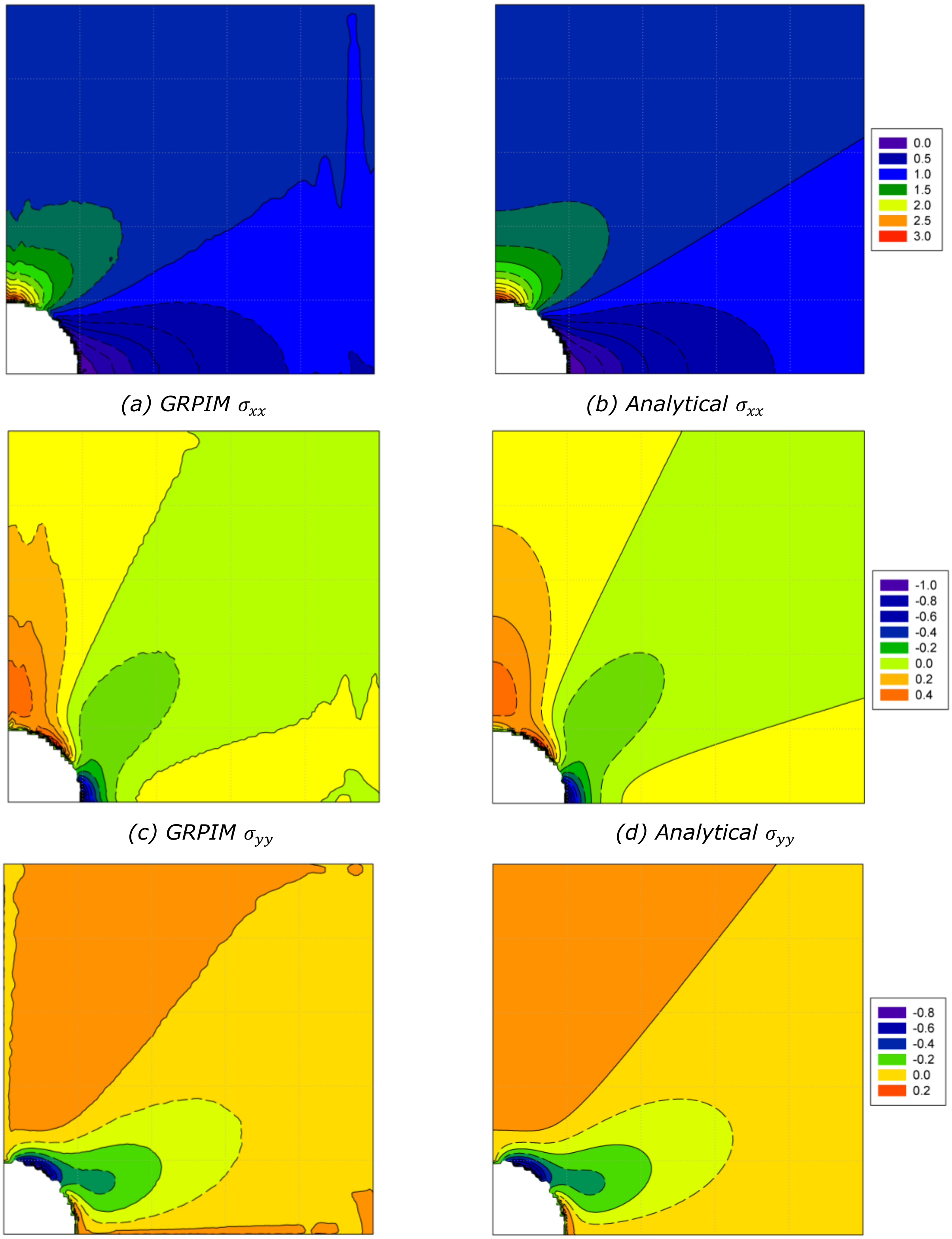

(a) GRPIM σ_{xx} *(b) Analytical* σ_{xx}

(c) GRPIM σ_{yy} *(d) Analytical* σ_{yy}

(e) GRPIM σ_{xy} *(f) Analytical* σ_{xy}

Figure 7.12: Stress contours predicted by NN2-MQ-GRPIM versus analytical solution. GRPIM analysis using regular discretization shown in Figure 7.4-a

7.5.2 Patch test

The patch test is a popular tool used in the development of isoparametric finite elements and consists of reproducing a linear displacement field (i.e., a constant strain state). Since good finite elements have the reproducing property and are continuous within each integration subdomain (element), they normally pass the patch test to within machine precision. Even though the GRPIM also has the reproducing property, it is well known that it cannot generally pass the patch test since discontinuities occur in the displacement variables as nodes enter or leave a support domain and the integration mesh generally does not correspond to the local support domain. In this section, it is shown that the MQ-GRPIM with the parameters from section 7.5.1 is nevertheless able to achieve a good level of accuracy on the patch test (consistent with what has been achieved elsewhere in the literature). The tested patch consisted of a 5x5 grid of nodes, shown in Figure 7.13 below:

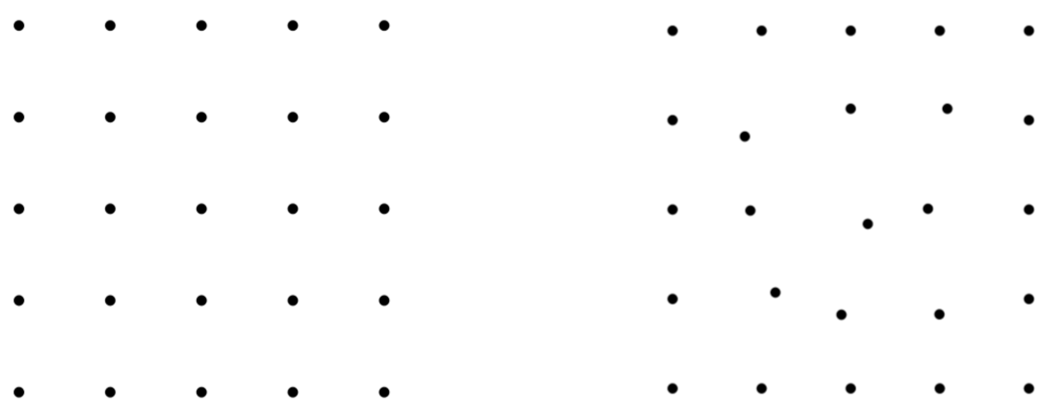

(a) Regular 5x5 grid *(b) Sample irregular 5x5 grid*

Figure 7.13: Grids used in the GRPIM patch test

The following linear displacement field was applied to the boundary nodes:

$$u_x(x,y) = 0.001\frac{(x+y)}{2} \tag{7.40-a}$$

$$u_y(x, y) = 0.001\frac{(y + x)}{2} \tag{7.40-b}$$

The results shown in Table 7.2 were obtained.

Table 7.2: GRPIM patch test results

Grid Type	$\boldsymbol{E_d}$	$\boldsymbol{E_e}$
Regular	1.73e-3	4.63e-3
Irregular	4.44e-3 (σ= 1.17e-3)	1.18e-2 (σ= 3.05e-3)

Comparing Table 7.2 to Table 7.1, it is evident that the errors for the patch test are similarly small or smaller than for the plate with a hole problem. The energy error norm for the regular grid patch test is only a fraction of a percent. As for the plate with a hole problem, the regular nodes produce better results than the irregular nodes for both error norms. Nevertheless, even for the highly irregular grids such as the one shown in Figure 9-b the error is still only around 1%. These figures are consistent with values reported in the literature [99, 100].

An alternative and original integration scheme is proposed in the following for use with the MQ-GRPIM, which is able to exactly pass the patch test. A search of the literature did not find any mention of this scheme to date. In the proposed scheme, in order to ensure that there are no discontinuities within a given integration domain, the integration domain and local support domains are set to be identical. This is done by:

1) Constructing a Voronoi tessellation of the domain (see Figure 6.5)

2) Triangulating each Voronoi polygon

3) Performing a Gauss integration over the resulting triangles

This scheme ensures that the support domain is constant within each integration domain. Discontinuities only occur on the polygon edges, on which no integration points are located. As long as a sufficient quadrature is used, the patch test can thus be passed exactly. For a 5x5 grid with extreme order quadrature ($N = 15$), the results presented in Table 7.3 were obtained:

Table 7.3: GRPIM patch test results using alternative integration scheme

Grid Type	E_d	E_e
Regular	1.2385e-12	2.6942e-12

These results prove that the patch test can be passed exactly, even for the nonconforming GRPIM, through use of clever numerical integration. However, the complex integration scheme and order of quadrature required do not make this a viable option in practice. Given the acceptable accuracy determined using the traditional quadrature method, the latter will be used in the rest of this work.

Reference is made here to a recently proposed extension of the RPIM method which ensures the conformability of the shape functions. This method, known as the Linearly Conforming GRPIM (LC-GRPIM) can pass the patch test exactly even when the integration domain and local support domains are not equal [107, 108]. Compatibility of the shape functions is universally ensured by means of constraints applied to the variational formulation. However, while the theory is relatively straightforward, this method is highly complex in terms of computational implementation. Furthermore, the gains in accuracy are relatively limited given the high level of accuracy that can already be achieved using the nonconforming GRPIM. It is therefore not implemented in this thesis, although it could potentially be implemented in future versions of the author’s computer code. It is reiterated that the inability of the nonconforming GRPIM to exactly pass the patch test does not destroy its convergence properties, as was shown in the convergence study in Figure 7.11. Stated more precisely by Liu: passing the patch test is sufficient but not a necessary condition for convergence [109].

7.5.3 Signorini-Hertz-Moreau problem

Finally, the HBB joint problem involves contact. In order to ensure that the MQ-GRPIM with the parameters of section 7.5.1 is able to achieve satisfactory performance for contact problems, the Signorini-Hertz-Moreau (HSM) problem was analyzed. This is a classical contact problem—one of few for which an analytical solution exists. In the HSM problem, a deformable, infinitely long cylinder undergoes unilateral, frictionless contact with a perfectly rigid plane. A point load F is applied to the top of the cylinder, as shown in Figure 7.14-a.

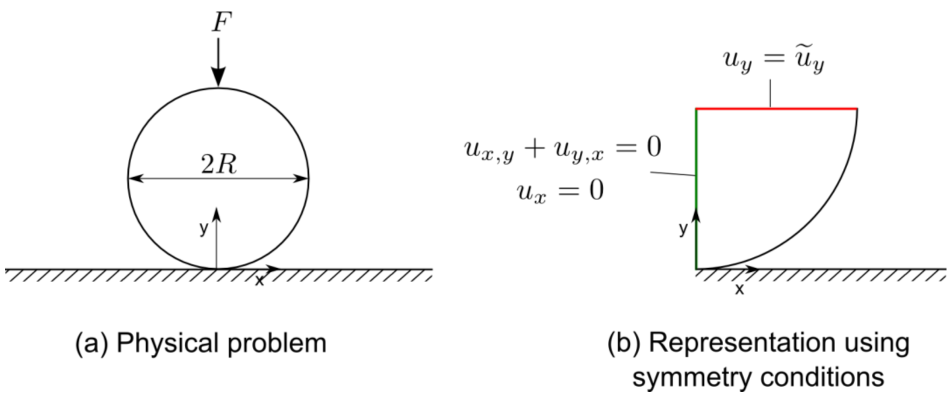

Figure 7.14: Hertz-Signorini-Moreau problem

The analytical solution to the HSM problem at a distance x from the origin is given as follows in Kikuchi and Oden [110]:

$$l_c = 2\sqrt{\frac{FR(1-\nu^2)}{E\pi}} \tag{7.41}$$

$$P_c = \frac{2F\sqrt{{l_c}^2 - x^2}}{\pi l_c} \tag{7.42}$$

where l_c is half the contact length (measured from the origin), F is the applied force and P_c is the contact pressure. The geometric and material parameters used were $R = 1$, $E =$ 2e+8 and $\nu = 0.3$.

For the MQ-GRPIM approximation to the analytical problem, a quarter of the cylinder was modelled, as shown in Figure 7.14-b. A symmetry condition was applied only to the left boundary and a displacement boundary condition was applied to the top boundary. This is akin to squeezing the cylinder between two rigid walls. The reaction force was hence obtained from the GRPIM solution. This force was applied in the analytical solution so that a direct comparison could be made between the two analyses. Three different displacements, corresponding to three different applied forces, were tested. The results are shown in Figure 7.15.

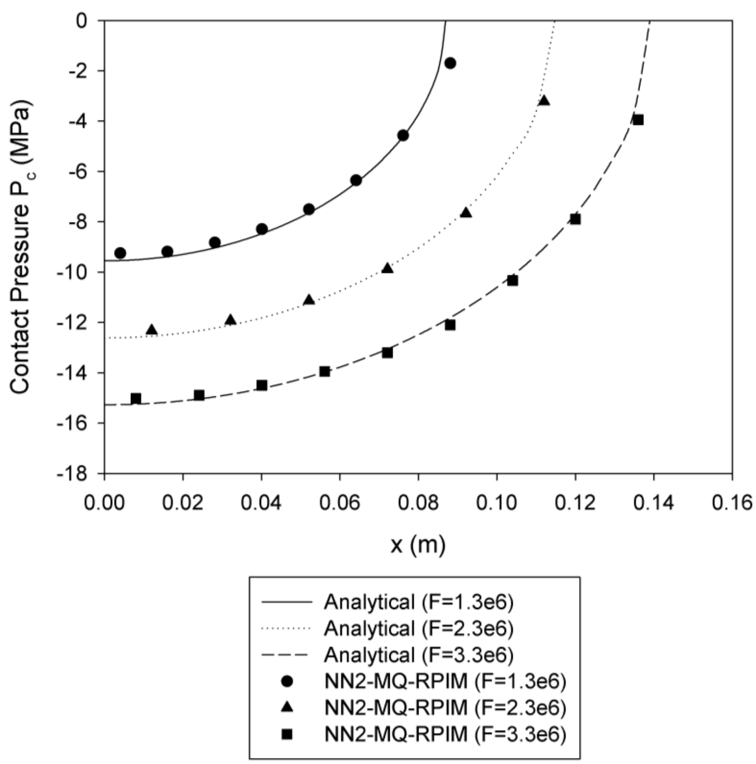

Figure 7.15: Comparison of Hertz-Signorini-Moreau solution obtained using NN2-MQ-RPIM and analytical solution.

Close agreement between the MQ-GRPIM with the optimized parameters and the analytical solution is evident. This supports the MQ-GRPIM's suitability for use in contact analyses with the optimized parameters of section 7.5.1.

Chapter 8: Meshless Solution of the Hybrid Bonded-Bolted Joint Model

The equations in Chapter 5 are called strong form equations. Considering the model formulation as a whole, they cannot be feasibly solved in an analytical form. Instead, in this chapter a numerical solution is obtained by casting the strong form equations into the weak form using the Principle of Virtual Displacements and substituting RPI functions for the displacement variables. The Newton-Raphson method is used to solve the resulting nonlinear system of equations.

8.1 Solution of Nonlinear Systems of Equations

Nonlinear systems of equations can be solved using a number of iterative techniques, of which the Newton-Raphson method is probably the most famous. A brief outline of this method is given in this section, based on the description in [111]. Consider a system of nonlinear equations with a potential solution vector $\mathbf{x}$:

$$F(\mathbf{x}) = 0 \tag{8.1}$$

Furthermore, let $\mathbf{x_0}$ denote the initial iterate, $\mathbf{x_n}$ the *n*th iterate and $\mathbf{x}^*$ the solution. Newton's method states that for certain functions and if the initial iterate is close enough to the solution, an improved approximation is:

$$\mathbf{x_{n+1}} = \mathbf{x_n} - \frac{F(\mathbf{x_n})}{F'(\mathbf{x_n})} \tag{8.2}$$

This adjustment is repeated until a sufficiently accurate solution is obtained:

$$\|\mathbf{x_{n+1}} - \mathbf{x_n}\| < e \tag{8.3}$$

where e is an arbitrary convergence tolerance. A geometric illustration of the method is provided in Figure 8.1. The Newton-Raphson method is used in the solution presented in this chapter due to its simplicity and renowned quadratic convergence property.

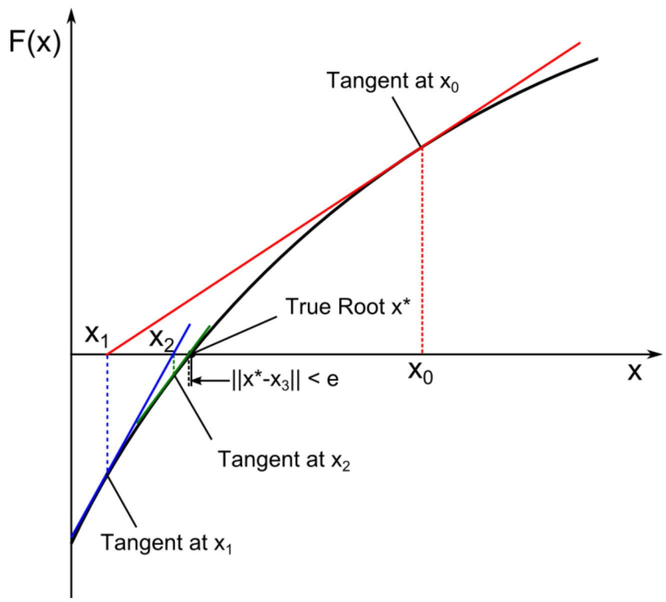

Figure 8.1: Geometric illustration of the Newton-Raphson method

8.2 Temporal Discretization of the HBB Joint Model

Due to the incremental nature of the adhesive elastoplastic constitutive equations, a time discretization of the model equations must be made. Specifically, a strain-driven problem is considered such that strain is a function of time in the interval $[0, T] = \cup_{n=0}^{N} [t_n, t_{n+1}]$. It is remarked that for the static analysis considered, time is generic since the structural response is in fact time independent. t thus merely denotes the load level. Following the principle of virtual work described in Chapter 7, at time t_n there is the equilibrium state:

$$\delta^{t_n}\mathbf{U}^{\mathrm{T}}\left({}^{t_n}\mathbf{F}^{\mathrm{int}} - {}^{t_n}\mathbf{F}^{\mathrm{ext}}\right) = 0 \tag{8.4}$$

Since the variations $\delta^{t_n}\mathbf{U}^{\mathrm{T}}$ are arbitrary:

$$^{t_n}\mathbf{F}^{\text{int}} - {}^{t_n}\mathbf{F}^{\text{ext}} = \mathbf{0} \tag{8.5}$$

where $\mathbf{F}^{\text{ext}}$ are the external forces and $\mathbf{F}^{\text{int}}$ are the internal forces. Eqn. (8.5) is the basis for all nonlinear analysis in continuum mechanics. From this equilibrium state, a load increment may be applied which is assumed to be independent of the displacement:

$$^{t_{n+1}}\mathbf{F}^{\text{ext}} = {}^{t_n}\mathbf{F}^{\text{ext}} + \Delta\mathbf{F}^{\text{ext}} \tag{8.6}$$

And the displacement increases in response to this load increment as:

$$^{t_{n+1}}\mathbf{U} = {}^{t}\mathbf{U} + \Delta\mathbf{U} \tag{8.7}$$

The objective is thus to calculate the displacement increment $\Delta\mathbf{U}$ such that at time t_{n+1}, Eqn. (8.5) is satisfied. To achieve this, a nonlinear solution technique, such as the Newton-Raphson technique described in section 8.1, must be used (since the internal force is a nonlinear function of the displacement). Correspondingly, a linearization of Eqn. (8.5) must be made. The linearized equations for the various HBB joint components are derived in the following sections, departing from their respective weak forms.

8.3 Weak Form Equations

Consider a HBB joint in a state of equilibrium. The internal virtual work due to the unrelated states (1) displacements $\boldsymbol{u}^*$ with consistent strains $\boldsymbol{\varepsilon}^*$ and (2) internal stresses $\boldsymbol{\sigma}$ with tractions $\boldsymbol{T}$ can be stated as follows for the various joint components. For the plates, the internal virtual work is:

$$\delta W_i^{(i)} = 2h^{(i)} \int_{\mathrm{A}^{(i)}} \boldsymbol{\varepsilon}^{*(i)^T} \boldsymbol{\sigma}^{(i)} dA \quad : \quad i \in \{1,2\} \tag{8.8}$$

For the adhesive it is:

$$\delta W_i^{(a)} = t_a \int_{\mathrm{A}^{(a)}} \boldsymbol{\varepsilon}^{*(a)^T} \boldsymbol{\sigma}^{(a)} dA \tag{8.9}$$

For the bolt it is:

$$\delta W_i^{(B_j)} = \int_{l^{(B_j)}} \boldsymbol{\varepsilon}^{*(b)^T} \boldsymbol{\sigma}^{(b)} ds \quad : \quad j \in [1, N_B] \tag{8.10}$$

And for the bolthead springs it is:

$$\delta W_i^{(S_j^i)} = \left[\delta\Delta\theta_x^{(S_j^i)}\right] k_{\theta x} \left[\Delta\theta_x^{(S_j^i)}\right] + \left[\delta\Delta\theta_y^{(S_j^i)}\right] k_{\theta y} \left[\Delta\theta_y^{(S_j^i)}\right] \quad : \quad i \in \{1,2\}, j \in [1, N_B] \tag{8.11}$$

where N_B is the number of bolts. The relative bolthead rotations $\Delta\theta_x^{S_j^i}$ and $\Delta\theta_y^{S_j^i}$ are:

$$\Delta\theta_x^{S_j^i} = \theta_x^{H_j^i} - \theta_x^{B_j^i} \tag{8.12}$$

$$\Delta\theta_y^{S_j^i} = \theta_x^{H_j^i} - \theta_x^{B_j^i} \tag{8.13}$$

Ignoring body forces, the external virtual work due to applied tractions $\mathbf{T}^{(i)}$ is:

$$\delta W_e = \int_{\Gamma^{(i)}} \mathbf{u}^{*(i)^T} \mathbf{T}^{(i)} d\Gamma \quad : \quad i \in \{1,2,a,B_j\} \tag{8.14}$$

In Eqn. 8.14, $\Gamma^{(i)}$ denotes the external boundaries of the model. Following the principle of virtual displacements, $\mathbf{u}^* \equiv \delta\mathbf{u}$ and $\boldsymbol{\varepsilon}^* \equiv \delta\boldsymbol{\varepsilon}$**.**

8.4 Discrete Weak Form

Using the meshless shape functions described in the previous two chapters, an approximation of the displacement field can be constructed as follows for the *i*th plate or bolt:

$$u_{\boldsymbol{x}}^{(i)} = \boldsymbol{\Phi}^{(i)}\overline{\mathbf{U}}_{\boldsymbol{x}}^{(i)} \tag{8.15}$$

$$u_{\boldsymbol{y}}^{(i)} = \boldsymbol{\Phi}^{(i)}\overline{\mathbf{U}}_{\boldsymbol{y}}^{(i)} \tag{8.16}$$

$$u_{\boldsymbol{z}}^{(i)} = \boldsymbol{\Phi}^{(i)}\overline{\mathbf{U}}_{\boldsymbol{z}}^{(i)} \tag{8.17}$$

$$\theta_{\boldsymbol{x}}^{(i)} = \boldsymbol{\Phi}^{(i)}\overline{\boldsymbol{\Theta}}_{\boldsymbol{x}}^{(i)} \tag{8.18}$$

$$\theta_{\boldsymbol{y}}^{(i)} = \boldsymbol{\Phi}^{(i)}\overline{\boldsymbol{\Theta}}_{\boldsymbol{y}}^{(i)} \tag{8.19}$$

where $i \in \{1,2,B_j\}$. $\overline{\mathbf{U}}_{\boldsymbol{x}}^{(i)}$, $\overline{\mathbf{U}}_{\boldsymbol{y}}^{(i)}$, … are the nodal solution vectors:

$$\begin{gathered}\overline{\mathbf{U}}_{\boldsymbol{x}}^{(i)\mathrm{T}} = \{\mathrm{U_{x1}} \quad \mathrm{U_{x2}} \quad \cdots \quad \mathrm{U}_{xN^{(i)}}\} \ \boldsymbol{,} \ \overline{\mathbf{U}}_{\boldsymbol{y}}^{(i)\mathrm{T}} = \{\mathrm{U_{y1}} \quad \mathrm{U_{y2}} \quad \cdots \quad \mathrm{U}_{yN^{(i)}}\} \\ \overline{\mathbf{U}}_{\boldsymbol{z}}^{(i)\mathrm{T}} = \{\mathrm{U_{z1}} \quad \mathrm{U_{z2}} \quad \cdots \quad \mathrm{U}_{zN^{(i)}}\} \ \boldsymbol{,} \ \overline{\boldsymbol{\Theta}}_{\boldsymbol{x}}^{(i)\mathrm{T}} = \{\Theta_{\mathrm{x1}} \quad \Theta_{\mathrm{x2}} \quad \cdots \quad \Theta_{xN^{(i)}}\} \\ \overline{\boldsymbol{\Theta}}_{\boldsymbol{y}}^{(i)\mathrm{T}} = \{\Theta_{\mathrm{y1}} \quad \Theta_{\mathrm{y2}} \quad \cdots \quad \Theta_{yN^{(i)}}\}\end{gathered} \tag{8.20}$$

$N^{(i)}$ is the number of nodes and of course $\boldsymbol{\Phi}^{(i)}$ are the meshless shape functions. These approximations shall be substituted into the weak forms (8.8-8.11) to obtain the discrete weak form equations.

8.4.1 Plates Discrete Weak Form

The internal virtual work expression for the *i*th plate can be expressed as:

$$\delta W_i^{(i)} = 2h^{(i)} \int_{A^{(i)}} \delta \bar{\boldsymbol{\varepsilon}}^{(i)^T} \bar{\boldsymbol{C}}^{(i)} \bar{\boldsymbol{\varepsilon}}^{(i)} \, dA \tag{8.21}$$

where:

$$\bar{\boldsymbol{\varepsilon}}^{(i)} = \begin{Bmatrix} \boldsymbol{\varepsilon} \\ \boldsymbol{\kappa} \\ \boldsymbol{\gamma} \end{Bmatrix}^{(i)} \quad , \quad \bar{\boldsymbol{C}}^{(i)} = \begin{bmatrix} \mathbf{A} & \mathbf{B} & \mathbf{0} \\ \mathbf{B} & \mathbf{D} & \mathbf{0} \\ \mathbf{0} & \mathbf{0} & \mathbf{G} \end{bmatrix}^{(i)} \tag{8.22}$$

The strain vector can at this stage be discretely written in terms of the plate solution vector as:

$$\bar{\boldsymbol{\varepsilon}}^{(i)} = \mathbf{B}^{(i)} \bar{\mathbf{U}}^{(i)} \tag{8.23}$$

where the strain-displacement matrix, in accordance with Eqn. 5.5, is:

$$\mathbf{B}^{(i)} = \begin{bmatrix} \boldsymbol{\Phi}_{,x}^{\mathrm{T}} & \mathbf{0} & \mathbf{0} & \mathbf{0} & \mathbf{0} \\ \mathbf{0} & \boldsymbol{\Phi}_{,y}^{\mathrm{T}} & \mathbf{0} & \mathbf{0} & \mathbf{0} \\ \boldsymbol{\Phi}_{,y}^{\mathrm{T}} & \boldsymbol{\Phi}_{,x}^{\mathrm{T}} & \mathbf{0} & \mathbf{0} & \mathbf{0} \\ \mathbf{0} & \mathbf{0} & \mathbf{0} & -\boldsymbol{\Phi}_{,x}^{\mathrm{T}} & \mathbf{0} \\ \mathbf{0} & \mathbf{0} & \mathbf{0} & \mathbf{0} & -\boldsymbol{\Phi}_{,y}^{\mathrm{T}} \\ \mathbf{0} & \mathbf{0} & \mathbf{0} & -\boldsymbol{\Phi}_{,y}^{\mathrm{T}} & -\boldsymbol{\Phi}_{,x}^{\mathrm{T}} \\ \mathbf{0} & \mathbf{0} & \boldsymbol{\Phi}_{,x}^{\mathrm{T}} & -\boldsymbol{\Phi}^{\mathrm{T}} & \mathbf{0} \\ \mathbf{0} & \mathbf{0} & \boldsymbol{\Phi}_{,y}^{\mathrm{T}} & \mathbf{0} & -\boldsymbol{\Phi}^{\mathrm{T}} \end{bmatrix}^{(i)} : i \in \{1,2\}$$

And the plate solution vector is:

$$\bar{\mathbf{U}}^{(i)\mathrm{T}} = \left\{ \bar{\mathbf{U}}_{\boldsymbol{x}}^{(i)}, \quad \bar{\mathbf{U}}_{\boldsymbol{y}}^{(i)}, \quad \bar{\mathbf{U}}_{\boldsymbol{z}}^{(i)}, \quad \bar{\boldsymbol{\Theta}}_{\boldsymbol{x}}^{(i)}, \quad \bar{\boldsymbol{\Theta}}_{\boldsymbol{y}}^{(i)} \right\} : i \in \{1,2,b\} \tag{8.24}$$

Substituting 8.23 into 8.21 results in the following discrete internal work weak form:

$$\delta W^{(i)} = \delta \bar{\mathbf{U}}^{(i)\mathrm{T}} \int_{dV} \mathbf{B}^{(i)^{\mathrm{T}}} \mathbf{C}^{(i)} \mathbf{B}^{(i)} \, dV \bar{\mathbf{U}}^{(i)} = \delta \bar{\mathbf{U}}^{(i)\mathrm{T}} \mathbf{K}^{(i)} \bar{\mathbf{U}}^{(i)} \tag{8.25}$$

where the plate stiffness matrix $\mathbf{K}^{(i)}$ is defined as:

$$\mathbf{K}^{(i)} = 2h^{(i)} \int_{A^{(i)}} \mathbf{B}^{(i)^{\mathrm{T}}} \mathbf{C}^{(i)} \mathbf{B}^{(i)} \, dA \tag{8.26}$$

A uniformly distributed tensile load N_x applied to the $\partial_R \Omega$ boundary results in the following external work for the lower plate:

$$\delta W_e^{(2)} = \int_{\partial_R \Omega} N_x \, \mathbf{H}_{\boldsymbol{x}} \delta \bar{\mathbf{U}}^{(i)} d\Gamma = \mathbf{P}^{(2)} \delta \bar{\mathbf{U}}^{(i)} \tag{8.27}$$

where $\mathbf{H}_{\boldsymbol{x}}$ relates u_x to the plate solution vector and is:

$$\mathbf{H}_{\boldsymbol{x}} = \{\boldsymbol{\Phi}^{\mathrm{T}}, \mathbf{0}, \mathbf{0}, \mathbf{0}, \mathbf{0}\} \tag{8.28}$$

and the lower plate force vector $\mathbf{P}^{(2)}$ is:

$$\mathbf{P}^{(2)} = \int_{\partial_R \Omega} N_x \, \mathbf{H}_{\boldsymbol{x}} d\Gamma \tag{8.29}$$

The overall discrete plate weak form is therefore:

$$\delta G^{(p)} = \delta W_i^{(1)} + \delta W_i^{(2)} + \delta W_e^{(2)} \tag{8.30}$$

8.4.2 Adhesive Discrete Weak Form

The adhesive strains depend on the displacements of both the upper and lower plate (thereby structurally coupling these two components). Since there are no external tractions applied to the adhesive directly, the discrete weak form expression is equal to the internal virtual work:

$$\delta G^{(a)} = t_a \int_{A^{(i)}} \delta \boldsymbol{\varepsilon}^{(a)^{\mathrm{T}}} \boldsymbol{\sigma}^{(a)} dA = 0 \tag{8.31}$$

The strain vector can again be written in terms of the plate nodal solution vectors as:

$$\boldsymbol{\varepsilon}^{(a)} = \mathbf{B}^{(a)} \overline{\mathbf{U}} \tag{8.32}$$

where:

$$\mathbf{B}^{(a)} = \frac{1}{2} \begin{bmatrix} \mathbf{\Phi}_{,x}^{\mathrm{T}} & \mathbf{0} & \mathbf{0} & h_1 \mathbf{\Phi}_{,x}^{\mathrm{T}} & \mathbf{0} & \mathbf{\Phi}_{,x}^{\mathrm{T}} & \mathbf{0} & \mathbf{0} & -h_2 \mathbf{\Phi}_{,x}^{\mathrm{T}} & \mathbf{0} \\ \mathbf{0} & \mathbf{\Phi}_{,y}^{\mathrm{T}} & \mathbf{0} & \mathbf{0} & h_1 \mathbf{\Phi}_{,y}^{\mathrm{T}} & \mathbf{0} & \mathbf{\Phi}_{,y}^{\mathrm{T}} & \mathbf{0} & \mathbf{0} & -h_2 \mathbf{\Phi}_{,y}^{\mathrm{T}} \\ \mathbf{0} & \mathbf{0} & \frac{2}{t_a} \mathbf{\Phi}^{\mathrm{T}} & \mathbf{0} & \mathbf{0} & \mathbf{0} & \mathbf{0} & -\frac{2}{t_a} \mathbf{\Phi}^{\mathrm{T}} & \mathbf{0} & \mathbf{0} \\ \mathbf{\Phi}_{,y}^{\mathrm{T}} & \mathbf{\Phi}_{,x}^{\mathrm{T}} & \mathbf{0} & h_1 \mathbf{\Phi}_{,y}^{\mathrm{T}} & h_1 \mathbf{\Phi}_{,x}^{\mathrm{T}} & \mathbf{\Phi}_{,y}^{\mathrm{T}} & \mathbf{\Phi}_{,x}^{\mathrm{T}} & \mathbf{0} & -h_2 \mathbf{\Phi}_{,y}^{\mathrm{T}} & -h_2 \mathbf{\Phi}_{,x}^{\mathrm{T}} \\ \frac{2}{t_a} \mathbf{\Phi}^{\mathrm{T}} & \mathbf{0} & \mathbf{0} & \frac{2h_1}{t_a} \mathbf{\Phi}_{,x}^{\mathrm{T}} & \mathbf{0} & -\frac{2}{t_a} \mathbf{\Phi}^{\mathrm{T}} & \mathbf{0} & \mathbf{0} & \frac{2h_2}{t_a} \mathbf{\Phi}_{,x}^{\mathrm{T}} & \mathbf{0} \\ \mathbf{0} & \frac{2}{t_a} \mathbf{\Phi}^{\mathrm{T}} & \mathbf{0} & \mathbf{0} & \frac{2h_1}{t_a} \mathbf{\Phi}_{,y}^{\mathrm{T}} & \mathbf{0} & -\frac{2}{t_a} \mathbf{\Phi}^{\mathrm{T}} & \mathbf{0} & \mathbf{0} & \frac{2h_2}{t_a} \mathbf{\Phi}_{,y}^{\mathrm{T}} \end{bmatrix} \tag{8.33}$$

Substituting 8.32 into 8.31, the adhesive discrete weak form expression is obtained as follows:

$$\delta G^{(a)} = \delta \overline{\mathbf{U}}^{\mathrm{T}} \int_{dV} \mathbf{B}^{(a)^{\mathrm{T}}} \boldsymbol{\sigma}^{(a)} dV \tag{8.34}$$

Note that $\overline{\mathbf{U}}$ is an overall plate nodal solution vector that combines the individual upper and lower plate solution vectors:

$$\overline{\mathbf{U}}^{\mathrm{T}} = \left\{ \overline{\mathbf{U}}^{(1)\mathrm{T}}, \overline{\mathbf{U}}^{(2)\mathrm{T}} \right\} \tag{8.35}$$

8.4.3 Bolts Discrete Weak Form

Based on Eqns. (5.25) and (8.10), the weak form of the bolts can be written as:

$$\begin{aligned}\delta G^{(B_j)} &= \int_{dV} \delta \boldsymbol{\epsilon}^{(B_j)^T} \left[\mathbf{C}^{(B_j)} \boldsymbol{\epsilon}^{(B_j)} + \mathbf{S}_{\mathbf{0}}^{(B_j)} \right] dV \\ &= \int_{l^{(B_j)}} \delta \overline{\boldsymbol{\varepsilon}}^{(B_j)^T} \boldsymbol{C}^{(B_j)} \overline{\boldsymbol{\varepsilon}}^{(B_j)}\, dL + A^{(B_j)} \int_{V} \delta \overline{\boldsymbol{\varepsilon}}^{(B_j)^T} \mathbf{S}_{\mathbf{0}}^{(B_j)} dV\end{aligned} \tag{8.36}$$

where $A^{(B_j)}$ is the cross-sectional area of the jth bolt and $\overline{\boldsymbol{\varepsilon}}^{(B_j)}$ and $\boldsymbol{C}^{(B_j)}$ are:

$$\overline{\boldsymbol{\varepsilon}}^{(B_j)} = \begin{Bmatrix} \varepsilon_{zz} \\ \kappa_x \\ \kappa_y \\ \gamma_{xz} \\ \gamma_{yz} \end{Bmatrix}^{(B_j)} , \quad \mathbf{C}^{(B_j)} = \begin{bmatrix} EA & 0 & 0 & 0 & 0 \\ 0 & EI & 0 & 0 & 0 \\ 0 & 0 & EI & 0 & 0 \\ 0 & 0 & 0 & k\mu A & 0 \\ 0 & 0 & 0 & 0 & k\mu A \end{bmatrix}^{(B_j)} \tag{8.37}$$

The strain, once again, can be written discretely in terms of the plate solution vector as:

$$\overline{\boldsymbol{\varepsilon}}^{(B_j)} = \mathbf{B}^{(B_j)} \overline{\mathbf{U}}^{(B_j)} \tag{8.38}$$

where the bolt strain-displacement matrix is:

$$\mathbf{B}^{(B_j)} = \begin{bmatrix} \boldsymbol{\Phi}_{,z}^{\mathrm{T}} & \mathbf{0} & \mathbf{0} & \mathbf{0} & \mathbf{0} \\ \mathbf{0} & \mathbf{0} & \mathbf{0} & \boldsymbol{\Phi}_{,z}^{\mathrm{T}} & \mathbf{0} \\ \mathbf{0} & \mathbf{0} & \mathbf{0} & \mathbf{0} & \boldsymbol{\Phi}_{,z}^{\mathrm{T}} \\ \mathbf{0} & \boldsymbol{\Phi}_{,z}^{\mathrm{T}} & \mathbf{0} & \boldsymbol{\Phi}^{\mathrm{T}} & \mathbf{0} \\ \mathbf{0} & \mathbf{0} & \boldsymbol{\Phi}_{,z}^{\mathrm{T}} & \mathbf{0} & \boldsymbol{\Phi}^{\mathrm{T}} \end{bmatrix}^{(B_j)} \tag{8.39}$$

and the bolt solution vector is:

$$\overline{\mathbf{U}}^{(B_j)\mathrm{T}} = \left\{\overline{\mathbf{U}}_{\boldsymbol{x}}^{(B_j)}, \quad \overline{\mathbf{U}}_{\boldsymbol{y}}^{(B_j)}, \quad \overline{\mathbf{U}}_{\boldsymbol{z}}^{(B_j)}, \quad \overline{\mathbf{\Theta}}_{\boldsymbol{x}}^{(B_j)}, \quad \overline{\mathbf{\Theta}}_{\boldsymbol{y}}^{(B_j)}\right\} \quad : \quad j \in [1, N_B] \tag{8.40}$$

Substituting (8.38) into (8.36) results in the following discrete weak form:

$$\delta G^{(B_j)} = \delta\overline{\mathbf{U}}^{(B_j)\mathrm{T}}\mathbf{K}^{(B_j)}\overline{\mathbf{U}}^{(B_j)} + \delta\overline{\mathbf{U}}^{(B_j)\mathrm{T}}\mathbf{P}^{(B_j)} \tag{8.41}$$

In Eqn. (8.41), the *j*th bolt stiffness matrix $\mathbf{K}^{(B_j)}$ is thus defined as:

$$\mathbf{K}^{(B_j)} = \int_{l^{(B_j)}} \boldsymbol{B}^{(B_j)^{\mathrm{T}}}\mathbf{C}^{(B_j)}\boldsymbol{B}^{(B_j)}\, dL \tag{8.42}$$

and the bolt clamp-up vector is:

$$\mathbf{P}^{(B_j)} = A^{(B_j)} \int_{l^{(B_j)}} \boldsymbol{B}^{(B_j)^{\mathrm{T}}}\mathbf{S}_{\mathbf{0}}^{(B_j)}\, dL \tag{8.43}$$

8.4.4 Bolthead Springs Discrete Weak Form

The matrix relating the relative bolthead rotation to the nodal solution vectors of the bolt and the bolthead degrees of freedom can be stated as:

$$\mathbf{H}^{\boldsymbol{B_j}} = \begin{bmatrix} \mathbf{H}_{\boldsymbol{x}}^{\mathbf{1}} & \mathbf{0} & -1 & 0 & 0 & 0 \\ \mathbf{0} & \mathbf{H}_{\boldsymbol{x}}^{\mathbf{2}} & 0 & -1 & 0 & 0 \\ \mathbf{H}_{\boldsymbol{x}}^{\mathbf{2}} & \mathbf{0} & 0 & 0 & -1 & 0 \\ \mathbf{0} & \mathbf{H}_{\boldsymbol{x}}^{\mathbf{2}} & 0 & 0 & 0 & -1 \end{bmatrix} \tag{8.44}$$

where:

$$\mathbf{H}_{\boldsymbol{x}}^{\mathbf{1}} = \left\{\mathbf{\Phi}^{\mathrm{T}}\left(l^{(B_j)}\right), \mathbf{0}, \mathbf{0}, \mathbf{0}, \mathbf{0}\right\}^{(B_j)} \quad , \quad \mathbf{H}_{\boldsymbol{x}}^{\mathbf{2}} = \{\mathbf{\Phi}^{\mathrm{T}}(0), \mathbf{0}, \mathbf{0}, \mathbf{0}, \mathbf{0}\}^{(B_j)} \tag{8.45}$$

$$\mathbf{H}_{\boldsymbol{y}}^{\mathbf{1}} = \left\{\mathbf{0}, \mathbf{\Phi}^{\mathrm{T}}\left(l^{(B_j)}\right), \mathbf{0}, \mathbf{0}, \mathbf{0}\right\}^{(B_j)} \quad , \quad \mathbf{H}_{\boldsymbol{y}}^{\mathbf{2}} = \{\mathbf{0}, \mathbf{\Phi}^{\mathrm{T}}(0), \mathbf{0}, \mathbf{0}, \mathbf{0}\}^{(B_j)} \tag{8.46}$$

Consequently, the relative bolthead rotations at the top of the bolt and bottom of the *j*th bolt, respectively, can be expressed in discrete form as:

$$\Delta\boldsymbol{\theta}^{(S_j)} = \left\{\Delta\theta_x^{S_j^1} \quad \Delta\theta_x^{S_j^2} \quad \Delta\theta_y^{S_j^1} \quad \Delta\theta_y^{S_j^2}\right\}^{\mathrm{T}} = \mathbf{H}^{\boldsymbol{B}_j}\mathbf{U}^{(B_j)} \tag{8.47}$$

where $\mathbf{U}^{(B_j)}$ is a combined solution vector that collects the solution vectors for the *j*th bolt and associated bolthead spring degrees of freedom:

$$\mathbf{U}^{(B_j)} = \left\{\overline{\mathbf{U}}^{(B_j)\mathrm{T}}, \theta_x^{B_j^1}, \theta_x^{B_j^2}, \theta_y^{B_j^1}, \theta_y^{B_j^2}\right\}^{\mathrm{T}} \tag{8.48}$$

Substituting Eqn. (8.47) into the weak form (8.11), the final bolthead spring discrete weak form is obtained:

$$\delta W_i^{\left(S_j^i\right)} = \delta\mathbf{U}^{(B_j)\mathrm{T}}\boldsymbol{k_\theta}\mathbf{U}^{(B_j)} \tag{8.49}$$

where the spring stiffness matrix $\boldsymbol{k_\theta}$ is defined as:

$$\boldsymbol{k_\theta} = \begin{bmatrix} k_{\theta x} & 0 & 0 & 0 \\ 0 & k_{\theta y} & 0 & 0 \\ 0 & 0 & k_{\theta x} & 0 \\ 0 & 0 & 0 & k_{\theta y} \end{bmatrix} \tag{8.50}$$

8.5 Consistent Linearization of the Discrete Weak Form

8.5.1 Linearization of the Adhesive Weak Form

In order to iteratively solve the nonlinear weak form using the Newton-Raphson method, it must be linearized. The adhesive weak form will be linearized first, since this is the only joint component for which plasticity is considered and is in fact one the main sources of nonlinearity in the model. It is recalled that $\boldsymbol{\sigma}^{(a)}$ is required to satisfy the local constitutive equations of associative J_2 plasticity. Given a displacement increment $\Delta\bar{\mathbf{U}}$ in some iteration k of the Newton-Raphson algorithm, and the corresponding strain increment $\Delta\boldsymbol{\varepsilon}^{(a)}$, the stress in the adhesive can be updated as described in Box 8.1. This is a local state updating algorithm called the return mapping algorithm which, for a given strain increment at a point, updates the plastic strain, stress and internal variables at that point in a manner that is consistent with Eqns. (5.17-5.19).

Box 8.1: Return mapping algorithm for associative J_2 plasticity [112]

Return mapping algorithm for associative J_2 plasticity

1) Given the strain field at $\mathbf{x} \in \Omega$: $\boldsymbol{\varepsilon}_{n+1} = \boldsymbol{\varepsilon}_n + \Delta\boldsymbol{\varepsilon}_n$

2) Compute the elastic trial stress and test for plastic loading

$$\boldsymbol{\sigma}_{n+1}^{trial} = C\!:\left(\boldsymbol{\varepsilon}_{n+1} - \boldsymbol{\varepsilon}_n^p\right)$$

$$f_{n+1}^{trial} = \left|\boldsymbol{\sigma}_{n+1}^{trial}\right| - \left[\sigma_y + H\alpha_n\right]$$

IF $f_{n+1}^{trial} \leq 0$ THEN

Elastic step: $(\cdot)_{n+1} = (\cdot)_{n+1}^{trial}$ and EXIT

ELSE

Plastic step: Proceed to step 3

END

3) Return mapping

$$\Delta\gamma = \left(\frac{f_{n+1}^{trial}}{3\mu + H}\right) > 0$$

$$\bar{\boldsymbol{N}}_{n+1} = \frac{\boldsymbol{s}_{n+1}^{trial}}{\left\|\boldsymbol{s}_{n+1}^{trial}\right\|}$$

$$\boldsymbol{\varepsilon}_{n+1}^p = \boldsymbol{\varepsilon}_n^p + \Delta\gamma\bar{\boldsymbol{N}}_{n+1}$$

$$\alpha_{n+1} = \alpha_n + \sqrt{\tfrac{2}{3}}\Delta\gamma$$

$$\boldsymbol{e}_{n+1} = \boldsymbol{\varepsilon}_{n+1} - \tfrac{1}{3}\mathrm{tr}(\boldsymbol{\varepsilon}_{n+1})$$

$$\boldsymbol{\sigma}_{n+1} = \kappa(tr[\boldsymbol{\varepsilon}_{n+1}])\mathbf{1} + 2\mu(\boldsymbol{e}_{n+1} - \Delta\gamma \boldsymbol{N}_{n+1})$$

Derivation of the equations in Box 8.1 can be found in e.g. [112, 113]. At this juncture and throughout the rest of this subsection, the superscript (k) will be adopted to denote that a field variable belongs to the *k*th iteration of the Newton-Raphson algorithm. To avoid confusion, the (a) superscript is dropped and the reader is expected to remember that the various variables and matrices in this subsection refer to the adhesive. The linearization is performed about the current state, defined by $\bar{\mathbf{U}}_{n+1}^{(k)}$. First, the Jacobian of the adhesive weak form δG is obtained by the Chain rule as follows:

$$\begin{aligned} D\delta G^{(k)} = \frac{\partial \delta G^{(k)}}{\partial \bar{\mathbf{U}}_{n+1}^{(k)}} &= \delta\bar{\mathbf{U}}^{\mathrm{T}} \int_V \mathbf{B}^{\mathrm{T}} \left[\frac{\partial \boldsymbol{\sigma}_{n+1}^{(k)}}{\partial \boldsymbol{\varepsilon}_{n+1}^{(k)}}\right] \frac{\partial \boldsymbol{\varepsilon}_{n+1}^{(k)}}{\partial \bar{\mathbf{U}}_{n+1}^{(k)}} dV \\ &= \delta\bar{\mathbf{U}}^{\mathrm{T}} \int_V \mathbf{B}^{\mathrm{T}} \left[\frac{\partial \boldsymbol{\sigma}_{n+1}^{(k)}}{\boldsymbol{\varepsilon}_{n+1}^{(k)}}\right] \mathbf{B} dV \end{aligned} \tag{8.51}$$

The matrix $\mathbf{K_T}_{n+1}^{(k)}$ can now be introduced:

$$\mathbf{K_T}_{n+1}^{(k)} = \int_V \mathbf{B}^{(a)^T} \left[\frac{\partial \boldsymbol{\sigma}_{n+1}^{(k)}}{\partial \boldsymbol{\varepsilon}_{n+1}^{(k)}}\right] \mathbf{B}^{(a)} dV \tag{8.52}$$

This is known as the adhesive tangent stiffness matrix. The missing item required to be able to calculate $\mathbf{K_T}_{n+1}^{(k)}$ is an explicit expression for the coefficient:

$$\mathbf{C}_{n+1}^{(k)} = \left[\frac{\partial \boldsymbol{\sigma}_{n+1}^{(k)}}{\partial \boldsymbol{\varepsilon}_{n+1}^{(k)}}\right] \tag{8.53}$$

$\mathbf{C}_{n+1}^{(k)}$ is also called the algorithmic tangent modulus, since it is the derivative of the algorithmic expression $\boldsymbol{\sigma}_{n+1}^{(k)}$. Recalling from Box 8.1 that the general update formula for the stress tensor for associative J_2 plasticity is given by:

$$\boldsymbol{\sigma}_{n+1}^{(k)} = \kappa\left(tr\left[\boldsymbol{\varepsilon}_{n+1}^{(k)}\right]\right)\mathbf{1} + 2\mu\left(\boldsymbol{e}_{n+1}^{(k)} - \Delta\gamma\boldsymbol{N}_{n+1}\right) \tag{8.54}$$

Differentiating this with respect to the strain tensor gives the expression for the algorithmic tangent modulus:

$$\boldsymbol{C}_{n+1}^{(k)} = \kappa\mathbf{1}\otimes\mathbf{1} + 2\mu\left[\boldsymbol{I} - \mathbf{1}\otimes\mathbf{1} - \frac{\boldsymbol{N}_{n+1}\otimes\boldsymbol{N}_{n+1}}{1+\frac{H}{3\mu}}\right] \tag{8.55}$$

And

$$\mathbf{K_T}_{n+1}^{(k)} = \int\limits_V \mathbf{B}^{(a)^T}\boldsymbol{C}_{n+1}^{(k)}\mathbf{B}^{(a)}dV \tag{8.56}$$

Substituting the Jacobian (Eqn. (8.51)) into a linear approximation of the weak form, the linearized discrete weak form of the adhesive in the *k*th iteration of a particular load increment in the Newton-Raphson algorithm is thus:

$$\delta W_i^{(k)} - \delta W_e^{(k)} + \delta\overline{\mathbf{U}}^{\mathrm{T}}\mathbf{K_T}_{n+1}^{(k)}\Delta\overline{\mathbf{U}}_{n+1}^{(k+1)} = 0 \tag{8.57}$$

8.5.2 Linearization of the Plate Weak Form

Next, linearization of the weak form of the plates is considered. This linearization is trivial since the plate constitutive equations are linear elastic. Taking the Jacobian of $\delta G^{(i)}$ in the *k*th iteration with respect to the displacement increment results in the following tangent modulus:

$$\mathbf{C}_{n+1}^{(k)} = \left[\frac{\partial \boldsymbol{\sigma}_{n+1}^{(k)}}{\partial \boldsymbol{\varepsilon}_{n+1}^{(k)}}\right] = \mathbf{C}^{(i)} \tag{8.58}$$

Therefore, the tangent modulus is simply the elastic modulus and the tangent stiffness matrix is equal to the elastic stiffness matrix defined in section 8.4.1. It is easily shown that the linearized weak form is thus:

$$\delta W_i^{(i)} - \delta W_e^{(i)} + \delta \overline{\mathbf{U}}^{(i)\mathrm{T}} \mathbf{K}^{(i)} \Delta \overline{\mathbf{U}}^{(i)}{}_{n+1}^{(k+1)} = 0 \tag{8.59}$$

8.5.3 Linearization of Bolts Weak Form

As for the plates, the tangent modulus is simply the elastic modulus. The linearized weak form is simply:

$$\delta W_i^{(B_j)} - \delta W_e^{(B_j)} + \delta \overline{\mathbf{U}}^{(B_j)\mathrm{T}} \mathbf{K}^{(B_j)} \Delta \overline{\mathbf{U}}^{(B_j)}{}_{n+1}^{(k+1)} = 0 \tag{8.60}$$

8.5.4 Linearization of Bolthead Springs Weak Form

In the case of a linear elastic spring such as for those used to model the bolthead-adherend interaction, the tangent modulus is simply the spring stiffness matrix. The linearized weak form in this case becomes:

$$\delta W_i^{\left(S_j^i\right)} - \delta W_e^{\left(S_j^i\right)} + \delta \mathbf{U}^{(B_j)\mathrm{T}} \boldsymbol{k_\theta} \Delta \mathbf{U}^{(B_j)}{}_{n+1}^{(k+1)} = \mathbf{0} \tag{8.61}$$

8.5.5 Global Linearized Weak Form

The global linearized weak form at time t_{n+1} and in the *k*th iteration of this load increment is simply the sum of the individual linearized weak forms derived in the preceding sections. To combine all of the system equations in the same matrix, the various matrices must be assembled. The resulting global linearized weak form can be written as:

$$\sum_{i\in s}[\delta W_i - \delta W_e]^{(i)^{(k)}} - \delta\mathbf{U}^T \begin{bmatrix} \mathbf{K}^{(1)} + \mathbf{K}^{(2)} + \mathbf{K_T}^{(a)} & \mathbf{0} & \cdots & \mathbf{0} \\ \mathbf{0} & \mathbf{K}^{(B_1)} & \cdots & \mathbf{0} \\ \vdots & \vdots & \ddots & \mathbf{0} \\ \mathbf{0} & \mathbf{0} & \mathbf{0} & \mathbf{K}^{\left(B_{N_b}\right)} \end{bmatrix}^{(k)} \begin{Bmatrix} \Delta\mathbf{U}_{n+1} \\ \Delta\mathbf{U}_{n+1}^{\left(B_j\right)} \\ \vdots \\ \Delta\mathbf{U}_{n+1}^{\left(B_{N_b}\right)} \end{Bmatrix}^{(k+1)} = 0 \tag{8.62}$$

or more succinctly:

$$\delta\mathbf{U}^T[\mathbf{F}^{\text{int}} - \mathbf{F}^{\text{ext}}]^{(k)} + \delta\mathbf{U}^T\mathbf{K}_\mathbf{T}^{(\text{k})}\Delta\mathbf{U}_{n+1}^{(k+1)} = 0 \tag{8.63}$$

where the global tangent stiffness matrix for the *k*th iteration $\mathbf{K}_\mathbf{T}^{(\text{k})}$ is:

$$\mathbf{K}_\mathbf{T}^{(\text{k})} = \begin{bmatrix} \overline{\mathbf{K}}^{(1)} + \overline{\mathbf{K}}^{(2)} + \mathbf{K_T}^{(a)} & \mathbf{0} & \cdots & \mathbf{0} \\ \mathbf{0} & \mathbf{K}^{(B_1)} & \cdots & \mathbf{0} \\ \vdots & \vdots & \ddots & \mathbf{0} \\ \mathbf{0} & \mathbf{0} & \mathbf{0} & \mathbf{K}^{\left(B_{N_b}\right)} \end{bmatrix}^{(k)} \tag{8.64}$$

8.6 Constrained System Equations

A number of kinematic constraints are incorporated in the model of Chapter 5, such as those given by Eqns. (5.13-5.14). These have so far not been considered. In order to impose these constraints on the model solution, the weak form of Eqn. (8.11) must be constrained. The (k) subscripts are dropped for clarity since in the present section they do not change from those given in Eqn. (8.11). Firstly, note that since the RPI functions possess the Kronecker-Delta property, the discrete kinematic constraints can be directly written as:

$$\boldsymbol{C}^{\mathrm{T}}\Delta\mathbf{U} - \boldsymbol{G_n} = \mathbf{0} \tag{8.65}$$

where $\boldsymbol{G_n}$ will be referred to as the gap vector and $\boldsymbol{C}$ is the constraint matrix. Introducing the vector of quantities known as the constraint forces or Lagrange multipliers $\Delta\boldsymbol{\lambda}^{\mathrm{T}}$:

$$\Delta\boldsymbol{\lambda}^{\mathrm{T}}\left(\boldsymbol{C}^{\mathrm{T}}\Delta\mathbf{U} - \boldsymbol{G_n}\right) = \mathbf{0} \tag{8.66}$$

The Δ symbol signifies that this quantity is incremental, since multiple load steps may be implemented and we consider the solution over any particular load step. Following the method of Lagrange multipliers, as described in any textbook on mathematical optimization, the linearized weak form (which is the expression to be minimized) can be incorporated into the following functional:

$$\delta\mathbf{U}^{\mathrm{T}}(\boldsymbol{K}\Delta\mathbf{U} + \Delta\boldsymbol{\lambda}\boldsymbol{C}) + \delta\boldsymbol{\lambda}^{\mathrm{T}}(\boldsymbol{C}\Delta\mathbf{U} - \boldsymbol{G_n}) = \mathbf{0} \tag{8.67}$$

This is also known as the Lagrangian or constrained weak form. Since both $\delta\mathbf{U}$ and $\delta\lambda$ are arbitrary it follows that:

$$\begin{bmatrix} \boldsymbol{K} & \boldsymbol{C} \\ \boldsymbol{C}^{\mathrm{T}} & \mathbf{0} \end{bmatrix} \begin{bmatrix} \Delta\mathbf{U} \\ \Delta\boldsymbol{\lambda} \end{bmatrix} = \begin{bmatrix} \mathbf{R} \\ \boldsymbol{G_n} \end{bmatrix} \tag{8.68}$$

The system shown in Eqn. (8.68) is the final, constrained system equations that are required to solve the model for a particular load increment. The constraint matrix will now $\boldsymbol{C}$ be defined. The bolt constraint matrix, which includes both the bolthead and contact constraints, can be written in discrete form as:

$$\tilde{\mathbf{C}}^{\mathrm{T}} = [\tilde{\mathbf{C}}^{(h_1)\mathrm{T}}, \quad \tilde{\mathbf{C}}^{(h_2)\mathrm{T}}, \quad \tilde{\mathbf{C}}^{(bh_1)\mathrm{T}}, \quad \tilde{\mathbf{C}}^{(bh_2)\mathrm{T}},] \quad , \tilde{\mathbf{C}}^{(h_i)\mathrm{T}} = \left[\mathbf{C}_1^{(h_i)\mathrm{T}}, \quad \mathbf{C}_2^{(h_i)\mathrm{T}}, \quad \cdots, \quad \mathbf{C}_{n_{h_i}}^{(h_i)\mathrm{T}}\right] \quad , \quad \tilde{\mathbf{C}}^{(bhi)\mathrm{T}} = \left[\mathbf{C}_1^{(bhi)\mathrm{T}}, \quad \mathbf{C}_2^{(bhi)\mathrm{T}}, \quad \cdots, \quad \mathbf{C}_{n_{bhi}}^{(bhi)\mathrm{T}}\right] \qquad \text{(8.69-a,b,c)}$$

where n_{bh1} and n_{bh2} are the number of nodes in the top and bottom substrate bolthead regions, respectively, and n_{h_1} and n_{h_2} are the number of active contact nodes on the upper and lower hole boundary, respectively. The bolthead constraints $\tilde{\mathbf{C}}^{(bhi)\mathrm{T}}$ are:

$$\begin{aligned} \mathbf{C}_i^{(bh_1)} &= \left\{\mathbf{0}_{1\times 2N_1}, \quad \boldsymbol{\Phi}^{(1)\mathrm{T}}(\boldsymbol{x}_i), \quad \mathbf{0}_{1\times 2N_1}, \quad \mathbf{0}_{1\times 5N_2}, \quad \mathbf{0}_{1\times 2N_B}, \quad -\boldsymbol{\Phi}^{(B_j)}\left(l_{B_j}\right), \quad \mathbf{0}_{1\times 2N_B}, \quad -\boldsymbol{r}_{\boldsymbol{x}}^{B_j}(\boldsymbol{x}_i), \quad 0, \quad -\boldsymbol{r}_{\boldsymbol{y}}^{B_j}(\boldsymbol{x}_i), \quad 0\right\} \\ \mathbf{C}_i^{(bh_2)} &= \left\{\mathbf{0}_{1\times 5N_1}, \quad \mathbf{0}_{1\times 2N_2}, \quad \boldsymbol{\Phi}^{(2)\mathrm{T}}(\boldsymbol{x}_i), \quad \mathbf{0}_{1\times 2N_2}, \quad \mathbf{0}_{1\times 2N_B}, \quad -\boldsymbol{\Phi}^{(B_j)}(0), \quad \mathbf{0}_{1\times 2N_B}, \quad 0, \quad -\boldsymbol{r}_{\boldsymbol{x}}^{B_j}(\boldsymbol{x}_i), \quad 0, \quad -\boldsymbol{r}_{\boldsymbol{y}}^{B_j}(\boldsymbol{x}_i)\right\} \end{aligned} \qquad \text{(8.70-a,b)}$$

The hole contact constraint forces are slightly more complex since the surface normal varies. The meshless discretization of just a particular hole edge is considered (see Figure 8.2). It is assumed that a given active contact set is known. Then, at each node in the active set, a normal vector $\mathbf{n_i} = \{n_x, n_x\}$ with respect to the initial configuration at is calculated (this normal remains constant during the analysis due to the small displacement assumption).

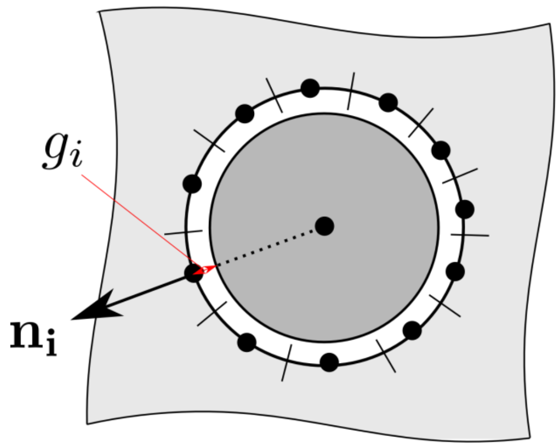

Figure 8.2: Bolt-hole contact boundary discretization

The discrete contact equations for the active contact nodes can thus be expressed as:

$$\mathbf{C}_i^{(h_1)} = \left[n_x \mathbf{\Phi}^{(1)\mathrm{T}}(\boldsymbol{x_i}),\quad n_y \mathbf{\Phi}^{(1)\mathrm{T}}(\boldsymbol{x_i}),\quad \mathbf{0}_{\mathbf{1\times3}\boldsymbol{N_1}},\quad \mathbf{0}_{\mathbf{1\times5}\boldsymbol{N_2}},\quad \mathbf{0}_{\mathbf{1\times}\boldsymbol{N_B}},\quad -n_x \mathbf{\Phi}^{(B_j)}\left(l_{B_j}\right),\quad -n_y \mathbf{\Phi}^{(B_j)}\left(l_{B_j}\right),\quad \mathbf{0}_{\mathbf{1\times2}\boldsymbol{N_B}},\quad \mathbf{0}_{\mathbf{1\times4}}\right]$$

$$\mathbf{C}_i^{(h_2)} = \left[\mathbf{0}_{\mathbf{1\times5}\boldsymbol{N_1}},\quad n_x \mathbf{\Phi}^{(2)\mathrm{T}}(\boldsymbol{x_i}),\quad n_y \mathbf{\Phi}^{(2)\mathrm{T}}(\boldsymbol{x_i}),\quad \mathbf{0}_{\mathbf{1\times3}\boldsymbol{N_2}},\quad \mathbf{0}_{\mathbf{1\times}\boldsymbol{N_B}},\quad -n_x \mathbf{\Phi}_x^{(b)}(0),\quad -n_y \mathbf{\Phi}^{(B_j)}(0),\quad \mathbf{0}_{\mathbf{1\times2}\boldsymbol{N_B}},\quad \mathbf{0}_{\mathbf{1\times4}}\right] \tag{8.71-a,b}$$

Finally, the contact constraints due to the clamping constraint may also be considered. This is simply:

$$\mathbf{C}^{(RHS)T} = \left[\mathbf{C}_1^{(RHS)\mathrm{T}},\quad \mathbf{C}_2^{(RHS)\mathrm{T}},\quad \cdots,\quad \mathbf{C}_{n_{h_i}}^{(RHS)\mathrm{T}}\right] \tag{8.72}$$

where:

$$\boldsymbol{C}_i^{(RHS)} = \left[\mathbf{0}_{\mathbf{1\times5}\boldsymbol{N_1}},\quad \mathbf{\Phi}^{(2)\mathrm{T}}(\boldsymbol{x_i}) - \mathbf{\Phi}^{(2)\mathrm{T}}(0, L),\quad \mathbf{0}_{\mathbf{1\times4}\boldsymbol{N_2}},\quad \mathbf{0}_{\mathbf{5\times}\boldsymbol{N_B}},\quad \mathbf{0}_{\mathbf{1\times4}}\right] \tag{8.73-a,b}$$

The overall constraint matrix $\boldsymbol{C}$ is therefore:

$$\boldsymbol{C} = [\tilde{\mathbf{C}}^{\mathrm{T}},\quad \mathbf{C}^{(RHS)\mathrm{T}}] \tag{8.74}$$

Eqn. (8.68) furthermore requires definition of the gap vector $\boldsymbol{G_n}$:

$$\boldsymbol{G_n} = \left\{\boldsymbol{G_n^{(h_1)}} \quad \boldsymbol{G_n^{(h_2)}} \quad \boldsymbol{0_{1\times(n_{bh1}+n_{bh2})}} \quad \boldsymbol{0_{1\times(n_{bh1})}}\right\}^{\mathrm{T}} \quad , \qquad \boldsymbol{G_n^{(h_i)}} = \left[g_1^{(h_i)} \quad g_2^{(h_i)} \quad \cdots \quad g_{n_{h_i}}^{(h_i)}\right] \tag{8.75-a,b}$$

where $g_{n_{h_i}}^{(h_i)}$ is the normal gap for *i*th active contact node at the start of the load increment. Finally, the corresponding Lagrange multiplier vector can be written as:

$$\begin{aligned} \boldsymbol{\Lambda}^T &= \left[\boldsymbol{\Lambda}^{(h_1)} \quad \boldsymbol{\Lambda}^{(h_2)} \quad \boldsymbol{\Lambda}^{(bh_1)} \quad \boldsymbol{\Lambda}^{(bh_2)} \quad \boldsymbol{\Lambda}^{(RHS)}\right] \quad , \\ \boldsymbol{\Lambda}^{(hi)} &= \left[\lambda_1^{(h_i)} \quad \lambda_2^{(h_i)} \quad \cdots \quad \lambda_{n_{h_i}}^{(h_i)}\right] \quad , \\ \boldsymbol{\Lambda}^{(bh_i)} &= \left[\lambda_1^{(bh_i)} \quad \lambda_2^{(bh_i)} \quad \cdots \quad \lambda_{n_{bh_i}}^{(bh_i)}\right] \quad , \\ \boldsymbol{\Lambda}^{(RHS)} &= \left[\lambda_1^{(RHS)} \quad \lambda_2^{(RHS)} \quad \cdots \quad \lambda_{n_{RHS}}^{(RHS)}\right] \end{aligned} \tag{8.76-a,b,c,d}$$

$\lambda_i^{(bh_j)}$ is the Lagrange Multiplier corresponding to the *i*th bolthead region node in the *j*th plate. Similarly, $\lambda_i^{(h_j)}$ is the Lagrange Multiplier corresponding to the *i*th active hole boundary node in the *j*th plate while n_{h_1} and n_{h_2} are the number of active nodes on the top and bottom substrate hole boundaries, respectively. $\lambda_i^{(RHS)}$ are the Lagrange Multipliers corresponding to the *i*th clamped node on the right hand side clamped boundary.

Having imposed appropriate boundary conditions on the constrained tangent stiffness matrix, the model solution can subsequently be obtained. The overall solution algorithm is described in section 8.7.

8.7 Solution algorithm

At this stage, all of the steps have been covered to obtain a linearized system of equations that is consistent with the local stress updating algorithm and Newton-

Raphson iterative solution method. The overall solution scheme for a given load increment is therefore presented in Box 8.2.

Box 8.2: Global nonlinear solution algorithm

Global Nonlinear Solution Algorithm

1) Assume an initial set of active contact nodes

2) Calculate the displacement and contact force increments based on the tangent stiffness for the current iteration and gap vector for the current increment

3) Verify whether Eqn. (8.66) is satisfied to within a desired tolerance. If not, repeat step 2 until convergence

4) Verify whether any of the active bolt-hole contact constraints violate the contact conditions (no penetration, no tensile contact forces). Update the active set if required and repeat steps 2-3 until the active set no longer changes

5) Update the gap vector, displacement vector, contact force vector, internal variables and stresses

Chapter 9: Model Verification

In order to verify that the proposed model solution works correctly and that the obtained predictions are in agreement with existing analyses for bonded joints and bolted joints separately, a number of reference solutions from the literature were analyzed. The results are compared in the following sections.

9.1 Single-Lap Bonded Joint Stress Verification

To verify the ability of the developed (meshless) model to predict the adhesive stresses in a linear elastic bonded joint, two models were considered. The first is the classical single-lap bonded joint model of Goland and Reissner [71]. The second is the detailed 3D FEM of Diaz et al. [114], which is considered to be a high fidelity solution to the bonded joint problem. In the meshless model, the bolt was omitted from the analysis in order to analyze just a bonded joint. The following two cases were compared: (a) isotropic aluminum adherends with linear elastic adhesive and (b) anisotropic CFRP adherends with linear elastic adhesive. The joint geometry, shown in Figure 9.1, was kept the same for both analyses and corresponds to the geometry defined by Diaz et al. [114]. Furthermore, as specified by Diaz et al., a 4448 N tensile load was applied to the joint.

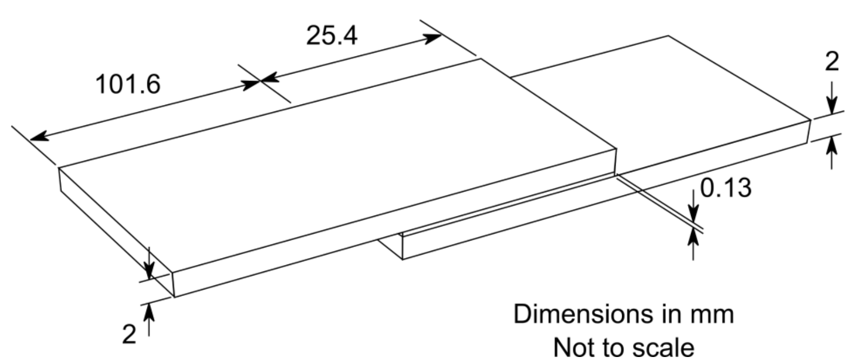

Figure 9.1: Bonded joint dimensions

The material properties for the adhesive, aluminum and composite are given in Table 9.1.

Table 9.1: Bonded joint material properties

Adhesive	Aluminum	Composite
$E = 3$ GPa	$E = 72$ GPa	$E_x = 138$ GPa
$\nu = 0.31$	$\nu = 0.31$	$E_y = 9.4$ GPa
		$G_{xy} = 6.7$ GPa
		$G_{yz} = 6.7$ GPa
		$\nu_{xy} = 0.32$
		$\nu_{xz} = 0.32$
		Layup = $[0/\pm45/0_2/\pm45/0]_s$

The Goland and Reissner (GR) and Diaz et al. solutions without nonlinear geometric deformation are used in the model verification, since geometric nonlinearity is not currently accounted for in the meshless model. For GR, this meant setting the bending moment factor to $k = 1$. All of the results are compared along the adhesive centerline, shown in Figure 9.2.

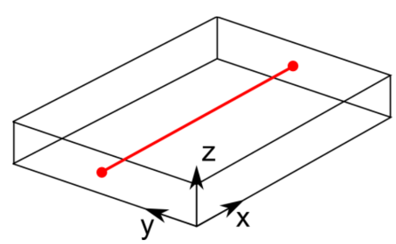

Figure 9.2: Adhesive centerline

Case A: The results for the adhesive shear stress and peel stress along the adhesive centerline are shown in Figures 9.3-9.4, respectively, for Case A.

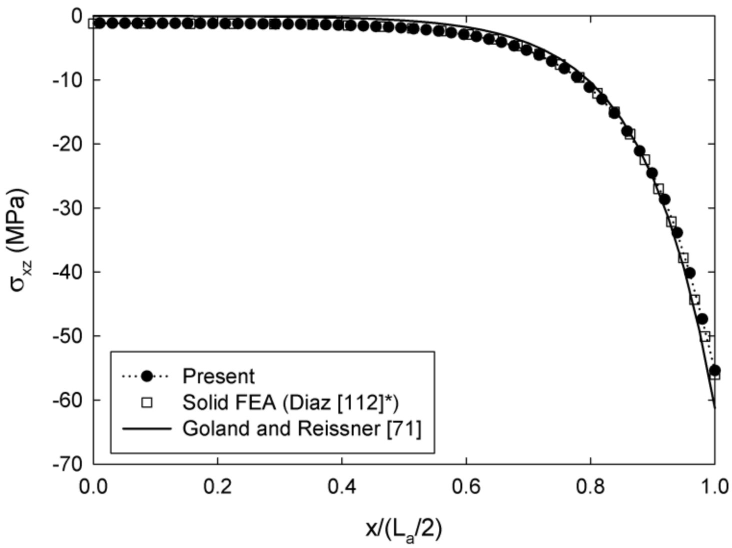

Figure 9.3: Shear stress in adhesive of linear elastic bonded joint with isotropic adherends

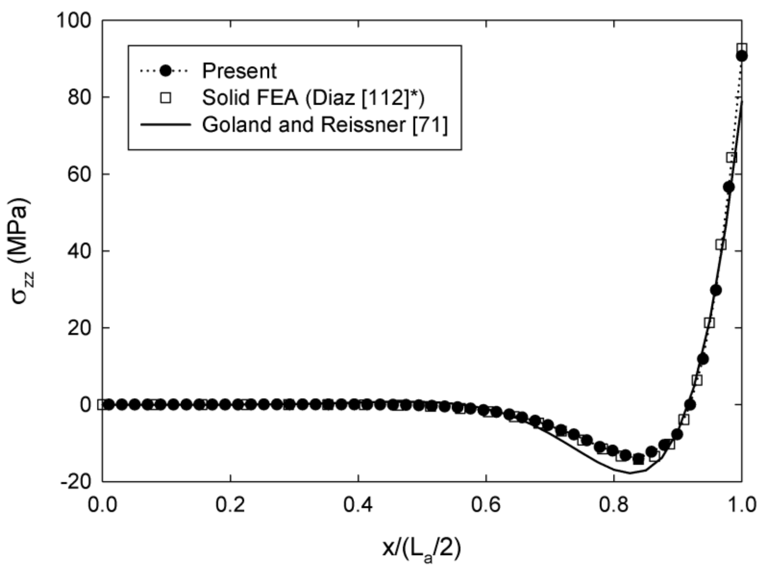

Figure 9.4: Peel stress in adhesive of linear elastic bonded joint with isotropic adherends

The comparison between the different models reveals that there is excellent agreement between the present model and the detailed solid FEM. The errors in the peak stress between these models are 1.3% and 3.2%, respectively. Reasonable agreement is in turn observed between the present/Solid FEM and GR results, although some deviation is evident at the overall edges and characteristic trough in the peel stress. The maximum error between the results is 10.7% and 14%. This can be explained by a number of reasons. Firstly, the GR model does not account for finite width, which the meshless model and solid FEM do. Also, the GR model does not account for transverse shear deformation of the adherends, which both the meshless model and solid FEM do. Finally, the most likely reason is that the GR model does not take into account the normal stress and strain components of the adhesive, while both of the other models consider these components.

Case B: Figures 9.5 and 9.6 show the results for the anisotropic adherends. In this case, there are no GR results since this model (in its original form) cannot account for anisotropic adherends. Thus, only the meshless model and solid FEM are compared. As for the isotropic adherends, the model results agree closely.

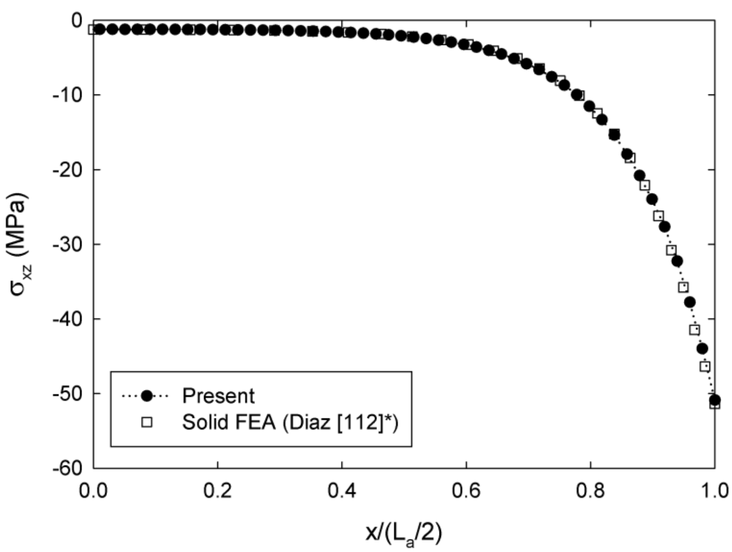

Figure 9.5: Shear stress in linear elastic bonded joint with anisotropic adherends

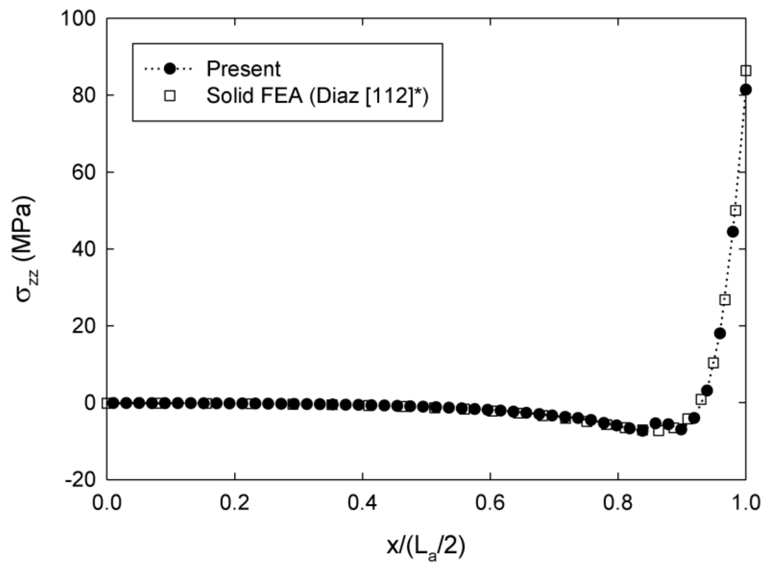

Figure 9.6: Peel stress in linear elastic bonded joint with anisotropic adherends

No suitable materially-nonlinear only (MNO) analysis was found in the literature to compare the meshless model nonlinear adhesive capability with. The latter is instead validated in the HBB joint analysis in section 9.3.

9.2 Bolted Joint Stress Verification

For the bolted joint stress verification, the results of the meshless model were compared with the detailed in-plane finite element analysis of Ireman et al. [115], and the complex potential semi-analytical solution of Kradinov et al. [116] for the same problem. The relevant geometry is given in Figure 9.7 in accordance with [115], where $W = 24$ mm and $D = 6$ mm. Two types of laminate were studied by Ireman et al.: (a) a 0° dominated layup and (b) a 90° dominated layup.

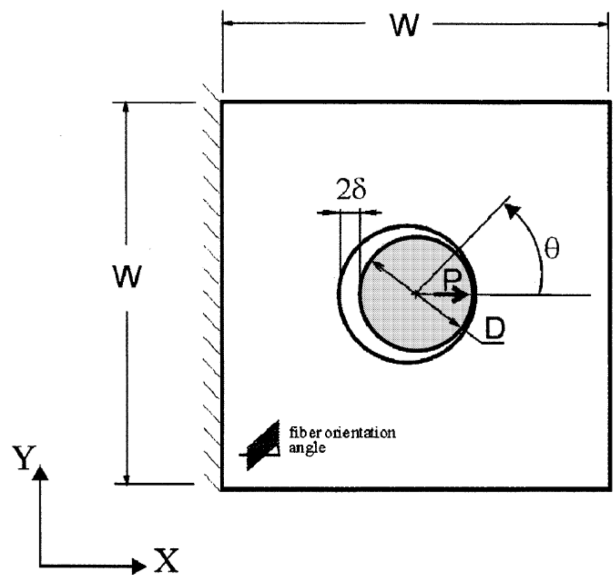

Figure 9.7: Bolted joint dimensions [116]

The material properties for these two laminates are provided in Table 9.2 below. Note that both Ireman et al. and Kradinov et al. used homogenized laminate properties, as specified in the table. Of course these are nevertheless anisotropic. Furthermore, a bolt-hole clearance of $\delta = 0.021$ mm was applied to the hole diameter. The externally applied load was 5483 N as specified in [115].

Table 9.2: Homogenized laminate properties

Laminate A	Laminate B
$E_x = 99.2$ GPa	$E_x = 35.5$ GPa
$E_y = 35.5$ GPa	$E_y = 99.2$ GPa
$G_{xy} = 8.5$ GPa	$G_{xy} = 8.5$ GPa
$\nu_{xz} = 0.24$	$\nu_{xz} = 0.08$

Bolted joints can be readily analyzed using the meshless model by setting a low adhesive thickness and specifying negligible adhesive properties. In the present case, the adhesive thickness was set to 0.1 mm and was assigned elastic properties of $E = 0.1$ MPa, $\nu = 0.42$.

Laminate A: The results for laminate A are shown in Figures 9.8-9.9 for radial stress and hoop stress, respectively. (These are normalized average values calculated through the thickness of the laminate) The results are plotted along the hole boundary, according to the angle convention of Figure 9.7.

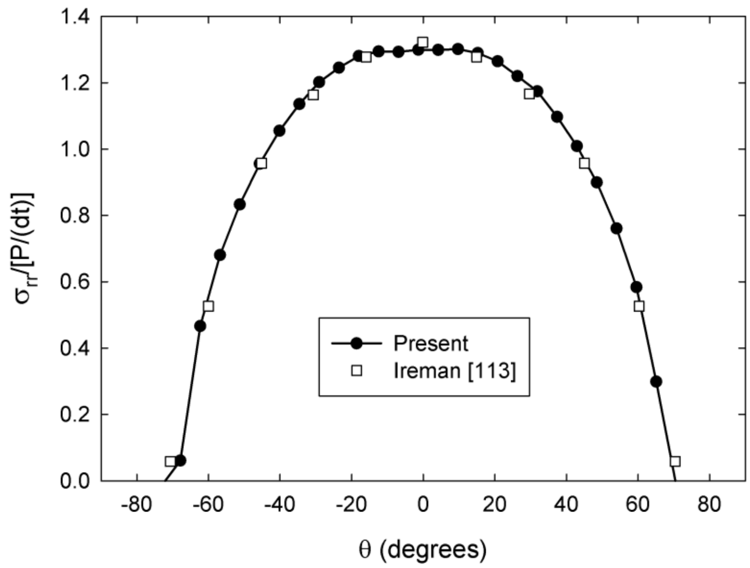

Figure 9.8: Laminate A hole boundary normalized radial stress

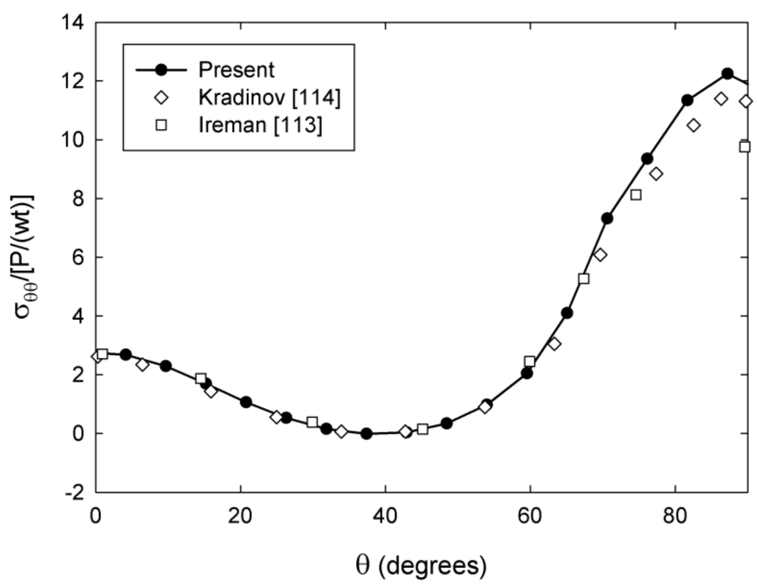

Figure 9.9: Laminate A hole boundary normalized hoop stress

Comparison of the results shows excellent agreement between the results of the new analysis and those of the reference solutions for the radial stress. The hoop stress also shows very good agreement, although there is some deviation in the results around the 90° location. It is notable that the results of Kradinov et al. and Ireman et al. between themselves show a noticeable disagreement at this radial location. In fact, the results of the Kradinov et al. are closer to the present analysis than those of Ireman et al. One reason that the present results are likely to deviate here somewhat is that in the new analysis, out-of-plane deformation of the laminate (due to shearing and bending) is considered, which is not considered in either of the others (which are purely in-plane). Overall, however, very good agreement can be concluded.

Laminate B: The same normalized stresses are compared in Figures 9.10 and 9.11 for laminate B. Interestingly, the radial stress distribution is quite different in this 90°-dominated laminate, showing a dip at the 0° location which is flanked by peaks on either side at around ±45°. All three analyses predict this behaviour very closely and again show excellent agreement.

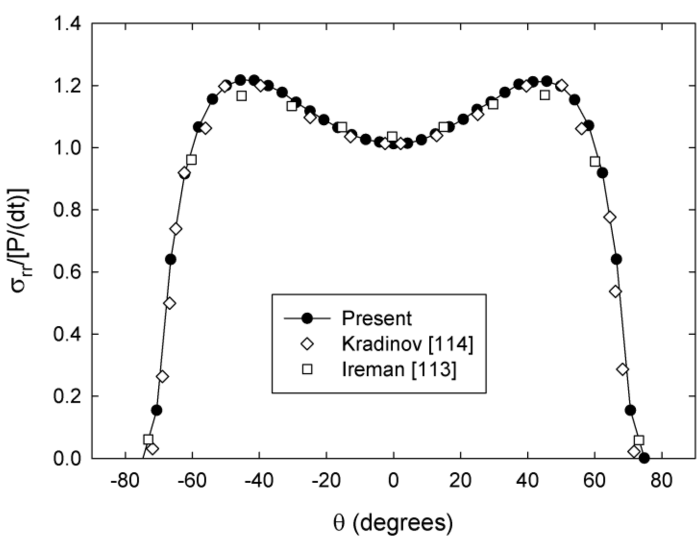

Figure 9.10: Laminate B hole boundary radial stress

The hoop stress results also show good agreement, again with some deviation around the 90° location. This is again attributed to the more complex deformation of the laminate in the current model, including the out-of-plane components. Overall, however, good agreement can be concluded.

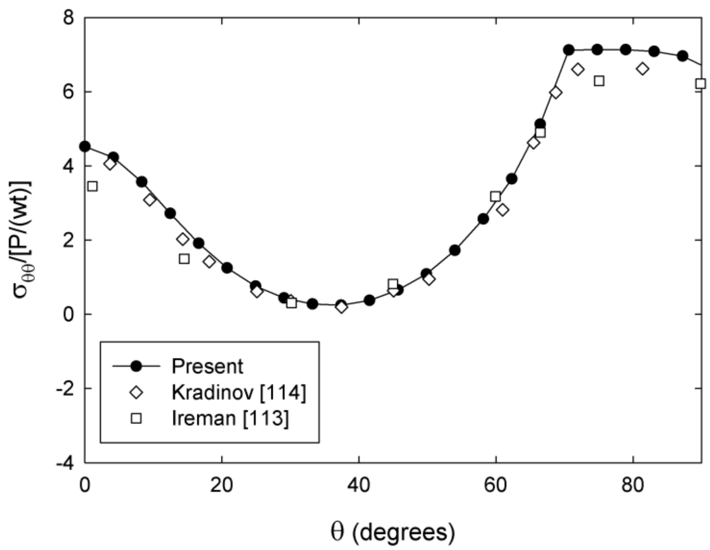

Figure 9.11: Laminate B hole boundary hoop stress

9.3 HBB Joint Load Sharing Validation

An essential requirement of any HBB joint model is that it should be able to capture the relative stiffness of the underlying joints. To demonstrate the ability of the present model to do so, its predictions are compared with the GHJM load sharing model developed in Chapter 3. The relevant joint geometry and material parameters are given in Table 9.3. A rigid bolthead and no washer are considered, such that a high bolthead stiffness of k_θ = 1e+9 N/rad is applicable in the meshless model. Both the case where the adhesive is elastic and the case where the adhesive is elastoplastic with bilinear stress-strain behaviour are considered. In all cases, the bolt is assumed to be steel (E = 205 GPa, ν = 0.33).

Table 9.3: HBB validation analysis parameters

Adhesive	Composite	Geometry
Elastic:	$E_x = 141$ GPa	$L_a = 28$ mm
$E = 370.3$ MPa	$E_y = 9.7$ GPa	$L_f = 32$ mm
$\nu = 0.42$	$G_{xy} = 5.4$ GPa	$D = 8$ mm
Plastic:	$G_{yz} = 3.2$ GPa	$E = 14$ mm
$\sigma_y = 9$ MPa	$\nu_{xy} = 0.33$	$W = 28$ mm
$H = 30$ MPa	$\nu_{xz} = 0.44$	$t_a = 0.5$ mm
	$t_{ply} = 0.137$ mm	clearance = 2 μm
	layup = $[45/0/-45/0]_{4s}$	

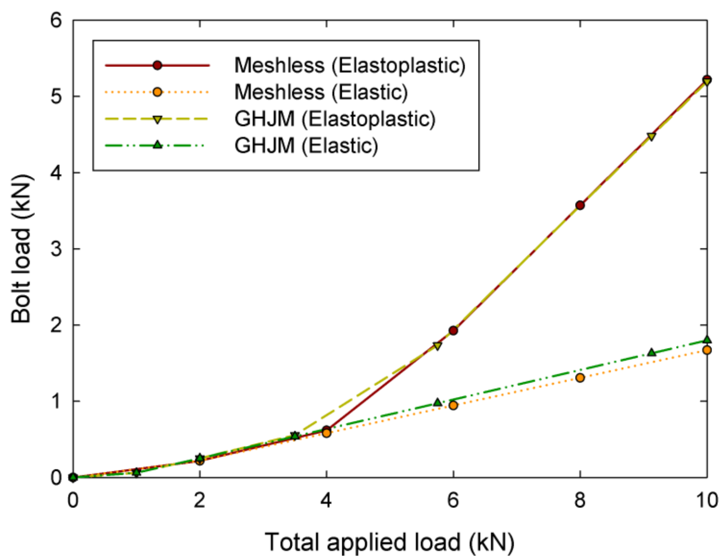

Figure 9.12: Meshless model and GHJM load sharing prediction comparison

Figure 9.12 demonstrates that there is close agreement between the predictions of the meshless model and the specialized load sharing model of Chapter 3 (*GHJM*) for both elastoplastic and elastic adhesive behaviour. This agreement is all the more remarkable given the significant simplification of the bolthead-laminate interaction in the meshless model. The results also clearly demonstrate, once again, perhaps the most important finding of Chapters 3-4. Even when a very low modulus adhesive is used, such as in the presented example, as long as the adhesive remains elastic then the bolt carries only a limited proportion of the overall load. Gross yielding of the adhesive significantly lowers the bonded joint stiffness, which allows load to be transferred to the bolt at a much greater rate.

9.4 Adhesive Stress & Strain Convergence

One of the reasons for developing the model of Chapter 5 was to eliminate the adhesive stress and strain singularities that occur in detailed solid finite element adhesive representations. This was verified by analyzing case (a) of section 9.1 with various nodal densities. The results of this study are shown in Figure 9.13.

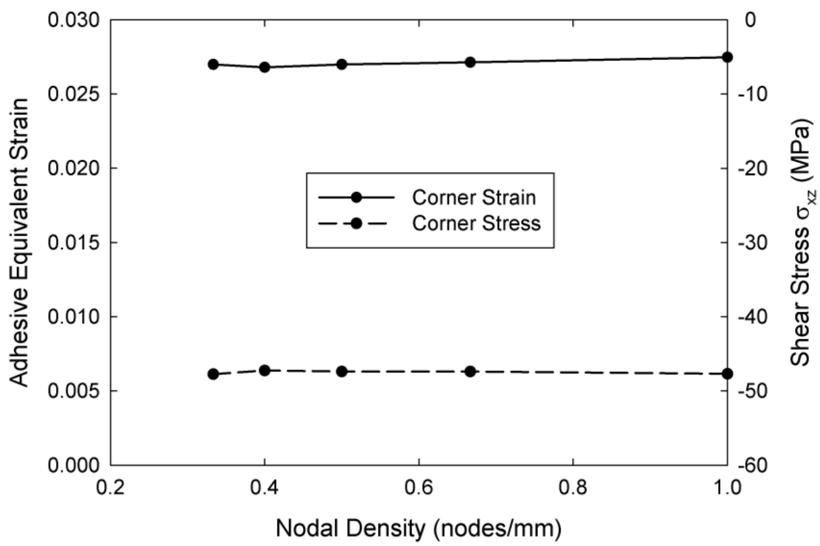

Figure 9.13: Discretization insensitivity of corner stress and strain in meshless model

The locations which are most sensitive to singularities in FEM, namely the corners of the adhesive region, were considered[9]. It is clearly seen in Figure 9.13 that both the adhesive stress and strain at this location are highly insensitive to nodal density. The maximum difference due to increasing the mesh density by a factor 3 is less than 1.8% for the stress and less than 1% for the strain. In other words, reliable, converged results are obtained for the adhesive stresses and strains for

[9] In particular, the corner located at $(x = L_f, y = 0)$ was considered.

even coarse discretizations and there is no evidence of any stress- or strain singularity. This is desirable since it allows for meaningful comparisons between different designs without the analyst needing to worry about whether the differences are a result of the numerical discretizations.

9.5 Conclusions

It is concluded that the meshless model developed in this part of the thesis can achieve a good prediction of load sharing, with similar accuracy to the GHJM (subject of course to the assumptions implicit in the model). Furthermore, its predictions of stresses and strains in bonded and bolted joints separately are in excellent agreement with reference solutions from the literature. Finally, the absence of adhesive stress and strain singularities was demonstrated. A good level of confidence has therefore been established in the predictions obtained by this method. Validation of its basic strength prediction capability is performed in the next chapter.

Chapter 10: Experimental Complements

In this chapter an experimental investigation of bonded, bolted and HBB joints is presented. One aim of this study is to assess the ability of the previously developed mathematical model to provide a basic prediction of the quasi-static stiffness and strength of the various joint types. In addition, the following hypothesis is tested:

10.1 Hypothesis

If the quasi-static performance (i.e., stiffness, strength and energy absorption) of a HBB joint relative to the underlying joints is related to the adhesive type/thickness, then varying the adhesive type/thickness will result in a change in the relative joint performance.

10.2 Test Matrix

To test the hypothesis, the test matrix presented in Table 10.1 was developed. Each cell corresponds to a particular configuration and contains the number of tested specimens in parentheses. For each joint type, the adhesive type/thickness was varied while the composite laminates and joint geometry were kept constant.

As shown, between 3 and 5 specimens were tested per configuration. Originally, it was intended to test 5 specimens per configuration. However, a manufacturing error (faulty layup) led to the scrapping of a number of specimens. Nevertheless, it is considered that even 3 repeats results in acceptable statistical precision.

Table 10.1: Test matrix

Joint Type \ Adhesive Type	Cytec FM300-2M Film Adhesive 0.25 mm nominal thickness	Hysol EA9361 Paste Adhesive 0.5 mm nominal thickness
Bonded	(5)	(3)
Bolted	(4)	
Hybrid Bonded-Bolted	(4)	(3)

10.3 Specimen Geometry & Manufacture

The specimen geometry that was tested is shown in Figure 10.1. As illustrated, the grip ends of the adherends were fitted with tabs.

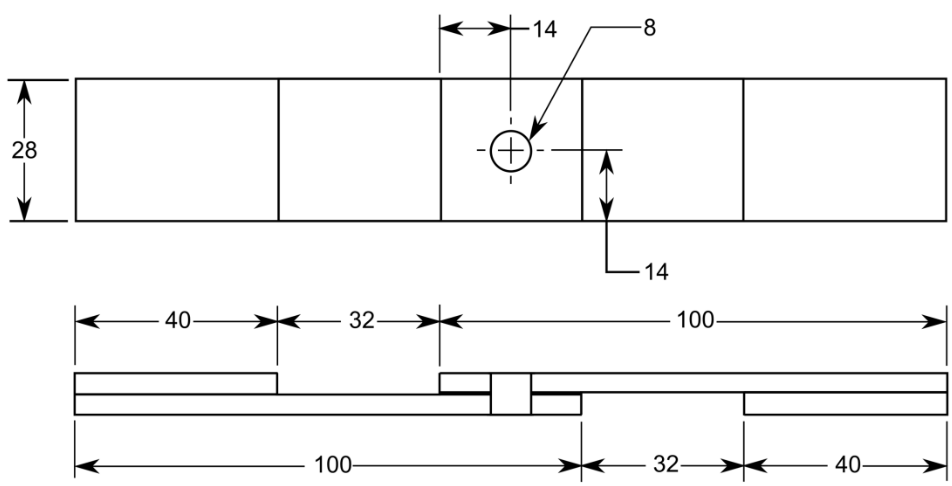

Figure 10.1: Quasi-static strength specimen geometry(dimensions in mm)

Both the adherends and the tabs were made from a laminated composite plate with a layup of $[45/0/-45/90]_{4s}$. This laminate was manufactured from Cycom T650/5320 unidirectional pre-impregnated CFRP tape. The manufacturer's recommended out-of-autoclave cure process was used, resulting in a measured post-cure laminate thickness of 4.42 ± 0.07 mm. A diamond-tipped saw was used to cut the adherends and tabs from the plate, following which the laminate quality was verified using microscopic void analysis of a number of samples obtained during the cutting process. Subsequently, the joints were manufactured.

To manufacture the bonded joints, the mold described in Chapter 3 was used (see Figure 3.6), allowing for precise control of the adherend alignment, overlap length and bondline thickness (for the paste adhesive). The latter two variables were controlled using a set of specially manufactured shims/spacers placed inside the mold. The bonding surfaces of the adherends and tabs were first de-greased with acetone and subsequently abraded using a sand blaster. Any dust generated was removed using compressed air. The adherends were hence bonded/assembled in the mold. Hysol EA9361, being a two-part paste adhesive, required mixing prior to application. This mixing was performed using a Thinky ARE-310 centrifugal mixer in order to achieve good uniformity and avoid entrapped air bubbles. The EA9361 joints were cured at 80°C for 60 minutes, while the FM300-2M joints were cured at 121°C for 90 minutes, following the manufacturers' specifications. Excess adhesive that spilled from the joints during cure was carefully removed using a hack saw and sanded down with fine grit sandpaper to appear flush with the joint. The average EA9361 bondline thickness was measured post-cure to be 0.460 ± 0.028 mm. This value was obtained by measuring the adherend thickness in the overlap region prior to bonding, and then measuring the bonded sandwich post-cure. The adhesive thickness was taken to be the difference between these two measurements. The closeness of the measured value to the desired nominal adhesive thickness of 0.5 mm and low scatter confirms the ability of the developed manufacturing system to produce controlled, consistent thickness bonds for the EA9361 adhesive. The FM300-2M bondline thickness was accurately controlled without the use of shims since this adhesive contains an embedded scrim cloth. It was thus simply assumed to be equal to the manufacturer's stated nominal thickness of 0.25 mm.

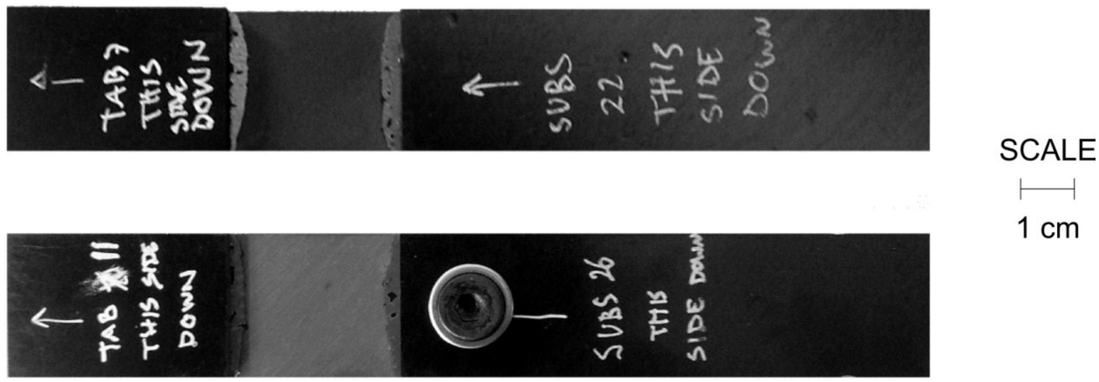

Figure 10.2: Example bonded joint and hybrid joint specimens

The HBB joints were created by first manufacturing the underlying bonded joint, followed by drilling an 8 mm hole at the center of the joint overlap using a CNC drill. The Corodrill 854 composite-specific drill bit from Chapter 3 was again used for optimal hole quality. The diametric tolerance of the hole was confirmed to be within 25.4 microns using a set of go/no-go gauges. The bolted joints were manufactured using the same process as the HBB joints, except that the overlap region was evidently not bonded. For both the bolted and hybrid joints, the bolts that were used were Misumi GDMSB8-13-F10-M8 steel bolts. DIN-125 flat washers were placed on either side of the joint between the bolthead and metric M8 heavy hex nut, as is visible in Figure 10.2. The nut was finger tightened prior to installation of the joint in the testing machine.

10.4 Test Procedure

The joints were tested under quasi-static tensile conditions at a displacement rate of 0.006 mm/s, consistent with the displacement rate at which the EA9361 adhesive was characterized. A 100 kN MTS tensile testing machine was used for this purpose. The following test procedure was used:

Box 10.1: Test procedure

Test Procedure

1) Install joint in lower grip and align upper grip
2) Zero load cell with top grip open
3) Clamp specimen at a pressure of 1750 kPsi
4) Adjust applied load to remove any tensile/compressive load imparted on the specimen due to clamping
5) Zero the displacement readout
6) Start test in displacement control
7) Remove failed specimen

During testing, the load and crosshead displacement were recorded. All tests were performed under RTD conditions. To minimize the effect of external influences, the tests for either type of adhesive were always performed within the same day.

10.5 Results & Discussion

10.5.1 Stiffness

Figure 10.3 shows the load-displacement curves for the EA9361 bonded and hybrid joints and the bolted joints. It is evident that the stiffness of the bonded and hybrid joints is initially similar. At a load of around 5 kN, the stiffness of the bonded joint significantly decreases. This is explained by plasticity spreading throughout the bonded area. When this happens, the adhesive loses much of its resistance to additional deformation, resulting in the observed stiffness decrease. The HBB joint stiffness also decreases at the same load; however, it remains greater than those of both the bonded joint and the bolted joint. This is explained as follows. Once the adhesive has plasticized, the HBB joint compliance—like the bonded joint—starts to significantly increase. However, the bolt-hole clearance soon becomes taken up and most of the additional load begins to be transferred through the bolt. The hybrid joint stiffness hence becomes equal to that of the bolted joint in addition to the residual bonded joint stiffness.

The bolted joint stiffness is initially lower than that of the unyielded bonded joint and is quasi-linear up to a load of around 16 kN. At this point, the composite begins to sustain damage and as this damage increases, the bolted joint stiffness gradually decreases with increasing load.

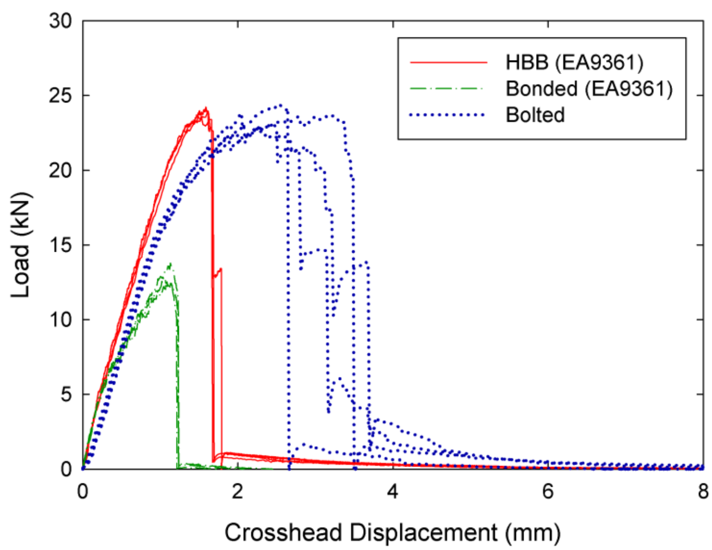

Figure 10.3: EA9361 load-displacement curves

The FM300-2M bonded and hybrid joints load-displacement curves are shown in Figure 10.4. Between 0 kN to 12 kN of applied load, the HBB joint and bonded joint exhibit identical stiffness—which is significantly greater than that of the bolted joint—and the load displacement curves are virtually linear. The distinct bilinear load-displacement behaviour of the EA9361 joints is not observed. At a load of around 12 kN, the adhesive fractures, leading to failure of the bonded joint and a discontinuous, drastic reduction in the load and stiffness of the HBB joint. The latter is able to continue sustaining load following the adhesive fracture with identical stiffness to the bolted joint.

The initial joint stiffness, calculated as the average slope of the load-displacement curves between 0 and 5 kN, is compared in detail in Figure 10.5 for the joints containing adhesive. It is clear that the choice of adhesive system (type/thickness) has an important effect on both the hybrid and bonded joint stiffness, with the FM300-2M joints being significantly stiffer than the EA9361 joints. As remarked before, it is clear that for both types of adhesive the hybrid and bonded joints initially have very similar stiffness. This indicates that the adhesive is the dominant load transfer mechanism in this initial region. The HBB stiffness is in each case slightly lower than the bonded stiffness, which is explained by the smaller bonded region due to the hole in these joints, although the difference is not statistically significant.

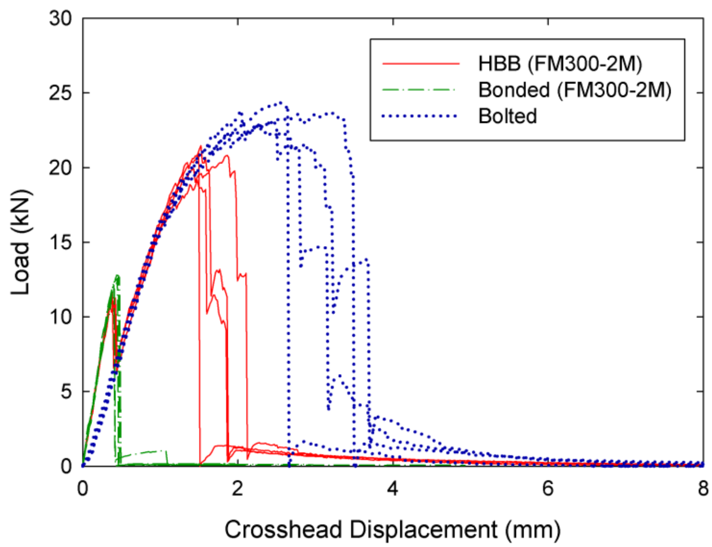

Figure 10.4: FM300-2M load-displacement curves

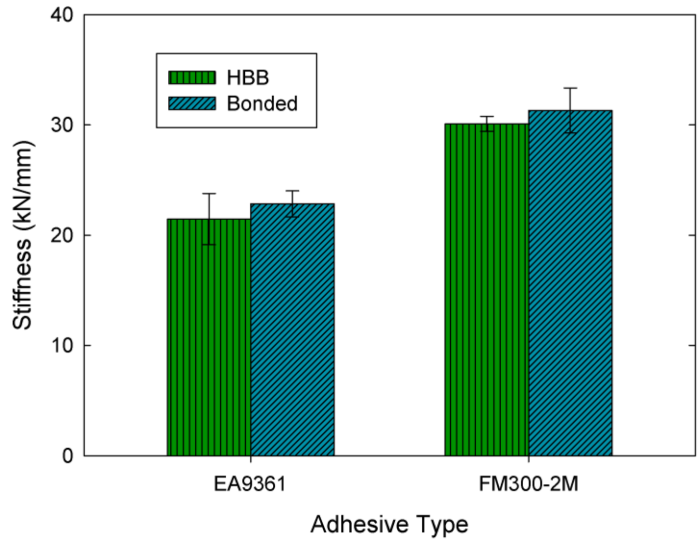

Figure 10.5: Comparison of joint stiffness in 0-5 kN range

10.5.2 Strength

The ultimate strengths of the various joint configurations are compared in Figure 10.6. In addition, the 2% yield strengths for the HBB and bolted joints are also shown. The relevant numerical values are presented in Table 10.2. For both the EA9361 and FM300-2M joints, it is evident that the bonded joint was weakest. For EA9361, the HBB joint and bolted joints have statistically similar ultimate strengths. Meanwhile, for FM300-2M the HBB joint actually has a significantly lower ultimate strength than the bolted joint. The yield strengths also show an interesting trend. For the EA9361 joints, the 2% offset yield strength of the HBB joint (corresponding to onset of damage in the composite) is 18% greater than that of the bolted joint. In other words, the adhesive delays the onset of damage in the composite to a load level that is 18% greater than in a joint without adhesive. Meanwhile, when comparing the yield strength of the FM300-2M joints, it can be seen that the damage onset in the hybrid joint was not affected compared to that of the bolted joint.

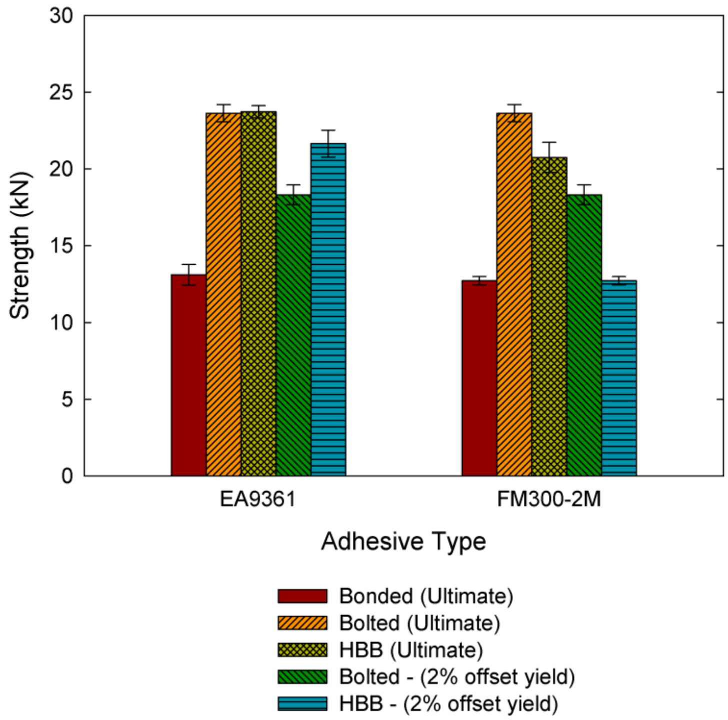

Figure 10.6: Comparison of joint strengths

Table 10.2: Joint ultimate strength data (N)

	EA9361			**FM300-2M**		
	Bonded	*Bolted*	*Hybrid*	*Bonded*	*Bolted*	*Hybrid*
	12537	23234	23657	12731	23234	19328
	13855	23136	24001	12465	23136	21120
	12919	23754	24241	12523	23754	20916
		24360		13151	24360	21612
				12708		
Mean	13104	23621	23966	12716	23621	20744
Std. Dev.	678	562	293	269	562	988

10.5.3 Failure Modes

Depending on the adhesive system, the bonded joints either experienced brittle fracture or ductile fracture. The FM300-2M joint fracture was more brittle, while the EA9361 joints demonstrated a more ductile fracture. This is clear from Figures 10.4-10.5; the displacement to failure for the EA9361 joints is approximately twice that of the FM300-2M joints. Furthermore, the load-displacement curves for the FM300-2M bonded joints show a sharp peak, while those for EA9361 have a slight rounding at the top. In both cases, however, the damage progression occurs very rapidly. The failure surfaces of the two types of bonded joint are shown in Figure 10.7. As desired, all of the tested specimens failed cohesively (inside the bondline), demonstrating that a good bond with the adherends was achieved. The striations of the adhesive on the EA9361 failure surface provide further evidence of ductile failure.

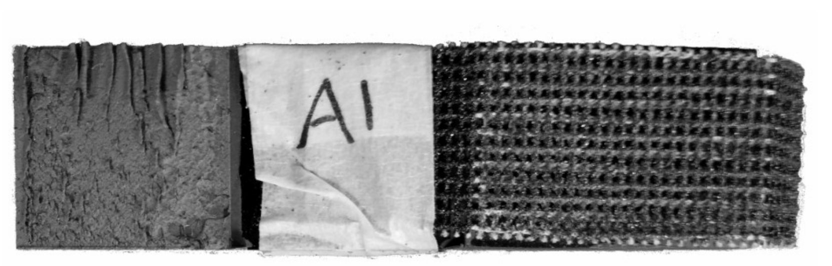

(a) EA9361 bonded joint

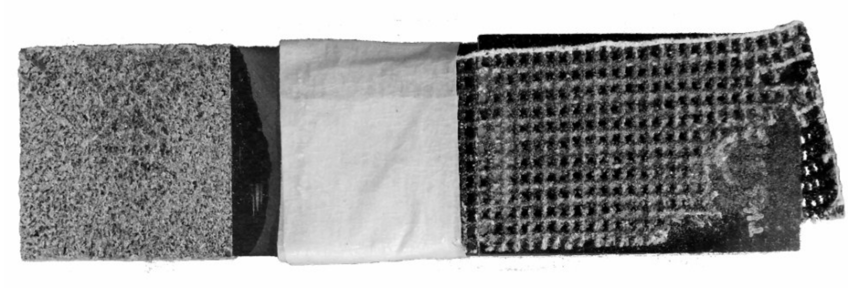

(b) FM300-2M bonded joint

Figure 10.7: Bonded joint failure surfaces

The bolted joint failure was a classical progressive net-section failure (Figure 10.8). As the joint loading was increased, the high hoop stresses at the hole boundary led to shear and tensile failures in critical plies along the net-section plane. This caused the joint to progressively lose stiffness. Although significant out-of-plane rotation of the overlap occurred during loading, delamination of the adherends was only observed to occur near the end of the test once the applied load had already peaked and thus would not have affected the ultimate joint strength. The finger tightening of the bolt is likely to have helped in suppressing this failure mode.

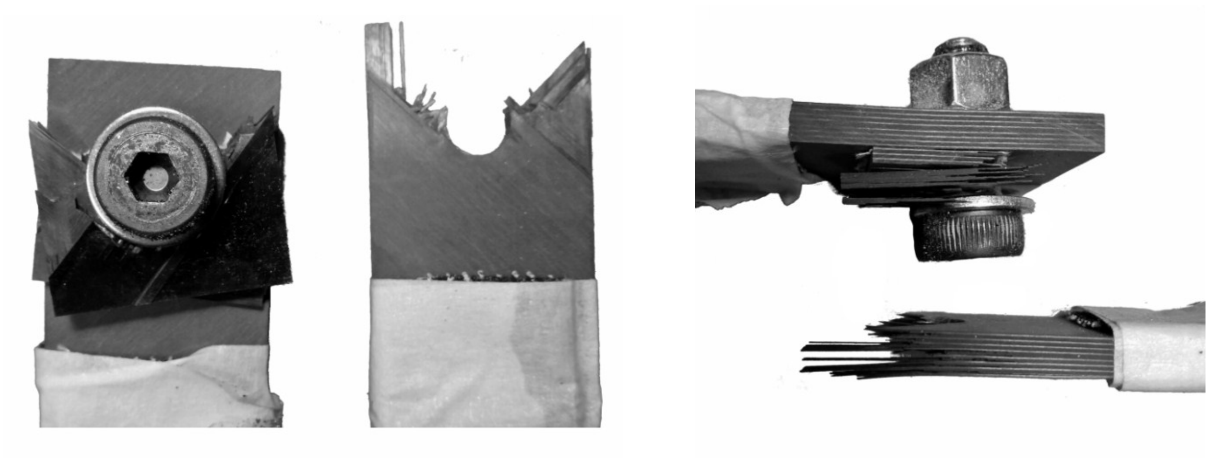

(a) Plane View *(b) Side View*

Figure 10.8: Bolted joint failure mode

The HBB joint failure mode was a combination of the bonded joint and bolted joint failure modes. In each case, the adhesive failed first. In the case of the FM300-2M hybrid joint, this was succeeded by near instantaneous separation of the entire bondline. It is hypothesized that this sudden, energetic and brittle event led to significant inertial forces being reacted by the bolt during the transition in load transfer mechanism. This is likely to have caused damage in the composite, and would explain why the FM300-2M hybrid joint ultimate strength was found to be 12% weaker than the bolted joint. The final failure mode was again net-section failure of the composite adherend, as shown in Figure 10.9.

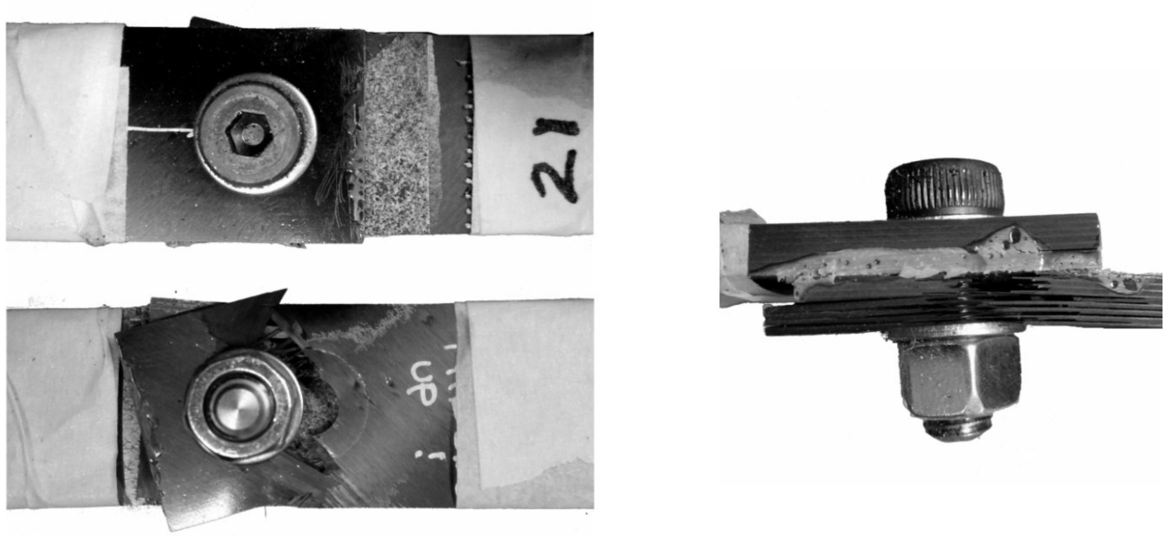

(a) Plane View *(b) Side View*

Figure 10.9: FM300-2M Hybrid joint failure mode

The EA9361 hybrid joint failure was slightly different, which is likely tied to the ductile failure that was observed for the EA9361 bonded joint. During the hybrid tests, it was visually observed that a crack started in the adhesive at the overlap edge. This roughly coincided with the loss of linearity in the second linear region of the load-displacement curve. Thus, it is hypothesized that the more ductile nature of the EA9361 failure allowed load to be transferred more gradually to the bolt, with the adhesive continuing to transfer a small amount of load until final failure.

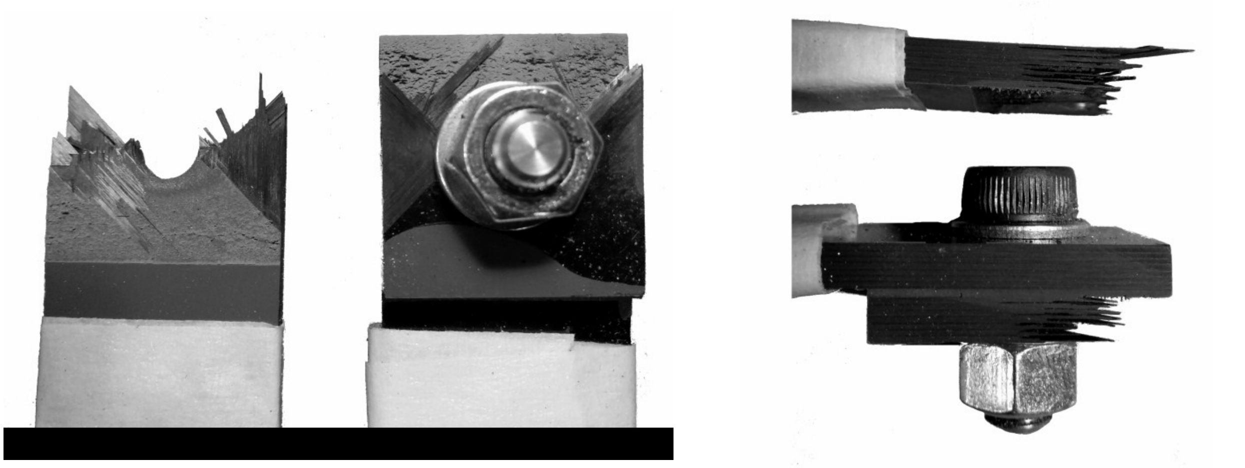

(a) Plane View (b) Side View

Figure 10.10: EA9361 Hybrid joint failure mode

10.5.4 Energy Absorption

One suggested advantage of HBB joints is that they may increase the amount of energy that the joint is able to dissipate during fracture, which could potentially be important for, for example, crashworthiness. The energy absorbed by the joint is the area underneath the load-displacement curves shown in Figures 10.3-10.4. Importantly, no studies on HBB composite joints have so far addressed this aspect of the technology. The results of this analysis considering quasi-static loading are shown in Figure 10.11 below.

Some important observations can be made from Figure 10.11. First, the brittle (FM300-2M) bonded joint dissipates the least energy by a considerable margin. The ductile (EA9361) bonded joint dissipates 2.99 times as much energy as the brittle joint, despite the strengths of these joints being almost identical (see section 10.5.3). The bolted and hybrid joints both dissipate substantially more energy during fracture than either of the bonded joints.

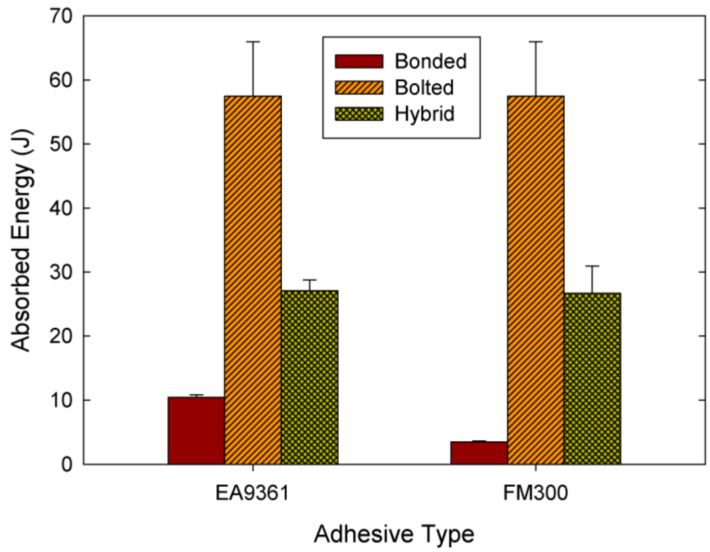

Figure 10.11: Comparison of energy absorption for different joint types

Examination of the bolted and hybrid joint fracture energies reveals a somewhat surprising result: the hybrid joint dissipates significantly less energy during fracture than the bolted joint for both EA9361 and FM300-2M adhesives. This is an important experimental observation, because it proves beyond a doubt that hybrid bonding-bolting is not necessarily the optimal solution with regards to energy absorption. While it is better than just bonding, it can be significantly worse than plain bolting.

A proposed explanation for this requires examination of Figures 10.3 and 10.4. First, for the EA9361 hybrid joint, the adhesive failure is delayed to a much higher load than in the EA9361 bonded joint. In fact, adhesive failure occurs at a load slightly above the ultimate strength of the plain bolted joint. Thus, once the adhesive fractures, the underlying bolted joint cannot sustain the load that is suddenly transferred to it by itself and fractures catastrophically and suddenly. The gradual, progressive failure that is experienced by the bolted joint does not occur and thus less energy is dissipated.

For the FM300-2M hybrid joint, the mechanism is slightly different. In this joint, the adhesive fails at a load level that the bolted joint by itself is able to sustain. However, during the abrupt adhesive failure, it is hypothesized that significant dynamic loads are exerted on the composite as the compliance of the joint suddenly drastically changes, leading to sudden, temporary acceleration of the components. This may lead to damage in the composite, leading to the reduced residual strength of these joints shown in Table 10.2. Thus, there is again reduced scope for progressive failure, leading to decreased energy absorption.

10.6 Comparison with Mathematical Model

An analysis was performed of the bonded, bolted and HBB experimental configurations for the EA9361 adhesive, since detailed material properties were available for this adhesive (these were obtained by a master's student at McGill University in the scope of the overarching research project of this thesis [79]). A bilinear model was fit to the detailed tensile stress-strain data, as required by the J_2 material model in the meshless model. The detailed curve and bilinear fit are both plotted in Figure 10.12. The parameters of the bilinear fit are E = 370.3 MPa, H = 30 MPa. It can be seen that this provides an excellent approximation of the true stress-strain curve.

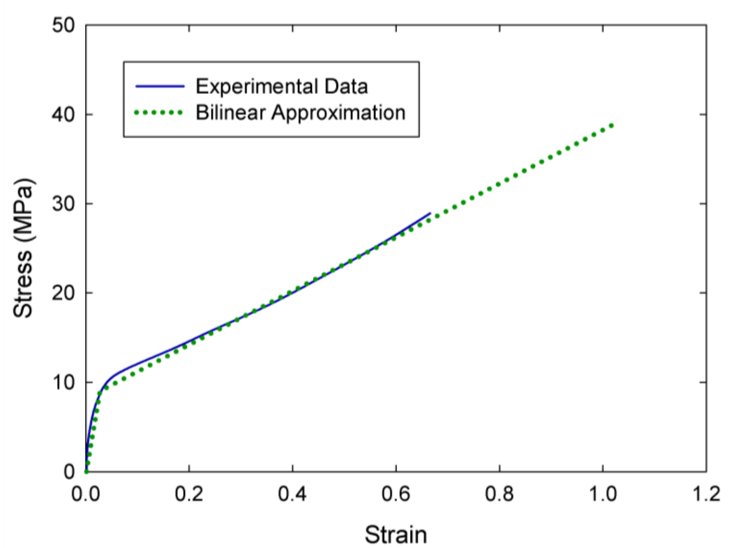

Figure 10.12: Fit of EA9361 adhesive true stress-strain curve. Experimental data from [79].

The ultimate equivalent von Mises strain, ε_{ult}, for EA9361 adhesive was determined from thick adherend shear test (TAST) results that were independently carried out by colleagues at Carleton University and shared in the context of the overarching research project [117]. These results are shown in Figure 10.13 below.

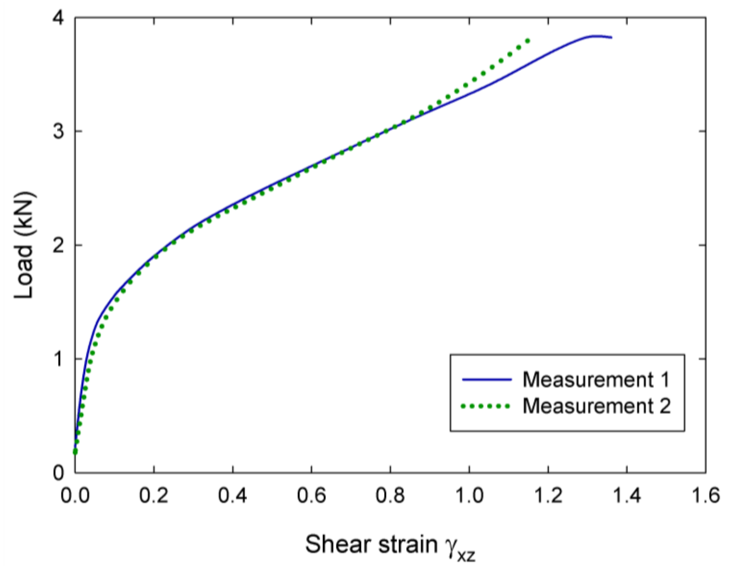

Figure 10.13: Experimental TAST measurements of EA9361 adhesive [117]

Based on these independently measured results, ε_{ult}—the average ε_{eqv} at failure (calculated using Eqn. (5.34))—was determined as 0.725. Next, the characteristic distance of the composite adherend was obtained by means of an analysis of manufacturer supplied notched specimen data. Based on an in-plane analysis, the characteristic distance was determined as 1.40 mm for a hole diameter of 6.35 mm. Since the bolt used in the experiment had an 8 mm diameter hole, this characteristic distance was linearly scaled as a first approximation, giving a characteristic distance of 1.76 mm. Finally, since a low clamp-up load was applied during the experiment, the bolthead spring constant k_θ had to be determined. This was done on the basis of the bolted joint experimental results, such that the correct slope was obtained for the bolted joint load-displacement curve relative to the slope of the bonded joint. This was determined as k_θ = 0.5e+3 N/rad, giving a ratio of adhesive-to-bolted-joint slopes of 1.36, compared to the experimental ratio of 1.41.

The results of the analyses are shown in Figure 10.14-a. Sample experimental results are shown in Figure 10.14-b for comparison. The model and experimental curves are not directly compared on the same plot. This is because the experimental displacement is that of the crosshead and is therefore not directly comparable with the joint displacement predicted by the meshless model (since crosshead displacement includes machine displacement, grip displacement, etc.). The stiffness comparison is thus qualitative. Comparing the two curves, it can be seen that the meshless model correctly predicts that the bonded and HBB joints initially have identical stiffness. At around 5 kN, this stiffness reduces. This is also observed in the experiment. The bonded joint stiffness reduces to less than the bolted joint, while the HBB stiffness remains greater than both that of the underlying joints.

At a load of around 15 kN, the bolted joint curve gradient decreases. This indicates the onset of damage in the laminate. Progressive damage is not accounted for in the meshless model; however, the yield limit appears to be well approximated at around 15 kN.

The failure initiation loads for the various joint types are compared in Figure 10.15. It can be seen that a very good prediction is achieved, in particular for the bonded and HBB joints. It is noted that the safety factor for the HBB joint laminates at adhesive failure was predicted as 1.31. Therefore, there was likely no in-plane damage in the composite adherend prior to adhesive rupture. This is important, because it suggests that the hybrid joint can be safely loaded to a higher level than the bolted joint without sustaining damage in the composite adherends. The bolted joint yield prediction with the experimental 2% offset yield strength also shows good agreement, especially considering the many simplifications in the analysis.

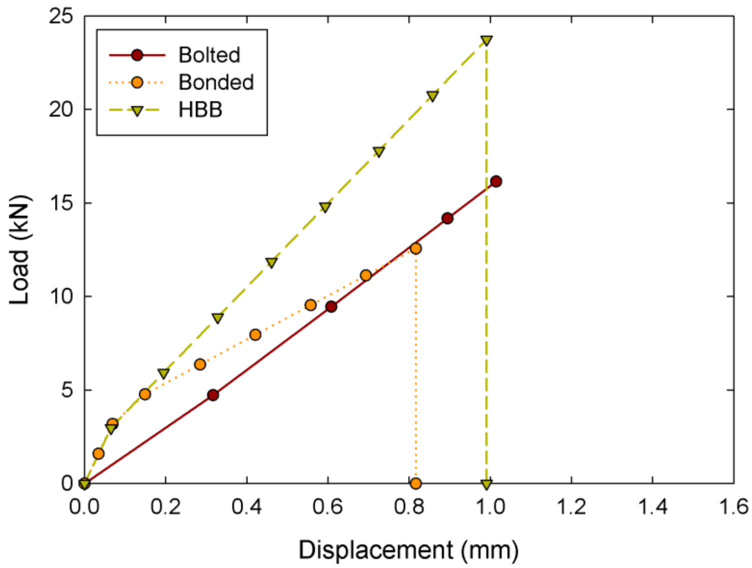

(a) Meshless model prediction

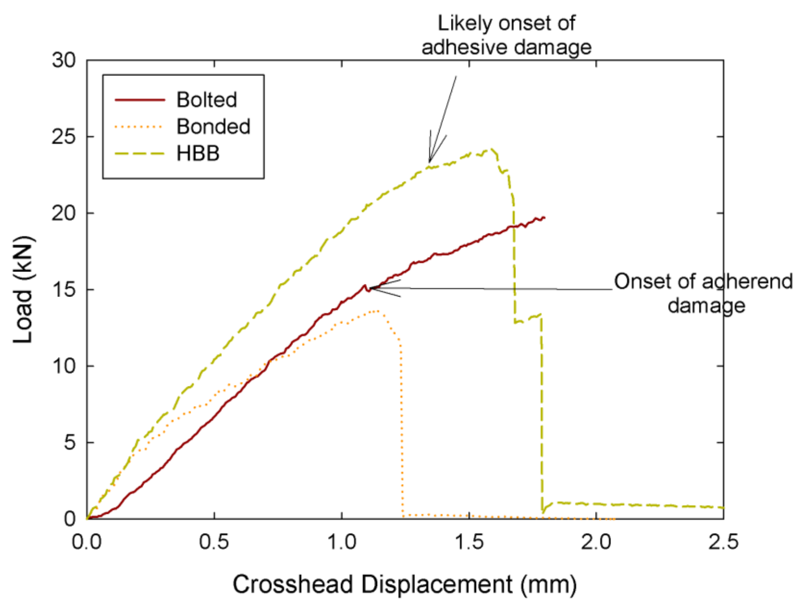

(b) Experimental measurements

Figure 10.14: Comparison between predicted and measured EA9361 joint behaviour

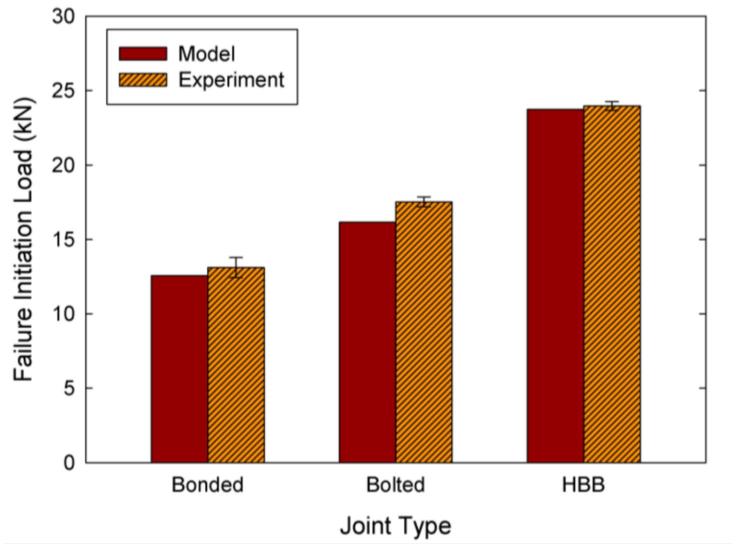

Figure 10.15: Comparison of predicted and experimental failure initiation loads

10.7 Conclusions

Based on the experiment presented in this chapter, the following conclusions can be drawn:

1) The adhesive system (type/thickness) has a major effect on both the absolute and relative stiffness of bonded and hybrid joints.

2) The adhesive system (type/thickness) has a major effect on the relative strength of bonded and hybrid joints.

3) When a ductile, flexible adhesive system is used, load is shared between the adhesive and bolted joint. This can greatly delay adhesive failure compared to a bonded joint and also delay the onset of damage in the composite adherends compared to a bolted joint. This is not the case when a brittle, stiff adhesive system is used.

4) While the ultimate load was not improved compared to the bolted joint for either the FM300-2M or EA9361 hybrids in the present experiment, it is possible to extrapolate from the experimental results or use the hybrid joint model to predict that if an adhesive with a higher strain-to-failure than EA9361 (but with otherwise similar properties) and/or a thicker bondline were to be used, the hybrid joint strength would eventually surpass the bolted joint strength.

5) The energy dissipated by a hybrid joint is not necessarily greater than that which would be dissipated by the underlying bolted joint by itself, and may in fact be significantly less. However, the dissipated energy would generally be expected to be greater than that of the underlying bonded joint by itself.

The hypothesis that the adhesive system has an effect on the hybrid joint performance is clearly supported by the conclusions presented in this section. In addition, the comparison of the experimental results and model predictions demonstrates that, despite its simplicity, the meshless model is able to provide a good basic prediction of the response and strength of bonded and hybrid joints.

Chapter 11: Illustrative Solutions

11.1 Insights into the Plastic Deformation Process

When bonded joints and HBB joints are loaded in uniaxial tension, they experience adhesive stress peaks near the overlap edges. At a critical load level, these high stresses cause the adhesive to locally yield (plasticize). As the load is further increased, the plasticity spreads through the overlap region (assuming sufficient adhesive ductility to allow this process to occur). An analysis was performed of both a bonded joint and a HBB joint loaded in uniaxial tension, to show how the plastic zone starts and develops during loading for both types of joint. The geometry and materials of the joints of Chapter 10 using EA9361 adhesive were used in the analysis.

As can be seen in Figure 11.1, in both cases the onset of plasticity occurs on the overlap edges. It occurs slightly earlier for the hybrid joint than for the bonded joint, which is logical since the average stress in the hybrid joint adhesive is slightly higher. This is because this joint has a smaller bonded area due to the hole cut-out in the overlap. As the load is increased, the plastic region grows from the edges inwards for both types of joint. Eventually, the entire bonded region becomes plastic. Whether the condition of full overlap plasticity can be attained depends critically on the ductility of the adhesive. For brittle adhesives, the adhesive will fail at very low strains and small yielded regions, such as those shown in Figures 11.1-a,b.

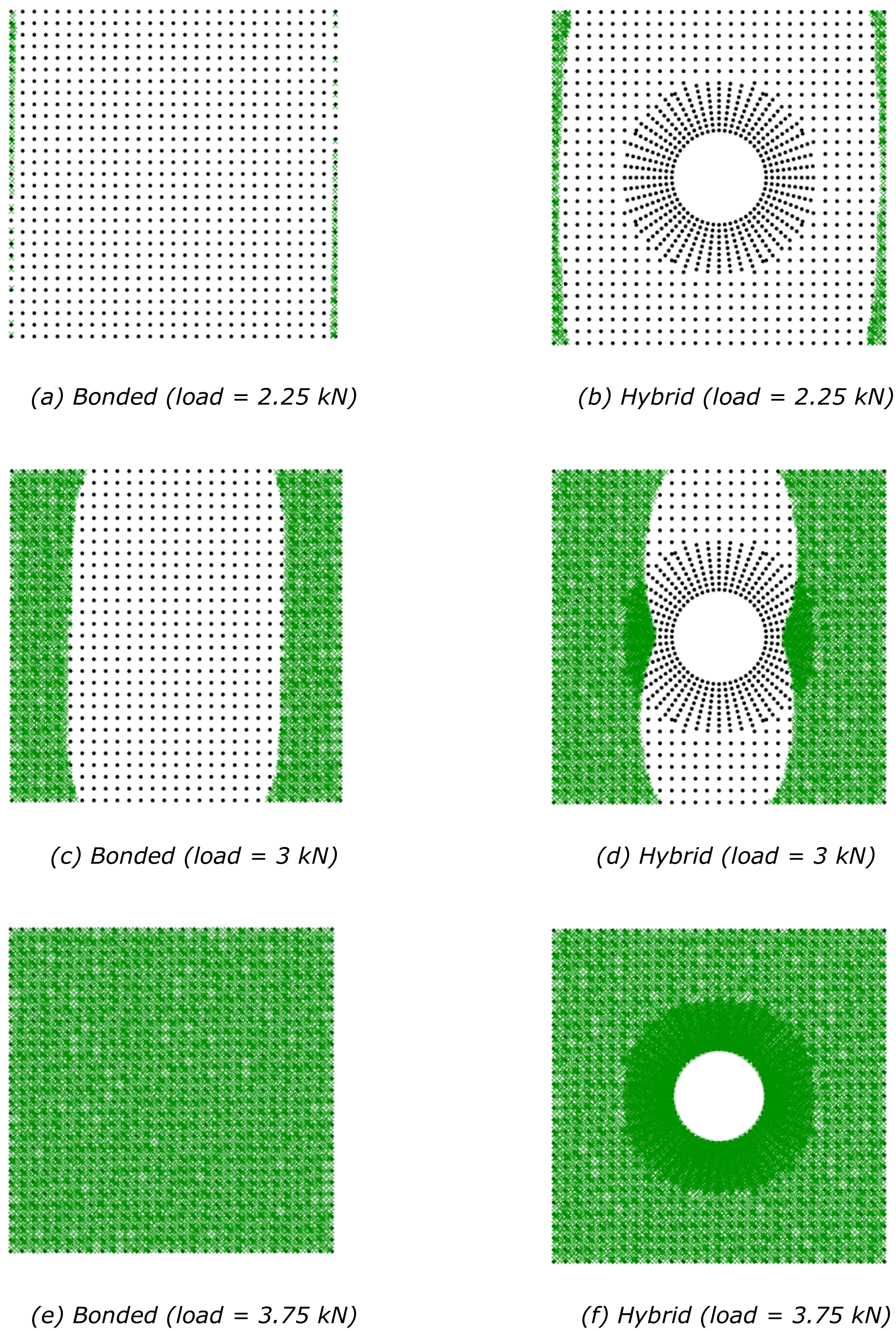

(a) Bonded (load = 2.25 kN)

(b) Hybrid (load = 2.25 kN)

(c) Bonded (load = 3 kN)

(d) Hybrid (load = 3 kN)

(e) Bonded (load = 3.75 kN)

(f) Hybrid (load = 3.75 kN)

Figure 11.1: Evolution of plastic zone of adhesive during loading. Plastic regions in green.

It was previously shown in Chapter 4 that plasticity is very important in transferring load to the bolt. This is because when the overlap region has fully plasticized, as shown in Figures 11.1-e,f, the bonded joint stiffness reduces significantly. This renders the bonded joint stiffness more similar to that of the bolted joint and allows load sharing to occur. As the joint continues to deform following plasticization of the overlap, the strains in the bonded joint increase rapidly until the critical equivalent failure strain is reached. However, in the hybrid joint, the bolt impedes the adhesive deformation and increases the load at which the critical failure strain is reached. Again, it must be kept in mind that this discussion assumes the use of a ductile adhesive.

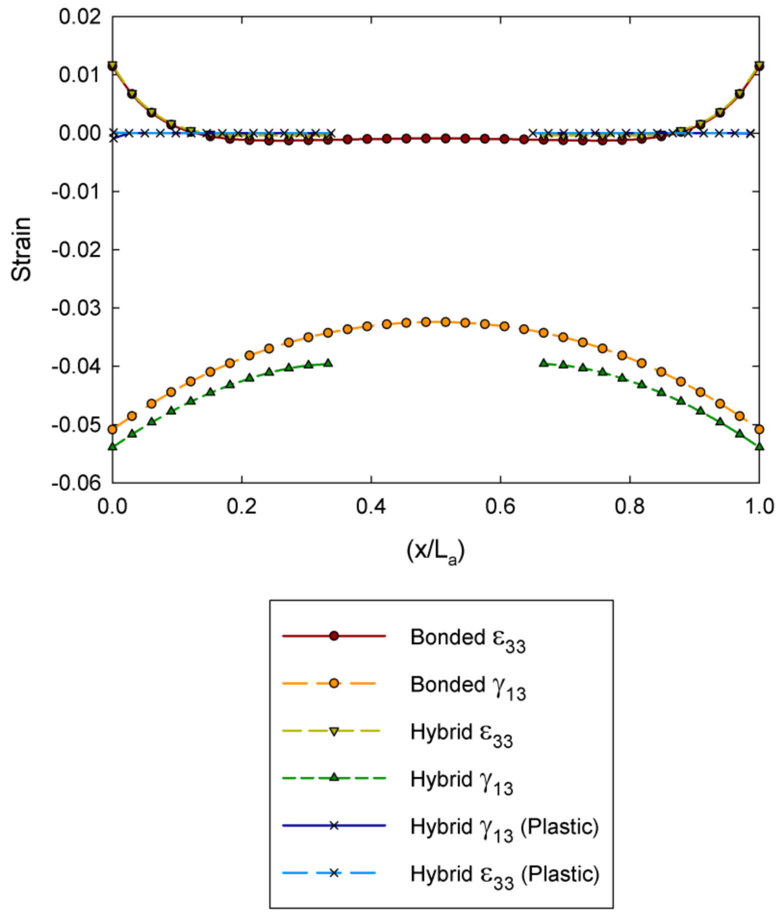

Figure 11.2: Strain components along adhesive centerline in bonded joint and hybrid joint, applied tensile load = 3 kN. Note that the curves for γ_{13} (plastic) and ε_{33} (plastic) nearly coincide.

Figures 11.2 and 11.3 show the effect of hybridizing a bonded joint on the adhesive strain (which is key in ductile adhesive failure), at a 3 kN load and a 7.5 kN load, respectively. As shown in Figure 11.2, at a load of 3 kN the peel and shear strains of the two joints are very similar. By considering the forces in the bolt, it is found that at this stage the bolt does not yet carry any load. The plastic strains, shown only for the hybrid joint, are clustered around the zero strain axis. Almost all of the developed strain is thus elastic.

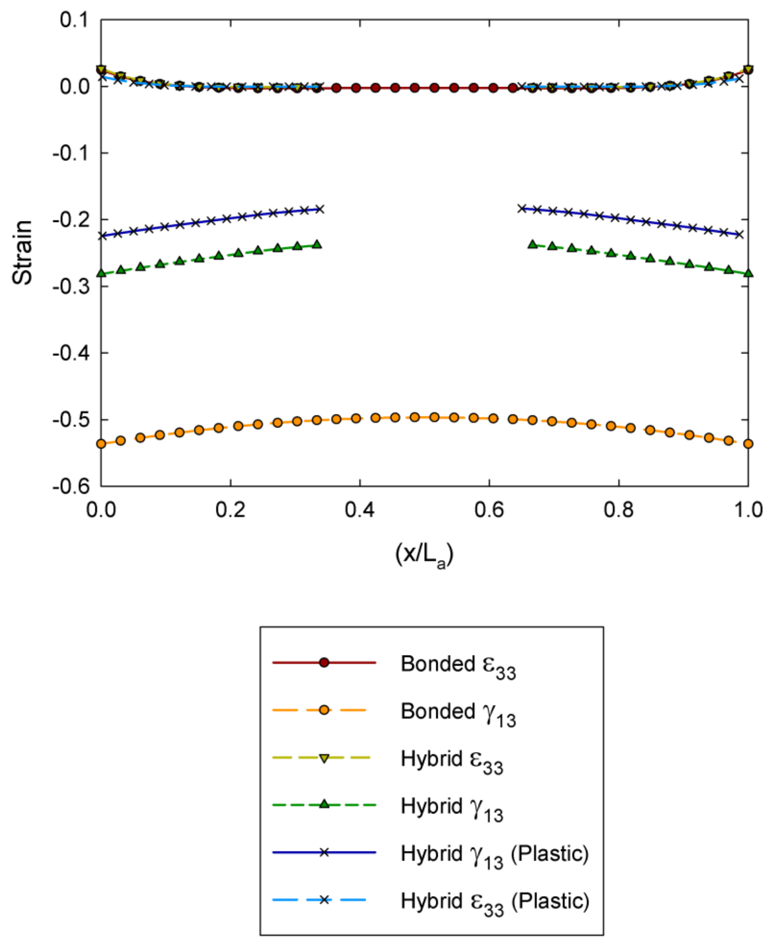

Figure 11.3: Strain components along adhesive centerline in bonded joint and hybrid joint, applied tensile load = 7.5 kN

Next, the higher load of 7.5 kN is considered. The adhesive centerline strains are again shown in Figure 11.3. At this load level, the peel strains between the bonded and hybrid joints are still almost identical. However, the shear strains are vastly different. The bolt, which now carries 29.2% of the overall applied load, has successfully reduced the hybrid joint compliance compared to the bonded joint, and limited the peak adhesive shear strain to 0.282 compared to 0.536 for the bonded joint. It is noted that all peel strains are relatively small and are clustered together near the zero strain axis, and may thus again be difficult to distinguish.

The analysis demonstrates that the addition of the bolt in the studied joint is useful in delaying adhesive failure to a much higher load, as was experimentally observed and described in Chapter 10. It is noteworthy that most of the strain is plastic, as expected (the elastic strains being essentially the same as they were at the onset of plasticity in Figure 11.2). Several salient insights are gleaned from this illustrative solution:

1) Plasticity starts on the overlap edges and grows inwards for both bonded and HBB lap joints in uniaxial tension.

2) The shear strain is the dominant component of strain in both bonded and hybrid bonded-bolted lap joints in uniaxial tension. All other components of strain are typically much smaller. Plastic strains account for a large proportion of the total strain at high load levels.

3) In a hybrid joint with a ductile adhesive and thick enough bondline (such that load sharing may occur) the bolt restricts the developed shear strains in the adhesive and thus helps to increase the load at which failure of the adhesive occurs.

4) Addition of the bolt, without any clamp-up applied, has little effect on the developed peel strains compared to a purely bonded joint.

11.2 Effect of Overlap Length on Joint Strength

The effect of varying the overlap length on the strength of HBB-, bonded-, and bolted joints was analyzed for the EA9361 joint configuration of Chapter 10. The results of this study are shown in Figure 11.4: this figure plots both the adhesive and adherend failure loads for various overlap lengths. Adhesive yielding is not counted as failure (only adhesive crack initiation is considered to be failure). Evidently, the lower of either adhesive or adherend initiation corresponds to the actual initiation load of the joint.

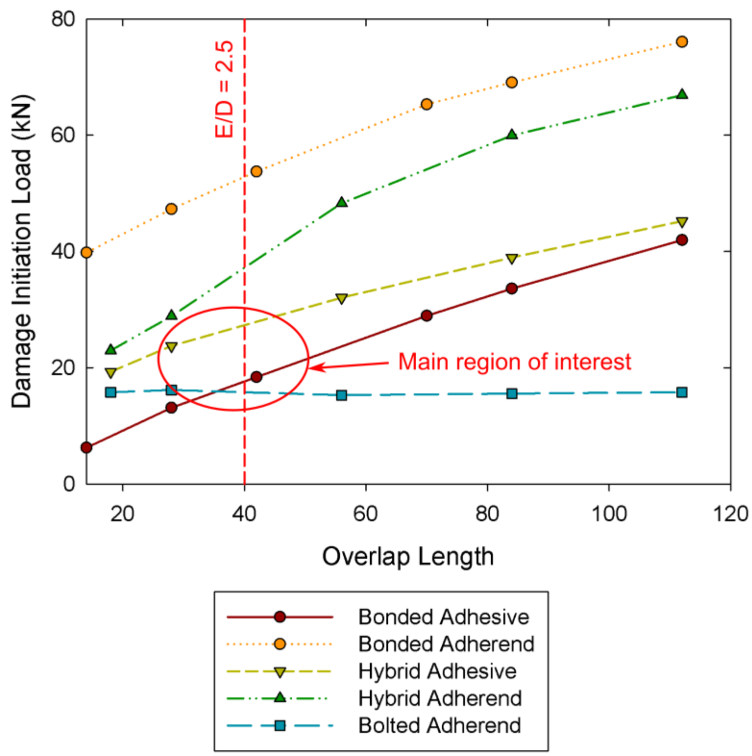

Figure 11.4: Damage initiation load versus overlap length

The analysis predicts that the bolted joint damage initiation load is relatively unaffected by the overlap length. There is actually a very slight decrease between the strengths at short overlap length and medium-long overlap length. The near constant initiation strength prediction is sensible; since the joint is a single-bolt joint, all of the load must be reacted at the bolt hole (whose size does not change).

The average bearing stress and bearing reaction load are thus constant between the different overlap lengths. In addition, since the joint width does not change, the average net-section stress is also constant. The difference is that the detailed adhesive stress field around the hole does change as more material is added behind the hole. The effect of this is to reduce the hoop stress concentration in the hole net-section plane and increase the size and magnitude of the compressive stress region behind the hole. This is clearly shown in Figures 11.5-11.6.

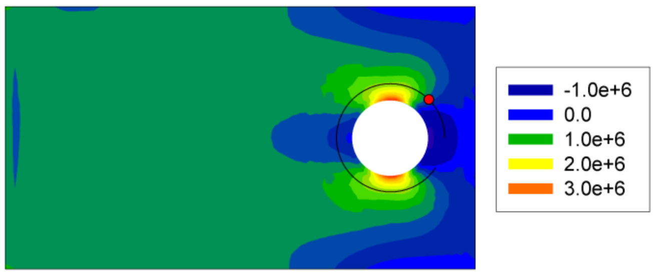

Figure 11.5: N_1 stress resultant (N/m) field in top laminate of bolted joint with 18 mm overlap length, 15 kN of applied load. Red circle indicates failure initiation location, corresponding to a cleavage or shear-out failure mode

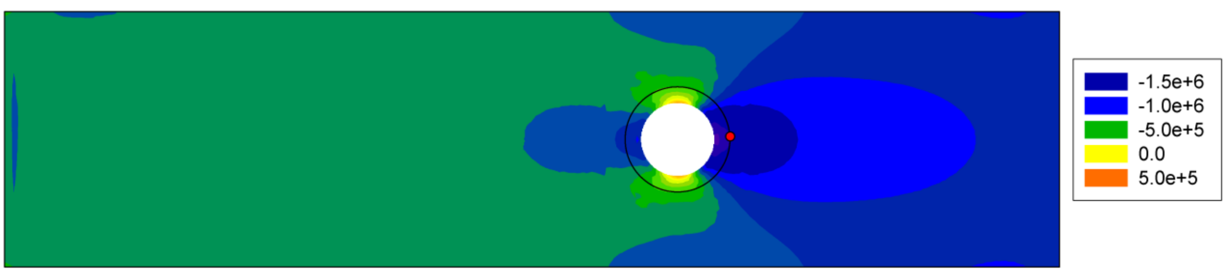

Figure 11.6: N_1 stress resultant (N/m) field in top laminate of bolted joint with 84 mm overlap length, 15 kN of applied load. Red circle indicates failure initiation location, corresponding to a bearing failure mode

Importantly, this is predicted to cause a change in the failure mode, from cleavage/shear-out (as seen in the experiment in Chapter 10) to a bearing failure at longer overlap lengths.

Next, considering the bonded joint, the adhesive is the weak link across the entire range of overlap lengths studied. Again, this is a plausible prediction, since in a bonded joint there are no major stress concentrations in the adherends and the studied adherends have a significant thickness of nearly 5 mm (the reader should of course keep in mind that, as mentioned previously, the analysis does not consider out-of-plane failure of the adherend). Considering the thickness of this laminate, this joint might in a real design situation be a potential candidate for a stepped-lap design, which could reduce the adhesive stress/strain concentrations and significantly increase the bonded joint strength, potentially to a level approaching the adherend strength.

Finally, the effect of overlap length on the HBB joint is considered. Interestingly, it is predicted that the HBB joint, for the joint configuration and adhesive thickness considered, will have damage initiation at a higher load than both the bonded joint and the bolted joint across the entire range of overlap lengths considered. The largest absolute strength advantage over both of the underlying joint simultaneously is observed at a relative short overlap length of 36 mm (E/D = 2.25). It is predicted that the hybrid joint will, for this overlap length, carry 26 kN of load at failure initiation, compared to only around 16 kN for the underlying joints separately.

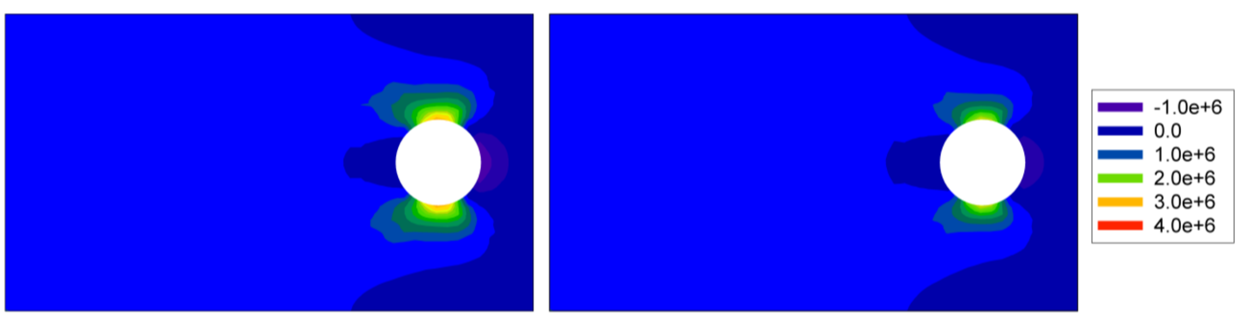

(a) Bolted joint (max. value = 3.52e+6) *(b) Hybrid joint (max. value = 2.55e+6)*

Figure 11.7: N_1 stress resultant in top laminate of bolted joint and HBB joint, 15 kN of applied load

The reason for this predicted strength improvement is elucidated in Figures 11.7-11.8, using the joints with 18 mm overlap length as an example. In Figure 11.7, the adherend stress resultants in the bolted joint and the HBB joint are compared. As can be seen, the stress concentration in the HBB joint is significantly reduced, by -27.6% compared to the bolted joint. This is a result of the adhesive transferring about one-third of the overall load (5.76 kN), thus relieving the hole contact stresses considerably and improving the adherend strength of the HBB joint compared to the bolted joint. Meanwhile, Figure 11.8 compares the adhesive equivalent von Mises strains in the bonded joint and the HBB joint. This time, it is evident that the HBB joint develops significantly smaller strains compared to the bonded joint. This is the result of the bolt restricting excessive deformation of the adhesive, and explains the improved adhesive strength of the HBB compared to the bonded joint.

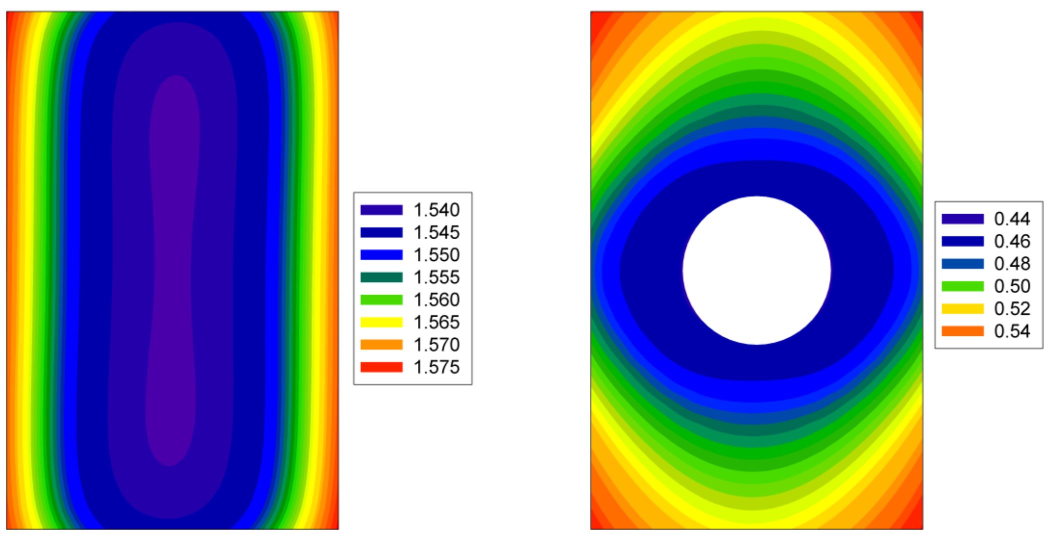

(a) Bonded joint (max. value = 1.58) *(b) Hybrid joint (max. value = 0.552)*

Figure 11.8: Equivalent von Mises strain in the adhesive of bonded joint and HBB joint, 15 kN of applied load

Another important observation from Figure 11.6 is that as the overlap length increases, the benefit of hybridization on the adhesive failure initiation load diminishes. Indeed, at an overlap length of 112 mm, the adhesive failure initiation loads of the bonded joint and HBB joint are almost identical. The reason for this is hypothesized to be as follows, supported by the analysis. In single-lap bonded joints with a long adhesive overlap, there is a significant strain gradient in the overlap, which increases with overlap length. In other words, significant strain develops on the overlap edges while there is much less strain at the center of the bonded region. Meanwhile, in the studied joint design, the bolt is located at the center of the overlap. It is recalled that the adhesive strain is directly related to the relative displacement of the adherends, and thus to achieve load transfer and the benefits of hybridization, there must be significant strain at the bolt location. However, when this occurs in a joint with a long overlap, the strain at the overlap edges has already become so high that it is approaching failure. Thus, only very limited load transfer can be achieved prior to adhesive failure. When the overlap length becomes long enough, the adhesive will actually fail before any load is transferred to the bolt at all.

The proposed hypothesis is illustrated with an example in Figure 11.9. Plotted is the *normalized* total adhesive shear strain along the adhesive centerline for a hybrid joint with 56 mm overlap and one with a 112 mm overlap. Both joints are loaded with the same average adhesive stress, i.e., $F/A_a = 8$ MPa. It is clear that the strain distribution in the long overlap is less uniform than in the shorter overlap. In the 112 mm overlap, the strain at the overlap edges is 2.4 times greater than at the bolt. In the 56 mm overlap, this factor is only around 1.6. These figures strongly support the proposed explanation for why there is a diminished benefit to hybridizing for very long overlap lengths. Importantly, the observed behaviour also suggests that by placing bolts near the overlap edges where the strains are relatively high, instead of at the center where they are low, further improvements may be achieved in joints with long overlaps. The salient conclusions that can be drawn from the present illustrated solution are thus:

1) Hybridization can, for joints with a flexible, ductile adhesive and relatively thick bondline, significantly delay quasi-static failure initiation across a range of overlap lengths.

2) This beneficial effect is decreased at long overlap lengths, due to significant adhesive strain gradients that occur in joints with long overlaps. This causes

adhesive failure to occur before any substantial load can be transferred to a centrally located bolt.

3) Placement of a bolt nearer the overlap edges rather than centrally, in joints with long overlaps, is likely to increase bolt load transfer and thereby further delay adhesive failure initiation.

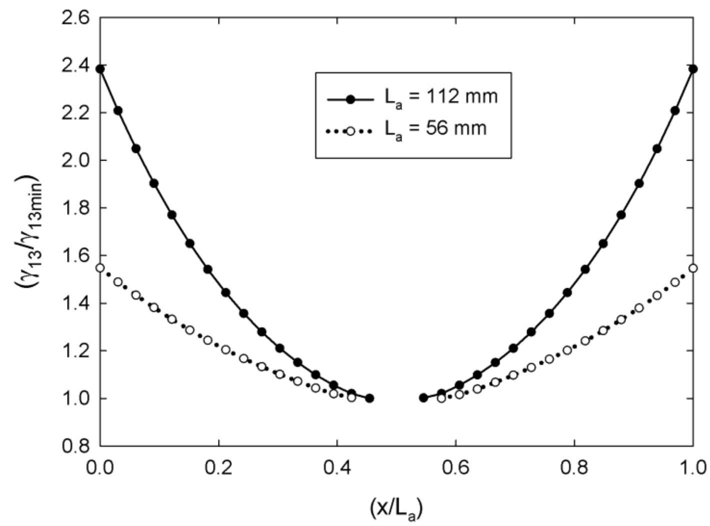

Figure 11.9: Effect of overlap length L_a on the normalized strain distribution along the adhesive centerline

11.3 Multi-Bolt Joints

In this illustrative solution, the effect of adding two bolts into a moderately long overlap is compared with adding only a single, centrally located bolt. Considering the example of section 11.2, it is likely that more load will be transferred to the bolts using such an approach, and adhesive failure will be delayed. The same geometry, materials and loading as example 11.2 were analyzed for a 56 mm overlap. The two bolts were installed at 1/3 and 2/3 of the distance along the overlap centerline, respectively (E/D = 2.33), while the 1-bolt joint had a centrally located bolt. The predicted load transferred by the bolts is shown in Figure 11.10. It is clear that, as suspected, the 2-bolt joint experiences a far greater level of bolt load transfer than the 1-bolt joint.

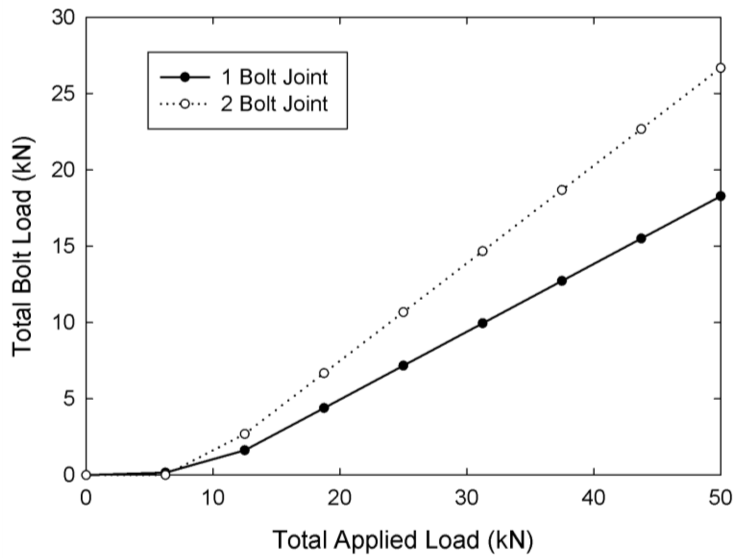

Figure 11.10: Bolt load in 1-bolt and 2-bolt hybrid joint

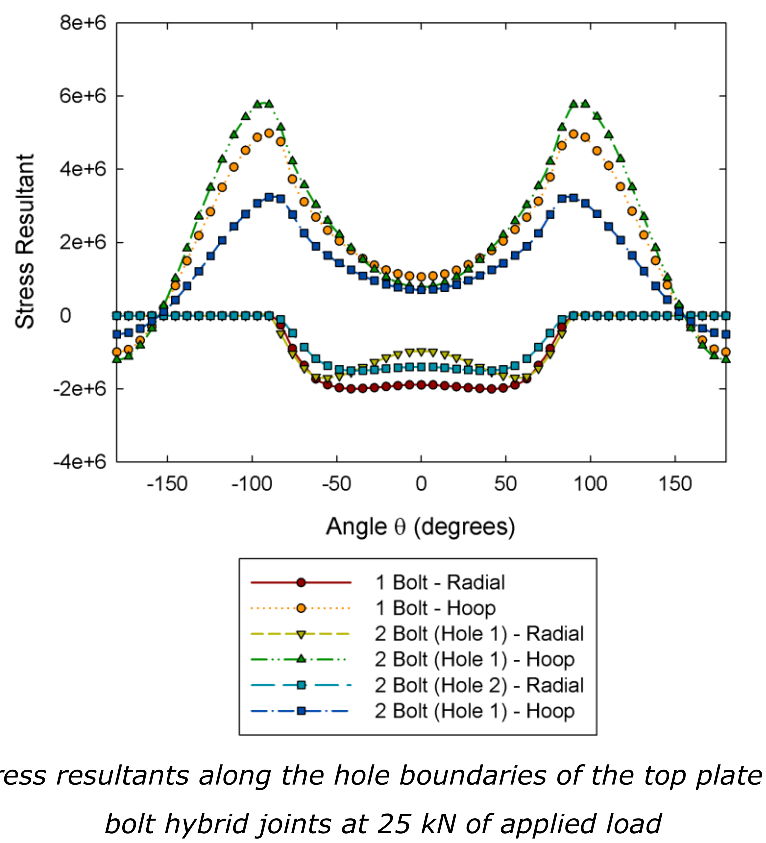

Figure 11.11: Stress resultants along the hole boundaries of the top plate for 1-bolt and 2-bolt hybrid joints at 25 kN of applied load

Figure 11.11 shows the laminate stress resultants along the hole boundaries of the top plate for both joints at 25 kN of applied load. It is clear that the radial stresses are highest in the 1-bolt joint, despite this joint experiencing a much lower overall bolt load. This is logical, since in the 2-bolt joint the load is reacted on two separate bolt holes, resulting in lower contact stresses. Note that in the 2-bolt joint, the left hole (hole 1) has significantly higher peak hoop stresses than the right hole (hole 2).

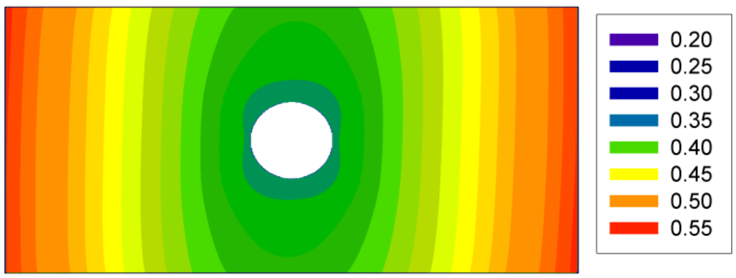

(a) 1-Bolt joint

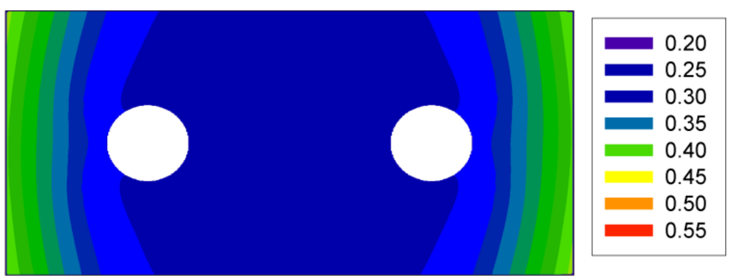

(b) 2-Bolt joint

Figure 11.12: Adhesive equivalent von Mises strain in single-bolt and double-bolt hybrid joints at 25 kN of applied load

The equivalent von Mises strains in the overlap region for both joints are also compared in Figure 11.12, at the same load of 25 kN. It is clear that the strains are higher in the 1-bolt joint, with a peak adhesive equivalent von Mises strain of around 0.55 versus around 0.4 for the 2-bolt joint. An additional interesting feature of the strain field in these two joints is that the 2-bolt joint has a large region of relatively low strain between the bolts. In the 1-bolt joint, the entire overlap region is highly strained. Nevertheless, the 2-bolt joint has a higher bolt-load transfer than the 1-bolt joint. The low strain region could prove to be beneficial in joint design, conceivably improving the fatigue life and thus durability of the joint when subjected to cyclic loading.

The load-displacement behaviour of the two joints is compared in Figure 11.13. It is evident that the 2-bolt joint is significantly stiffer than the 1-bolt joint. This also explains why this joint has a higher bolt load transfer.

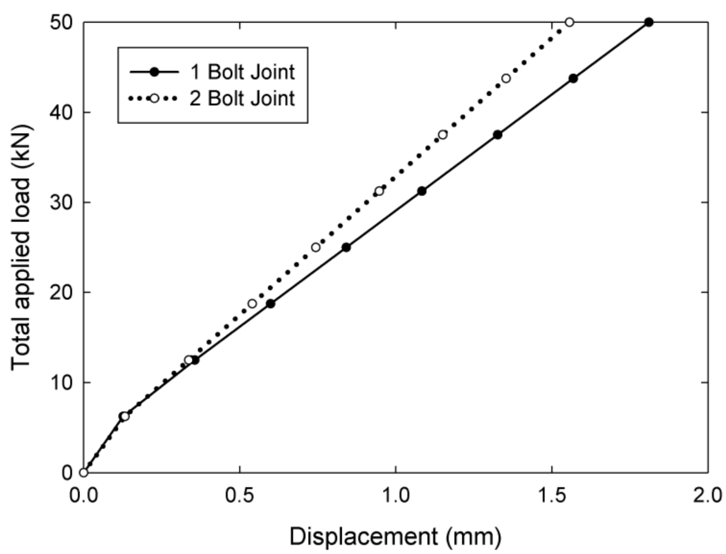

Figure 11.13: Comparison of single-bolt and double-bolt load displacement curves

Finally, the predicted strengths of the two joints are compared in Table 11.1. As anticipated, the strength of the 2-bolt joint at failure initiation is significantly greater. It is predicted that joint failure will occur at 41443 N instead of 32062 N for the single bolt joint, a 29% strength improvement. This strength surpasses even the strength of the HBB joint with a 112 mm overlap from section 11.2, while requiring only 56 mm of overlap. The adherend initiation load is lowered by only 2%, being critical at hole 1. This load remains well above the adhesive initiation load. The similarity in the adherend initiation is explained by Figure 11.11; the hoop stress resultants of the laminates of both joints at hole 1 at a 45° angle are almost identical, causing both to have the first damage initiation in a shear mode at a similar load level.

Table 11.1: Comparison of failure initiation loads of 1-bolt and 2-bolt hybrid joints

Joint Type	**Adherend Initiation (kN)**	**Adhesive Initiation (kN)**	**Overall Initiation Strength (kN)**
1-Bolt Hybrid	48298	32062	32062
2-Bolt Hybrid	47440 (hole 1)	41443	41443

11.4 Effect of Bolt-Hole Clearance

To demonstrate the effect of bolt-hole clearance on an active HBB joint, three cases are considered. In each case, the joint geometry and materials correspond to those of the EA9361 HBB joint from Chapter 10. A 40 micron interference fit, 25.4 micron sliding fit (representative of high precision drilling) and 100 micron running fit (representative of sloppy drilling by aerospace industry standards) were analyzed. The predicted bolt load transfer for all three clearances is compared in Figure 11.14.

This plot confirms that the bolt load transfer is slightly delayed by having a larger bolt-hole clearance compared to a smaller clearance. This is likely to decrease the joint strength somewhat; a strength analysis was thus also performed. From this analysis, it was found that the adhesive initiation loads are critical for both clearance fit joints, at 21.5 kN and 23.8 kN, respectively. The large clearance is thus predicted to reduce the joint strength by 10.6% compared to a more controlled clearance, which is a considerable impact. Nevertheless, even with a sloppy hole tolerance the hybrid is still significantly stronger than the underlying bonded joint (the latter has a strength of only 12.6 kN).

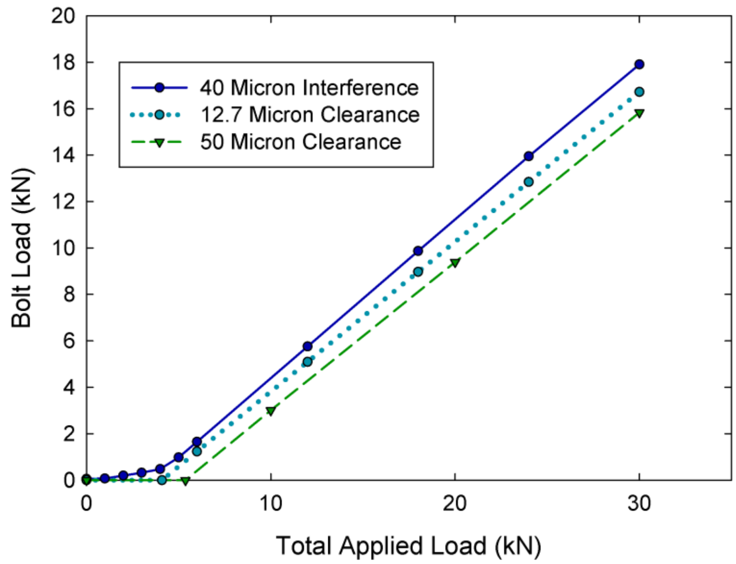

Figure 11.14: Effect of bolt-hole clearance on bolt load transfer. Note that a 40 micron interference corresponds to negative clearance of 20 microns. Similarly for other interference values

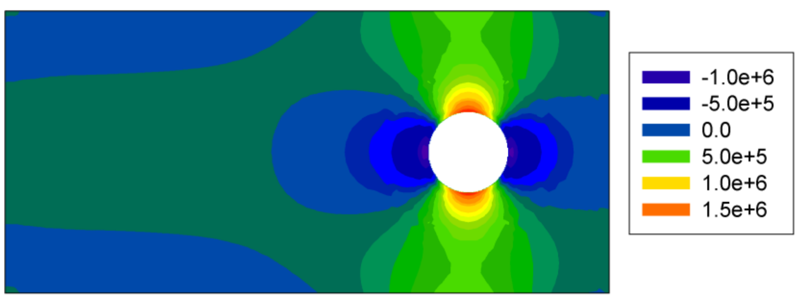

Figure 11.15: Adherend N_1 stress resultant field (N/m) due to 40 micron bolt-hole interference only (no external loading)

Finally, the effect of interference is also considered. To this end, a bolt-hole interference of 0.5% (40 microns) was applied to the hole. The adherend N_1 stress resultant is plotted in Figure 11.15. As can be seen, the interference creates an initial stress state in the composite adherend. The small amount of interference also creates stresses and strains in the adhesive, but not enough to cause plasticity.

Figure 11.14, which plots the bolt load transfer for the three cases, shows that the joint with the interference fit actually experiences a similar level of bolt load at low loads to the low clearance hole. However, the interference results in a stiffer bolted joint, which is logical as it can effectively be considered that the laminate is "gripping" the bolt shank as a result of the interference. This leads to a higher level of bolt load transfer and lower adhesive strains. This effect is clearly visible in Figure 11.14 and is reflected in the higher slope of the interference joint to that of the clearance joints.

Based on another strength analysis, it was found that failure of the interference fit joint was predicted to take place due to adhesive crack initiation at a load of 26.8 kN, representing a 12.7% improvement compared to the high precision hole and a 24.9% improvement compared to the sloppy hole. Salient observations from this illustrative example are thus:

1) As clearances increase, bolt load transfer is delayed. This leads to greater adhesive strains and can significantly reduce the joint strength. In a HBB joint clearances should thus be minimized.

2) Bolt-hole interference causes the opposite effect and can improve the joint strength by reducing joint compliance and increasing joint stiffness, thus limiting the adhesive strain at a given load.

3) Nevertheless, even with sloppy clearances, significant strength improvements compared to the underlying bonded joint can still be achieved.

11.5 Effect of Bolt Clamp-Up

The effect of bolt clamp-up on adhesive peel stress in a HBB joint is studied in this final illustrative solution. A 4 kN clamp-up load is applied to the bolt prior to the application of a tensile load to the joint. The peel stress field in the adhesive following bolt clamp-up is shown in Figure 11.16-a. As can be seen, in the region immediately underneath the bolthead, there is a negative peel state of approximately 8 MPa. This stress rapidly increases at the bolthead edge and returns to approximately zero in the far-field (unclamped region away from the bolt).

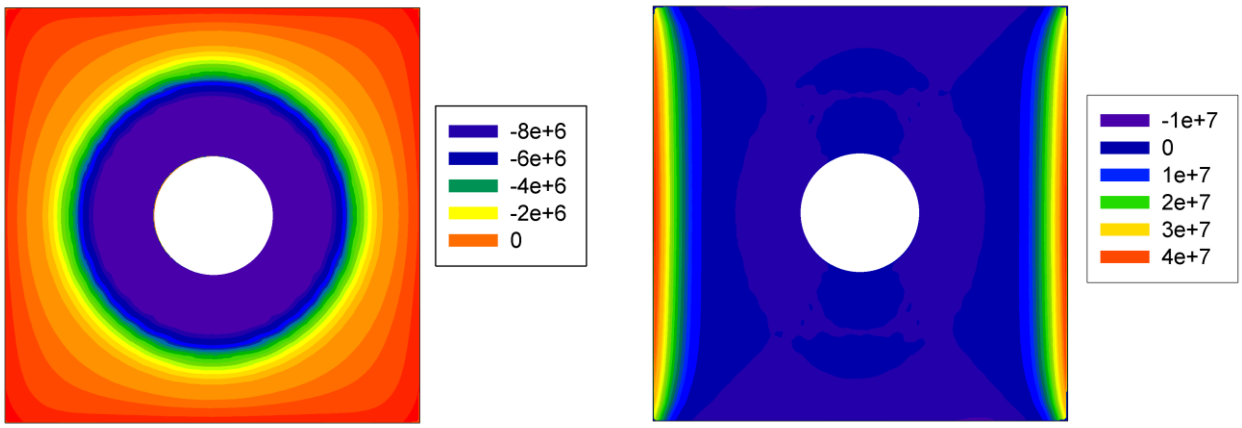

(a) 0 kN applied tensile load

(b) 15 kN applied tensile load

Figure 11.16: Peel stress (Pa) in adhesive of HBB joint, 4 kN clamp-up load

Following the application of a 15 kN tensile load, the peel stress state shown in Figure 11.16-b is obtained. The usual peel stress peaks at the overlap edges are clearly visible. However, in the washer region a compressive stress state is maintained.

To contrast the clamp-up solution, an analysis without any clamp-up was also performed. The results, plotted in Figure 11.17, show that there is a 0 MPa peel stress prior to tensile loading. This is expected given the absence of clamp-up. Following the application of a 15 kN tensile load, the region near the center of the overlap experiences negligible adhesive peel stress, while significant peel stress concentrations once again occur along the overlap edges in the loading direction.

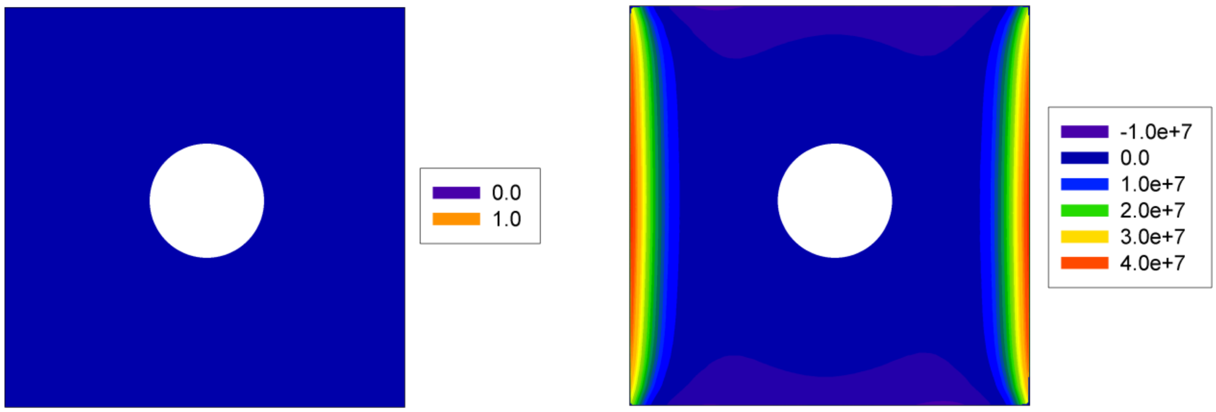

(a) 0 kN applied tensile load *(b) 15 kN applied tensile load*

Figure 11.17: Peel stress (Pa) in adhesive of HBB joint, 0 kN clamp-up load

Clamp-up is thus able to create a compressive stress state that persists during joint loading; the effect of this on joint fatigue may be significant, as was demonstrated experimentally by Fu et al. [45] and more recently by Chowdhury et al. [118]. The reason for this is that crack propagation is generally inhibited when the material is in a compressive state, since the crack cannot easily open. Although the compressive stress in the laminate cannot be accurately gauged from the current model (since the Mindlin-Reissner formulation does not account for transverse laminate extension), based on equilibrium consideration it is a given that there must also be compression in the composite laminate underneath the washer. Thus, the clamp-up compression could slow the propagation of laminate cracks and delaminations underneath the bolthead, where the laminate stresses are highest and failure is most likely.

Chapter 12: Conclusions

In the preceding chapters, a number of open questions have been considered. Insights into these questions have been considered in the thesis:

1) In which circumstances is it useful to hybridize bonded and bolted joints? (Chapters 4 and Chapter 11)

2) What are the most important factors contributing to load sharing in hybrid joints? (Chapter 4)

3) How can hybrid bond joints be efficiently modelled and can a basic prediction of their static strength be obtained? (Chapters 3 and 5-10)

4) How much energy do HBB joints absorb in comparison to their constituents as a function of the adhesive system? (Chapter 10)

5) What are the effects of basic design choices (multi-bolt joints, clamp-up, bolt-hole clearance) on HBB joint response and/or strength? (Chapter 11)

Referring back to the thesis objectives set out in sections 2.9.1-2.9.3, these have been suitably addressed by points 2-4 in the above list.

12.1 Original Contributions

Many original developments and ideas originated from trying to answer these questions, including:

- The first experimental HBB joint load sharing measurement of an “academic” hybrid joint (i.e., a hybrid joint with no spew fillet, corresponding to an important assumption of classical analytical bonded joint models)

- A new finite element approach for predicting load sharing

- The first quantitative global sensitivity analysis of load sharing in hybrid joints

- An original extension of Goland and Reissner’s adhesive kinematic model, rendering it fully compatible with the mathematical theory of nonlinear elasticity

- A new mathematical model of a HBB joint that simplifies the physics to the essentials, but nevertheless accounts for most of the major, complex behaviours of these joints

- Solution of this mathematical model using the meshless Galerkin method (first known application of this method to the analysis of structural joints)

- Identification of optimal meshless parameters for the HBB joint problem

- Clarification of existence of the meshless interpolation

- The first comprehensive review in the scientific literature of hybrid bonded-fastened joints, bringing together two bodies of work that have much in common but whose proponents are largely ignorant of one another

The original contributions of this thesis resulted in a number of publications in peer-reviewed journals, as well as conference publications. These are listed below.

12.1.1 Journal papers

Bodjona K, Lessard L. "Hybrid bonded-fastened joints and their application in composite structures: A general review." Journal of Reinforced Plastics and Composites 2016; 35(9): 764-781.

Bodjona K, Lessard L. "Nonlinear static analysis of a composite bonded/bolted single-lap joint using the meshfree radial point interpolation method." Composite Structures 2015; 134: 1024-1035.

Bodjona K, Lessard L. "Load sharing in single-lap bonded/bolted composite joints. Part II: Global sensitivity analysis." Composite Structures 2015; 129: 276-283.

Bodjona K, Lim GH, Raju KP, Lessard L. "Load sharing in single-lap bonded/bolted composite joints. Part I: Model development and validation." Composite Structures 2015; 129: 268-275.

Bodjona K, Lessard L. "Strength and energy absorption of composite single-lap bonded/bolted joints." Journal of Reinforced Plastics and Composites 2016 (Manuscript in preparation).

Raju K, Bodjona K, Lim G, Lessard L. Improving load sharing in hybrid bonded/bolted composite joints using an interference-fit bolt." Composite Structures 2016; 149: 329-338.

12.1.2 Conference papers

Bodjona K, Lessard L. "Quasi-static strength of hybrid bonded/bolted single-lap joints" ECCM 17th European Conference on Composite Materials, Munich, Germany, June 26-30, 2016.

Bodjona K, Lim GH, Raju KP, Lessard L. "Numerical and Experimental Investigation of Load Sharing in Composite Bonded-Bolted Joints" ICCM 20th International Conference on Composite Materials, Copenhagen, Denmark, July 19-24, 2015.

Bodjona K, Lessard L. "Meshless Analysis of Stresses in a Single Lap Bonded-Bolted Composite Joint." ICCS 18th International Conference on Composite Structures, Lisbon, Portugal, June 15-18, 2015.

12.2 Concluding remarks

The work in this thesis can in some ways be considered a feasibility study of the fundamental viability of HBB joints. Based on the presented investigation and results, it is the author's belief that this is a potentially viable technology. A number of final concluding remarks are listed below, based on the results of the preceding chapters:

1) In order to achieve any sort of weight advantage by means of hybrid bonded-bolted joining of aerospace structures, it is imperative that the target strength and minimum acceptable residual strength following adhesive failure are different. (For aerospace structures these might, for example, correspond to ultimate load and limit load, respectively) The difference between these two loads is where an advantage may be gained, by relying on the bolted joint to provide the limit strength (certification requirement) and taking advantage of hybridization to attain the ultimate strength.

2) Hybridization only leads to an improvement in the static strength over the underlying joints when there is load sharing between the adhesive and bolt. In the experiment of Chapter 10, significant load sharing was induced and improved the underlying bonded joint ultimate strength by 91% and the underlying bolted joint yield strength by 18%. In the absence of load

sharing, hybridization was actually found to lower the strength of the underlying joints.

3) Load sharing is most effectively achieved by lowering the bonded joint stiffness, which for an elastoplastic adhesive is most effectively done by
   - Yielding the adhesive (by means of low yield strength, short overlap length) since the plastic tangent modulus is typically an order of magnitude (or more) lower than the Young's modulus and
   - Increasing the adhesive thickness

4) The reduction or potential elimination of bolt-hole clearance in a load sharing joint can significantly delay ductile adhesive failure and improve the joint strength. It does this by restricting the developed plastic strain in the adhesive and delaying its failure. Optimal hybrid joints will therefore have little to no clearance or potentially some interference.

5) Contrary to expectation, hybrid bonded-bolted joints do not necessarily absorb more energy during fracture than their constituents separately. In the experiment of Chapter 10, it was shown that while more energy was absorbed during fracture compared to the underlying bonded joint, the underlying bolted joint by itself absorbed the most energy of all three joints.

6) The relatively stiff initial response that is characteristic of both brittle and ductile adhesives should not necessarily be looked upon as problematic. This initial stiffness allows the adhesive to actually transmit notable structural load. It must however be complemented by a secondary, less stiff response in order to allow load to be transferred to the bolt. Although in this thesis this behaviour was due to plasticity, ideally an adhesive should be identified where this behaviour is due to other underlying behaviour that does not lead to permanent deformation. In other words, the ideal adhesive should possess reversible large strain behaviour, due to for example hyperelasticity. This is

the case for many elastomeric adhesives (the issue being to find an elastomer with sufficient initial stiffness!).

7) Importantly, the mathematical model proposed in Chapter 5 of this thesis is fully compatible with theories of hyperelasticity and could thus be adapted with relative ease for use in future design studies and/or research with elastomeric adhesives.

12.3 Future Outlook

While the fundamental concept of hybrid bonding-bolting has been deemed to be viable, there are a few potential stumbling blocks that have not as yet been investigated and that could prove to be problematic in the further development of these joints. These include:

- Rate effects
- Temperature effects
- Certification
- Inspectability
- Cost
- Fatigue

Further research into these issues is of great importance in order to advance the technology readiness level of HBB joining.

Bibliography

1. Roeseler, W.G., et al. *Composite structures: the first 100 years*. in *16th International Conference on Composite Materials*. 2007.
2. Boeing. 2014; 787 Program Fact Sheet]. Available from: http://www.boeing.com/boeing/commercial/787family/programfacts.page.
3. Wood, K., *Wind turbine blades: Glass vs. carbon fiber*, in *CompositesWorld*. 2012, Gardner Business Media, Inc.
4. *Compete to Win: Final Report June 2008*. 2008, Industry Canada: Ottawa ON.
5. Messler, R.W., *Joining of materials and structures: From pragmatic process to enabling technology*. 2004: Butterworth-Heinemann.
6. Hart-Smith, L.J., *The key to designing efficient bolted composite joints.* Composites, 1994. **25**: p. 835-837.
7. Gardiner, G., *Certification of bonded composite primary structures*, in *CompositesWorld*. 2014, Gardner Business Media, Inc.
8. Ilcewicz, J.T.K.S.G.D.L., *Assessment of industry practices for aircraft bonded joints and structures*. 2005, National Institute for Aviation Research (NIAR): Wichita, KS. p. 243.
9. Matthews, F.L., P.F. Kilty, and E.W. Godwin, *A review of the the strength of joints in fibre-reinforced plastics. Part 2. Adhesively bonded joints.* Composites, 1982. **13**(1): p. 29-37.
10. Pearce, G.M., et al., *Experimental investigation of dynamically loaded bolted joints in carbon fibre composite structures.* Applied Composite Materials, 2010. **17**(3): p. 271-291.
11. *Code of Federal Regulations 14, Section 25.601*, FAA, Editor.
12. Brotherhood, C., B. Drinkwater, and S. Dixon, *The detectability of kissing bonds in adhesive joints using ultrasonic techniques.* Ultrasonics, 2003. **41**(7): p. 521-529.
13. Pethrick, R., *Bond inspection in composite structures*, in *Comprehensive Composite Materials*, A. Kelly and C. Zweben, Editors. 2000, Pergamon: Oxford. p. 359-392.
14. Tserpes, K., G. Peikert, and I. Floros, *Crack stopping in composite adhesively bonded joints through corrugation.* Theoretical and Applied Fracture Mechanics, 2015.
15. Tong, L., et al., *Failure of transversely stitched RTM lap joints.* Composites Science and Technology, 1998. **58**(2): p. 221-227.
16. Hart-Smith, L.J., *Design methodology for bonded-bolted composite joints vol. 1: analysis derivations and illustrative solution*. 1982, McDonnel Douglas Corporation.
17. Bois, C., et al., *An analytical model for the strength prediction of hybrid (bolted/bonded) composite joints.* Composite Structures, 2013. **97**: p. 252-260.
18. Kelly, G., *Load transfer in hybrid (bonded/bolted) composite single-lap joints.* Composite Structures, 2005. **69**: p. 35-43.
19. Kelly, G., *Quasi-static strength and fatigue life of hybrid (Bonded/bolted) composite single-lap joints.* Composite Structures, 2006. **72**: p. 119-129.

20. Adams, R.D. and P. Cawley, *A review of defect types and nondestructive testing techniques for composites and bonded joints.* NDT International, 1988. **21**(4): p. 208-222.
21. Adams, R.D. and P. Cawley, *Strength predictions for lap joints, especially with composite adherends. A review.* The Journal of Adhesion, 1989. **30**(4): p. 219-242.
22. Camanho, P.P. and F.L. Matthews, *Stress analysis and strength prediction of mechanically fastened joints in FRP: a review.* Composites Part A: Applied Science and Manufacturing, 1997. **28**(6): p. 529-547.
23. Godwin, E.W. and F.L. Matthews, *A review of the strength of joints in fibre-reinforced plastics. Part 1. Mechanically fastened joints.* Composites, 1980. **11**(3): p. 155-160.
24. Thoppul, S.D., J. Finegan, and R.F. Gibson, *Mechanics of mechanically fastened joints in polymer-matrix composite structures – a review.* Composites Science and Technology, 2009. **69**(4): p. 301-329.
25. Bodjona, K. and L. Lessard, *Hybrid bonded-fastened joints and their application in composite structures: A general review.* Journal of Reinforced Plastics and Composites, 2016. **35**(9): p. 764-781.
26. Comer, A.J., et al., *Thermo-mechanical fatigue analysis of liquid shim in mechanically fastened hybrid joints for aerospace applications.* Composite Structures, 2012. **94**: p. 2181-2187.
27. Huhne, C., et al., *Progressive damage analysis of composite bolted joints with liquid shim layers using constant and continuous degradation models.* Composite Structures, 2010. **92**: p. 189-200.
28. Zhai, Y., D. Li, and L. Wang, *An experimental study on the effect of joining interface condition on bearing response of single-lap, countersunk composite-aluminum bolted joints.* Composite Structures, 2015. **134**: p. 190-198.
29. Matsuzaki, R., M. Shibata, and A. Todoroki, *Improving performance of GFRP/aluminum single lap joints using bolted/co-cured hybrid method.* Composites Part A, 2008. **39**: p. 154-163.
30. Graham, D.P., et al., *The development and scalability of a high strength, damage tolerant, hybrid joining scheme for composite-metal structures.* Composites Part A, 2014. **64**: p. 11-24.
31. International, A., *Standard Test Method for Apparent Shear Strength of Single-Lap-Joint Adhesively Bonded Metal Specimens by Tension Loading (Metal-to-Metal)*, in *ASTM D1002-10*. 2010.
32. International, A., *Standard test method for strength properties of adhesives in shear by tension loading of single-lap-joint laminated assemblies*, in *ASTM Standard D3165*. 2014.
33. Li, G., et al., *Static strength of a composite butt joint configuration with different attachments.* Composite Structures, 2012. **94**: p. 1736-1744.
34. Hart-Smith, L.J., *Mechanically-fastened joints for advanced composites – phenomenological considerations and simple analyses*, in *Fibrous Composites in Structural Design*, E.M. Lenoe, D.W. Oplinger, and J.J. Burke, Editors. 1980, Plenum Press. p. 543-574.

35. Chowdhury, N.M., et al., *Static and fatigue testing thin riveted, bonded and hybrid carbon fiber double lap joints used in aircraft structures.* Composite Structures, 2015. **121**: p. 315-323.
36. Chowdhury, N.M., et al., *Experimental and finite element studies of thin bonded and hybrid carbon fibre double lap joints used in aircraft structures.* Composites Part B, 2016. **85**: p. 233-242.
37. Di Franco, G., L. Fratini, and A. Pasta, *Analysis of the mechanical performance of hybrid (SPR/bonded) single-lap joints between CFRP panels and aluminum blanks.* International Journal of Adhesion and Adhesives, 2013. **41**: p. 24-32.
38. Fiore, V., et al., *Effect of curing time on the performances of hybrid/mixed joints.* Composites Part B, 2013. **45**: p. 911-918.
39. Marannano, G. and B. Zuccarello, *Numerical experimental analysis of hybrid double lap aluminum-CFRP joints.* Composites Part B, 2015. **71**: p. 29-39.
40. Campbell Jr, F.C., *Manufacturing technology for aerospace structural materials*. 2011: Elsevier.
41. *MIL Military Handbook. HDBK-17-3F: Composite Materials Handbook, Volume 3 Polymer Matrix Composites Materials Usage, Design and Analysis*. Vol. 6. 2002: US Department of Defense.
42. Kweon, J.H., et al., *Failure of carbon composite-to-aluminum joints with combined mechanical fastening and adhesive bonding.* Composite Structures, 2006. **75**: p. 192-198.
43. Jen, M.H.R. and W.H. Lin, *Innovative fracture tests of single-lapped bolted and bonded composite joints.* Journal of reinforced plastics and composites, 2000. **19**: p. 1444-1473.
44. Lin, W.H. and M.H.R. Jen, *The strength of bolted and bonded single-lapped composite joints in tension.* Journal of Composite Materials, 1999. **33**: p. 640-666.
45. Fu, M. and P.K. Mallick, *Fatigue of hybrid (adhesive/bolted) joints in SRIM composites.* International Journal of Adhesion & Adhesives, 2001. **21**: p. 145-159.
46. Lees, J.M. and G. Makarov, *Mechanical/bonded joints for advanced composite structures.* Structures \& Buildings, 2004. **157**: p. 91-97.
47. Allred, R.E. and T.R. Guess, *Efficiency of double-lapped composite joints in bending.* Composites, 1978. **9**: p. 112-118.
48. Lee, Y.H., et al., *Failure load evaluation and prediction of hybrid composite double lap joints.* Composite Structures, 2010. **92**: p. 2916-2926.
49. Gomez, S., J. Onoro, and J. Pecharroman, *A simple mechanical model of a structural hybrid adhesive/riveted single lap joint.* International Journal of Adhesion & Adhesives, 2007. **27**: p. 263-267.
50. Sadowski, T., P. Golewski, and E. Zarzeka-Raczkowska, *Damage and failure processes of hybrid joints: adhesive bonded aluminum plates reinforced by rivets.* Computational Materials Science, 2010. **50**: p. 1256-1262.
51. Bodjona, K. and L. Lessard, *Load sharing in single-lap bonded/bolted composite joints. Part II: Global sensitivity analysis.* Composite Structures, 2015. **129**: p. 276-283.

52. Paroissien, E., et al., *Hybrid (bolted/bonded) joints applied to aeronautic parts: Analytical two-dimensional model of a single-lap joint.* Journal of Aircraft, 2007. **44**(2): p. 573-582.
53. Bodjona, K. and L. Lessard, *Nonlinear static analysis of a composite bonded/bolted single-lap joint using the meshfree radial point interpolation method.* Composite Structures, 2015. **134**: p. 1024-1035.
54. Pirondi, A. and F. Moroni, *Clinch-bonded and rivet-bonded hybrid joints: application of damage models for simulation of forming and failure.* Journal of Adhesion Science and Technology, 2009. **23**: p. 1547-1574.
55. Chakherlou, T.N., et al., *Investigation of the fatigue life and crack growth in torque tightened bolted joints.* Aerospace Science and Technology, 2011. **15**: p. 304-313.
56. Oskouei, R.H. and T.N. Chakherlou, *Reduction in clamping force due to applied longitudinal load to aerospace structural bolted plates.* Aerospace Science and Technology, 2009. **13**: p. 325-330.
57. Chen, H.S., *The static and fatigue strength of bolted joints in composites with hygrothermal cycling.* Composite Structures, 2001. **52**(3): p. 295-306.
58. Crews, J.H. and K.N. Shivakumar, *An equation for bolt clamp-up relaxation in transient environments.* Journal of Composites, Technology and Research, 1982. **4**: p. 132-135.
59. Bodjona, K., et al., *Load sharing in single-lap bonded/bolted composite joints. Part I: Model development and validation.* Composite Structures, 2015. **129**: p. 268-275.
60. Paroissien, E., *Contribution aux assemblages hybrides (boulonnés/collés) - Application aux jonctions aéronautiques*, in *Institut Génie Mécanique*. 2006, Université Toulouse III - Paul Sabatier: Toulouse. p. 287.
61. da Silva, L.F.M., et al., *Effect of adhesive type and thickness on the lap shear strength.* The journal of adhesion, 2006. **82**(11): p. 1091-1115.
62. Lehman, G.M. and A.V. Hawley, *Joint and attachment investigation volume 1. Technical discussion and summary*. 1969, United States Air Force.
63. Gray, P.J., R.M. O'Higgins, and C.T. McCarthy, *Effect of thickness and laminate taper on the stiffness, strength and secondary bending of single-lap, single-bolt countersunk composite joints.* Composite Structures, 2014. **107**: p. 315-324.
64. Gray, P.J., R.M. O'Higgins, and C.T. McCarthy, *Effects of laminate thickness, tapering and missing fasteners on the mechanical behaviour of single-lap, multi-bolt, countersunk composite joints.* Composite Structures, 2014. **107**: p. 219-230.
65. Esmaeili, F., T.N. Chakherlou, and M. Zehsaz, *Investigation of bolt clamping force on the fatigue life of double lap simple bolted and hybrid (bolted/bonded) joints via experimental and numerical analysis.* Engineering Failure Analysis, 2014. **45**: p. 406-420.
66. Imanaka, M., K. Haraga, and T. Nishikawa, *Fatigue strength of adhesive/rivet combined lap joints.* The journal of Adhesion, 1995. **49**: p. 197-209.
67. Esmaeili, F., M. Zehsaz, and T.N. Chakherlou, *Investigation the effect of tightening toque on the fatigue strength of double lap simple bolted and hybrid (bolted-bonded) joints using volumetric method.* Materials and Design, 2014. **63**: p. 349-359.

68. Hoang-Ngoc, C.T. and E. Paroissien, *Simulation of single-lap bonded and hybrid (bolted/bonded) joints with flexible adhesive.* International Journal of Adhesion and Adhesives, 2010. **30**: p. 117-129.
69. Paroissien, E., et al. *Improving the fatigue life of aeronautical single-lap bolted joints thanks to the hybrid (bolted/bonded) joining technology*. in *25th Symposium of the International Committee on Aeronautical Fatigue*. 2009. Rotterdam: Springer Netherlands.
70. Volkersen, O., *Die nietkraftverteilung in zugbeanspruchten nietverbindungen mit konstanten laschenquerschnitten.* Luftfahrtforschung, 1938. **15**: p. 41-47.
71. Goland, M. and E. Reissner, *The Stresses in Cemented Joints.* Journal of Applied Mechanics, 1944. **66**: p. 17-27.
72. Barut, A. and E. Madenci, *Analysis of Bolted-Bonded Composite Single-Lap Joints under Combined In-Plane and Transverse Loading.* Composite Structures, 2009. **88**(4): p. 579-594.
73. International, A., *Standard test method for bearing response of polymer matrix composite laminates*, in *ASTM Standard D5961/D5961M-13*. 2013.
74. McCarthy, M., et al., *Three-dimensional finite element analysis of single-bolt, single-lap composite bolted joints: part I—model development and validation.* Composite structures, 2005. **71**(2): p. 140-158.
75. Gray, P. and C. McCarthy, *A global bolted joint model for finite element analysis of load distributions in multi-bolt composite joints.* Composites Part B: Engineering, 2010. **41**(4): p. 317-325.
76. Hyer, M., E.C. Klang, and D.E. Cooper, *The effects of pin elasticity, clearance, and friction on the stresses in a pin-loaded orthotropic plate.* Journal of Composite Materials, 1987. **21**(3): p. 190-206.
77. Wang, C.H. and P. Chalkley, *Plastic yielding of a film adhesive under multiaxial stresses.* International Journal of Adhesion and Adhesives, 2000. **20**(2): p. 155-164.
78. International, A., *Standard test method for tensile properties of plastics*, in *ASTM D638*. 2014.
79. Lim, G.H., *Mechanical characterization of flexible epoxy adhesive and its influence on hybrid joint design*, in *Mechanical Engineering*. 2016, McGill University: Montreal.
80. Saltelli, A., et al., *Variance based sensitivity analysis of model output. Design and estimator for the total sensitivity index.* Computer Physics Communications, 2010. **181**(2): p. 259-270.
81. Sobol, I.M., *Global sensitivity indices for nonlinear mathematical models and their Monte Carlo estimates.* Mathematics and Computers in Simulation, 2001. **55**: p. 271-280.
82. Saltelli, A., S. Tarantola, and K.P.-S. Chan, *A quantitative model-independent method for global sensitivity analysis of model output.* Technometrics, 1999. **41**(1): p. 39-56.
83. Godwin, E.W. and F.L. Matthews, *A review of the strength of joints in fibre-reinforced plastics: part 1. Mechanically fastened joints.* Composites, 1980. **11**(3): p. 155-160.

84. Gleich, D.M., M.J.L. Van Tooren, and A. Beukers, *Analysis and evaluation of bondline thickness on failure load in adhesively bonded structures.* Journal of Adhesion Science and Technology, 2001. **15**(9): p. 1091-1101.
85. McCarthy, M.A. and V.P. Lawlor, *Measurement of bolt pre-load in torqued composite joints.* Strain, 2005. **41**(3): p. 109-112.
86. DiNicola, A.J. and S.C. Fantle, *Bearing strength behavior of clearance-fit fastener holes in toughened graphite/epoxy laminates.* ASTM Special Technical Publication, 1993. **1206**: p. 220-237.
87. McCarthy, M.A., V.P. Lawlor, and W.F. Stanley, *An Experimental Study of Bolt-Hole Clearance Effects in Single-lap, Multibolt composite joints.* Journal of Composite Materials, 2005. **39**(9): p. 799-825.
88. da Silva, L.F.M., A. Ochsner, and R.D. Adams, *Handbook of adhesion technology: with 97 tables*. 2011, Berlin Heidelberg: Springer.
89. Groth, H., *Stress singularities and fracture at interface corners in bonded joints.* International Journal of Adhesion and Adhesives, 1988. **8**(2): p. 107-113.
90. Wang, C. and L. Rose, *Compact solutions for the corner singularity in bonded lap joints.* International journal of adhesion and adhesives, 2000. **20**(2): p. 145-154.
91. Yang, P.C., C.H. Norris, and Y. Stavsky, *Elastic wave propagation in heterogeneous plates.* International Journal of Solids and Structures, 1966. **2**(4): p. 665-684.
92. Hoyt, D., P.J. Minguet, and S.H. Ward, *Strength and fatigue life modeling of bonded joints in composite structure.* Journal of Composites, Technology and Research, 2002. **24**(3): p. 188-208.
93. Ramkumar, R., et al., *Strength Analysis of Composite and Metallic Plates Bolted Together by a Single Fastener*. 1985, DTIC Document.
94. Chang, F.-K., R.A. Scott, and G.S. Springer, *Failure strength of nonlinearly elastic composite laminates containing a pin loaded hole.* Journal of Composite Materials, 1984. **18**(5): p. 464-477.
95. Yamada, S. and C. Sun, *Analysis of laminate strength and its distribution.* Journal of Composite Materials, 1978. **12**(3): p. 275-284.
96. Belytschko, T., et al., *Meshless methods: an overview and recent developments.* Computer methods in applied mechanics and engineering, 1996. **139**(1): p. 3-47.
97. Fasshauer, G.E., *Meshfree approximation methods with MATLAB*. Vol. 6. 2007: World Scientific.
98. Dinis, L., R.N. Jorge, and J. Belinha, *Analysis of plates and laminates using the natural neighbour radial point interpolation method.* Engineering Analysis with Boundary Elements, 2008. **32**(3): p. 267-279.
99. Liu, G.-R., *Meshfree methods: moving beyond the finite element method*. 2009: Taylor & Francis.
100. Belinha, J., *Meshless Methods in Biomechanics*. 2014: Springer.
101. Duflot, M., *Application des méthodes sans maillage en mécanique de la rupture*, in *Département d'Aérospatiale et Mécanique*. 2004, Université de Liège.

102. Hertz, P., *Über den gegenseitigen durchschnittlichen Abstand von Punkten, die mit bekannter mittlerer Dichte im Raume angeordnet sind.* Mathematische Annalen, 1909. **67**(3): p. 387-398.
103. Corti, C.W., P. Cotterill, and G.A. Fitzpatrick, *The Evaluation of the Interparticle Spacing in Dispersion Alloys.* International Metallurgical Reviews, 1974. **19**(1): p. 77-88.
104. Liu, G., et al., *A nodal integration technique for meshfree radial point interpolation method (NI-RPIM).* International Journal of Solids and Structures, 2007. **44**(11): p. 3840-3860.
105. Timoshenko, S.P. and S. Woinowsky-Krieger, *Theory of plates and shells*. 1959: McGraw-hill.
106. Marler, R.T. and J.S. Arora, *The weighted sum method for multi-objective optimization: new insights.* Structural and multidisciplinary optimization, 2010. **41**(6): p. 853-862.
107. Liu, G., et al., *A linearly conforming radial point interpolation method for solid mechanics problems.* International Journal of Computational Methods, 2006. **3**(04): p. 401-428.
108. Zhao, X., et al., *A linearly conforming radial point interpolation method (LC-RPIM) for shells.* Computational Mechanics, 2009. **43**(3): p. 403-413.
109. Felippa, C. *FEM Convergence Requirements*. Introduction to Finite Element Methods 24/02/2016]; Available from: http://www.colorado.edu/engineering/CAS/courses.d/IFEM.d/IFEM.Ch19.d/IFEM.Ch19.pdf.
110. Kikuchi, N. and J.T. Oden, *Contact problems in elasticity: a study of variational inequalities and finite element methods*. Vol. 8. 1988: siam.
111. Kelley, C.T., *Solving nonlinear equations with Newton's method*. Vol. 1. 2003: Siam.
112. Simo, J.C. and T.J. Hughes, *Computational inelasticity*. Vol. 7. 2006: Springer Science & Business Media.
113. Wriggers, P. and T.A. Laursen, *Computational contact mechanics*. Vol. 30167. 2006: Springer.
114. Diaz, J., et al., *Benchmarking of three-dimensional finite element models of CFRP single-lap bonded joints.* International Journal of Adhesion and Adhesives, 2010. **30**(3): p. 178-189.
115. Ireman, T., T. Nyman, and K. Hellbom, *On design methods for bolted joints in composite aircraft structures.* Composite Structures, 1993. **25**(1-4): p. 567-578.
116. Kradinov, V., et al., *Bolted double-lap composite joints under mechanical and thermal loading.* International journal of solids and structures, 2001. **38**(44): p. 7801-7837.
117. Phillips, S.L.-C., Pedro

Laliberte, Jeremy and L. Lessard, *Influence of Adhesive Modulus on Load Transfer in Hybrid Bolted/Bonded Composite Joints.* (Journal paper in preparation), 2016.

118. Chowdhury, N.M., et al., *Static and fatigue testing bolted, bonded and hybrid step lap joints of thick carbon fibre/epoxy laminates used on aircraft structures.* Composite Structures, 2016. **142**: p. 96-106.
119. Hahn, H. and S. Choi, *The effect of loading parameters on fatigue of composite laminates: part V*. 2001, DTIC Document.

120. Kradinov, V., E. Madenci, and D. Ambur, *Combined in-plane and through-the-thickness analysis for failure prediction of bolted composite joints.* Composite structures, 2007. **77**(2): p. 127-147.

Appendix A. Joint Edge Load Derivation

The bolt is assumed to be made of S82 aerospace grade steel (τ_y = 882 MPa). Since it is practically impossible to determine the failure loads of all of the laminates in the design space *a priori*, it is assumed that bolt yield is the limiting design case. It is hence required to calculate the greatest possible bolt shear load. This occurs for designs having the maximum W/D = 10 and minimum E/D = 3. Since in the worst case the adhesive will have yielded all the way the through, and given a minimum σ_{yt} = 6 MPa for the adhesive, the least force F_a that the adhesive by itself will sustain is:

$$F_a = 6 \times 10^6 \left(2\frac{E}{D}D\right)\left(\frac{W}{D}D\right) \tag{A.1}$$

The total applied load F_t is:

$$F_t = N_1 \left(\frac{W}{D} \cdot D\right) \tag{A.2}$$

Furthermore the maximum bolt load F_b is:

$$F_b = \tau_y \frac{\pi D^2}{4} \tag{A.3}$$

Finally, the static equilibrium of forces is invoked;

$$F_t = F_a + F_b \tag{A.4}$$

The only unknown is N_1, the edge load causing bolt failure. Solving Eqns. A.1-A.4 simultaneously, it is found that the limit load $N_1 \approx$ 650,000 N/m. Other loads are also considered: a medium fatigue load that is 60% of this figure, i.e., $N_1 \approx$ 450,000 N/m (the reasoning for this is given in [119]) as well as a low fatigue load that is 40% of the limit load i.e. $N_1 \approx 250{,}000$ N).

Appendix B. Method for Calculating Through-Thickness Stress Concentration

The method of Kradinov et al. [120], based on the original method by Ramkumar and Saether [93], consists of the following procedure:

1) Determine the bolt load distribution based on an analysis such as the one proposed in Chapter 5, then isolate each bolt and model it as a beam on an elastic foundation (see Figure B.1)
2) Calculate the beam deflection and spring forces. The obtained spring forces are considered as the corrected ply loads. The stress concentration factor for a particular ply is thus the ratio of its spring force uncorrected ply load (based on the in-plane contact stresses)
3) Evaluate ply level failure along a concentric path that is a characteristic distance away from the hole edge (based the corrected ply stresses)

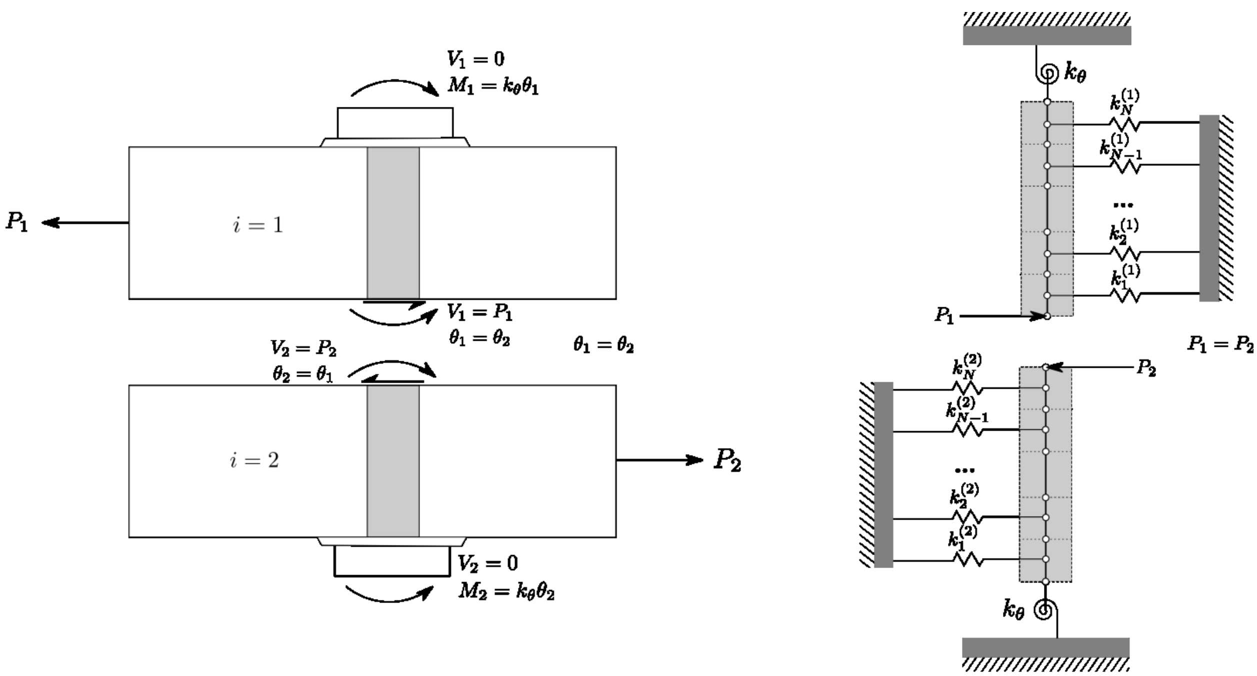

(a) Free body diagram of through-thickness section **(b) Mathematical representation**

Figure B-1: Mathematical representation of through-thickness problem

The bolt load is easily extracted from the model described in Chapter 5 as the bolt shear stress resultant at the center of the bondline. Considering the beam on an elastic foundation analysis, the method for calculating the spring constants is as follows. The ply load resultant $p_{k,i}^{(l)}$ for the *k*th ply of the *i*th laminate $i \in \{1,2\}$ due to just in-plane loading is calculated as:

$$p_{k,i}^{(l)} = \sqrt{\left(p_{(k,i)x}^{(l)}\right)^2 + \left(p_{(k,i)y}^{(l)}\right)^2} \tag{B.1}$$

where the ply load x and y components are:

$$p_{(k,i)x}^{(l)} = a_{k,l} t \int_0^{2\pi} \sigma_{rr}(r = a_{k,l}) \cos\theta \, d\theta \tag{B.2}$$

and:

$$p_{(k,i)y}^{(l)} = a_{k,l} t \int_0^{2\pi} \sigma_{rr}(r = a_{k,l}) \sin\theta \, d\theta \tag{B.3}$$

The spring constants, applied to the center of each ply, should reflect the ply stiffnesses. They are thus approximated as the ratio of the maximum hole enlargement to the ply load $p_{k,i}^{(l)}$. Note that the maximum hole enlargement is constant for all plies in the adherend. Thus:

$$k_{k,i}^{(l)} = \frac{p_{k,i}^{(l)}}{\gamma_k^{(l)}} \quad , \quad i = [1, N_k] \tag{B.4}$$

The actual beam on elastic foundation model, shown in Figure B.1, is simply a model of a Timoshenko beam with translational springs at the ply center locations and rotational springs attached to its ends. The spring constant of the rotational springs is equal to the bolthead spring constant k_θ used in the model of Chapter 5. At the interface, continuity of the beam is enforced. This model can easily be solved using a simple matrix method. The solution is described in detail by Kradinov et al. [120] and is therefore not further addressed in this thesis.